DESIGN, MEASUREMENT AND ANALYSIS OF MULTIMODE LIGHT GUIDES AND WAVEGUIDES FOR DISPLAY SYSTEMS AND OPTICAL BACKPLANE INTERCONNECTIONS

Kai Wang

Department of Electronic and Electrical Engineering

University College London, (UCL)

PhD Thesis

July 2014

Supervisors

Dr. D. R. Selviah

Dr. F.A. Fernández

Declaration

I, Kai Wang confirm that the work presented in this thesis is my own. Where information has been derived from other sources, I confirm that this has been indicated in the thesis.

Signature: **Date:** 21 July 2014

Abstract

The aim of the research in this thesis was to design and model multimode lightguides for optimising visible light for liquid crystal display systems and to design, model and experimentally test infrared light propagation within polymer multimode waveguides as board-to-board interconnects for high data rate communication.

Ray tracing models the behaviour of a novel LCD colour separating backlight to optimize its efficiency by establishing the optimum dimensions and position for a unique micro-mirror array within the light guide. The output efficiency increased by 38.2% compared to the case without the embedded mirror array.

A novel simulation technique combined a model of liquid crystal director orientation and a non-sequential ray tracing program was used first time to compute the reflected intensity from a LCOS device for a rear projection TV system. The performance of the LCOS display was characterised by computing the contrast ratio over a $\pm 15^\circ$ viewing cone.

Photolithographically manufactured embedded multimode waveguides made from acrylate Truemode® polymer are characterized by measuring the optical transmission loss of key waveguide components including. straight, bend and crossing. Design rules derived from the experimental measurement were used to optimize optical PCB (OPCB) layout. A most compact and complex optical interconnects layout up-to-date for data centres, including parallel straight waveguide sections, cascaded 90° bends and waveguide crossing other than 90° angles, was designed, tested and used in an optic-electrical demonstration platform to convey a 10.3 Gb/s data. A further new method for reducing the end facet roughness and so the coupling loss, by curing a thin layer of core material at the end of the waveguide facet to cover the roughness fluctuations, was proposed and successfully demonstrated giving the best results reported to date resulting in an improvement of 2.8 dB which was better than the results obtained by using index matching fluid.

Table of Contents

Acknowledgements

During the course of my research I was inspired, motivated and advised by my supervisors, Dr David R. Selviah, Dr Anibal Fernandez and Dr Sally Day, who selflessly helped me through the process, especially, David who acted as a tutor, a friend and a father. He set a right example for me by showing his passion in innovations, meticulous attitude in research and kindness to people. I learnt from him how to be a good researcher.

I would send great appreciations to Dr. Tony Kenyon, Dr. Chin-Pang Liu, Dr. John Mitchell and Dr Benn Thomsen for their advice and helpful suggestions; Tom Crummey, Lee Heagney, Scott Landers, Andrew Moss and Gerald Mcbrearty for their essential technical supports; my colleagues Dr. Ioannis PAPAKONSTANTINOU, Teruyuki Kataoka, Dr. Hadi Baghsiahi, Dr. Janti Shawash, Ze Chen, Dr. Eero Willman and Dr. Richard James for helpful advises and made a pleasant working environment. I am really grateful about the precious time we have spent together.

I would like to thank the Department of Electronics and Electrical Engineering, UCL for giving me the opportunity to peruse my research ambition. I like to thank The Institution of Engineering and Technology, the IET, for offering me two research scholarships. They were not only the praises of my research achievements but also the financial supports during the first two years of my study at UCL. I am grateful to UCL Advances for allowing me to explore the commercial potential of my research by awarding me a PhD scholarship and to Dr Mike Arnott and Timothy Barnes for being inspiring mentors in this business case study.

I thank the European Commission for supporting the project of LCOS4LCOS, Liquid Crystal on Silicon for Low Cost Optical Systems, under the Framework 5 programme project No IST-2001-34591, TSB (latterly DTI) for funding via StorLite: Storage Systems Optical Networking, GR/S28136/01 and Flagship Project: Integrated and Optical and Electronic Interconnect PCB Manufacturing, FS/06/01/01 funded from EPSRC via An Innovative Electronics Manufacturing Research Centre, I*e*MRC, EP/H03014X/1, and Photonic Enabled Data Transport from Millimetric to Megametric Scales, EP/D037026/1,

I thank Dave Milward, for managing the OPCB project, Ken Hopkins, Paul Stevens and Richard Pitwon, Xyratex Technology Ltd, for helpful discussions. Navin Suyal, Habib Rehman, Exxelis for preparation of the Truemode® polymer and photolithographic

fabrication of the waveguides, Karen Hueston, David J. Deshazer, Dow Corning Corporation for supply of the polysiloxane waveguides, Gary Hinde, Cadence for software support and Jeremy Rygate, Jonathan Calver and Witold Kandulski, Stevenage Circuits Limited, for manufacturing and assembling the optical back planes.

Most of all, I am very grateful for the supports from my families. To Zhaoying Zhang, my wife, for her love, patience, and taking care of our family. To my parents and my aunt, for bring me up and looking after me and encouraging me to pursue my dreams. Without them always standing by my side, I would never be who I am.

Table of Abbreviations

µm	Micro metre
ASAP	Advanced system analysis program
BPM	Beam propagation method
CCFLs	Cold cathode fluorescent lamps
cm	Centimetre
CR	Contrast ratios
CRT	Cathode ray tube
CW	Continuous Wave
E-CAD	Electronic Computer Aided Design
FDTD	Finite Difference Time Domain
FEM	Finite element method
Gbit/s	Giga bit per second
GRIN	Gradient-index
IC	Integrated circuits
IR	Infra Red
IT	Information technology
LC	Liquid crystal
LCD	Liquid Crystal Display
LCOS	Liquid Crystal on Silicon
LCOS4LCOS	Liquid Crystal On Silicon For Low Cost Optical Systems
LED	Light Emitting Diode
MHz	Mega Hertz
mm	milli metre
MM	Multi mode
MMF	Multi mode fibre
MT	Mechanical Transfer
MTN	Mixed twisted nematic
NA	Numerical Aperture
OLED	Organic light emitting diode
OPCB	Optical Printed Circuit Board
PBS	Polarizing beam splitter

PCB	Printed Circuit Board
PD	Photo detector
PMMA	Poly-methylmethacrylate
RGB	Reg, Green, Blue
RMS	Root Mean Squre
RPTV	Rear Projection TV
SI	Step index
SM	Single mode
SMF	Single mode fibre
ST	Straight Tip
TFT	Thin film transistor
UCL	University College London
UV	UltraViolet
VAN	Vertically Aligned Nematic
VCSEL	Vertical-cavity surface-emitting laser
W	Watt
WDM	Wavelength Division Multiplexing
XFP	10 Gigabit Small Form Factor Pluggable

Table of Figures

Table of Tables

Chapter 1 Introduction

This thesis covers 3 research topics:

1) The use of a multimode optical lightguide as a backlight for liquid crystal displays (LCDs). The backlight was used to improve output efficiency and reduce overall power consumption of a LCD system (chapter 5).

2) The use of a liquid crystal on silicon (LCOS) chip for a rear projection television (RPTV) system. The research was focused on modelling of the optical properties of the LCOS chip to improve the viewing angle of the RPTV (chapter 6).

3) The use of multimode polymer optical waveguides as board-to-board interconnects on opto-electrical printed circuits board (OPCB). The optical insertion loss of polymer waveguides was investigated to derive design rules for laying out the geometry of waveguide interconnects (chapter 7-9).

A ray tracing method was used to model all of the three systems.

1.1 The Aim

The aim of the work is to carry out design, modelling, measurement and development of a novel hybrid ray tracing technique that combined either a dynamic liquid crystal director model or image processing techniques to analyse in novel ways

- the optical performance of multimode light guides including a novel colour separating backlight for LCDs,
- the effect of angular variation of the optical properties of a nematic liquid crystal in an LCOS for a rear projection TV system
- the design of a compact polymer multimode optical waveguides interconnects layout incorporating cascaded bends and non-orthogonal crossings for high bit rate (>10 Gb/s) communication on OPCB

1.2 Motivation

1.2.1 Colour Separating Backlight for Liquid Crystal Displays (LCDs)

LCD technology has been improved significantly over the past 20 years, from small, binary colour displays to advanced modules with large panel, large colour gamut and fast scanning frequency [1-1] (200 Hz is commonly offered in the market). The

competition of the display market is becoming extremely intense, new and emerging technologies: 3D [1-2, 3], LED [1-4,5], touch screens [1-6], OLED lighting and displays [1-7-9], flexible displays [1-10,11] and e-paper [1-12,13] are increasingly penetrating the market [1-14,15]. Companies have to invest seriously at all opportunities to improve the quality and to lower price in order to make their products stand out in the market.

One of the major challenges is to increase the efficiency of the backlight illumination system [1-16] for LCD, as inefficient backlights for LCDs are the vital drawback for the power consumption and battery lifetime in portable devices. Currently only about 4% of the light generated by the light source (typically light emitting diodes - LEDs, or cold cathode fluorescent lamps - CCFLs) is available to the viewer: about 60% light could emerge from the light guide [1-17], approximately 50% is lost in the polarizer [1-18] (although there are ways of recovering some of this loss [1-19,20]), a further 50% of light is lost through absorption by the black mask aperture, typically used to separate pixels and protect the thin film transistor structures (TFTs) [1-21,22], 27% of the remaining light is lost within the colour filters [1-23,24] used to generate the red, green and blue sub-pixels required for a colour display.

The research reported in this thesis describes a novel colour separating backlight illumination for LCDs. Non-sequential ray tracing technology was used to optimise the design. The detailed computer modelling results show that the backlight can successfully extract and separate three colours, red, green and blue, from a light source and will potentially allow manufacturers to remove the costly colour filter layer of the LCD, which according to an interview with a Sharp senior executive (Jonathan Mather [1-25]), represents 30 – 40% of the module's cost. A design of a micro mirror layer embedded in the backlight to improve the efficiency of the colour separating backlight was invented and the modelled result showed 38.2% increase of the backlight output efficiency.

1.2.2 Modelling of LCOS for a Rear Projection Television

A new modelling technique combining a ray-tracing program, a full dynamic liquid crystal director model and a LC optics model to simulate the performance of a Rear-projection television (RPTV) system using an LCOS panel was proposed. Detailed

simulation of the system performance was required because of the necessity to maintain very high contrast ratios and intensity uniformity in such systems and because of the variable viewing angle characteristics of LCDs. The author demonstrated how combined ray tracing and LC modelling could reveal useful information about viewing angle variation over the LCOS panel area, which would not be apparent from LC modelling alone. The effects of non-uniform illumination over different areas of the LCOS chip on the contrast ratio and reflectivity were shown.

1.2.3 Optical Printed Circuit Board with Optics and Electronics

Optical interconnections are one of the attractive approaches to replace electrical copper interconnections for high data rate, i.e. higher than 10 Gbit/s, communication. Low manufacturing costs of the optical interconnections can be achieved by using a form of waveguide with a higher refractive index polymer core surrounded by a lower refractive index polymer cladding [1-26-29], fabricated on integrated optical PCBs containing optical and electrical interconnections (OPCBs) [1-30]. OPCB technology offers significant performance over conventional PCBs, higher data rates, no electromagnetic interference, reduction in power consumption and over a 50% reduction in PCB size and weight. There are large and rapidly growing demands for OPCB product by many industries including the IT, telecommunications, aerospace and space sectors [1-31].

Optical waveguide research, however, has been limited to the academic sector and has not been adapted in any commercial product. This research is to address the problems in PCB manufacture, polymer waveguide design, optical PCB connectors, system architecture, and CAD design to develop and exploit OPCB technologies to make it commercially available. Figure 1-1 is an OPCB architecture that could be used in electronic cabinets or racks that form the heart of a variety of IT systems and incorporate connectors to allow other line cards to be attached at right angles.

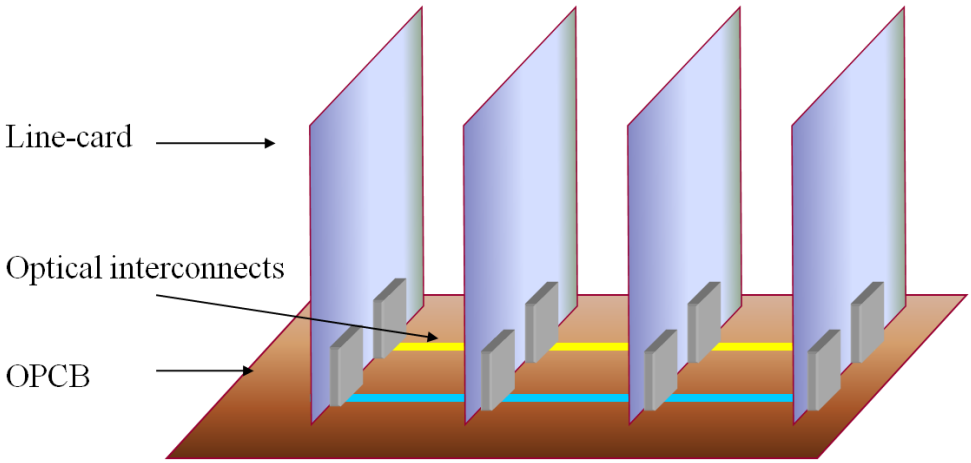

Figure 1-1 Schematic system integrated electrical and optical interconnections on a backplane and 4 connected line cards

The line cards need to be fully connected by optical interconnections. The author characterized every waveguide component used in each of the interconnections to assess the cascaded optical transmission loss per connection and to limit it to less than the error free threshold in its corresponding optical receiver (-12 dBm). The waveguide key structures included straight waveguides of various widths, 90 ° bends of a range of radii and novel crossings between two waveguides at a range of angles. Once the optical loss had been measured in novel ways for each photolithography fabricated waveguide component (Exxelis Ltd), the author established waveguide design rules for each fabrication technique and incorporated them into a commercial automatic design rule checker and constraint manager layout software for PCBs so that PCB designers can easily include optical connection layers without detailed knowledge of the optics involved. The optical board layout can then be optimised to minimise the waveguide optical transmission loss and optical cross-talk. The author used Cadence and designed the most compact and complex optical waveguide interconnections layout up-to-date for an electrical-optical printed circuit board. Based on the feedbacks from the author, Cadence added new design functions to Allegro versions 16.2 in 2009 including connect arcs and line segments by snapping to their geometry start and end points, which improved its ability of design and layout of electronic and photonic interconnect.

1.3 Structure of Thesis

Technical literature reviews are in chapters 2, 3 and 4. The new research is presented in chapters 5 to 9. The conclusions and future work are in chapter 10. A

commercialization assessment report is presented in appendix A and a list of the author's publications arising from the research in this thesis is given in appendix B.

Chapter 2 reviews optical modelling tools for modelling multimode light guides and waveguides. It compares the limitations of each tool and explains the reason for choosing non-sequential ray tracing as the most suitable method for the simulation for different types of light guides for the research in this thesis, including backlight for liquid crystal displays, and light engines for rear projection displays. Closest works carried out by other researchers have been reviewed.

Chapter 3 reviews simulations and measurements that have been carried out by various groups in other universities, companies and institutes on the insertion loss and crosstalk of waveguide crossings.

In chapter 4, the research on designing the optical interconnects for board-to-board systems and establishing the optical loss of various waveguide components are reviewed. Previous research on the optical coupling loss due to the waveguide end facet roughness is also reviewed. For a University College London (UCL) optically interconnected system, the contribution from Seagate Technology PLC (formerly Xyratex Technology Ltd) and other projects partners such as IBM are introduced and acknowledged where appropriate.

Chapter 5 introduces the structure of the novel colour separating backlight for liquid crystal displays (LCDs) and shows how the output efficiency of the light guide is improved by optimising the design of each optical component used in the backlight.

Chapter 6 describes how a model of the liquid crystal director orientation is combined with a non-sequential ray tracing program to compute the reflected intensity from an LCOS device for a rear projection TV system. The effects of non-uniform illumination over different areas of the LCOS chip on the contrast ratio and reflectivity are shown.

Chapter 7 describes the ray tracing simulation and experimental measurement of the optical loss and crosstalk of multimode step-index photolithographically fabricated polyacrylate polymer (Trumode^{TM}) waveguide crossings.

Chapter 8 investigates the optical insertion transmission losses of several multimode polymer waveguide components, i.e. straight waveguides, crossings at non-orthogonal angles and 90° bends and describes how design rules are established for photolithographically manufactured acrylate polymer optical multimode waveguide components by optical experimental measurements made on the manufactured waveguide component. A new technique for measuring the transmitted power at waveguide crossings is reported. The result of environmental testing of such polymer waveguides against temperature and humidity is reported for the first time.

Chapter 9 reports the most compact and complex optical waveguide interconnections layout to date for an electrical-optical printed circuit board. A method for low cost, high precision, passive optical assembly is presented. A demonstration platform was constructed and high speed optical data transfer at 10.3125 Gb/s is demonstrated through a polymer waveguide interconnect layer embedded into a 262 mm × 240 mm × 4.3 mm electro-optical midplane. A further new method for reducing the end facet roughness and so the coupling loss, by curing a thin layer of core material at the end of the waveguide facet to cover the roughness fluctuations is presented.

In chapter 10, the conclusions of the new research reported in the thesis are discussed and further research is suggested.

Chapter 1 References

[1-1]. B.-D. Choi, “Line-Time Extension Driving Method with Image Quality Enhancement for LCD Monitors and TVs,” IEEE Transactions on Consumer Electronics, vol. 55, 2009, pp. 2257-2263.

[1-2]. R. Brar, P. Surman, and I. Sexton, “Laser-Based Head-Tracked 3D Display Research,” Journal of Display Technology, vol. 6, 2010, pp. 531-547.

[1-3]. M. Kuwata and K. Sakamoto, “Glasses-Free 3D Display System Using Grating Film for Viewing Angle Control,” Entertainment Computing - ICEC 2010, vol. 6243, 2010, pp. 449-451.

[1-4]. Y. Liu, Z. Yang, and S. Wang, “A Novel Sequential-Color RGB-LED Backlight Driving System with Local Dimming Control and Dynamic Bus Voltage Regulation,” IEEE Transactions on Consumer Electronics, vol. 56, 2010, pp. 2445-2452.

[1-5]. S. Hsia and J. Kuo, “Cost Effective Design and Implementation of Scanning-Based LED Backlight for LCD Module,” IEEE Transactions on Consumer Electronics, vol. 56, 2010, pp. 2037-2042.

[1-6]. Y. Lee, “Comparison of the conventional point-based and a proposed finger probe-based touch screen interaction techniques in a target selection task,” International Journal of Industrial Ergonomics, vol. 40, 2010, pp. 655-662.

[1-7]. Y. Nakajima, T. Takei, Y. Fujisaki, H. Fukagawa, M. Suzuki, G. Motomura, H. Sato, T. Yamamoto, and S. Tokito, “Improvement in image quality of a 5.8-in. OTFT-driven flexible AMOLED display,” Journal of the Society for Information Display, vol. 19, 2011, p. 94.

[1-8]. T. Arai, N. Morosawa, and K. Tokunaga, “Highly reliable oxide-semiconductor TFT for AMOLED displays,” Journal of the Society for Information Display, vol. 19, 2011, pp. 205-211.

[1-9]. C. Han, Y. Tak, and B. Ahn, “15-in. RGBW panel using two-stacked white OLED and color filters for large-sized display applications,” Journal of the Society for Information Display, vol. 19, 2011, pp. 190-195.

[1-10]. M. Christophersen and B. Phlips, “Recent Patents on Electrophoretic Displays and Materials,” Recent Patents on Nanotechnology, vol. 4, 2010, pp. 137-149.

[1-11]. J. Liu, T. Lee, and C. Wen, “High-performance organic-inorganic hybrid plastic substrate for flexible displays and electronics,” Journal of the Society for Information Display, vol. 19, 2011, pp. 63-69.

[1-12]. N. Kim and K. Han, “Future direction of direct writing,” Journal of Applied Physics, vol. 108, 2010.

[1-13]. J. Heikenfeld, P. Drzaic, and J. Yeo, “A critical review of the present and future prospects for electronic paper,” Journal of the Society for Information Display, vol. 19, 2011, pp. 129-156.

[1-14]. J.D. Hamilton, “US FPD Conference Keynotes to Address Economic Recovery and the Future of CE Retail,” DisplaySearch [Online], 2011.

[1-15]. Q. Technology, “New displays for e-readers: Read all about it,” The Economist [Online], 2009.

[1-16]. M.-H. Huang, Y.-C. Tsai, and K.-H. Chen, “Energy-Recycling (ER) Technique for a Direct-Lit Intelligent Power Management Backlight Unit (BLU),” IEEE Transactions on Power Electronics, vol. 25, Oct. 2010, pp. 2588-2598.

[1-17]. L. S. Chou and I.-H. Lin, “Design of White LED Light Source for Noble LCD Backlight Module,” Mol. Cryst. Liq. Cryst., vol. 495, pp. 80–96, Nov. 2008.

[1-18]. Y.-L. Lo, Y.-B. Chen, and T.-Y. Yang, with Nghia Nguyen-Huu, “Realization of integrated polarizer and color filters based on subwavelength metallic gratings using a hybrid numerical scheme,” APPLIED OPTICS, vol. 50, 2011, pp. 415-426.

[1-19]. C.-C. Sun, W.-T. Chien, I. Moreno, C.-T. Hsieh, M.-C. Lin, S.-L. Hsiao, and X.-H. Lee, “Calculating model of light transmission efficiency of diffusers attached to a lighting cavity,” Optics Express, vol. 18, 2010, pp. 6137-6148.

[1-20]. B.-Y. Joo and D.-H. Shin, “Design guidance of backlight optic for improvement of the brightness in the conventional edge-lit LCD backlight,” Displays, vol. 31, Apr. 2010, pp. 87-92.

[1-21]. H. Yun, Y. Lim, S. Choi, J. Bin, J. Park, M. Park, Y. Lee, S. Ihm, and Y.J. Lim, “A High Aperture Mobile in the FFS TFT-LCD by the using Fine Patterning Process.”

[1-22]. H.-F. Lin, K.-Y. Huang, and K.-Y. Lin, “Fabrication the high transmittance TFT-LCD displays using photosensitive low-k spin on glass (SOG) films.”

[1-23]. S.-J. Kim, B.-H. Kim, S.-W. Kim, S.-J. Shin, A. Salleo, S. Ready, and R. Street, “Study of Ink Jet Printing Parameters to Fabricate LCD Color Filter,” Journal of Imaging Science and Technology, vol. 54, 2010, p. 050307.

[1-24]. R.-J. Xie, N. Hirosaki, and T. Takeda, “Wide Color Gamut Backlight for Liquid Crystal Displays Using Three-Band Phosphor-Converted White Light-Emitting Diodes,” Applied Physics Express, vol. 2, Jan. 2009, p. 022401.

[1-25]. J. Mather (2004, Dec. 01), “Inter-Network Talk,” [Online], Available e-mail: Jonathan.Mather@sharp.co.uk Message: Costs for Colour Filters, 2004.

[1-26]. E. Griese, “An Optical Interconnection Technology for Multilayer Printed Circuit Boards,” Computing, pp. 230-231.

[1-27]. E. Griese and S. Member, “A High-Performance Hybrid Electrical – Optical Interconnection Technology for High-Speed,” Interconnection Technology, vol. 24, 2001, pp. 375-383.

[1-28]. N. Bamiedakis, J. Beals, R.V. Penty, S. Member, I.H. White, J.V. Degroot, T.V. Clapp, and A. Cost-effective, “Cost-Effective Multimode Polymer Waveguides for High-Speed On-Board Optical Interconnects,” Quantum, vol. 45, 2009, pp. 415-424.

[1-29]. F. Mederer, R. Jäger, H.J. Unold, R. Michalzik, K.J. Ebeling, S. Lehmacher, A. Neyer, and E. Griese, “3-Gb / s Data Transmission With GaAs VCSELs Over PCB Integrated Polymer Waveguides,” Technology, vol. 13, 2001, pp. 1032-1034.

[1-30]. Z. Yu, F. Luo, X. Di, W. Zhou, B. Li, G. Wang, and J. Chen, “Highly reliable optical interconnection network on printed circuit board for distributed computer systems,” Optics & Laser Technology, vol. 42, Nov. 2010, pp. 1332-1336.

[1-31]. D.R. Selviah, A.C. Walker, D.A. Hutt, K. Wang, A. McCarthy, F.A. Fernández, I. Papakonstantinou, H. Baghsiahi, H. Suyal, M. Taghizadeh, P. Conway, J. Chappell, S.S. Zakariyah, D. Milward, R. Pitwon, K. Hopkins, M. Muggeridge, J. Rygate, J. Calver, W. Kandulski, D.J. Deshazer, K. Hueston, D.J. Ives, R. Ferguson, S. Harris, G. Hinde, M. Cole, H. White, N. Suyal, H. ur Rehman, and C. Bryson, “Integrated optical and electronic interconnect PCB manufacturing research,” Circuit World, vol. 36, 2010, pp. 5-19.

Chapter 2. Review of Ray Tracing Models of Optical Light Guides for Displays

2.1 Introduction

Optical waveguides or light guides have been used in the display industry, especially for liquid crystal display (LCD) and light-emitting diode (LED) displays, as one of the most important components in the back illumination for the displays. Waveguides guide light from light sources and provide uniform and highly efficient illumination to viewers [2-1–4]. The research prior to this thesis is reviewed.

2.2 Review of Modelling Tools

6 modelling techniques were compared in order to identify a suitable technique for the research. The advantages and disadvantages of each modelling technology arelisted in Table 2-1.

Table 2-1 Comparison of Modelling Techniques

Modelling Technique	Advantages	Disadvantages
Beam Propagation Method, BPM [2-5]	Calculates intensity and modes within bent and tapered waveguide structures	Only valid for paraxial rays up to ±15 º and ±40 º using wide angle BPM
Finite Difference Time Domain, FDTD [2-6]	Solves Maxwell's equations	long computation time
Finite-Element Methods [2-7]	Considers both optical structures and the microwave fields	Not suitable for optical system design when there are open spaces between optical elements, e.g. lens
Jones Matrix [2-8]	Model polarized light	Only deals with incident light normal to a surface
Extended Jones Matrix [2-9][2-10]	Deals with polarised light includes incident light at an arbitrary angle	Does not calculate reflections
Ray Tracing [2-11][2-12]	Based on the classical laws of geometrical optics, easy to model multimode wave and complicated structures	Can be problematic when model waveguides with wall roughness.

The suitability of each modelling technique for modelling a light guide structure for a display system is listed and compared in Table 2-2

Table 2-2 Comparison of Modelling Techniques for Light Guide Structures

Modelling Technique	Optical Structures to be Modelled						
	Slab waveguide	Waveguide channel	Crossings	Bends	Taper	Liquid Crystal	Illumination (including lens)
BPM	√	√	O	√	√	×	×
FDTD	√	√	√	√	√	√	O
FEM	√	√	√	√	√	√	O
Jones Matrix	×	×	×	×	×	O	O
Extended Jones Matrix	×	×	×	×	×	O	O
Ray Tracing	√	√	O	O	O	O	√

Note: √ good, × cannot, O under certain conditions.

The ray tracing method was chosen as the modelling tool for this research because it has the following advantages when modelling light propagation in highly multimode waveguides.

– Ray trace modelling can deal with polarised light, off-axis beams [2-13], reflections, large system structures with large elements (10 times larger than wavelength). Therefore, it is very good for illumination system design and does not need complicated mathematical equations explicitly as these are integrated in the program.
– Rays are traced from the optical source to the optical detector monitoring them as they pass individual optical elements, so that an analysis can be made at any point in a system.
– Ray tracing can analyse multimode light guides [2-14–16].
– The conventional sequential ray tracing requires the user to specify the order of the optical surfaces. It becomes extremely inefficient when the system is complicated. Non-sequential ray tracing, however, overcomes the problem.
– Non-sequential ray tracing [2-17–19] automatically determines which surface a ray will be incident on next. Optical elements may be located anywhere; rays can follow any path and can reflect on the same surface many times following physically realizable paths, encountering objects in any order as appropriate. Ray splitting occurs automatically at the boundary of media and the reflected, refracted, diffracted, polarized, and scattered components can be analyzed at a desired position.

Note: all the modelling results shown in this thesis are obtained by using Advanced System Analysis Program (ASAP), Breault Inc..

2.3 Fundamental of ASAP Ray Tracing

The content of the fundamental ASAP program includes radiometric and photometric definitions and concepts and the association of the International System of Units (SI) definition of radiometric and photometric quantities with the equivalent ASAP procedures and commands for performing related calculations.

Radiometry is the science of measuring light intensity in any portion of the electromagnetic spectrum, which is between the wavelength 0.01 μm and 1000 μm. Radiometry means the calculation of radiation in ASAP.

Photometry is a normalized form of radiometry and is the response of the human eye.

Radiant energy, *Q*, presents electromagnetic radiation through space. The spectral radiant energy is defined as the amount of radiant energy per unit wavelength interval at wavelength λ [2-20].

$$Q_\lambda = dQ/d\lambda \qquad \textbf{Eq (2-1)}$$

Q_λ is measured in joules per nanometre.

Power is the time rate of change of energy, or the amount of energy expended per unit time, and the unit is the watt (W) or Joules per second.

$$\Phi = dQ/dt \qquad \textbf{Eq (2-2)}$$

In ASAP ray tracing, the flow of light through space is represented by geometrical rays of light, which can be thought of as a lot of thin lines drawn through a defined space that indicate the direction of flow of radiant light. Power, *Φ*, is represented by the energy "flux" in ASAP.

Radiant flux density is the radiant flux per unit area emitted by or received on a surface. *Irradiance* is the flux arriving from any direction above the surface, as indicated by the rays in Figure 2-1.

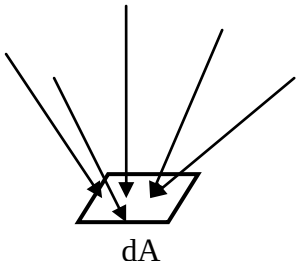

Figure 2-1 Irradiance

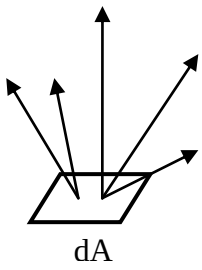

Figure 2-2 Radiant exitance

$$E = d\Phi / dA \qquad \textbf{Eq (2-3)}$$

Radiant exitance is the flux leaving the surface due to emission and/or reflection (Figure 2-2). The definition of radiant exitance is:

$$M = d\Phi / dA \qquad \textbf{Eq (2-4)}$$

where *dA* is the differential area surrounding the point. The SI units of *Irradiance* and *Radiant exitance* are watts per square meter (W/m^2)

Radiance is the amount of radiant flux emitted in a certain direction; therefore, the radiant intensity (*I*) is an angular flux density (see Figure 2-3). It is defined as power per unit solid angle:

$$I = d\Phi / d\omega \qquad \textbf{Eq (2-5)}$$

Its SI units are watts per steradian (W/sr).

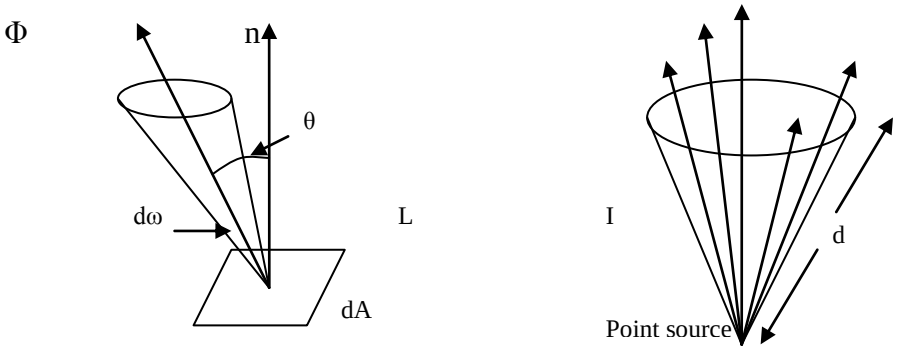

Figure 2-3 Radiance

where, ω, is the solid angle which is the projection of an area onto a sphere (Figure 2-4). The definition of the differential solid angle is:

$$d\omega = dA_p / r^2 = dA\cos\theta / r^2 = dA_{sphere} / r^2 = r^2 \sin\theta \cdot d\theta \cdot d\varphi / r^2 = \sin\theta \cdot d\theta \cdot d\varphi \quad \textbf{Eq (2-6)}$$

where θ is the angle between the ray and the surface normal, φ is the Azimuth angle from 0 to 2π

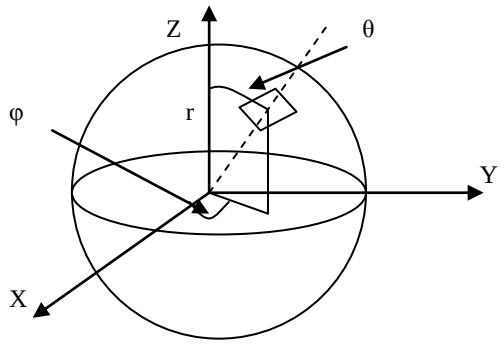

Figure 2-4 Solid angle

Assume light arriving at or leaving a differential area *dA* at angle θ, the cross-sectional area of the ray is $A_p = dA\cos\theta$, as shown in Figure 2-5.

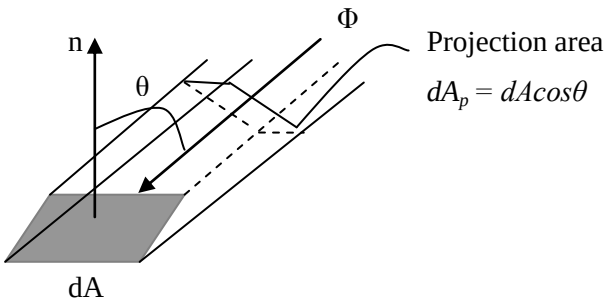

Figure 2-5 Projected area

the radiance is defined to be *L* [2-20]:

$$L = d^2\Phi / [dA(d\omega\cos\theta)] = d^2\Phi / dA_p d\omega \quad \textbf{Eq (2-7)}$$

It is an angular-area flux density and measured in watts per square meter per steradian.

ASAP linearly superposes the energy densities of light sources to model the phenomena of diffraction, e.g. a transmission grating in Figure 2-6. A detailed design and ray tracing model of a grating is reported in Chapter 5.

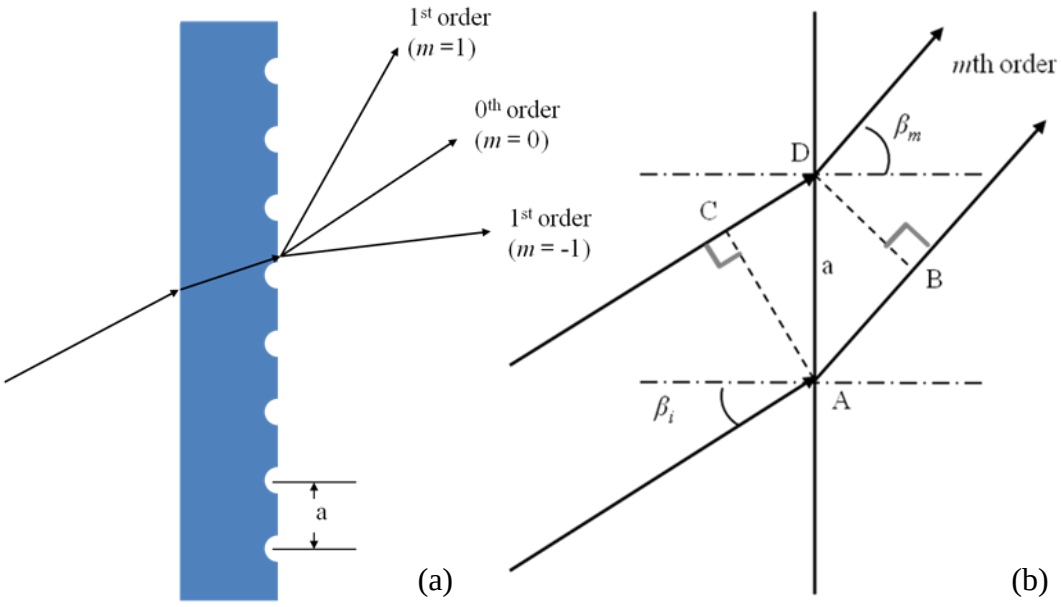

Figure 2-6 A transmission grating

The sine of the incident angle is:

$$\sin\beta_i = \frac{CD}{a} \qquad \textbf{Eq. 2-1}$$

where "a" is the pitch of the grating. Similarly the sine of the diffracted order angle is

$$\sin\beta_m = \frac{AB}{a} \qquad \textbf{Eq. 2-2}$$

We can have the following relationship

$$AB - CD = a(\sin\beta_m - \sin\beta_i) \qquad \textbf{Eq. 2-3}$$

Based on the Huygens-Fresnel principle [2-21], [2-22], the grating equation [2-23], [2-24], for both transmission and reflection, is

$$a(\sin\beta_m - \sin\beta_i) = m\lambda \qquad \textbf{Eq. 2-4}$$

where, "*m*", specifies the order of the various principal maxima. The grating equation is the same even in the case of the phase reflection grating. The grating equation is dependent on the wavelength (λ) of the incoming light. Multiple wavelengths of the incoming light would be angularly separated to slightly different angles (β_m), and spatially spread out, when $\beta_i \neq 0$.

A monochromatic source of radiation in ASAP has a single wavelength assigned to it with the **WAVELENGTH** command. A multi-wavelength source is made up of

several individual single wavelength sources. Once sources and objects are defined in a system, the program traces rays from sources through multiple layers of medium intersections. All sources in ray tracing are modelled with rays. The spatial start point of the ray vector is its 3 dimensional location in space. The direction of the ray vector is the propagation direction of the radiation. Each ray has an individual power or flux that contributes to the total flux of the source. ASAP stores more than 100 pieces of information associated with each ray and can recall part of the information, such as its position, direction and flux, from the stored database. Rays terminate when they encounter and stop on a totally absorbing object. The number of rays and their associated fluxes on the object can be counted as power. This concept is used to simulate an optical detector that can detect all rays incident on it.

2.4 Review of Designs and Modelling in Displays

Waveguides with total internal reflection [2-25], tapered or wedge shaped [2-26] and integrated diffuser [2-11], [2-27] and micro structures [2-28], [2-29] are used appropriately to achieve uniform illumination.

The National Institute for Research Development in Micro-technologies, Romania [2-30] presented a method to find the optimum distribution of scattering elements in an edge-lit light guide plate (LGP) for rendering a uniform distribution of the output light, Figure 2-7. They used ZEMAX, ray tracing simulations to determine the value of the output coefficient of an individual scattering element from the irradiance (or radiance) measurements.

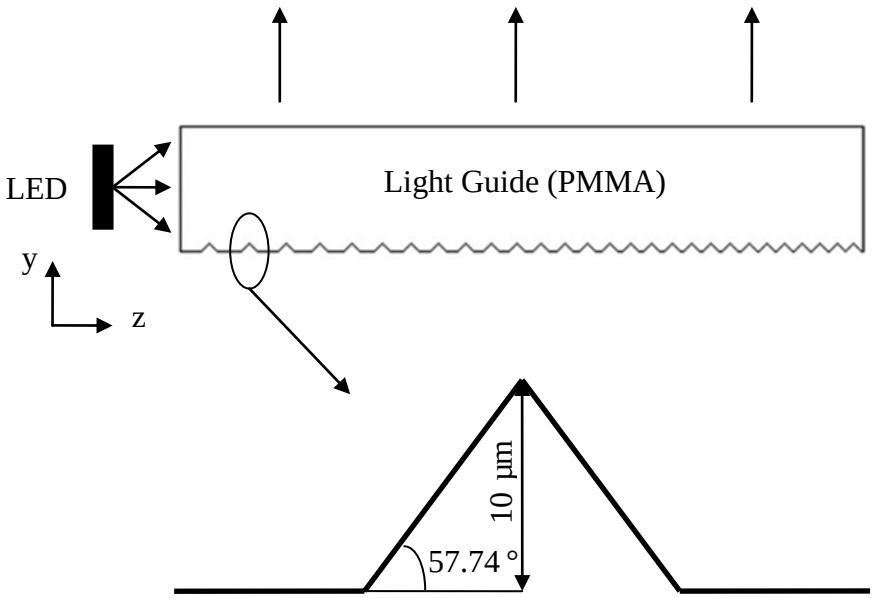

Figure 2-7 schematic of the simulated Light guide plate (LGP), the embossed LGP (top) the scattering element (bottom), after [2-30]

National Yunlin University of Science & Technology, Taiwan [2-19] designed and modelled a micro-prism array optical film which could be attached on LCDs up to 2.2 inches in width. The ray tracing method was used to select the appropriate vertex angles of each micro-prism to deliver two images to left and right viewing zones of the panel.

Yuuto Okuda and Ichiro Fujieda in Ritsumeikan University [2-31] used an acrylate plate substrate as backlight and made a spiral trench in it. A multimode fibre with periodic grooves was embedded in the trench to guide light across the backlight panel. Figure 2-8 shows the cross section of the backlight with embedded optical fibre with several grooves

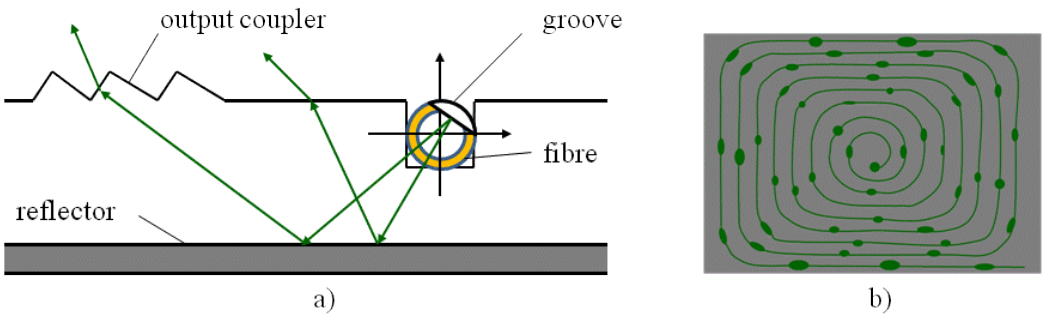

Figure 2-8 Cross section of a backlight with embedded optical fibre with grooves, a) schematic side view, b) schematic of top view, after [2-31]

Light coupled into the backlight panel from the fibre at each of the grooves and reflected at the back of the panel and redirected towards the top surface where some micro-structures, denoted as output coupler, extracted the light out of the plate.

The ray tracing models of similar micro optical components for LCDs were also carried out by Y.-H. Ju [2-11], Nghia Nguyen-Huu [2-29], J. Lee [2-32] and J.-H. Park [2-33]. J. a. Herlocker, et al from the Breault Research Organization [2-34] examined non-uniform polarization effects in the simulation of modern display devices using realistic polarizer and retarder models in a non-sequential ray-tracing environment. These models improved the uniformity and efficiency of the light guide for LCDs. However, they still required colour filters to separate colours.

Some researchers developed colour separating backlights without using colour filters for LCDs, e.g. R. Hicks [2-35], P. Erbach [2-36] used diffractive lens array, Q. Tan, et al [2-37], [2-38] reported a method based on the fractional Talbot effect of Talbot grating, C.-H. Chen and H.-Y. Lin [2-39] proposed a method based on Fresnel diffraction theory to separate light into different colours. However, all of the proposed concepts required collimated white light as the input light source. H. D. Shieh [2-40] proposed a completely different approach using field-sequential-colour (FSC) technologies to separate light into different colours. Other researchers successfully used ray tracing to model wavelength separating gratings, e.g T. Sugita [2-41].

To the best of our knowledge, no one has proposed the idea of a colour-separating backlight that optimised efficiency by inserting a micromirror array within a light guide. The capability of ray tracing has also been extended by the author to investigate the impact of localised liquid crystal on silicon (LCOS) switching defects on the final projected TV image by combining liquid crystal (LC) device level simulations with ray-tracing simulation of the projection system [2-42][2-43]. The program was used to determine the reflectivity from the LCOS layer using the Extended Jones matrix method for normal incident rays in selected regions of the LCOS device. No previous report has been found combining a ray-tracing program, a full dynamic liquid crystal director model and a LC optics model to simulate the performance of a Rear-projection television (RPTV) system using an LCOS panel to this thesis submission.

Chapter 2 References

[2-1] J. Liu, T. Lee, and C. Wen, "High-performance organic-inorganic hybrid plastic substrate for flexible displays and electronics," *J. Soc. Inf. Disp.*, vol. 19, no. 1, pp. 63–69, 2011.

[2-2] J.-R. Yan, Q.-H. Wang, D.-H. Li, and J.-D. Zhang, "Edge-Lighting Light Guide Plate Based on Micro-Prism for Liquid Crystal Display," *J. Disp. Technol.*, vol. 5, no. 9, pp. 355–357, Sep. 2009.

[2-3] M.-H. Huang, Y.-C. Tsai, and K.-H. Chen, "Energy-Recycling (ER) Technique for a Direct-Lit Intelligent Power Management Backlight Unit (BLU)," *IEEE Trans. Power Electron.*, vol. 25, no. 10, pp. 2588–2598, Oct. 2010.

[2-4] B.-Y. Joo and D.-H. Shin, "Design guidance of backlight optic for improvement of the brightness in the conventional edge-lit LCD backlight," *Displays*, vol. 31, no. 2, pp. 87–92, Apr. 2010.

[2-5] T. M. Benson, B. B. Hu, A. Vukovic, and P. Sewell, "What is the future for beam propagation methods?," *Proc. SPIE*, vol. 5579, pp. 351–358, 2004.

[2-6] S. Tanabe, "Transition analysis of magnetic recording heads using FDTD," *J. Magn. Magn. Mater.*, vol. 235, no. 1–3, pp. 388–392, Oct. 2001.

[2-7] R. James, F. A. Fernandez, S. E. Day, S. Bulja, and D. Mirshekar-Syahkal, "Accurate Modeling for Wideband Characterization of Nematic Liquid Crystals for Microwave Applications," *IEEE Trans. Microw. Theory Tech.*, vol. 57, no. 12, pp. 3293–3297, Dec. 2009.

[2-8] J. M. López-Higuera, "Handbook of optical fibre sensing technology," John Wiley and Sons, 2002, p. 795.

[2-9] K. Yang, "Nematic liquid crystal modes for Si wafer-based reflective spatial light modulators," *Displays*, vol. 20, no. 5, pp. 211–219, Dec. 1999.

[2-10] Y. J. Lim, J. H. Kim, J. H. Her, K. H. Park, J. H. Lee, B. K. Kim, W.-S. Kang, G.-D. Lee, and S. H. Lee, "Viewing angle switching of liquid crystal display

using fringe-field switching to control off-axis phase retardation," *J. Phys. D. Appl. Phys.*, vol. 43, no. 8, p. 085501, Mar. 2010.

[2-11] Y.-H. Ju, J.-H. Park, J.-H. Lee, J.-Y. Lee, K.-B. Nahm, J.-H. Ko, and J.-H. Kim, "Study on the Simulation Model for the Optimization of Optical Structures of Edge-lit Backlight for LCD Applications," *J. Opt. Soc. Korea,* vol. 12, no. 1, pp. 25–30, Mar. 2008.

[2-12] J. Chang, C. Lin, C. Hwang, and R. Yang, "Optical Design and Analysis of LCD Backlight Units Using ASAP," *Opt. Eng.*, vol. 4, no. June, pp. 1–15, 2003.

[2-13] L. A. Griffiths, J. M. Baird, and R. F. Bowers, "Arbitrary Shape Radome 3D Ray Trace Analysis and Data Visualization," *IEEE ANTENNAS Propag. Soc. Int. Symp.*, vol. 1–12, pp. 3265–3268, 2007.

[2-14] A. Himmler, E. Griese, and G. Mrozynski, "A ray tracing approach to model wave propagation in highly multimode graded index optical waveguides," *Int. J. Appl. Electromagn. Mech.*, vol. 17, pp. 157–168, 2003.

[2-15] T. Ishigure, K. Shitanda, T. Kudo, S. Takayama, T. Mori, K. Moriya, and K. Choki, "Low-loss design and fabrication of multimode polymer optical waveguide circuit with crossings for high-density optical PCB," *2013 IEEE 63rd Electron. Components Technol. Conf.*, pp. 297–304, May 2013.

[2-16] S. Uhlig, "Ray-Tracing Studies on Optical Periscopes Suitable for Out-of-Plane Interconnects on Optical Backplanes," *IEEE Trans. Electron. Packag. Manuf.*, vol. 33, no. 1, pp. 55–64, 2010.

[2-17] J. F. Van Derlofske, "Computer modeling of LED light pipe systems for uniform display illumination," *Proc. SPIE*, pp. 119–129, 2001.

[2-18] N. Raman, "Optical design of a tiled large-area photoluminescent liquid-crystal display," *Opt. Eng.*, vol. 43, no. 1, p. 91, Jan. 2004.

[2-19] C.-Y. Chen, T.-Y. Hsieh, Q.-L. Deng, W.-C. Su, and Z.-S. Cheng, "Design of a novel symmetric microprism array for dual-view display," *Displays*, vol. 31, no. 2, pp. 99–103, Apr. 2010.

[2-20] "The ASAP Primer," *Breault Res. Organ. Inc*, pp. 371–381, 2006.

[2-21] H. Dammann, "Color separation gratings," *Appl. Opt.*, vol. 17, no. 15, 1978.

[2-22] E. Hecht, "No Title," in *Optics*, Addison Wesley, U.S, International 4th Edition, 2002, pp. 444–446.

[2-23] H. Ichikawa, J. Turunen, and M. R. Taghizadeh, "Analysis of hybrid holographic gratings by thin graing decomposition method," *J. Opt. Soc. Am. A-Optics Image Sci. Vis.*, vol. 10, no. 6, pp. 1176–1183, 1993.

[2-24] B. R. Organization, "Diffraction Gratings and DOEs," in *ASAP Technical Guide*, Breault Research Organization, Inc., 2002.

[2-25] F. Fournier, W. J. Cassarly, and J. P. Rolland, "Method to improve spatial uniformity with lightpipes," *Opt. Lett.*, vol. 33, no. 11, p. 1165, May 2008.

[2-26] Z. Tang, "Optimization of fiber-optic coupling and alignment tolerance for coupling between a laser diode and a wedged single-mode fiber," *Opt. Commun.*, vol. 199, no. 1–4, pp. 95–101, Nov. 2001.

[2-27] K. Imai and I. Fujieda, "Illumination uniformity of an edge-lit backlight with emission angle control.," *Opt. Express*, vol. 16, no. 16, pp. 11969–74, Aug. 2008.

[2-28] J. H. Min, H. Y. Choi, M. G. Lee, J. S. Choi, J. H. Kim, and S. M. Lee, "Holographic backlight unit for mobile LCD devices," *J. Soc. Inf. Disp.*, vol. 11, no. 4, p. 653, 2003.

[2-29] C. Lin, C. Wu, P. Yang, and T. Kuo, "Application of Taguchi Method in Light-Emitting Diode Backlight Design for Wide Color," vol. 5, no. 8, pp. 323–330, 2009.

[2-30] M. Kusko, C. Kusko, and D. Cristea, "Method of determination of light-scatterer distribution in edge-lit backlight units using an analytical approach.," *J. Opt. Soc. Am. A. Opt. Image Sci. Vis.*, vol. 27, no. 9, pp. 2015–20, Sep. 2010.

[2-31] Y. Okuda and I. Fujieda, "Polymer waveguide technology for flexible display applications," in *Proceedings of SPIE, Advances in display technologies*, 2012, vol. 8280, pp. 122–131.

[2-32] J. Lee, Y. Kim, and K. Nahm, "Optical simulation of micro-pyramid arrays for the applications in the field of backlight unit of LCD," *IMID/IDMC 2006 6TH Int. Meet. Inf. DISPLAY/THE 5TH Int. Disp. Manuf. Conf. Dig. Tech. Pap.*, pp. 1343–1346, 2006.

[2-33] J.-H. Park and J.-H. Ko, "Optimization of the emitting structure of flat fluorescent lamps for LCD backlight applications.pdf," *J. Opt. Soc. Korea*, vol. 11, no. 3, pp. 118–123, 2007.

[2-34] J. a. Herlocker, J. Jiang, and K. J. Garcia, "Display system analysis with critical polarization elements in a non-sequential ray tracing environment," *Proc. SPIE*, vol. 7060, pp. 70600Y–1–8, 2008.

[2-35] R. Hicks, W. Halstead, and T. Gunn, "Diffractive color separation for high efficiency LCD's," *Proc. Soc. Photo-Optical Instrum. Eng.*, vol. 3057, pp. 200–211, 1997.

[2-36] P. Erbach, G. Borek, D. Brown, and T. Gunn, "Diffractive color separation filter for high efficiency LCD panels," *Proc. Soc. Photo-Optical Instrum. Eng.*, vol. 3636, pp. 48–59, 1999.

[2-37] Q. Tan, Y. Zhang, Y. Yan, and G. Jin, "High-efficiency color separation method based on fractional Talbot effect for color liquid crystal display," *Opt. Commun.*, vol. 281, no. 24, pp. 5949–5953, Dec. 2008.

[2-38] Q. Tan, Y. Zhang, and G. Jin, "High-efficiency spatial color separation method based on fractional Talbot ef fect," *Chinese Opt. Lett.*, vol. 7, no. 11, pp. 975–977, 2009.

[2-39] C.-H. Chen and H.-Y. Lin, "Design and Analysis of Color Separation Grating by Using Fresnel Diffraction Theory," *6th Int. Meet. Inf. Displays/5th Int. Disp. Manuf. Conf.*, pp. 1505–1509, 2006.

[2-40] H. D. Shieh, "Eco-Displays: The Color LCD's Without Color Filters and Polarizers," *J. Disp. Technol.*, vol. 7, no. 12, pp. 630–632, Dec. 2011.

[2-41] T. Sugita, K. Hirano, T. Abe, and Y. Itoh, "Aberration properties in a chirped grating for coarse wavelength division demultiplexing," *Appl. Opt.*, vol. 45, no. 22, pp. 5597–5606, 2006.

[2-42] F. A. Fernandez, S. E. Day, P. Trwoga, H. F. Deng, and R. James, "Three-Dimensional Modelling of Liquid Crystal Display Cells using Finite Elements," *Mol. Cryst. Liq. Cryst.*, vol. 375, pp. 291–299, 2002.

[2-43] M. C. Gardner, S. E. Day, F. A. Fernandez, and K. Sarayeddine, "6 . 3 : Three-Dimensional Modelling of a Projection TV System by Dynamic Liquid-Crystal Simulation and Ray Tracing," *SID Symp. Dig. Tech. Pap.*, vol. 35, pp. 68–71, 2004.

Chapter 3. Review of Modelling and Measurement for Crossing Waveguides

3.1. Introduction

High data rate (>10 Gb/s) interconnections can be made in a single layer using optical waveguides and they can cross on the same layer, while copper interconnections in electrical PCBs have to use sufficient separation space and multiple layers to reduce electromagnetic interference (EMI) between the data links [3-1]. To achieve an effective and complex integrated optical circuit, optical PCB designers inevitably need various elements in their designs such as bends, splitters, couplers and crossing waveguides [3-1], [3-2] to route around cutout areas, electrical components and obstacles and to interconnect desired transceivers on an OPCB. Waveguide crossings where two waveguides intersect in the same optical layer (as shown in Figure 3-1) are particularly important components as they offer OPCB layout designers additional flexibility to solve layout problems such as routing through other waveguides on an OPCB [3-1] and to reduction in PCB size and weight [3-3]. Despite all of the advantages of waveguide crossings, and although most of the light travels along the intended waveguide, a proportion of the optical power in one waveguide couples into the shallowly crossed (<20) waveguide [3-4] after passing each intersection point (Figure 3-1) or couples out of the original waveguide and into the cladding.

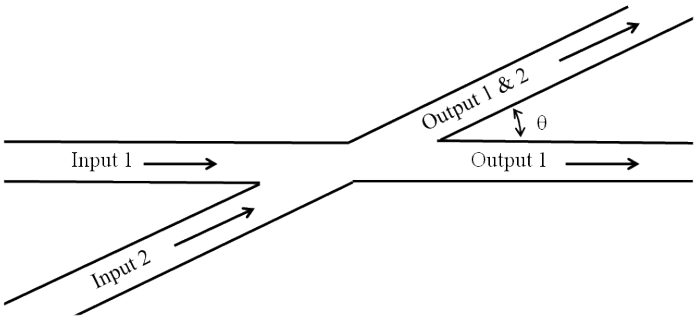

Figure 3-1 Top schematic view of a waveguide crossing with crossing angle θ

This coupling phenomenon causes optical loss and crosstalk in the system [3-5], [3-6]. The amount of loss and crosstalk depends on the material of the waveguide polymer[3-7], [3-8], the waveguide fabrication technique [3-4], [3-9], the size of the waveguide cross section [3-10–12] and the crossing angle between waveguides [3-8].

Therefore, the crossings in OPCBs need to be carefully designed to reduce both loss and crosstalk to improve the performance of an OPCB.

The designs for optical interconnects in optical backplanes are reviewed in chapter 4, however, the research review on crossings has been put in a separate chapter as it is particularly relevant to the new research reported in chapter 7 in this thesis and is compared so that the new aspects of the new research reported can be clearly distinguished from earlier research carried out by other researchers.

3.2. Review of Modelling and Measurement for Waveguide Crossings

Waveguide crossings attracted a lot of attention in recent years because of their important roles in integrated optical systems such as power splitters, combiners, hybrid integrated optical transceivers and optical sensors. Modelling and measurement have been carried out to assess the performance of the waveguide crossing.

Various modelling techniques such as 3D finite-difference time-domain (3D FDTD) [3-13], finite-difference beam-propagation method (FD-BPM) [3-14], finite-difference time- domain (FDTD) [3-15], wavefront matching (WFM) method [3-10] and others have been used to analyze silicon wire waveguide with a subwavelength grating (SWG) crossings, silica-based waveguide in Quadrature amplitude modulation (QAM) and Y- junction for submicron silicon waveguide. The cross sections of those waveguides are normally small, less than 6 μm x 6 μm and sometimes less than 1 μm x 1 μm for a silicon waveguide.

The ray tracing simulations have been used to model and investigate waveguides with large core cross section (>30 μm x 30 μm), e.g. in out-of-plane [3-16–19] and in-plane [3-20–22] optical interconnects and also in special waveguides [3-23]. Ray tracing is useful to evaluate the misalignment tolerance of an active device, e.g. VCSEL, to the waveguide [3-24] and coupling efficiency [3-25], [3-26]. More sophisticated models, for example: combined ray tracing and wave optical analysis method [3-27], included waveguide end facets roughness [3-21], and were used to analyze signal propagation in slab waveguides with rough surfaces.

The closest research compared to the author's work was carried out by Hadi Baghsiahi [3-28] in Optical Devices and Systems laboratory of the Photonics Research Group at UCL supervised by Dr David R. Selviah. He simulated the waveguide crossing structure using the beam propagation method (BPM) and ray trace method. The crossing angles from 5 °to 20 °were simulated by using BPM due to the limitation in BPM algorithm [3-29] which implies that the electric field changes slowly along the light propagation direction and can become inaccurate when the light is travelling in the waveguide at a large angle relative to the initial propagation direction, Therefore, crossing angles from 10° to 90° in steps of 10 °were simulated using the ray tracing method. However, Hadi only modelled a waveguide with square cross section and did not give a detailed model of input light sources.

T. Ishigure, et al in the Faculty of Science and Technology, Keio University [3-9] have theoretically and experimentally analysed waveguide crossings with graded-index (GI) cores and step-index (SI) cores, respectively. The light losses of crossed waveguides with SI and GI cores were simulated using a ray tracing simulation. The loss is achieved in the GI-core crossed waveguide (only a loss of 0.095 dB for 50 perpendicular crossings), which is less than one-tenth of the leakage loss in the SI-core crossed waveguide (2.5 dB for 50 perpendicular crossings). $50 \times 50\ \mu m^2$ GI core waveguide was fabricated using "photo-address method" which is a same technique as photolithography. The differences are the UV sensitive material used and a heating procedure involved. In the case of the photo-address method the refractive index of polynorbornene resin [3-30] (provided by Sumitomo Bakelite Co Ltd.) was varied depending on the UV exposing patterns via photo masks. The core and cladding of waveguides are formed through a continuous single process without employing an etching process. SI core waveguide was made of using the same material, polynorbornene. A waveguide with 50 crossings was simulated by using ray trace method; however, there were only 4 types of crossing angles: 30°, 50°, 60° and 90° investigated in the work.

W. Ni, et al in Zhejiang University, China reported crossing components in their design of optical interconnect [3-31]. Waveguides were made from a UV-curable polyurethane acrylate prepolymer (DeSolite®) and were fabricated by soft lithography

techniques. Crosstalk as a function of cross angle (from 5° to 55°) for crossing interconnects of polymer waveguides with various cross-sections, 50 × 50 μm^2, 100 × 100 μm^2, 200 × 200 μm^2 and 300 × 300 μm^2, were measured. The crossing losses were only accessed by wide angle BPM in the report.

N. S. Mohamed-Kassim [3-7] demonstrated a design of a highly multimode Y-junction optical waveguide coupler (see Figure 3-2) with a v-shaped tip compared to a standard design for better optical power splitter/combiner. He used ZEMAX, non-sequential ray tracing technique to model the branching angles (θ), from 8° to 14° and 0.5 mm Gaussian beam was used at a wavelength of 650 nm. His simulation showed that a maximum of 94% power could be detected at the two output ports, which demonstrated the lowest crossing loss was 0.27 dB. The acrylic-based waveguide had a 1 mm x 1 mm waveguide cross section, and was measured using 98/1000 μm polymer optical fibre (POF) as input and outputs.The waveguide is much larger than the one, 50 × 50 μm^2, that author used; therefore, the work is not suitable for a direct comparison to the research conducted by the author.

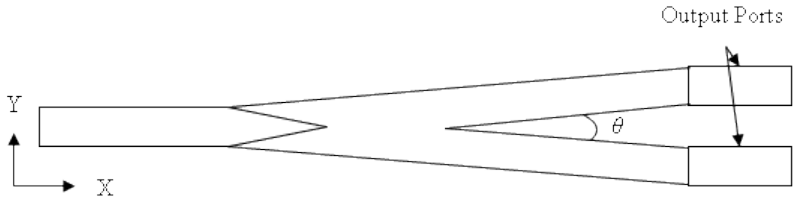

Figure 3-2 Schematic of Mohamed-Kassim designed Y-junction coupler, after [3-7]

B. J. Offrein in IBM Zurich Research Labs measured crossing losses of 90° waveguide crossings at 850 nm wavelength [3-12] using the waveguide layout shown in Figure 3-3 and reported an optical loss of 0.02 dB for 90 ºcrossings.

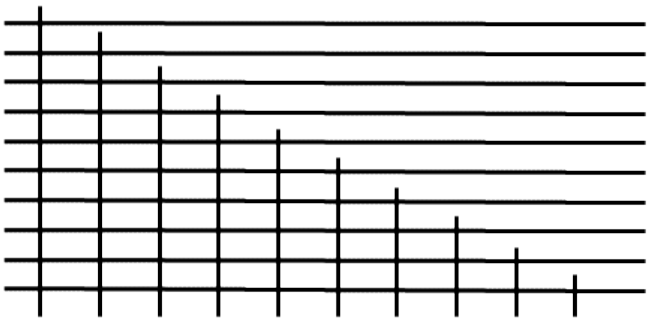

Figure 3-3 Mask layout of waveguide crossings from IBM to assess crossing losses, after [3-12]

NTT Photonics Laboratories [3-32], Japan, experimentally measured the optical loss of multimode polymer waveguide circuits with crossings at a range of angles of 30 º, 45 º, 60 º, and 90 º. They reported the excess loss with 100 90 ° crossings was 2.2 dB when the image magnification from a VCSEL to a waveguide was 2.3 (see Figure 3-4 for the experimental setup). They also obtained error-free (i.e., bit error rate < 10^{-11}) optical interconnection at 1.0625 Gbps regardless of the number of crossings or the magnification.

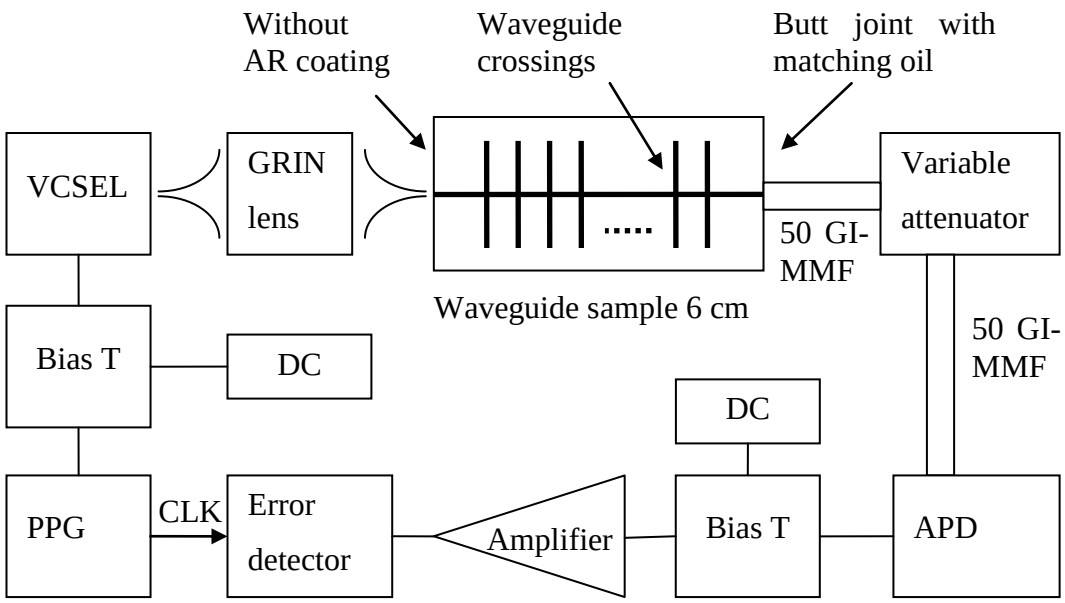

Figure 3-4 NTT's Experimental setup for waveguide transmission characteristics measurement, after [3-32]

N. Bamiedakis, et al, in University of Cambridge analysed waveguide intersections and claimed that in-plane crossings should be at 90 ° (Figure 3-5) to minimise crossing loss and crosstalk. When employing an multimode fibre (MMF) launch, crossing losses were experimentally determined to be around 0.01 dB/crossing, while crosstalk values in intersecting waveguides were below −60 dB [3-33]

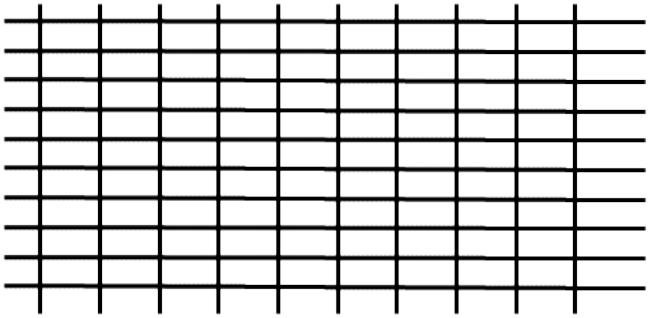

Figure 3-5 Plan-view drawing of waveguide crossings, after [3-33]

D. A. Zauner, et al, in the Technical University of Denmark [3-34] photolithographically fabricated some polymer waveguides consisting of epoxy-based negative photoresist (NANO SU-8 25 from MICROCHEM) cores sandwiched by glass and PMMA as lower and upper cladding, respectively, and air at the sides. The refractive index of the core material was 1.58 and that of the cladding material was 1.47. Waveguide crossings with the cross section 40 μm × 40 μm were investigated experimentally (Figure 3-6), and for crossing angles above 35 ° the optical loss was below 0.15 dB and no measurement data were reported for a 90 ° crossing. A halogen lamp with wavelength span approximately 500 to 1100 nm was used as the input light source and the light was coupled into a waveguide via a multimode fibre in order to find the relationship between the optical loss and the input wavelength. There was no simulation carried out with the reported work.

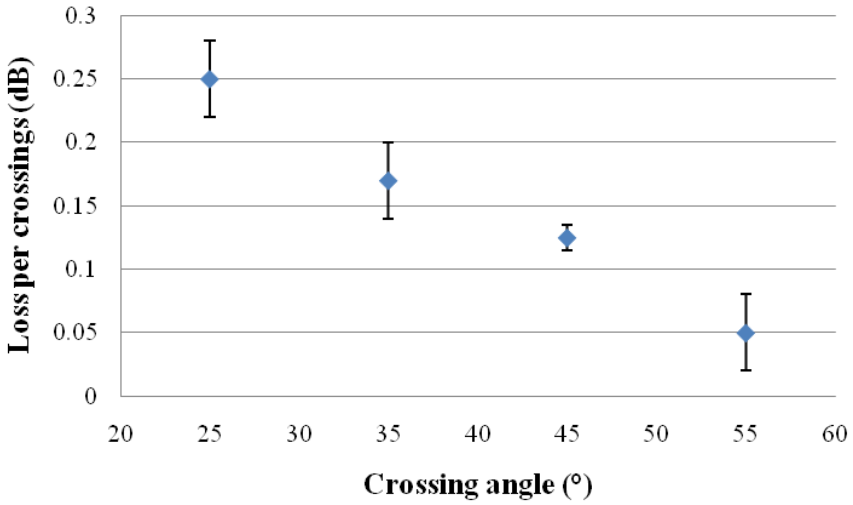

Figure 3-6 Loss per crossing as a function of the crossing angle of two 40 × 40 μm^2 waveguides, each point in the figure is the slope from an insertion loss versus number of crossings plot. The wavelength was λ = 800 nm, after [3-34]

3.3. Measurement and Simulation Results Comparison

Some of the waveguides measured by other researchers around the world with the closest specification to author's are listed in the following Table 3-1.

Table 3-1 Comparison of measurements of waveguide crossings

Institution	Material	Fabrication technique	Refractive index Core/cladding	Waveguide size w × h (μm)	Crossing angles (°)	Minimum Loss (dB)
Keio University	polynorbornene resin	photo-address	1.552 / 1.536	50 × 50	30, 50, 60, 90	0.002 GI core 0.05 SI core
IBM Zurich Research Laboratory	Polysiloxane	Laser direct write	NA	30 × 30	90	0.02 at 850 nm
Zhejiang University, P.R. China	polyurethane acrylate prepolymer (DeSolite®)	Soft-lithographic	1.50 / 1.48	50 × 50	10 - 55	0.70 average at 850 nm
University of Cambridge	Siloxane OE-4140 (core), OE-4141 (cladding)	Photo lithographic	1.52 / 1.50	50 × 50	90	0.01 at 850 nm
NTT Photonics Laboratories, Japan	PMMA (core), UV curable epoxy resin (cladding)	Photo lithographic	1.489 / 1.471 at 830 nm	40 × 42.5	30, 45, 60, 90	0.022 at 850 nm
MIC-Department of Micro and Nanotechnology, Technical University of Denmark, Denmark	epoxy-based negative photoresist,NANO SU-8 25 (core), thermal oxide (lower cladding), PMMA (upper cladding)	Photo lithographic	1.58 / 1.45 (lower cladding), 1.47 (upper cladding), air in side ways	40 × 40	25, 35, 45, 55, 90	0.05 at 55° at 800 nm, no loss was detected at 90°

There are other types of cross components: crossovers [3-35], [3-36], silicon based waveguides [3-8], [3-10] and large core polymer splitters [3-7]. The research on those waveguides is interesting and helpful to the author to obtain the knowledge on their fabrication, measurement and simulation techniques. However, the waveguides were either made of silicon which normally had small cross section, 7 μm × 7 μm, or made of polymer but have very large cross section, so that they were not listed in the above comparison table. The University of Cambridge [3-33] claimed the lowest optical crossing losses for a step index core waveguide, 0.01 dB per 90° waveguide crossing and Keio University, Japan, claimed the lowest loss in a grade index core waveguide, 0.002 dB per 90° waveguide.

The measured and simulated results are also plotted in the Figure 3-7 for direct comparison with the research reported in this thesis. The Technical University of Denmark used a halogen lamp with a wide wavelength approximately 500 to 1100 nm as input source. This may cause their measurement results to be different to others.

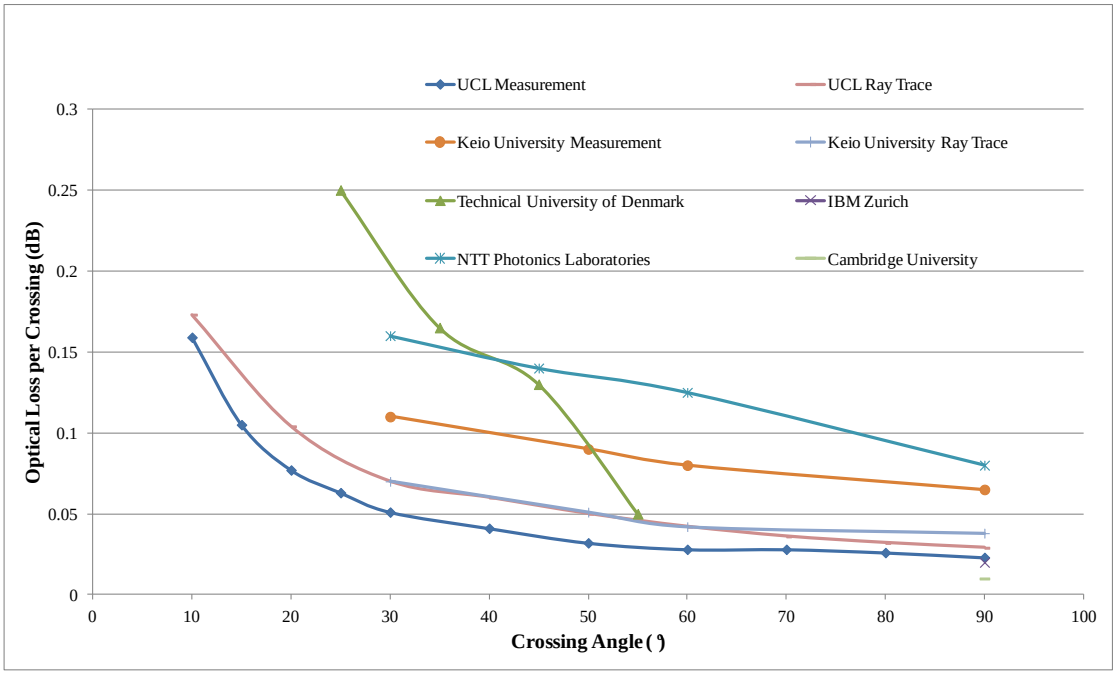

Figure 3-7 Comparison of experiment and simulation results of the optical loss per crossing as a function of crossing angle done by different researchers

UCL is the only institution so far to have reported the results of simulation and measurements [3-4] for multimode waveguide crossings over a wide range of angles (from 10 ° to 90 °). The experiment was carried out by the author and Dr. Guoyu Yu in Optical Devices and Systems laboratory of the Photonics Research Group at UCL. Dr. Hadi Baghsiahi [3-28] recently did the simulation on waveguide crossing structures using BPM and ray trace method. However, the detailed model of input light sources and the model of waveguides based on a realistic cross section shape of a waveguide have never been reported. This thesis addresses these areas by carrying out this new research; the results are reported in chapter 7.

Chapter 3 References

[3-1] R. C. A. Pitwon, K. Wang, J. Graham-Jones, I. Papakonstantinou, H. Baghsiahi, B. Offrein, R. Dangel, D. Milward, and D. R. Selviah, "FirstLight: Pluggable Optical Interconnect Technologies for Polymeric Electro-Optical Printed Circuit Boards in Data Centers," *J. Light. Technol.*, vol. 30, no. 21, pp. 3316–3329, 2012.

[3-2] N. Bamiedakis, J. Y. Ha, F. Yang, A. Wonfor, R. V. Penty, I. H. White, J. V DeGroot, and T. V. Clapp, "Multimode SCM-based PON architecture for computer network applications using a low-cost polymer 1×8 splitter/combiner," *2007 Quantum Electron. Laser Sci. Conf.*, pp. 1–2, May 2007.

[3-3] R. C. A. Pitwon, K. Hopkins, K. Wang, D. R. Selviah, H. Baghsiahi, B. J. Offrein, R. Dangel, F. Horst, M. Halter, and M. Gmür, "Design and implementation of an electro-optical backplane with pluggable in-plane connectors," *Proc. SPIE*, p. 76070J–76070J–12, 2010.

[3-4] K. Wang, D. R. Selviah, I. Papakonstantinou, H. Baghsiahi, and F. A. Fernandez, "Photolithographically manufactured acrylate polymer multimode optical waveguide loss design rules," in *2008 2nd Electronics Systemintegration Technology Conference*, 2008, pp. 1251–1256.

[3-5] Y. Zhang, W. Huang, and B. Li, "Broadband, high-transmission and low-crosstalk intersection for strip waveguides embedded in two-dimensional photonic crystals," *J. Opt. A Pure Appl. Opt.*, vol. 10, no. 9, p. 095302, Sep. 2008.

[3-6] M. Torres-Cisneros, L. A. Aguilera-Cortés, M. A. Meneses-Nava, J. J. Sánchez-Mondragón, and G. E. Torres-Cisneros, "Mechanisms of crossing for an X-junction based on dark spatial solitons," *J. Opt. B Quantum Semiclassical Opt.*, vol. 6, pp. s430–s435, 2004.

[3-7] N. S. Mohamed-kassim, A. A. Ehsan, M. H. M. Yusoff, and M. K. Abd-rahman, "New Design of Y-Junction Coupler Based on Highly Multimode Polymer Waveguide," *Physics (College. Park. Md).*, pp. 161–164, 2010.

[3-8] P. Sanchis, "Low-Crosstalk in Silicon-On-Insulator Waveguide Crossings With Optimized-Angle," *IEEE Photonics Technol. Lett.*, vol. 27, no. 20, pp. 1567–1585, Oct. 2007.

[3-9] T. Ishigure, K. Shitanda, T. Kudo, S. Takayama, T. Mori, K. Moriya, and K. Choki, "Low-loss design and fabrication of multimode polymer optical waveguide circuit with crossings for high-density optical PCB," *2013 IEEE 63rd Electron. Components Technol. Conf.*, pp. 297–304, May 2013.

[3-10] Y. Sakamaki, "Low Loss and Low Crosstalk Waveguide Crossings Designed by Wavefront Matching Method," *IEEE Photonics Technol. Lett.*, vol. 25, no. 19, pp. 730–2007, Oct. 2006.

[3-11] M. Oh, S. Cho, and H. Lee, "Fabrication of large-core single-mode polymer waveguide connecting to a thermally expanded core fiber for increased alignment tolerance," *Opt. Commun.*, vol. 246, no. 4–6, pp. 337–343, Feb. 2005.

[3-12] B. J. Offrein, "High-speed parallel optical interconnects on printed circuit boards," *UK-Swiss Photonics Work.*, 2005.

[3-13] P. J. Bock, P. Cheben, J. H. Schmid, J. Lapointe, A. Delâge, D.-X. XU, S. Janz, A. Densmore, and T. J. Hall, "Subwavelength grating crossings for silicon wire waveguides," *Opt. Express*, vol. 18, no. 15, pp. 16146–16155, 2010.

[3-14] K. Inoshita, H. Kishikawa, Y. Makimoto, N. Goto, and S. Yanagiya, "Proposal of Optical Waveguide Circuits for Recognition of Optical QAM Codes," *J. Light. Technol.*, vol. 31, no. 13, pp. 2271–2278, Jul. 2013.

[3-15] Y. Zhang, S. Yang, A. E.-J. Lim, G.-Q. Lo, C. Galland, T. Baehr-Jones, and M. Hochberg, "A compact and low loss Y-junction for submicron silicon waveguide.," *Opt. Express*, vol. 21, no. 1, pp. 1310–6, Jan. 2013.

[3-16] S. Uhlig, "Ray-Tracing Studies on Optical Periscopes Suitable for Out-of-Plane Interconnects on Optical Backplanes," *IEEE Trans. Electron. Packag. Manuf.*, vol. 33, no. 1, pp. 55–64, 2010.

[3-17] M. Kwack, M. Kanda, O. Mikami, M. Yonemura, and M. Kagami, "180 Light Path Conversion Device With Tapered Self-Written Waveguide for Optical Interconnection," *IEEE Photonics Technol. Lett.*, vol. 22, no. 15, pp. 1126–1128, 2010.

[3-18] H. Lee, I. Park, K. Soo, and E. Lee, "Microelectronic Engineering Fabrication of micro-lenses for optical interconnection using micro ink-jetting technique," *Microelectron. Eng.*, vol. 87, no. 5–8, pp. 1447–1450, 2010.

[3-19] K. Yasuda, K. Ota, M. Matsushima, K. Fujimoto, and M. Science, "Bended Interconnection using Graded Index Optical Waveguide for High Speed Optical Communication," *Electronics*, pp. 963–968, 2008.

[3-20] M. Kanda, T. Ogawa, and O. Mikami, "New Chip Device with Built-in Optical Outlet Rod for Easy Assembly and High Optical Coupling in Optical Interconnection," *Science (80-.).*, pp. 2092–2097, 2009.

[3-21] H.-H. Hsu and T. Ishigure, "High-density channel alignment of graded index core polymer optical waveguide and its crosstalk analysis with ray tracing method.," *Opt. Express*, vol. 18, no. 13, pp. 13368–78, Jun. 2010.

[3-22] H. Hsu, T. Ishigure, and S. Nakagawa, "Characterization and analysis of graded index optical waveguides for the realization of low-power , high-density , and high-speed optical link," *Proc. SPIE*, vol. 8267, pp. 1–6, 2012.

[3-23] D. Izquierdo, I. Salinas, V. Cadarso, A. Llobera, J. Ignacio, G. De Tecnolog ás, F. Instituto, D. Investigación, I. De Aragón, and U. De Zaragoza, "Hollow waveguides ray-tracing analysis," *Proc. SPIE*, vol. 6992, no. 16, pp. 1–8, 2008.

[3-24] W. Lee and G. W. Kim, "High-reliability flexible optical printed circuit board for opto-electric interconnections," *Opt. Eng.*, vol. 48, no. 1, pp. 015401–1–015401–7, 2009.

[3-25] M. E. Teitelbaum and E. D. Wetzel, "Cost-effective integration of plastic optical fiber and total internal reflection mirrors in printed circuit boards for

parallel optical interconnects," *Opt. Eng.*, vol. 49, no. 6, pp. 065401–1–065401–7, 2010.

[3-26] G. Langer, V. Satzinger, V. Schmidt, G. Schmid, and W. R. Leeb, "PCB with fully integrated optical interconnects," *Proc. SPIE*, vol. 7944, pp. 1–15, 2011.

[3-27] T. Bierhoff, "Ray tracing technique and its verification for the analysis of highly multimode optical waveguides with rough surfaces," *IEEE Trans. Magn.*, vol. 28, no. 5, pp. 1321–3310, 2001.

[3-28] H. Baghsiahi, "Multimode Optical Waveguides and Lightguides for Backplane Interconnection and Laser Illuminated Display Systems," *PhD Thesis*, pp. 137–158, 2012.

[3-29] H. Liu, H. Tam, P. Wai, and E. Pun, "Low-loss waveguide crossing using a multimode interference structure," *Opt. Commun.*, vol. 241, no. 1–3, pp. 99–104, Nov. 2004.

[3-30] Fujiwara, M., Shirato, Y., Owari, and H., "High performance polynorbornene optical waveguide for Opto-Electric interconnections," pp. 193–197, 2007.

[3-31] W. Ni, J. Wu, and X. Wu, "Crossing and branching nodes in soft-lithography-based optical interconnects.," *Opt. Express*, vol. 15, no. 20, pp. 12872–81, Oct. 2007.

[3-32] T. Sakamoto, H. Tsuda, and M. Hikita, "Optical Interconnection Using VCSELs and Polymeric Waveguide Circuits," *J. Light. Technol.*, vol. 18, no. 11, pp. 1487–1492, 2000.

[3-33] N. Bamiedakis, J. Beals, R. V Penty, S. Member, I. H. White, J. V Degroot, T. V. Clapp, and A. Cost-effective, "Cost-Effective Multimode Polymer Waveguides for High-Speed On-Board Optical Interconnects," *IEEE J. Quantum Electron.*, vol. 45, no. 4, pp. 415–424, 2009.

[3-34] D. A. Zauner, A. M. Jorgensen, T. a Anhoj, and J. Hübner, "High-density multimode integrated polymer optics," *J. Opt. A Pure Appl. Opt.*, vol. 7, no. 9, pp. 445–450, Sep. 2005.

[3-35] Z. J. Cheng, Z. L. Peng, K. X. Chen, H. P. Chan, C. X. Yu, and P. L. Chu, "Polymer-waveguide-based vertical coupler," *Opt. Commun.*, vol. 260, no. 2, pp. 511–513, Apr. 2006.

[3-36] R. Deck, "Loss in a rectangular optical waveguide induced by the crossover of a second waveguide," *Opt. Laser Technol.*, vol. 34, no. 5, pp. 351–356, Jul. 2002.

Chapter 4. Review of Designs and Measurement Technologies for Optical Interconnects in Optical Backplanes

4.1 Introduction

The research on optical printed circuit board (OPCB) systems with embedded optical channel waveguides is reviewed. In non-blocking switch matrices, blade servers and RAID hard disc storage arrays in 19" racks there is increasingly a requirement for dense connections at 10 Gb/s and above on a backplane, midplane or motherboard to interconnect the many daughter, line, mezzanine or drive cards. Hybrid printed circuit boards incorporating both copper tracks for power and low bit rate control and optical multimode waveguide high bit rate connections [4-1], [4-2] are seen as a cost effective approach to avoid the EMI crosstalk and loss necessitating the use of costly low loss tangent dielectric material, pulse pre-emphasis and equalization in multilayer copper track PCBs. The structuring of polymer waveguides is usually done photolithographically (other fabrication techniques are also available). Virtually any optical system can be implemented. This is a big advantage over the lamination of optical fibres [4-3]. Multimode waveguides have large cores which are easier to align at optical connectors, compared to single mode ones, so reducing the alignment tolerances necessary and the connector cost.

Several groups of international researchers and companies have carried out a range of OPCB research (among others). IBM Zurich [4-4] and Vario-print [4-3] are companies in Switzerland working on OPCBs and UCL collaborated with them in the opical backplane project. In the UK, Herriot-Watt University [4-5], Loughborough University [4-6], Exxelis Ltd and Xyratex Technology Ltd [4-7–10] have collaborated with UCL. Ghent University (Ghent, Belgium) [4-11], University of Cambridge (UK) [4-12], Helsinki University of Technology (Finland) [4-13], Dortmund University (Germany) [4-14], the University of Hagen (Germany) [4-15], Linköping University (Sweden) [4-16], Georgia Institute of Technology Packaging Research Center (Atlanta, USA) [4-17], University of Washington (USA) [4-18], Huazhong University of Science and Technology (China) [4-19], Keio University (Japan) [4-20–23], Electronics and Telecommunication University Daejeon (Korea) [4-24] and Pusan

National University (Korea) [4-25] are international universities working on optical interconnections.

Chrysler Research Center, Ulm (Germany) [4-26], ETH Zurich, Electronics Laboratory (Switzerland) [4-27], INTEXYS Photonics (France) [4-28], Siemens C-Lab [4-15], Fraunhofer Institute [4-29], [4-30] (Germany), Hewlett Packard (HP) Laboratories (USA) [4-31], VTT Electronics (Finland) [4-32], Nippon Telegraph and Telephone (NTT) (Japan) [4-33], Hitachi Chemical (Japan) [4-34], Mitsubishi (Japan) [4-35] and [4-36] (Korea) are industrial companies working on an OPCB project.

4.2 Review of Optical Backplanes

Some of the research most relevant to the author's work on optical backplanes is list below.

4.2.1 University of Cambridge Backplane Architecture

J. Beals IV, et al. in the University of Cambridge [4-37] presented backplane architecture exploiting 850 nm VCSEL and photodiode arrays that can be mounted on each of the line cards and connected to the backplane via ribbon fibres. Using a polymer waveguides interconnects mesh (as shown in Figure 4-1), a card can transmit serial data to any other card (or do loop-back) by addressing the appropriate VCSEL in its transmitter array to address a receiver on the desired destination board. The authors claimed that the backplane exhibited excellent routing characteristics and crosstalk performance at data rates of 10 Gb/s per waveguide with a very small power penalty of approximately 0.2 dB. The backplane could accommodate up to 100 on-board links each capable of error-free transmission at 10 Gb/s.

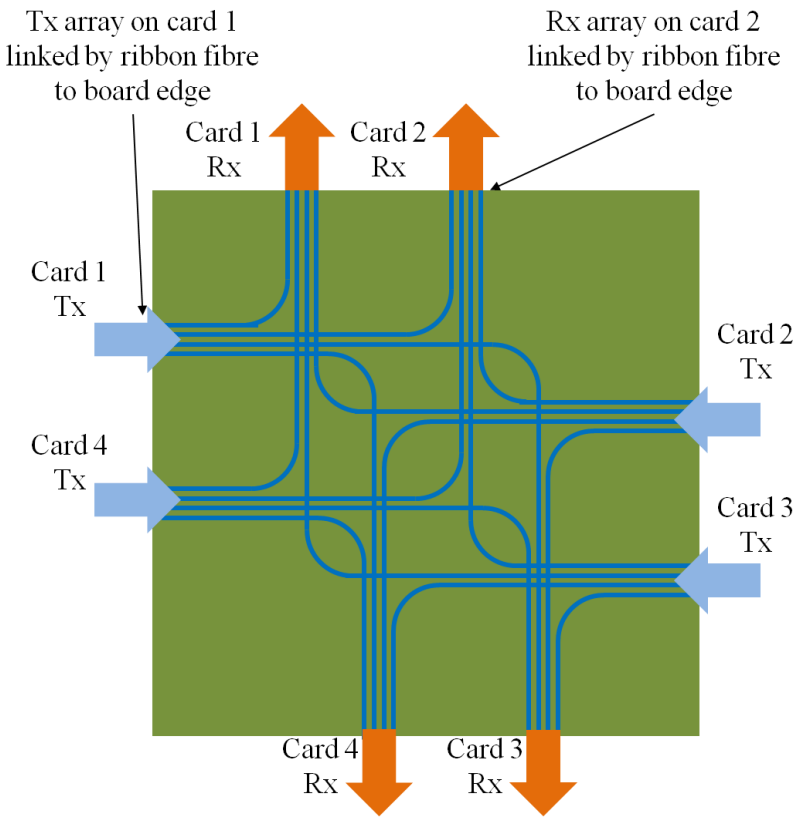

Figure 4-1 Schematic of backplane configurations. Detail of planar polymer waveguide routing that would enable complete interconnection for four cards, while the same basic waveguide layout pattern readily scales to accommodate a larger number of n cards (the total number of waveguides is n^2), after [4-37]

4.2.2 Zhejiang University 2×2 Cross-over Circuit

W. Ni, et al. in Zhejiang University, China, reported a detailed design of a 2×2 cross-over circuit Figure 4-2 [4-38], which achieved acceptable crosstalk at a cross angle of greater than 12 °in weak confinement. They also found a suitable branching angle of a 1×2 branching node for the purpose of reducing leakage in the Y junction. Prototypes of in-plane circuits have been fabricated photolithographically and tested, and the experimental performance results match their BPM simulation. Crosstalk as a function of cross angle (from 5 °to 55 °) for crossing interconnects of polymer waveguides with various cross-sections, 50 × 50 μm^2, 100 × 100 μm^2, 200 × 200 μm^2 and 300 × 300 μm^2, were measured. However, the crossing losses were only accessed by wide angle BPM in the report.

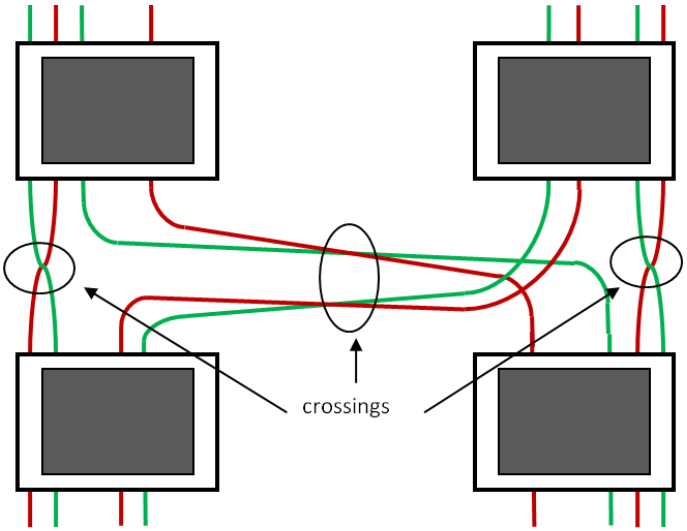

Figure 4-2 Schematic of part of a single layer inter-chip optical interconnection of Zhejiang University's design, after [4-38]

4.2.3 Huazhong University of Science and Technology OPCB for Distributed Computer Systems

Z. Yu, et al. in Huazhong University of Science and Technology [4-19] demonstrated a 3.125 Gb/s optical propagation through a 2×2 optical chip to chip interconnection network embedded in a PCB (as shown in Figure 4-3). A bit error rate (BER) was measured to be up to 1.27×10^{-18} for the reported data rate.

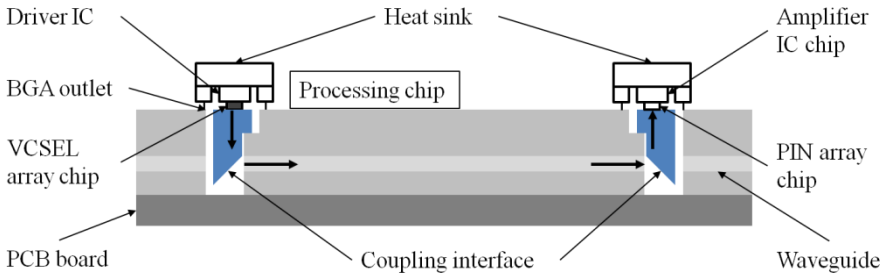

Figure 4-3 Schematic diagram of waveguide-based optical interconnect, after [4-19]

The architecture of inter-chip optical interconnects on PCB includes a VCSEL array, a photodiode array and a polymer channel waveguide array as the optical interconnects. The VCSEL is placed close to an MT coupler with a 45 °end facet so that light from the VCSEL array can be reflected by 90 °and coupled into the embedded waveguide with a cross section of 60 μm × 60 μm. The VCSEL and PD array along with their driver IC chips were bonded to their VLSI chips by ball-grid array (BGA) technology. The VLSI chips with VCSEL and PD arrays were bonded upon the PCB by surface-mount technology (SMT).

4.2.4 IBM Board-level Optical Interconnects

F. E. Doany, et al. IBM [4-39], [4-40] demonstrated the Terabus/DARPA C2OI program which focused on developing module-to-module board-level optical interconnects for parallel optical transceivers. The optical engine modules rely on a Si carrier with electrical and optical through-silicon vias (TSVs) to integrate top-emitting 850 nm optical engine arrays with CMOS ICs. The optical engine modules were assembled to the o-PCB using a ball grid array process provides both electrical and optical interconnections. A 48-channel flex-waveguide plain was laminated onto the electronic board and was fabricated using a lithographic process. The waveguide link was 15 cm long and contains 48 channels with 33 μm × 35 μm cores. Lens arrays were employed to provide optical coupling to/from the o-PCB. The driving conditions for the optomodules were optimized for 15 Gb/s/ch and a bit error ratio of $< 10^{-12}$ was demonstrated at 15 Gb/s/ch data rate. The 24-channel transceiver modules achieved a bidirectional aggregate bandwidth of 360 Gb/s (24 × 15 Gb/s/ch).

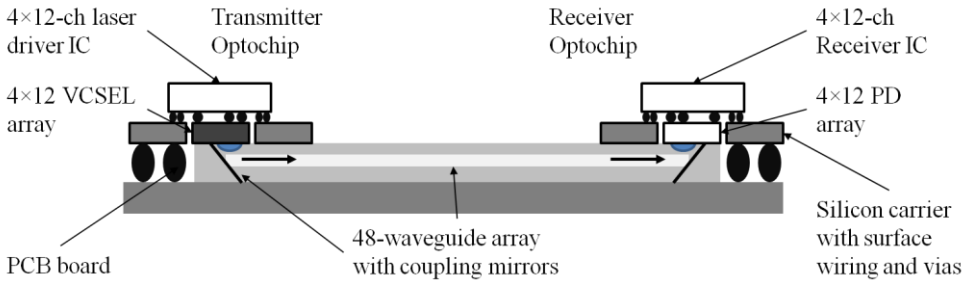

Figure 4-4 Schematic view of the Terabus package composed of an Optocard with optical waveguides and transmitter and receiver Optochips, after [4-41]

L. Schares, et al. in IBM reported the first generation Terabus 985 nm optical transceiver, which was based on a chip-like optoelectronic packaging structure (Optochip) that was assembled directly onto an organic card with integrated parallel waveguides, forming both electrical and optical connections [4-41]. Fully functional 24 T_X and 24 R_X optomodules were fabricated and tested. The test result demonstrated a transmitter operation of up to 20 Gb/s per channel and a receiver operation of up to 14-Gb/s.

4.2.5 Austria Technologie & Systemtechnik AG and Partners 3-Dimensional Optical Interconnects

G. Langer, et al. in the Austria Technologie & Systemtechnik AG, Institute of Surface Technology and Photonics, Joanneum Research, and Vienna University of

Technology, Institute of Telecommunications jointly reported [4-30] a method for coupling of optical waveguides to electro-optical components based on a two-photon absorption effect in the optical material that locally increases the refractive index of the material. This method gives precise alignment of the waveguide end faces to the transceiver components, more importantly it offered a 3-dimensional routing capability of the waveguides. Langer et al. [4-30] built a 15 × 5 cm^2 rectangular optical PCB based on ORMOCER® proprietary polymer waveguide material with two optical layers (Figure 4-5). The light is guided by two skew waveguides, i.e. each connecting the laser mounted at one level with the photodiode mounted on the other level and the two waveguides cross over horizontally and vertically. They do not penetrate each other but pass with a closest centre to centre distance of 85 μm. Data rates of 4 Gb/s and of 8.25 Gb/s with BER ≤ 10^{-9} was transmitted simultaneously on the two channels with negligible mutual influence. Each waveguide consists of seven adjacent waveguides with a core diameter of about 25 μm each and a centre-to-centre pitch distance of about 25 μm. The diameter of the waveguide bundle is approximately 68 μm × 75 μm.

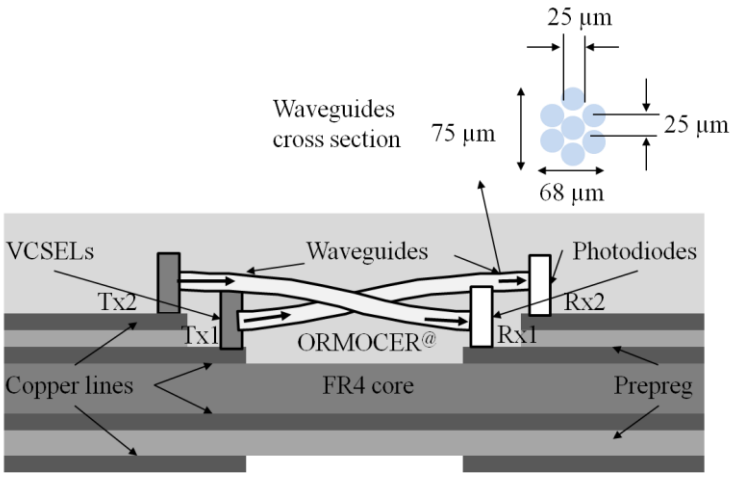

Figure 4-5. Board equipped with two pairs of VCSELs and photodiodes at two different levels above the FR4 substrate, after [4-30]

4.2.6 Fujitsu Laboratories Ltd. Optical Interconnect Architecture for Servers

J. Matsui, et al. from Fujitsu Laboratories Ltd. and Furukawa Electric Co. Ltd., Japan [4-42] proposed an optical interconnect architecture in a blade server for PCI-e extension and memory extension. The prototype was able to achieve a compact optical mid-plane on which it was possible to compactly arrange 1920 fibres instead of embedded optical waveguides. A 10 Gb/s signal was transmitted in each channel,

which gave aggregation capacity of 20 Tb/s. The authors also verified the capability of bus signal transmission with PCI-e Gen. 2.0.

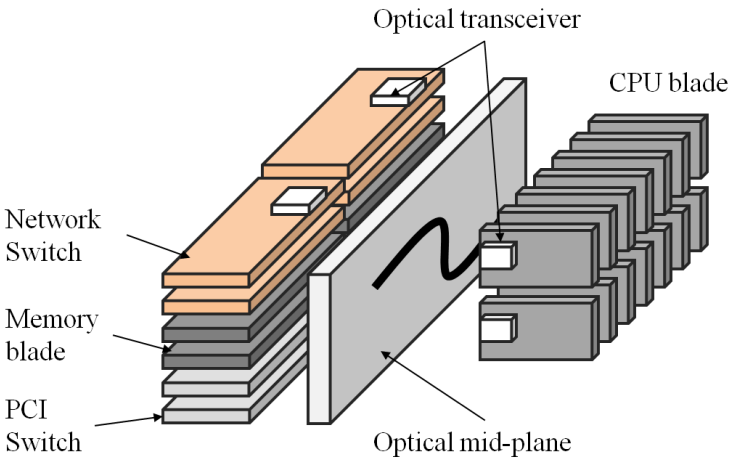

Figure 4-6 Optical mid-plane configuration of blade server with optical interconnection architecture proposed by Fujitsu Laboratories Ltd. after [4-42]

4.3 Review of Measurement Techniques

The measurement of optical loss of optical interconnects is strongly dependent on the choice of optical source, the roughness of the end facets of the waveguides, the type of light source, the type of output photo detector (PD) and, more importantly, the relative positions of all sources, detectors and waveguides, particularly for multimode optical waveguides. Therefore, the measurement techniques used by other researchers have to be reviewed in order to have a better understanding of the measured results.

4.3.1 Optical Loss Measurement by Imaging the Scattered Light from the Top Surface of a Waveguide

F. Wang, et al. in the Georgia Institute of Technology Packaging Research Center [4-17], [4-43] used photolithographically fabricated waveguides using the LightLink, a polysiloxane based material developed by Rohm and Haas Electronic Materials. They used a non-destructive and real-time technique (as shown in Figure 4-7) for characterization of the propagation properties of planar optical waveguides based on imaging the scattered light from the optical waveguide using a sensitive charge-coupled device (CCD) camera with built-in integration functionality and obtained optical loss of 0.065 dB/cm at a wavelength of 850 nm, and measurement error was less than 0.01 dB/cm.

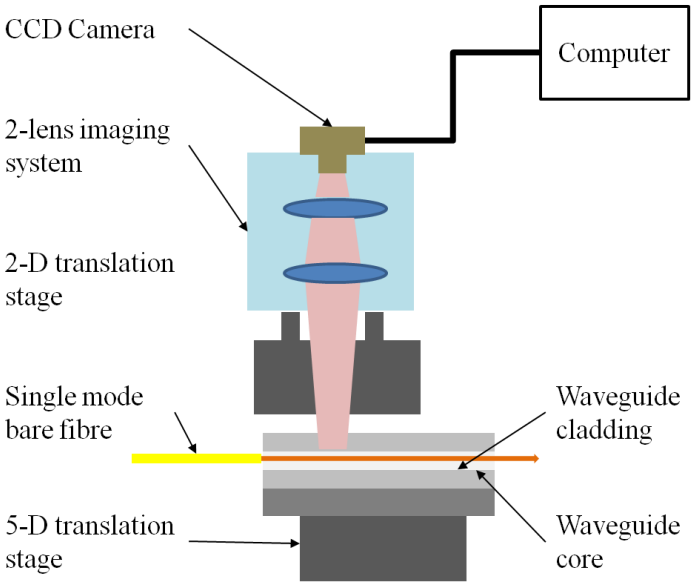

Figure 4-7 The experimental setup used to characterize the propagation of the polymer waveguides. A single-mode bare fibre is used as the facet coupler to excite the waveguide modes. The polymer waveguide is mounted on a five-axis precision stage. The adjustable two lens imaging system with numerical aperture of 0.15 along with the CCD camera is mounted on a 2-D large-range translation stage, after [4-17]

This measurement technique is strongly dependent on the transparency of the waveguide cladding and structure of optical PCBs, for instance, the method will not be valid if the optical layers are embedded between PCB layers.

4.3.2 Butt Coupled Optical Loss Measurement using Multimode Fibre

Y. Takeyoshi, et al. in the Keio University [4-35] reported the interfacial-gel polymerization technique as a fabrication process for preforms for high-bandwidth graded index (GI) polymer optical waveguides which were composed of general acrylic polymer (PMMA) with numerical aperture (NA) higher than 0.17. To measure optical performance, a 50 μm core multimode fibre (MMF) was utilized for launching into a channel of the waveguide, and a 100 μm core MMF probe with an NA of 0.2 was used to guide the output light from the launched core to a detector. The cut back method was used to assess the propagation losses at 850 nm and 980 nm which were 0.028 dB/cm and 0.061 dB/cm, respectively. They also used a UV-curable polymer (TPIR-202) supplied from Tokyo Ohka Kogyo Co., Ltd. to form GI core waveguide and used a non-destructive method using a monomer (TPIR-202) filled PMMA capillary to measure propagation loss [4-44]. However, this method was to evaluate the loss of polymer material itself rather than for a specific waveguide.

D. Cai and A. Neyer in the Technische Universität Dortmund demonstrated that PDMS (polydimethylsiloxane) had outstanding optical, thermal, and mechanical properties, and low shrinking (<0.3%) during polymerization [4-14]. They developed a new waveguide fabrication technology based on casting of thermal curing of two-component PDMS on copper-clad FR4 substrates. The PDMS was co-developed with Wacker Chemie, Burghausen, Germany, RT 601 for cladding and SLM 77522 for core. The waveguides were replicated using a high quality mould with low surface roughness (<30 nm). They carried out: A.) Tests against reliability during fabrication (1) Lamination conditions: 180 °C for 2 hours, 16 kp/cm^2 (to copper-clad FR4); (2) solder floating: 3 times 10 s solder floating at 260 °C. B.) Tests against reliability during operation (1) Damp heat: 40 °C, 93% humidity, 96 h; (2) dry heat: 150 °C for 3–10 days; (3) thermal shock: −50 ºC to 125 ºC, 30 °C/min, 100 cycles; (4) total test: test items B 1–3 as well as test item A were performed on the same specimen. The measurement was conducted by launching 850 nm laser light into the waveguides through a 50 µm GI fibre and detected by a 200 µm SI fibre (no detailed description was provided). The results showed that the PDMS waveguides exhibited low and stable optical loss values 0.035 dB/cm and <0.1 dB/cm before and after extreme environmental condition tests respectively.

4.3.3 Butt Coupled Optical Loss and Bit Error Rate (BER) Measurement using Multimode Fibre

Korea Photonics Technology Institute Integrated Optical Module Laboratory [4-45], [4-46] used waveguide materials supplied by ChemOptics, Inc. and used a dry-etch technique to produce flexible waveguides with core sizes of 50 µm × 50 µm and centre to centre pitch of 250 µm. They modulated an 850 nm VCSEL at a data rate of 2.5 Gb/s with a 2^7-1 pseudorandom bit sequence and coupled to a 50/125 MMF, while the output optical power from the waveguide was detected and amplified by a PIN-PD via a 62.5/125 MMF. The measured optical propagation loss of a 5 cm long waveguide was 0.24 dB/cm. Considering that the circular MMF core area is less than the rectangular waveguide core area, the actual coupling efficiency at the PD should be better than their experiment. The Korea researchers simulated solder reflow conditions for PCB packaging by exposing the waveguide at 225 °C for 30 seconds. The difference in optical insertion loss in the before-and-after tests was measured to be less than ±0.5 dB. The result showed high temperature resistance of the flexible

waveguide material, but also indicated the large error bar of the measurement technique.

4.3.4 Butt Coupled Optical Loss Measurement using Multimode and Single Fibre

J. Beals IV, et al. in the University of Cambridge [4-37] fabricated waveguides on an FR4 substrate from Dow Corning PDMS polymers using standard UV (I-line) photolithography. The core polymer (OE-4140) had a refractive index of ~1.52, and the top and bottom cladding polymer (OE-4141) had an index of ~1.50, giving a NA of 0.24. The insertion loss and crosstalk measurements were conducted using both a cleaved 50/125 μm multimode fibre and a cleaved 8/125 μm SMF-28 fibre input. An 850 nm multimode VCSEL was used as a source while a 50/125 μm multimode fibre was used to collect the light emitted at the waveguide output. For all measurements, index matching gel was employed at the waveguide facets to increase coupling efficiency. The receiving standard MMF normally has a NA of 0.2, which is less than the waveguide NA of 0.24. Some level of extra loss will occur at the waveguide exit facet due to the NA mismatch.

4.3.5 Butt Coupled Optical Loss Measurement using Single Mode Fibre Coupler

B. Chan, et al. in Endicott Interconnect (EI) Technologies [4-47] used the LIGHTLINK™ CLAD and CORE Optical Waveguide Technology material produced by Dow Chemical, specifically XP-5202A Waveguide Clad and XP-6701A Waveguide Core. The material is a siloxane based polymer and can be processed in much the same way as a liquid photoresist. A combination of doctor blading and inkjet printing methods were used to fabricate waveguides. A measurement system, shown schematically in Figure 4-8, is used for characterization of the waveguides fabricated at EI.

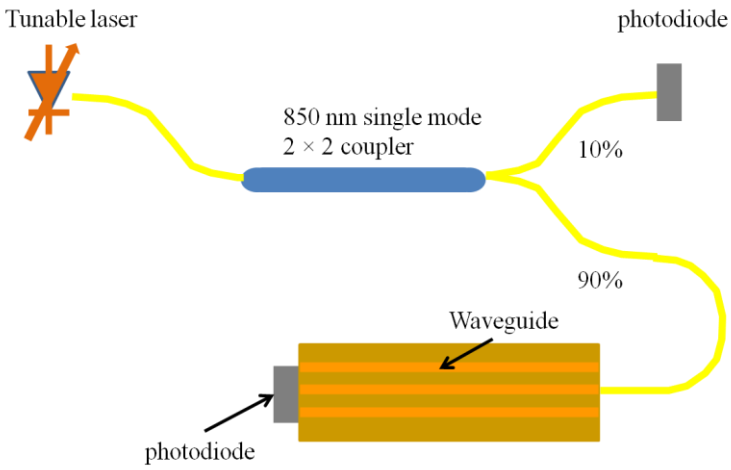

Figure 4-8 Experiment arrangement used by EI Technologies, after [4-47]

A tuneable 850 nm laser was used as the light source coupling into a 10:90 single mode 850 nm tap coupler. The laser power was monitored at the 10% tap using a calibrated power meter, while the 90% was used for loss measurement by butt coupling the laser light into the waveguide. The coupling loss at the waveguide end facets was offset by subtracting the measured insertion loss from a shorter waveguide of similar construction and geometry. EI have achieved a waveguide propagation loss of about 0.05 dB/cm at 850 nm.

4.3.6 Optical Loss Measurement using a 45 °Mirror Coupler

Yu et al. [4-19] reported using Polydimethylsiloxane materials (PDMS) and SU-8 2000 photoresist mould to form the waveguide and measured propagation loss at 850 nm lower than 0.16 dB/cm. They used a measurement configuration unique to their system, as shown in Figure 4-9.

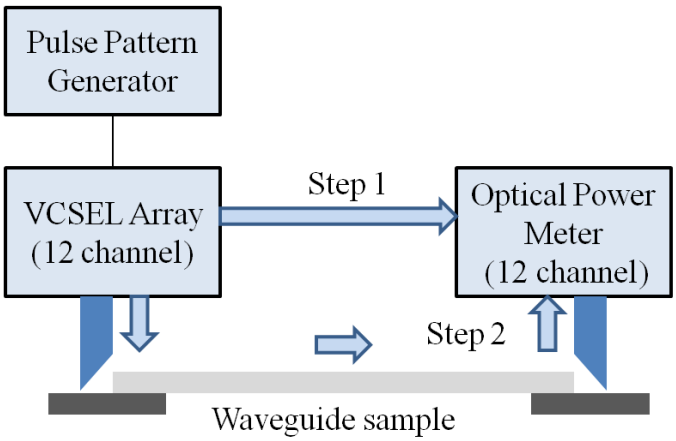

Figure 4-9 Schematic diagram of measurement of propagation losses, after [4-19]

Optical power through a 45° mirror coupler and waveguide was compared with the direct measurement of the output power of the VCSEL array. An averaged total insertion loss of 2.5 dB was reported.

4.3.7 Crosstalk Measurement

W. Lee and G. W. Kim in Korea Photonics Technology Institute [4-45] measured the optical crosstalk between the neighbouring channels of their flexible waveguide to be less than −35 dB.

T. Ishigure, et al. in Keio University experimentally measured the inter-channel crosstalk in their GI-core and SI-core waveguides [4-23], [4-44], [4-48] using both SMF and 50 μm MMF to launch an 850 nm VCSEL light source and using 50 μm MMF and an optical power meter to detect output power from waveguides. The results are shown in the following table.

Table 4-1 Comparison of crosstalk value in GI-core and SI-core waveguides under different launch conditions.

Waveguide	Probe	Ch. 1	Ch. 2	Ch. 4	Ch. 5
SI Core	SMF	−19.1 dB	−16.3 dB	−12.6 dB	−17.5 dB
GI Core		−32.0 dB	−23.2 dB	−22.3 dB	−29.2 dB
SI Core	MMF	−17.4 dB	−15.3 dB	−14.8 dB	−16.8 dB
SI Core		−25.9 dB	−20.7 dB	−19.2 dB	−23.7 dB

Note: Ch 3. is the monitored waveguide

There is a noticeable trend that the crosstalk values in the SI-core waveguides are 5~10 dB higher than those in the GI core waveguides However, the crosstalk values in all the channels are higher than those of GI core waveguides previously reported [4-35] which were -34.0 dB from a neighbouring waveguide for an array of 50 μm core and 120 μm pitch waveguides. The crosstalk was reduced to less than -68 dB when carbon black doped cladding was used [4-49].

N. Bamiedakis, et al. in the University of Cambridge [4-12] studied waveguide groups with different separations (100 to 250 μm) and reported crosstalk levels below 30 dB both for SMF and 50 μm MMF inputs.The longest straight waveguides that were most

susceptible to crosstalk (lengths of 125 mm) measured values were approximately 50 dB for an SMF input and 35 dB for a 50 μm MMF input respectively.

4.3.8 Optical Loss Measurement in Bends

To allow connectors to be arbitrarily placed across the backplane area, the waveguides must have bends but these can introduce loss, crosstalk through radiated waves and reflections. Although the loss as a function of bend radius has been studied in single mode waveguides [4-50], [4-51] and in single mode [4-52], [4-53] and multimode silica and plastic fibres [4-1], [4-54], [4-55] limited research has been reported on the bend loss of polymer multimode waveguides for use in backplanes [4-51], [4-56]. In this thesis the author extend the earlier research by measuring the insertion loss of a cascade of straight - curved - straight waveguides and by separating out the various loss mechanisms. Waveguide bend losses below 1 dB were reported for radii of curvature larger than 4.5 mm for an SMF input and larger than 8 mm for a 50 μm MMF input by N. Bamiedakis, et al. in the University of Cambridge [4-12].

4.4 Review of other UCL Research in Polymer Waveguide Optical Backplane

UCL has been actively involved in research on polymer waveguide optical backplanes in the last decade and has closely worked with industrial companies and other universities including, e.g. Xyratex Technology Ltd., Exxelis Ltd., the National Physical Laboratory (NPL), University of Edinburgh, Loughborough University and Heriot-Watt University. There were two major projects carried out in UCL previously: StorLite [4-57], [4-58], a 27 month EPSRC funded research project via the LINK Information Storage and Displays grant GR/S28136/01 and Integrated Optical and Electronic Interconnect PCB Manufacturing [4-5], [4-7], [4-10], [4-59–62], a 36-month flagship project funded by EPSRC via the Innovative electronics Manufacturing Research Centre (I*e*MRC) grant FS/06/01/01. In total two optical PCB demonstrators incorporating embedded optical waveguides had been built at the end of the two projects. The overall goal of the research was to develop polymer waveguide technology into a more advanced state, whereby it could be used to make optical printed circuit boards to operate data in excess of 10 Gb/s for board-to-board optical communication as requested by collaborator Xyratex Technology to solve the industrial constraints in data centres. The related research by these collaborators is

reviewed in this section. The author of this thesis was involved in the two projects and so the author's contribution was also acknowledged where appropriate.

4.4.1 Photolithographic Fabrication Technique

The waveguide samples investigated in this thesis had been photolithographically fabricated (samples fabricated using other techniques are being investigated and will be reported in the near future). They were fabricated by Exxelis Limited using Truemode® polyacrylate polymer [4-63], [4-64] (a UV curable transparent polymer developed by Exxelis Limited) following the manufacturing technique illustrated in Figure 4-10.

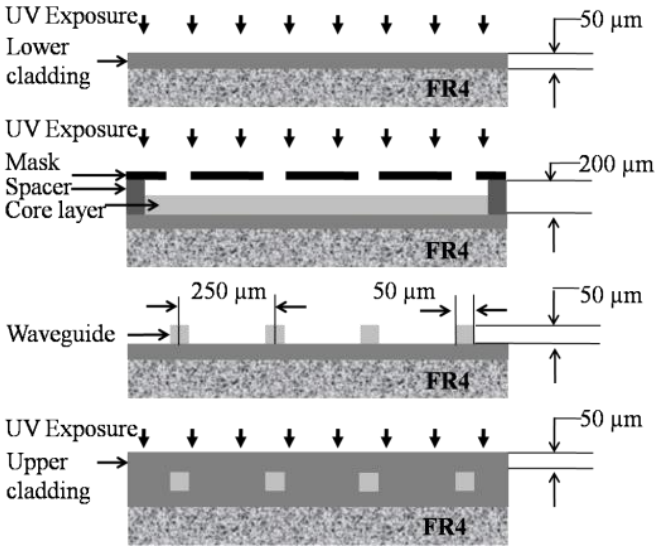

Figure 4-10 Photolithographically manufactured buried channel waveguides on FR4 PCB substrate, 50 μm × 50 μm core

In step 1, the procedure began by depositing the liquid cladding polymer material on an FR4 (glass reinforced epoxy) substrate and spin coating (130 rpm for 30 seconds) at an optimized acceleration rate to achieve uniform thickness of the lower cladding layer.

In step 2, the lower cladding polymer was cured in a UV (350 nm – 450 nm, the wavelength depends on the formula of the polymer used) chamber exposed to 15 mW/cm^2 power for 5 minutes.

In step 3, a 30 minute 100 ℃ baking procedure was adopted to remove the solvent residuals from the lower cladding substrate. The lower cladding covered the roughness of the FR4 surface [4-65] and provided a smooth interface for the core layer (Figure 4-11).

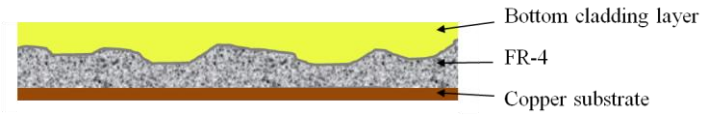

Figure 4-11 First layer of cladding covered the rough FR4 layer

In step 4, a similar spin coating method as in the lower cladding case was used to deposit liquid core polymer material onto the lower cladding. An e-beam high resolution mask designed by Dr. Guoyu Yu and Dr. Ioannis Papakonstantinou in the Optical Devices and Systems Research Laboratory in UCLwas aligned with the wafer using a UV mask aligner. 200 μm spacers were used to maintain the separation between the mask and the wet film to prevent physical contact.

In step 5, the wafer was covered with nitrogen gas for 1 minute to exclude oxygen. The core layer was then exposed to UV light through the patterned mask.

In step 6, any remaining uncured polymer material was washed away.

In step 7, an additional 2 minute, 15 mW/cm^2, UV exposure completely polymerized the waveguides

In step 8, a 30 minute 100 ℃ baking procedure was used to remove the solvent residuals from the waveguide core.

In step 9, the same technique used to produce bottom cladding layer was applied to deposit and UV-cure the upper cladding.

In step 10, a 30 minute 100 ℃ baking was used procedure to remove the solvent residuals from the upper cladding.

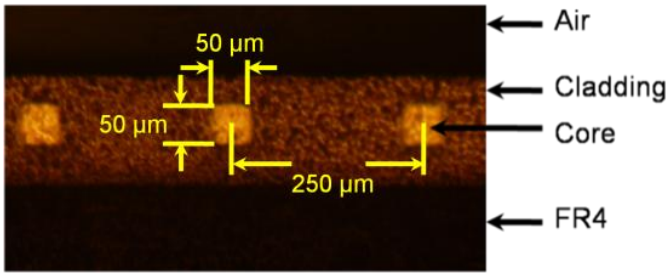

Figure 4-12 End facets of 50 μm × 50 μm straight waveguides photographed through a Nomarski Microscope using both back and front illumination

Figure 4-12 shows a photograph of the end facet of a polymer waveguide array observed through a Nomarski microscope. The refractive index of the core was 1.5560; slightly higher than the cladding (1.5264), giving a theoretical numerical aperture (NA) of 0.302. Waveguides analyzed and reported in this chapter had 50 μm thick cores unless otherwise stated, and the pitch between two adjacent waveguides

was 250 μm. The Truemode® polyacrylate polymer has been measured previously by Dr. Ioannis Papakonstantinou using 1 m spiral waveguides and had a propagation loss of 0.08 ± 0.01 dB/cm at 850 nm [4-58].

4.4.2 Demonstrator 1 - StorLite

The "StorLite" demonstrator was made by Xyratex and UCL. Figure 4-13 shows a photograph of StorLite taken from the daughter boards looking towards the separate electrical backplane (green board at the right side) and optical backplanes (orange board in the centre). The aim was to extend this to design and demonstrate a single hybrid optical and electrical backplane. Both of the laser diodes and photodiodes are attached to and powered from the daughterboard. The daughterboards engaged to the backplane via special connectors which enable the lasers and photodiodes to couple directly to the backplane waveguide by butt coupling. Dr. David R. Selviah in UCL invented a low cost method for passive self-alignment of the laser source and photodiodes to the waveguides. The author participated in most of the experimental measurement with Dr. Ioannis Papakonstantinou.

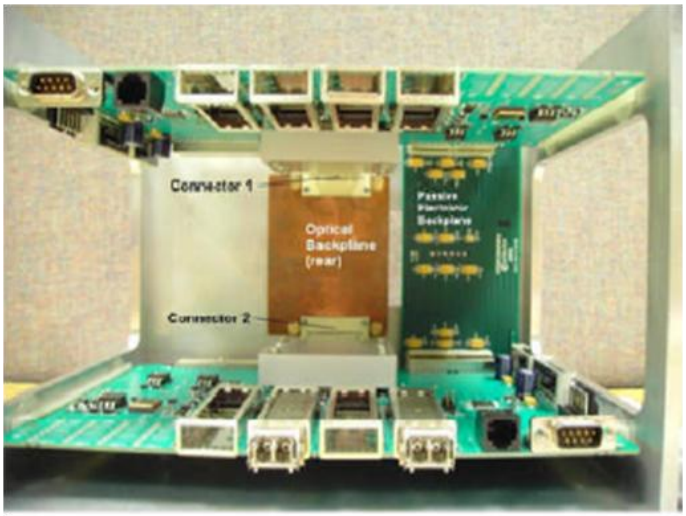

Figure 4-13 A picture of daughterboard connected to the optical backplane (courtesy of Xyratex)

4.4.3 Demonstrator 2 – FirstLight

In order to evaluate the viability of OPCB technology in a data centre environment, Xyratex constructed a demonstration platform, which comprised a 10 U (445 mm) high Compact PCI chassis with a single board computer, an electro-optical midplane and 4 peripheral test cards, each housing a pluggable optical connector.

The peripheral test cards (Figure 4-14) were designed to relay external 10.3125 Gb/s 10 GbE LAN test data to each other optically across the midplane through the pluggable connectors. Each test card included a reconfigurable crosspoint switch to map test data from 4 commercial 10 Gigabit Small Form Factor Pluggable (XFP) ports on the front edge to the transceiver housed in the connector on the peripheral test card (back) edge. The switch also supported multicasting, whereby, test data on any of its inputs could be copied to multiple outputs. This way, one external test stream could be mapped to all 4 VCSEL transmitters in the connector simultaneously allowing it be characterised while fully stressed. An FPGA was present on the board to allow user communication with the XFPs, crosspoint switch and FirstLight transceiver. A PCI bridge chip allowed a user communications interface to be established between the single board computer and all the line cards via the electrical Compact PCI bus and connectors on the electro-optical midplane.

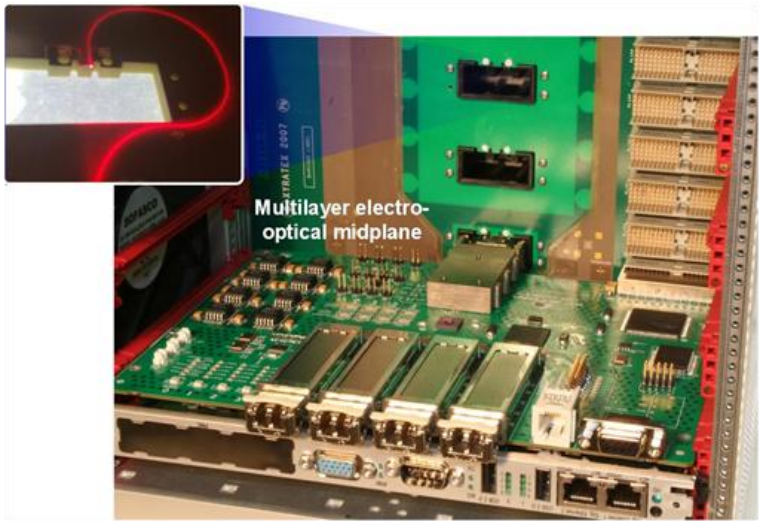

Figure 4-14 A peripheral test card and pluggable optical connector attached to an OPCB. Inset is a waveguide illuminated with 635 nm laser for aid of visualization.

Figure 4-15 shows the fully assembled demonstration platform. An external Xyratex proprietary 10 Gb Ethernet LAN traffic source was arranged to convey a 10.3125 Gb/s test data stream along a fiber-optic cable to one of the commercial XFP devices on the front edge of a peripheral test card in the demonstration platform. The XFP device converted the input optical data stream to a serial electronic data stream on the test card, which was then mapped by the crosspoint switch to one of the VCSEL transmitters in the connector attached to that card and reconverted into an optical data stream. As the connector was optically engaged to the midplane, the optical data

stream was launched into a waveguide and conveyed to the receive element of another connector on a different test card in the chassis. The data was then converted to a serial electronic data stream, mapped to an XFP port on that test card and reconverted to an optical data stream on the output of the XFP device. Finally, a fiber-optic cable was connected between the XFP output port to a Tektronix CSA8000B communications signal analyzer where the test data was characterised.

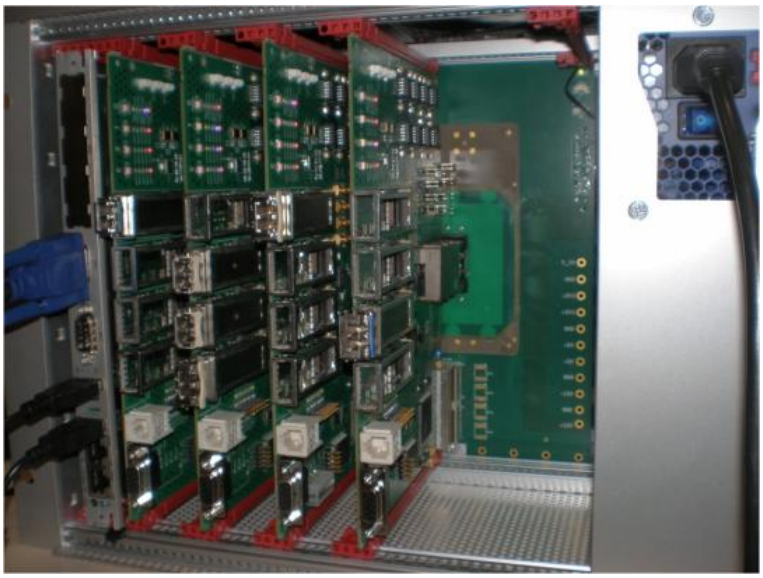

Figure 4-15 Demonstrator containing integrated electronic and optical interconnections on the backplane and 4 connected line cards

4.5 Conclusions

This chapter reviewed some of the research most relevant to the author's work on optical backplane systems. There is a large diversity in the optical polymer materials and the fabrication techniques used to make the waveguides. It is difficult to identify the dominant technology and even more difficult to compare them due to the different measurement techniques employed to assess the performance of the waveguides. Most optical systems have on-board optical transceivers and use waveguides to deliver light via 45° mirrors or butt coupled connectors. The size of the waveguides varied from 25 μm × 25 μm to 300 μm × 300 μm depending on the application, fabrication techniques and alignment methods used. A low loss, scalable and compact optical layer is the most crucial element in an optical backplane system. A polymer waveguides interconnects with a scalable mesh was reported only in [4-37]. A lot of work still needs to be done to standardize the measurement methods and to improve the fabrication and design of the optical interconnects.

Chapter 4 References

[4-1] M. Y. Loke and J. N. McMullin, "Simulation and Measurement of Radiation Loss at Multimode Fiber Macrobends," *J. Light. Technol.*, vol. 8, no. 8, pp. 1250–1256, 1990.

[4-2] M. A. Losada, I. Garces, J. Mateo, I. Salinas, J. Lou, and J. Zubia, "Mode coupling contribution to radiation losses in curvatures for high and low numerical aperture plastic optical fibers," *J. Light. Technol.*, vol. 20, no. 7, pp. 1160–1164, Jul. 2002.

[4-3] F. Betschon, "Challenges in Mass Production of Electro-Optical Circuit Boards Summary of the correspondent presentation on 2010 IEEE Winter Topicals," *Photonics Soc. Winter Top. Meet. Ser.*, vol. 1, pp. 89–90, 2010.

[4-4] M. B. Ritter, Y. Vlasov, J. a Kash, and a Benner, "Optical technologies for data communication in large parallel systems," *J. Instrum.*, vol. 6, no. 01, pp. C01012–C01012, Jan. 2011.

[4-5] D. R. Selviah, A. C. Walker, D. A. Hutt, K. Wang, A. McCarthy, F. A. Fernández, I. Papakonstantinou, H. Baghsiahi, H. Suyal, M. Taghizadeh, P. Conway, J. Chappell, S. S. Zakariyah, D. Milward, R. C. A. Pitwon, K. Hopkins, M. Muggeridge, J. Rygate, J. Calver, W. Kandulski, D. J. Deshazer, K. Hueston, D. J. Ives, R. Ferguson, S. Harris, G. Hinde, M. Cole, H. White, N. Suyal, H. ur Rehman, and C. Bryson, "Integrated optical and electronic interconnect PCB manufacturing research," *Circuit World*, vol. 36, no. 2, pp. 5–19, 2010.

[4-6] S. S. Zakariyah, P. P. Conway, D. A. Hutt, D. R. Selviah, K. Wang, H. Baghsiahi, J. Rygate, J. Calver, and W. Kandulski, "Polymer Optical Waveguide Fabrication Using Laser Ablation," *Electron. Packag. Technol. Conf.*, pp. 936–941, 2009.

[4-7] R. C. A. Pitwon, D. R. Selviah, and I. Papakonstantinou, "Optical wavelength division multiplexed multiplexer/demultiplexer for an optical printed circuit

board and a method of manufacturing the same," Patent number: US7,805,0332010.

[4-8] R. Pitwon and H. Schröder, "Embedded planar glass waveguide optical interconnect for data centre applications," *Proc. SPIE*, vol. 8630, no. 0, 2013.

[4-9] R. C. A. Pitwon, C. Smith, K. Wang, J. Graham-Jones, D. R. Selviah, M. Halter, and A. Worrall, "Polymer optical waveguides with reduced in-plane bend loss for electro-optical PCBs," *Proc. SPIE*, vol. 8264, 2012.

[4-10] I. D. Johnson, R. C. A. Pitwon, D. R. Selviah, and I. Papakonstantinou, "Optical printed circuit board and manufacturing method," Patent number: US7,936,9532011.

[4-11] E. Bosman, G. Van Steenberge, B. Van Hoe, S. Member, J. Missinne, J. Vanfleteren, and P. Van Daele, "Highly Reliable Flexible Active Optical Links," vol. 22, no. 5, pp. 2009–2011, 2010.

[4-12] N. Bamiedakis, J. Beals, R. V Penty, S. Member, I. H. White, J. V Degroot, T. V. Clapp, and A. Cost-effective, "Cost-Effective Multimode Polymer Waveguides for High-Speed On-Board Optical Interconnects," *IEEE J. Quantum Electron.*, vol. 45, no. 4, pp. 415–424, 2009.

[4-13] M. Karppinen, T. Alajoki, A. Tanskanen, K. Kataja, J. Mäkinen, K. Kautio, and P. Karioja, "Parallel Optical Interconnect between Ceramic BGA Packages on FR4 Board using Embedded Waveguides and Passive Optical Alignments," *Components*, pp. 799–805, 2006.

[4-14] D. Cai and A. Neyer, "Sensors and Actuators B : Chemical Polydimethylsiloxane (PDMS) based optical interconnect with copper-clad FR4 substrates," *Sensors Actuators B. Chem.*, vol. 160, no. 1, pp. 777–783, 2011.

[4-15] R. Barbieri, P. Benabes, T. Bierhoff, J. J. Caswell, A. Gauthier, J. Jahns, M. Jarczynski, P. Lukowicz, J. Oksman, G. a Russell, J. Schrage, J. F. Snowdon, O. Stübbe, G. Troster, and M. Wirz, "Design and construction of the high-speed

optoelectronic memory system demonstrator.," *Appl. Opt.*, vol. 47, no. 19, pp. 3500–12, Jul. 2008.

[4-16] S. Uhlig, "Ray-Tracing Studies on Optical Periscopes Suitable for Out-of-Plane Interconnects on Optical Backplanes," *IEEE Trans. Electron. Packag. Manuf.*, vol. 33, no. 1, pp. 55–64, 2010.

[4-17] F. Wang, F. Liu, G.-K. Chang, and A. Adibi, "Precision measurements for propagation properties of high-definition polymer waveguides by imaging of scattered light," *Opt. Eng.*, vol. 47, no. 2, p. 024602, Feb. 2008.

[4-18] H. Ma, A. K. Y. Jen, and L. R. Dalton, "Polymer-Based Optical Waveguides : Materials , Processing , and Devices," *Adv. Mater.*, vol. 14, no. 19, pp. 1339–1365, 2002.

[4-19] Z. Yu, F. Luo, X. Di, W. Zhou, B. Li, G. Wang, and J. Chen, "Highly reliable optical interconnection network on printed circuit board for distributed computer systems," *Opt. Laser Technol.*, vol. 42, no. 8, pp. 1332–1336, Nov. 2010.

[4-20] T. Ishigure and Y. Nitta, "Polymer optical waveguide with multiple graded-index cores for on-board interconnects fabricated using soft-lithography.," *Opt. Express*, vol. 18, no. 13, pp. 14191–14201, 2010.

[4-21] K. Matsuo, R. Yamazaki, and T. Ishigure, "Propagation mode analysis for polymer optical waveguide with graded index rectangular core," *2010 IEEE Photinic Soc. 23rd Annu. Meet.*, vol. 2, no. 1, pp. 16–17, Nov. 2010.

[4-22] H. Hsu, T. Ishigure, and S. Nakagawa, "Characterization and analysis of graded index optical waveguides for the realization of low-power , high-density , and high-speed optical link," *Proc. SPIE*, vol. 8267, pp. 1–6, 2012.

[4-23] T. Ishigure, K. Matsuo, Y. Nitta, Y. Sugimori, and S. Morikawa, "Densely-aligned graded-index multiple-core polymer optical waveguide : fabrication and inter-channel crosstalk property," *Proc. SPIE*, vol. 7944, pp. 1–8, 2011.

[4-24] D. Im, J. Kim, M. Hee, D. Kim, S. Kim, and J. Choi, "Thermally stable and low-loss optical waveguide using optical-fiber- embedded epoxy matrix for optical printed-circuit board applications," *Proc. SPIE*, vol. 7607, pp. 1–8, 2010.

[4-25] J.-W. Kim, N.-S. Son, J.-H. Jang, K.-J. Kim, and M.-C. Oh, "Ultra-low inter-channel crosstalk in array waveguide device incorporating self-assembled microsphere diffraction layer.," *Opt. Express*, vol. 19, no. 21, pp. 20904–9, Oct. 2011.

[4-26] J. Moisel, J. Guttmann, H.-P. Huber, O. Krumpholz, M. Rode, R. Bogenberger, and K.-P. Kuhn, "Optical backplanes with integrated polymer waveguides," *Opt. Eng.*, vol. 39, pp. 673–679, 2000.

[4-27] P. Lukowicz, J. Jahns, R. Barbieri, P. Benabes, T. Bierhoff, a. Gauthier, M. Jarczynski, G. a. Russell, J. Schrage, W. Sullau, J. F. Snowdon, M. Wirz, and G. Troster, "Optoelectronic interconnection technology in the holms system," *IEEE J. Sel. Top. Quantum Electron.*, vol. 9, no. 2, pp. 624–635, Mar. 2003.

[4-28] R. Dangel, C. Berger, R. Beyeler, L. Dellmann, M. Gmur, R é. Hamelin, F. Horst, T. Lamprecht, T. Morf, S. Oggioni, M. Spreafico, and B. J. Offrein, "Polymer-Waveguide-Based Board-Level Optical Interconnect Technology for Datacom Applications," *IEEE Trans. Adv. Packag.*, vol. 31, no. 4, pp. 759–767, Nov. 2008.

[4-29] H. Schröder, "Waveguides : Materials and Technology," *Int. Symp. Photonic Packag.*, 2006.

[4-30] G. Langer, V. Satzinger, V. Schmidt, G. Schmid, and W. R. Leeb, "PCB with fully integrated optical interconnects," *Proc. SPIE*, vol. 7944, pp. 1–15, 2011.

[4-31] D. Liang, G. Kurczveil, C. Chen, M. Fiorentino, Z. Peng, and R. G. Beausoleil, "Silicon Photonic Integrated Devices For Optical Interconnects Silicon Photonic Integrated Devices For Optical Interconnects," 2013.

[4-32] M. Immonen, M. Karppinen, and J. K. Kivilahti, "Fabrication and Characterization of Polymer Optical Waveguides With Integrated Micromirrors

for Optical Interconnects," *IEEE Trans. Electron. Packag. Manuf.*, vol. 28, no. 4, pp. 304–311, 2005.

[4-33] Y. Ishii, S. Koike, Y. Arai, and Y. Ando, "Interface for Interchip Optical Interconnections," vol. 26, no. 2, pp. 122–127, 2003.

[4-34] T. Okumura, T. Ishikawa, A. Tagaya, and Y. Koike, "Optical design of liquid crystal display backlighting with highly scattering optical transmission polymer," *J. Opt. A Pure Appl. Opt.*, vol. 5, no. 5, pp. S269–S275, Sep. 2003.

[4-35] Y. Takeyoshi, S. Member, and T. Ishigure, "High-Density 2 4 Channel Polymer Optical Waveguide With Graded-Index Circular Cores," *J. Light. Technol.*, vol. 27, no. 14, pp. 2852–2861, 2009.

[4-36] K. Koo, H. Cho, P. Kapur, and K. C. Saraswat, "Performance Comparisons Between Carbon Nanotubes, Optical, and Cu for Future High-Performance On-Chip Interconnect Applications," *IEEE Trans. Electron Devices*, vol. 54, no. 12, pp. 3206–3215, 2007.

[4-37] J. Beals IV, N. Bamiedakis, A. Wonfor, R. V. Penty, I. H. White, J. V. DeGroot Jr, K. Hueston, T. V. Clapp, and M. Glick, "A terabit capacity passive polymer optical backplane based on a novel meshed waveguide architecture," *Appl. Phys. A*, pp. 983–988, 2009.

[4-38] W. Ni, J. Wu, and X. Wu, "Crossing and branching nodes in soft-lithography-based optical interconnects.," *Opt. Express*, vol. 15, no. 20, pp. 12872–81, Oct. 2007.

[4-39] F. E. Doany, C. L. Schow, S. Member, B. G. Lee, R. A. Budd, C. W. Baks, C. K. Tsang, J. U. Knickerbocker, R. Dangel, B. Chan, H. Lin, C. Carver, J. Huang, J. Berry, D. Bajkowski, F. Libsch, and J. A. Kash, "Terabit / s-Class Optical PCB Links Incorporating Optical Transceivers," *J. Light. Technol.*, vol. 30, no. 4, pp. 560–571, 2012.

[4-40] F. E. Doany, C. L. Schow, B. G. Lee, R. Budd, C. Baks, R. Dangel, R. John, F. Libsch, J. A. Kash, B. Chan, H. Lin, C. Carver, J. Huang, J. Berry, and D.

Bajkowski, “Terabit / sec-Class Board-Level Optical Interconnects Through Polymer Waveguides Using 24-Channel Bidirectional Transceiver Modules,” *Electron. Components Technol. Conf.*, pp. 790–797, 2011.

[4-41] L. Schares, J. A. Kash, F. E. Doany, C. L. Schow, C. Schuster, S. Member, D. M. Kuchta, P. K. Pepeljugoski, J. M. Trewhella, C. W. Baks, R. A. John, L. Shan, Y. H. Kwark, R. A. Budd, P. Chiniwalla, F. R. Libsch, J. Rosner, C. K. Tsang, C. S. Patel, J. D. Schaub, R. Dangel, F. Horst, B. J. Offrein, D. Kucharski, D. Guckenberger, S. Hegde, H. Nyikal, C. Lin, A. Tandon, G. R. Trott, M. Nystrom, D. P. Bour, M. R. T. Tan, and D. W. Dolfi, “Terabus: Terabit / Second-Class Card-Level Optical Interconnect Technologies,” *J. Quantum Electron.*, vol. 12, no. 5, pp. 1032–1044, 2006.

[4-42] J. Matsui, T. Yamamoto, K. Tanaka, T. Ikeuchi, S. Ide, S. Aoki, T. Aoki, and T. Ishihara, “Optical Interconnect Architecture for Servers using High Bandwidth Optical Mid-plane,” *OFC/NFOEC Tech. Dig.*, pp. 3–5, 2012.

[4-43] F. Wang, F. Liu, and A. Adibi, “45 Degree Polymer Micromirror Integration for Board-Level Three-Dimensional Optical Interconnects,” *Opt. Express*, vol. 17, no. 13, pp. 10514–10521, 2009.

[4-44] T. Ishigure and Y. Nitta, “Polymer optical waveguide with multiple graded-index cores for on-board interconnects fabricated using soft-lithography.,” *Opt. Express*, vol. 18, no. 13, pp. 14191–201, Jun. 2010.

[4-45] W. Lee and G. W. Kim, “High-reliability flexible optical printed circuit board for opto-electric interconnections,” *Opt. Eng.*, vol. 48, no. 1, pp. 015401–1–015401–7, 2009.

[4-46] W. Lee, S. H. Hwang, J. W. Lim, C. H. Cho, G. W. Kim, and B. S. Rho, “Optical Interconnection Module Integrated on a Flexible Optical / Electrical Hybrid Printed Circuit Board,” *Electron. Components Technol. Conf.*, pp. 1802–1805, 2009.

[4-47] B. Chan, H. Lin, C. Carver, J. Huang, and J. Berry, "Organic Optical Waveguide Fabrication in a Manufacturing Environment," *Electron. Components Technol. Conf.*, pp. 2012–2018, 2010.

[4-48] H.-H. Hsu and T. Ishigure, "High-density channel alignment of graded index core polymer optical waveguide and its crosstalk analysis with ray tracing method.," *Opt. Express*, vol. 18, no. 13, pp. 13368–78, Jun. 2010.

[4-49] H. Uno and T. Ishigure, "GI-core polymer parallel optical waveguide with high-loss, carbon-black-doped cladding for extra low inter-channel crosstalk.," *Opt. Express*, vol. 19, no. 11, pp. 10931–9, May 2011.

[4-50] Q. Wu, Y. Semenova, P. Wang, A. M. Hatta, and G. Farrell, "Experimental demonstration of a simple displacement sensor based on a bent single-mode–multimode–single-mode fiber structure," *Meas. Sci. Technol.*, vol. 22, no. 2, p. 025203, Feb. 2011.

[4-51] J. Cardenas, L. Li, S. Kim, and G. Nordin, "Compact low loss single air interface bends in polymer waveguides," *Opt. Express*, vol. 12, no. 22, pp. 5314–5324, 2004.

[4-52] M. HEIBLUM and J. HARRIS, "ANALYSIS OF CURVED OPTICAL-WAVEGUIDES BY CONFORMAL TRANSFORMATION," *IEEE J. Quantum Electron.*, vol. QE11, no. 2, pp. 75–83, 1975.

[4-53] C. WINKLER, J. D. LOVE, and A. K. GHATAK, "Loss Calculations in Bent Multimode Optical-Waveguides," *Opt. Quantum Electron.*, vol. 11, no. 2, pp. 173–183, 1979.

[4-54] M. A. Losada, I. Garces, J. Mateo, I. Salinas, J. Lou, and J. Zubia, "Mode coupling contribution to radiation losses in curvatures for high and low numerical aperture plastic optical fibers," *J. Light. Technol.*, vol. 20, no. 7, pp. 1160–1164, Jul. 2002.

[4-55] A. A. P. Boechat, D. Su, D. R. Hall, and J. D. C. Jones, "BEND LOSS IN LARGE CORE MULTIMODE OPTICAL FIBER BEAM DELIVERY SYSTEMS," *Appl. Opt.*, vol. 30, no. 3, pp. 321–327, 1991.

[4-56] S. Musa, A. Borreman, A. Kok, and M. Diemeer, "Experimental study of bent multimode optical waveguides," *Appl. Opt.*, vol. 43, no. 30, pp. 5705–5707, 2004.

[4-57] I. Papakonstantinou, D. R. Selviah, K. Wang, R. A. Pitwon, K. Hopkins, and D. Milward, "Optical 8-Channel , 10 Gb / s MT Pluggable Connector Alignment Technology for Precision Coupling of Laser and Photodiode Arrays to Polymer Waveguide Arrays for Optical Board-to-Board Interconnects," *58TH Electron. COMPONENTS Technol. Conf. Proc.*, pp. 1769–1775, 2008.

[4-58] I. Papakonstantinou, D. R. Selviah, R. C. A. Pitwon, and D. Milward, "Low-Cost, Precision, Self-Alignment Technique for Coupling Laser and Photodiode Arrays to Polymer Waveguide Arrays on Multilayer PCBs," *IEEE Trans. Adv. Packag.*, vol. 31, no. 3, pp. 502–511, Aug. 2008.

[4-59]D. R. Selviah, F. A. Fernández, I. Papakonstantinou, K. Wang, H. Bagshiahi, A. Walker, A. Mccarthy, H. Suyal, M. Taghizadeh, D. Hutt, K. Williams, J. Chappell, S. S. Zakariyah, and D. Milward, "Integrated Optical and Electronic Interconnect Printed Circuit Board Manufacturing," *Circuit World*, vol. 34, no. 2, pp. 21–26, 2008.

[4-60] D. R. Selviah, A. Walker, D. Hutt, K. Wang, A. Mccarthy, F. A. Fernández, I. Papakonstantinou, H. Bagshiahi, H. Suyal, M. Taghizadeh, P. Conway, J. Chappell, S. S. Zakariyah, D. Milward, R. C. A. Pitwon, K. Hopkins, M. Muggeridge, J. Rygate, J. Calver, W. Kandulski, D. J. Deshazer, K. Hueston, D. J. Ives, R. Ferguson, S. Harris, G. Hinde, M. Cole, H. White, N. Suyal, H. ur Rehman, and C. Bryson, "Integrated Optical and Electronic Interconnect PCB Manufacturing Research," *Circuit World*, vol. 36, no. 2, pp. 5–19, 2010.

[4-61] K. Wang, D. R. Selviah, H. Baghsiahi, I. Fernández, F.A., Papakonstantinou, and G. Yu, "Design Rules for Polymer Waveguides and Measurement

Techniques," in *2nd International IEEE Symposium on Photonic Packaging Electrical Optical Circuit Board and Optical Backplane,IEEE-CPMT and IEEE-LEOS Messe München Munich, co-located with Electronica, Germany, 13th November 2008*.

[4-62] D. R. Selviah, "Polymer multimode waveguide optical and electronic PCB manufacturing," *Proc. SPIE*, pp. 721905–721905–10, 2009.

[4-63] Tetahertz-Photonics, "Truemode Backplane Enabling optical backplanes," *www.thzonline.com*, no. April, pp. 1–5, 2003.

[4-64] "Truemode™ wetfilm core datasheet," *Exxelis Limited*. [Online]. Available: http://www.exxelis.com/products/Truemode-datasheet-f.pdf. [Accessed: 01-Mar-2014].

[4-65] R. C. A. Pitwon, K. Wang, J. Graham-Jones, I. Papakonstantinou, H. Baghsiahi, B. Offrein, R. Dangel, D. Milward, and D. R. Selviah, "FirstLight: Pluggable Optical Interconnect Technologies for Polymeric Electro-Optical Printed Circuit Boards in Data Centers," *J. Light. Technol.*, vol. 30, no. 21, pp. 3316–3329, 2012.

Chapter 5 Ray Trace Model of a Novel Liquid Crystal Display Backlight

5.1 Introduction

This chapter reports a novel structure for an efficient novel backlight for liquid crystal display (LCD) systems in which the three primary colours of the light are separated by a diffraction grating and each colour illuminates a separate column of sub-pixels in the display. A discrete reflective mirror layer inside the backlight designed by the author to improve the efficiency of the backlight is reported for the first time [5-1]. Non-sequential ray trace modelling is used to improve the design of the novel structure.

5.2 Disadvantages of Conventional Liquid Crystal Displays

The basic operation of the Conventional LCD Backlight System, Figure 5-1, can be thought of as a discrete column matrix of liquid crystal molecules able to twist the polarisation axis of light passing though them. With the help of two layers of polarisers, and transistors controlling the amount of change in the polarisation axis, it is possible to vary the amount of light emerging from the top layer. Due to the difference in the operating principle, the LCDs can be categorized as Passive LCDs and Active LCDs [5-2][5-3].

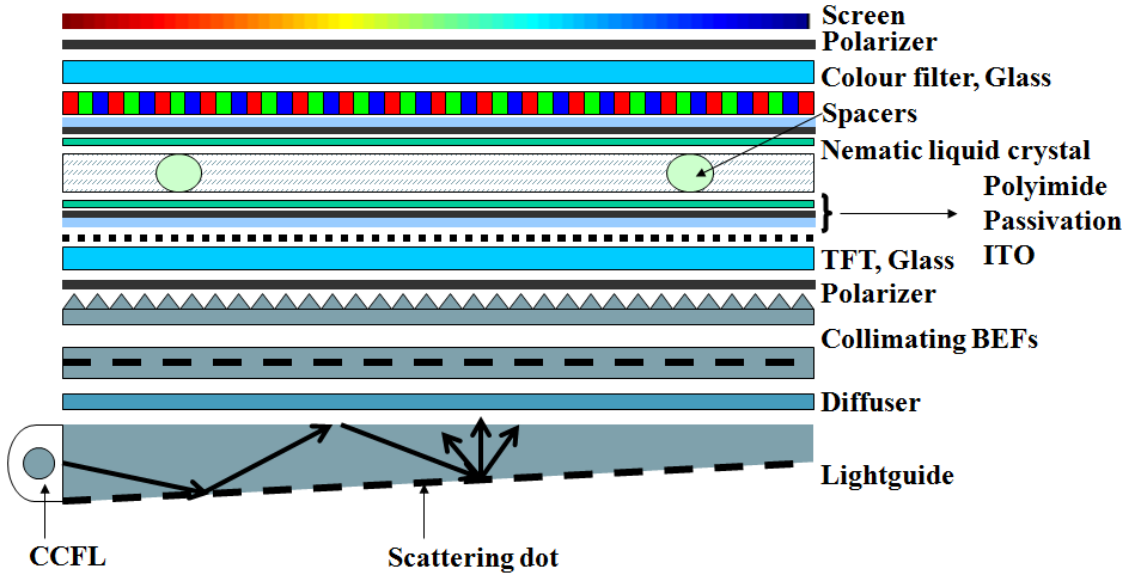

Figure 5-1 Conventional LCD backlight structure

In a passive matrix LCD, light from an extended light source, e.g. a Cold Cathode Fluorescent Lamp (CCFL) is guided by a glass or polymer light guide. The light guide

is usually designed in a wedge shape to achieve better uniformity. A sheet of scattering dots is placed either on the bottom to reflect light or the top layer of the light guide to extract light towards the direction of the screen. The dots on the scattering sheet have a Bezier arrangement [5-4] in order to provide uniform illumination. Additional Brightness Enhancement Films (BEFs) [5-5] can be used to collimate the extended light normal to the display and increase the efficiency of the light guide by reflecting more light toward the viewer. A polarizer is attached to the front (facing the incoming light from the backlight) glass plate in order to polarize the incoming light in a single direction. An Indium Tin Oxide (ITO) layer is used as a transparent electrode. A passivation (hard coat) layer based on SiO_x is coated over the ITO to electrically insulate the surface. Polyimide is printed over the passivation layer. The polyimide layer is rubbed to align the LC parallel to the polarizer direction. The liquid crystal is sensitive to electric fields and the LC molecules change orientation when an electric field is applied. The liquid crystal is also optically active and rotates the polarization direction of the incoming light. The thickness of the LC layer is determined by spacers, which keep the two glass plates apart by a fixed distance. When there is no electric potential from the front piece of glass to the rear piece of glass, the polarised light is rotated 90 ° as it passes through the liquid crystal layer. When an electric potential is applied from one plate to the other plate normal to the plates the light is not rotated. After the light has passed through the liquid crystal, it passes through another set of layers of polyimide, ITO electrode, and the rear glass (a glass sheet above the ITO). When it reaches the analyzer it is either transmitted or absorbed, depending on whether or not it has been rotated 90 °.

Active matrix technology uses thin-film transistors (TFTs) of either amorphous or polycrystalline silicon applied to the rear LCD glass plate (the glass plate placed above the ITO). Amorphous silicon TFTs are easier to produce so they are widely used for most large displays nowadays. On the other hand, poly-silicon TFTs have a better performance, but require a higher deposition temperature. They are produced in tube furnaces [5-6] and, therefore, only small displays can be manufactured.

In colour LCDs, colour filters are placed inside of the rear glass sheet and should be finely aligned with TFTs. Three colours red, blue and green and a black matrix are

used. With the conventional backlight design, only a few percent of the light generated by the backlight emerges from the display screen [5-7]. At least two thirds of the light is absorbed by the colour filters [5-8] and at least a further half by the polarisers. The backlight illumination is usually continuous over the whole display but only light falling onto the pixel apertures passes through the display, causing loss by this fill factor or aperture ratio. The statistics of the loss at each optical component are listed in Table 5-1.

Table 5-1 Transmission of various LCD components

BACKLIGHT ELEMENTS	LIGHT TRANSMISSION
Lightguide	60% [5-7]
Diffusers	95% [5-9]
Addressed Cell Assembly (ACA)	6.5%* *includes Rear Polarizer and Analyzer 50% [5-10] TFT 48% [5-11] Colour filters 27% [5-8], [12]
Total	3.7%

The performance of the liquid crystal display can be improved in several respects: improved conversion efficiency of light generated by the backlight to modulated light emitted [5-13] from the front of the display to the viewer; ideally no polarisers or colour filters; lower electrical power consumption; small size efficient light source [5-14], e.g. LED; higher contrast ratio; good uniformity of illumination; low cost and ease of fabrication of the backlight [5-15] and wide viewing angle [5-16]. In each application the priority of each of these attributes varies.

5.3 Novel Backlight Design

David R. Selviah and the author invented, designed, modelled and fabricated a new design of backlight for LCDs in order to improve the output efficiency of the backlight by separating and collimating the three primary colours (red, green and blue) so that they pass through the centre of each corresponding sub-pixel avoiding the need to use the highly lossy and costly colour filters. The prototype designed and built by David R. Selviah and Lawrence Commander was the first colour separation backlight for LCDs in the world and the ray tracing model of the light guide was also novel

research at the time the author conducted the work in 2004 [5-1]. The novel backlight (Figure 5-2) contained a light source (red, green and blue or white LEDs), a single thin light guide, an array of periodic gratings on the top surface of the light guide, an array of micro-mirrors in a layer inside the light guide, and an array of double convex cylindrical lenses directly above each grating aperture. David designed a rectangular light guide instead of the conventional wedge-shape one so that it could easily integrate multiple light sources at either or both sides of the light guide.

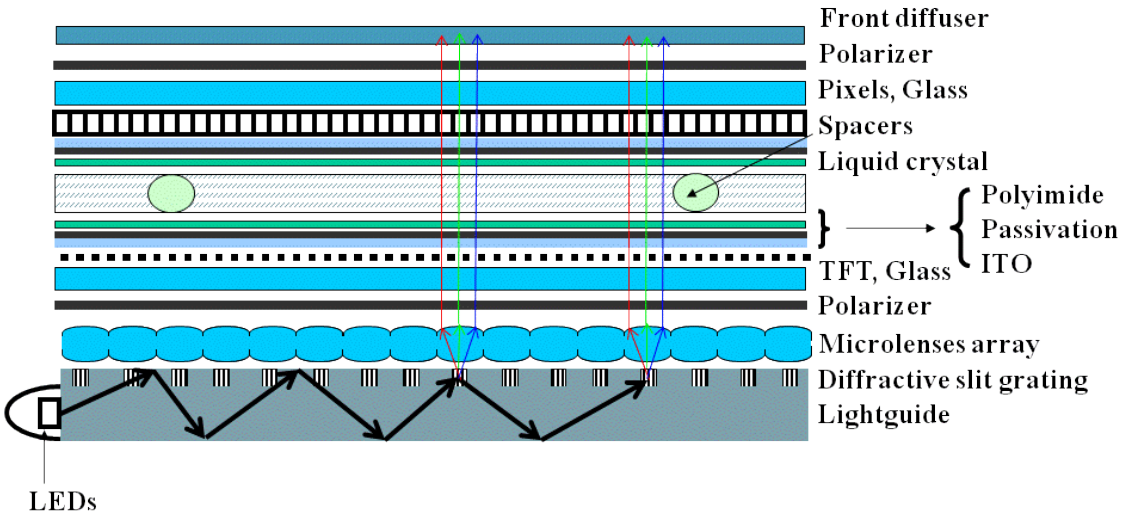

Figure 5-2 Advanced LCD backlight

In the backlight system, the light guide had, on its upper surface, a periodic array of discrete gratings, each of limited extent along the light guide surface, through which light periodically exits from the light guide. The gratings were the most crucial elements in the system. They not only extracted light from light guide but also angularly separated the white light into its constituent colours by diffraction.

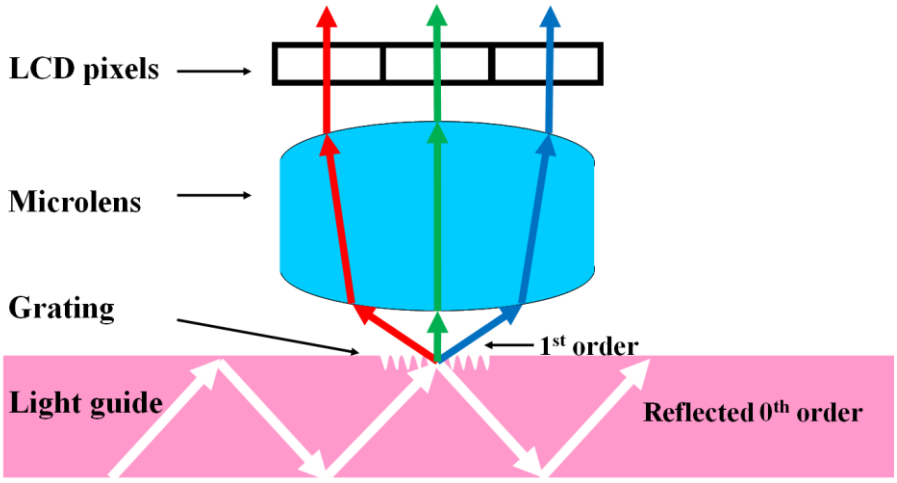

Figure 5-3 One pixel of advanced backlight

Figure 5-3 shows one of the micro-optical subsystems in the backlight used to illuminate a set of three red, green and blue pixels. This system is replicated many times to form an array along the length of the light guide. The three primary colour light beams exit the light guide at different angles are then captured by an microlens array positioned above the grating and collimated normal to the display screen to pass though the centre of each LCD sub-pixel. Therefore, the colour filters have been removed and the rest of the LCD assembly remains unchanged, with the important exception that a light of specific colour is switched throughout the liquid crystal layer, and emerges at the top polarizer layer.

Much of the scientific challenge of this novel technology is in the design of the diffraction gratings and the light guide in order to minimise various reflections and losses at the medium interfaces. The ray tracing method was used to model the system. Firstly, 4 LED Models were investigated to find a suitable light source as the illumination of the backlight system. Secondly, a model of light guide with integrated periodic gratings was modelled. Finally, the performance of an array of embedded mirrors was simulated to improve the output efficiency of the light guide.

5.4 Ray Trace Model of Colour Separating Backlight

5.4.1 Model of LEDs

The benefits of using LEDs as a light source for edge-lit backlights have been previously reported [5-17–20]. The LED backlight illumination system normally contains three colours of LEDs, red, green and blue, or extra bright white LEDs to form an array along the edge of the highly multimode light guide. The light is injected into a light guide, which mixes the three colours to give a uniform white light distributed along the length of the light guide [5-21–24]. This section covers the simulation of several different light source models using the ray trace method to simulate the light output profile of an LED array mounted at the entrance of the light guide. Ray trace software ASAP (Advanced Systems Analysis Program) was used as a modelling tool for the simulation. More details of modelling of the multimode light guide are reviewed later in this chapter.

The dimension detail of the emitting surface of a chip LED from CREE Optoelectronics was used to create an LED light model in ray trace. The model is the CxxxMB290-Sxx00 white LED [5-25] (see Figure 5-4). The top surface of the chip LED consists of three parts: substrate, junction area, which produces light, and a metal electrode that covers the centre of the junction. Each LED module has the package dimension of 300 μm × 300 μm and emitting area, Mesa (junction), is 240 μm × 240 μm.

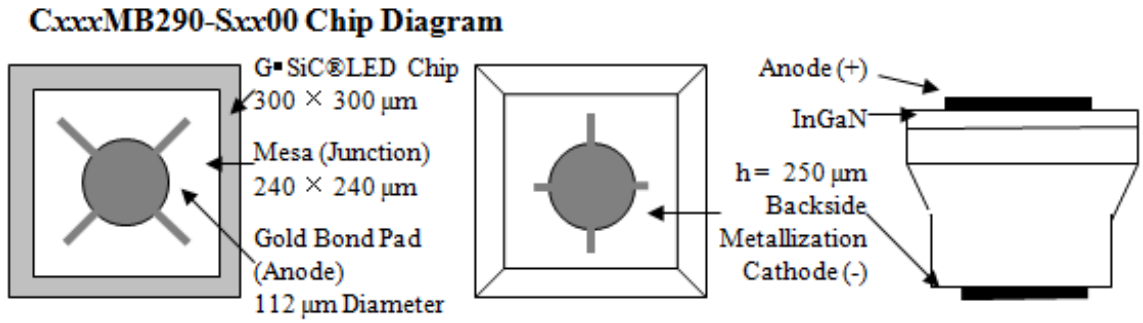

Figure 5-4 CxxxMB290-Sxx00 chip diagram, after [5-25]

The dimensions and shape of the Mesa area of the CREE LED was used to define the spatial size of the LED light source model in ray trace. The modelled LEDs were aligned in a 1D array with a uniform centre-to-centre pitch of 331 μm, matching the package size of the CREE LED (as shown in Figure 5-5)

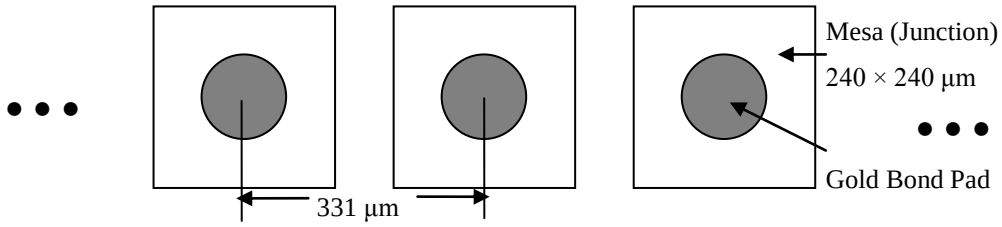

Figure 5-5 Geometry of the LEDs used for modelling

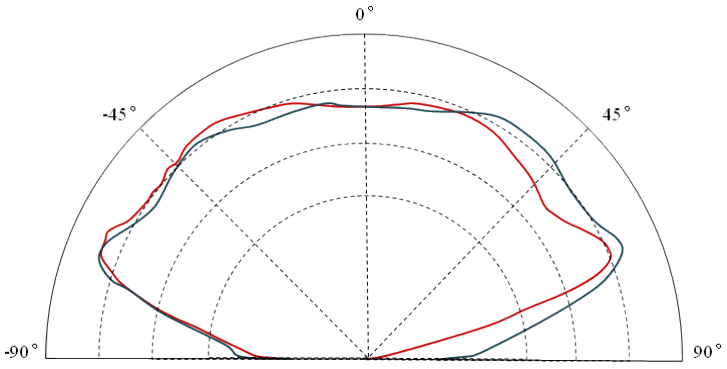

Figure 5-6 Radiation pattern of the CREE CxxxMB290 white chip LED, after [5-25]

The angular distribution of an LED is nearly a Lambertian source (Figure 5-6) [5-17], [5-26–28], so that a Lambertian emission profile is used to simulate the angular intensity distribution of an LED. A schematic model of a Lambertian emitter is illustrated in Figure 5-7. If define the radiance along the normal as, *I*, and total energy emitted into the vertical sector as $I \cdot d\Omega \cdot dA$, the energy emitted into the sector at an angle θ to the normal is $I \cdot d\Omega \cdot dA \cdot \cos\theta$.

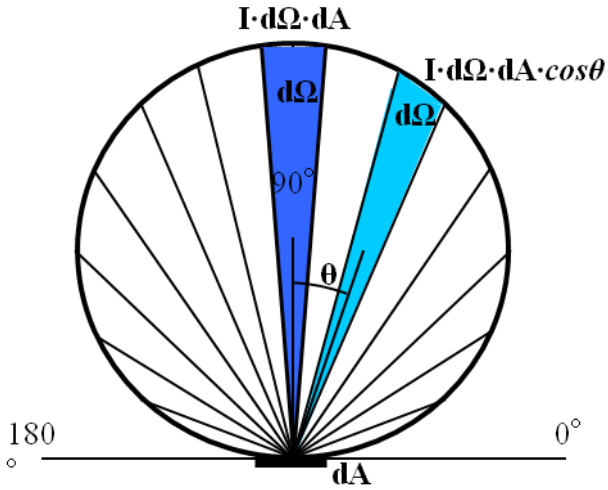

Figure 5-7 Lambertian intensity distribution

5.4.1.1 LED Model Using a Point Source

The first method, which was also the simplest one, was a virtual point source combined with a fine spatial uniform grid as shown in Figure 5-8. The grid was divided into small square sub-areas and the number of these sub-areas defined the total number of rays emitting from the point source. Figure 5-8 demonstrated how a 5 × 5 grid defined a point source and the grid structure.

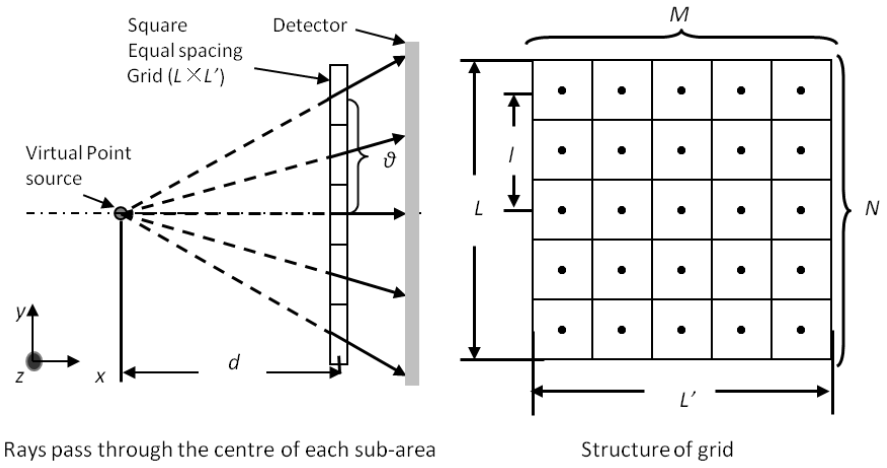

Figure 5-8 Schematic structure of a point source

Each beam arising from the virtual point source travels through the centre of its corresponding sub-area of the grid; therefore, the grid is the actual emitting surface and the locations of the sub-areas are the spatial coordinates of the output rays. The divergence of the point light source depends on the size ($L \times L'$) of the grid and the distance, d, to the point source. The half divergent angle, for example, on the y axis is:

$$\theta = \arctan\left(l/d\right) \qquad \textbf{Eq. 5-1}$$

Where, d, is the distance between the virtual point and the centre of the grid, l, is the distance from the centre of the grid to the centre of the furthest sub-area on the y axis, which is

$$l = \frac{L}{2} - \frac{1}{2} \bullet \frac{L}{N} \qquad \textbf{Eq. 5-2}$$

Where L is the geometrical height of the grid along the y axis and N is the number of sub-areas along the y axis.

Define a source in ASAP ray tracing requires the following 3 steps:

1. The initial location of each ray.
2. The initial direction of each ray.
3. The flux or power of each ray (optional).

The following command lines show the structure of a grid source in ASAP.

```
WAVELENGTH 525 NM
GRID RECT X -((331E-6)/2)-1E-6 (-JUNCTION)/2 (+JUNCTION)/2 (-JUNCTION)/2 (+JUNCTION)/2 1001 1001
SOURCE POSITION -((331E-6)/2)-2E-6 0 0
FLUX TOTAL 100
```

If d = 1 μm, according to equations Eq. 5-1 and Eq. 5-2, the point source has a half divergence angle of 89.52 ° which is similar to the divergence angle in the radiation pattern in Figure 5-6. The area of the grid was set to be 240 μm × 240 μm, matching the size of the emitting area of the chip LED and divided into 1,001 × 1,001 sub-areas. There were two reasons to design the grid like this. Firstly, an odd number was selected because it was easier to locate a ray at the centre of the distribution. Secondly, ASAP predicts luminance by using Monte-Carlo ray-trace methods, so that a large number of rays must be traced to obtain useful results. There were about one million rays (1,001 × 1,001 = 1,002,001) be generated from the point source, whereby the number was sufficient to trace through the whole length of a backlight structure to be modelled and to produce accurate results. One can define the relative flux of rays so

that the sum of all ray fluxes can be a desired number, exactly 100 in author's case. The unit of flux can be "labelled" appropriately according to its application.

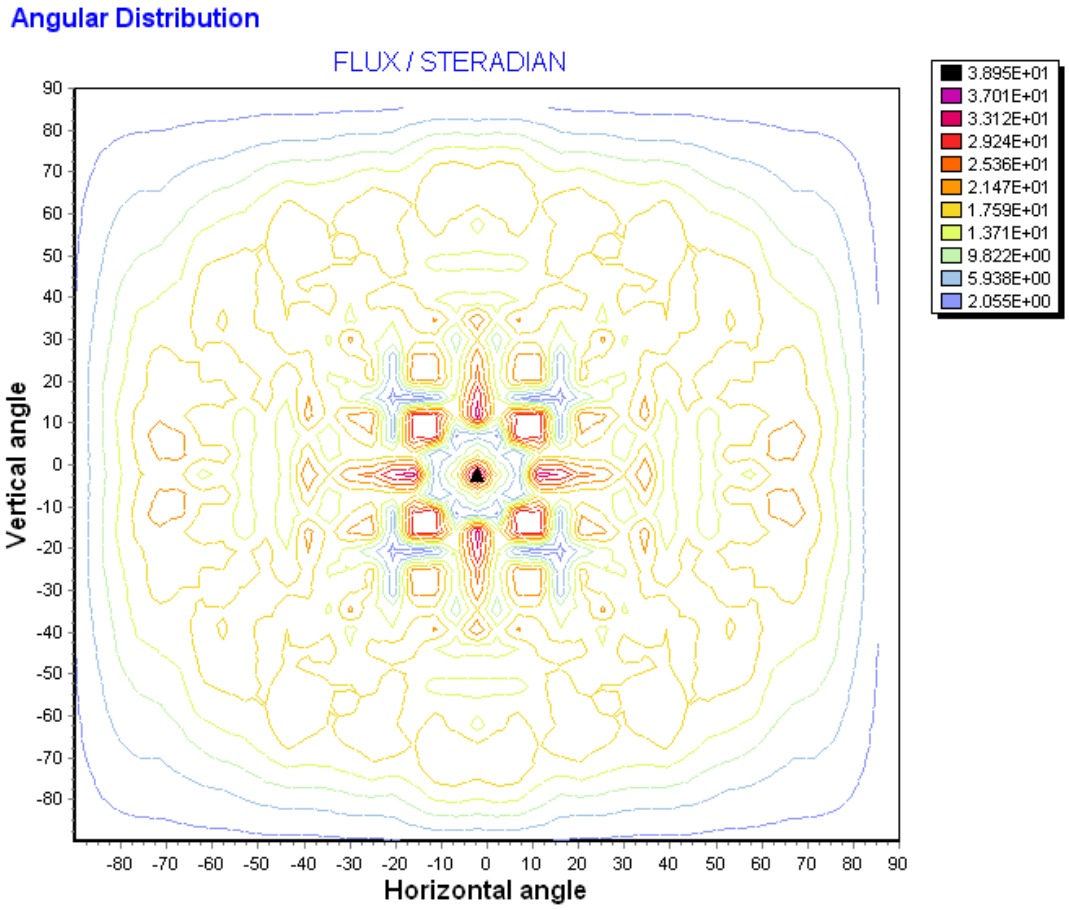

Figure 5-9 Contour map of angular distribution of a point source

Figure 5-9 shows the contour plot of the angular intensity distribution of light emerging from the grid. The angular distribution extended from -89.52 ° to 89.52 ° in both horizontal and vertical directions. A polar plot (Figure 5-10) of a central cross section of the angular energy distribution shows additional detail of the angular power profile. The highest intensity appears in the centre and diminishes to zero at ±90 °. Some symmetric discrete patterns of squares appear on the contour plot. They were because all of the beams passed through a spatially uniform grid rather than an angularly uniform grid. All of the rays were aligned with the centre of each square sub-area of the grid and propagated as a regular matrix in space. The number of rays per unit solid angle near the edge of a grid was larger than the number in the centre

area. Therefore, the effect of the grid was more severe in the centre compared to the surrounding area, although more than 1 million rays were used for modelling.

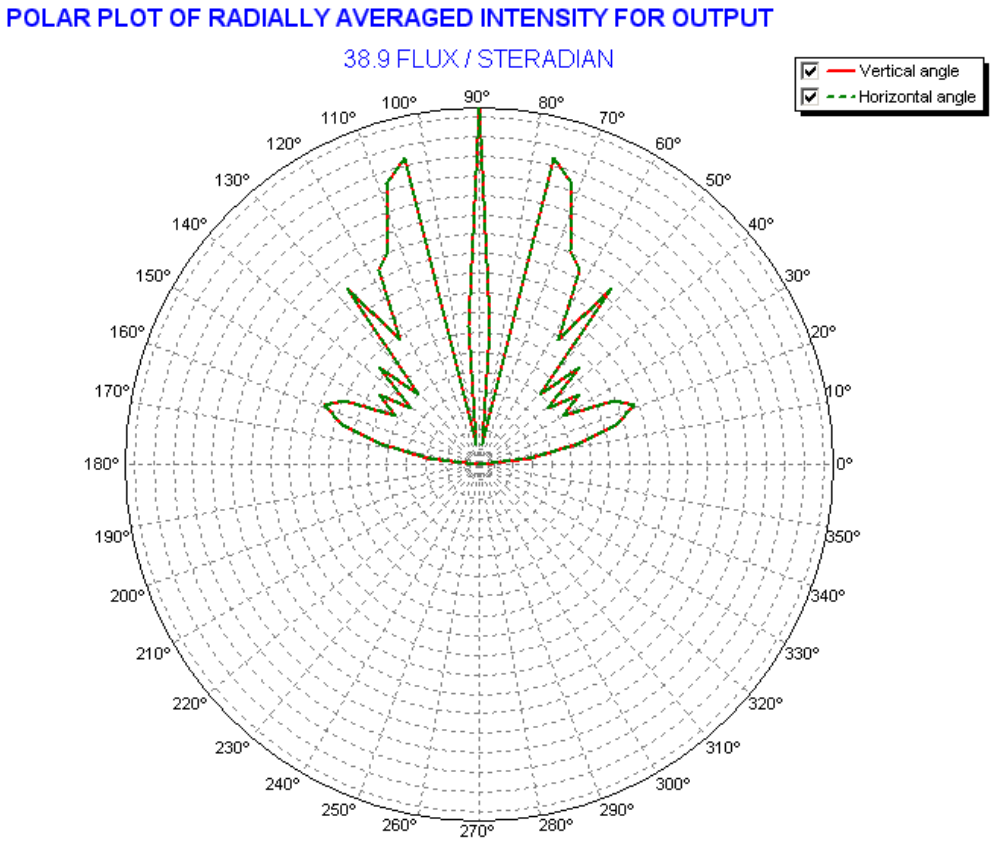

Figure 5-10 Polar diagram of the cross sections of the output intensity from regular grids

5.4.1.2 LED Model Using a Point Source with a Lambertian Diffuser

In order to achieve a Lambertian output profile, a scattering plane that defines the Lambertian angular distribution of radiation is placed immediately in front of the point source.. The ray tracing automatically scales the power of the scattered rays, based on the Lambertian function assigned to the scattering surface and produces quantitative results, based on a large sample of scattered rays. The author set 1:100 scattering ratio for the diffuser, which meant that every input ray that incident on the diffuser would split into 100 new rays. The new scattered rays has the same input intensity but follows a Lambertian distribution. Figure 5-11 presents the angular intensity distribution from the diffuser. Though, there are only 101 × 101 rays generated from the grid, because the diffuser had 100 times split rate, eventually more than one million rays were created as input.

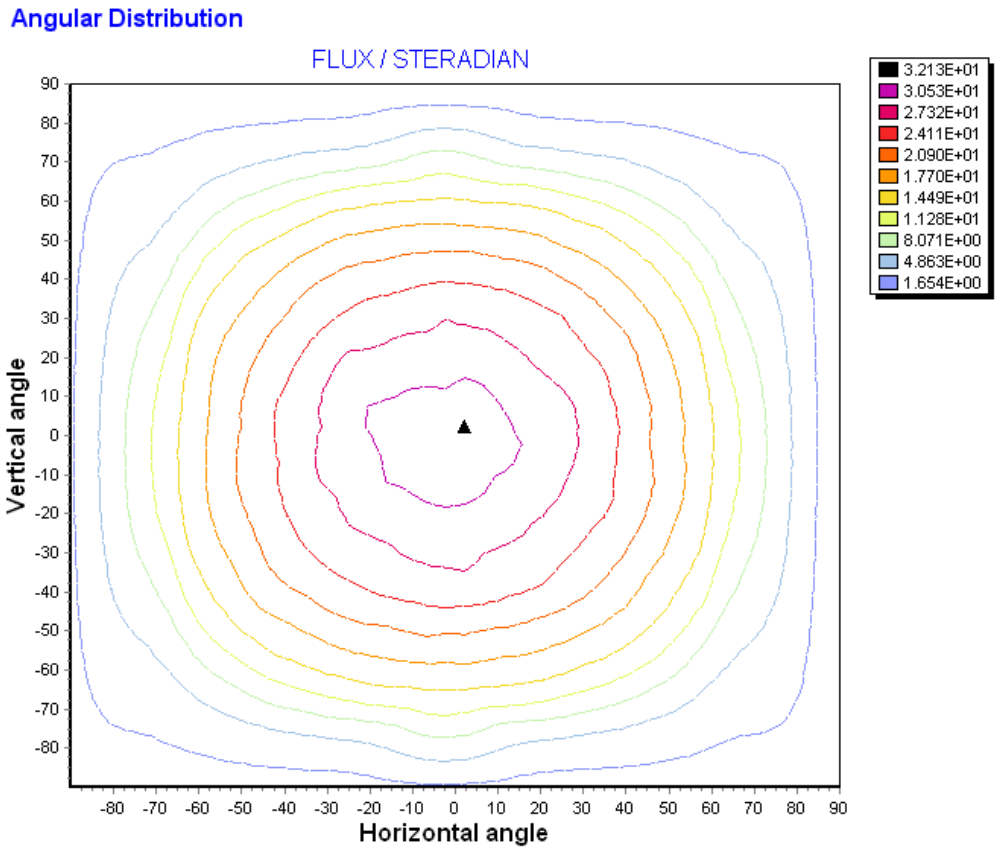

Figure 5-11 Contour map of angular distribution from a Lambertian diffuser

According to this contour plot, the angular intensity appeared homogenous at all solid angles. It was because the diffuser destroyed the regularity of the grid structure.

The diffuser source can be recognised as a 2 dimensional point source matrix formed by 10,201 (101 × 101) point sources on the 2D plane and each point emitting 100 rays in a Lambertian distribution.

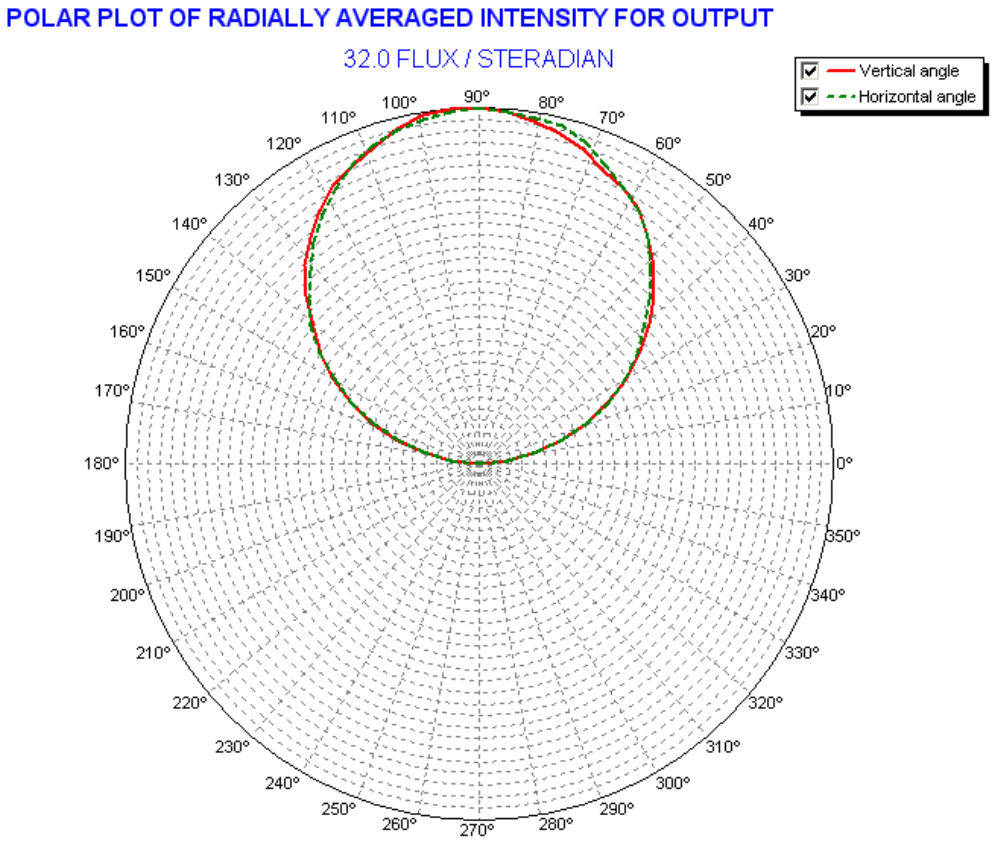

Figure 5-12 Polar diagram of the cross sections of the output intensity from Lambertian diffuser

The polar diagram Figure 5-12 clearly indicated that the output angular intensity distribution from the diffuser matched a Lambertian intensity distribution much better than the grid source case.

5.4.1.3 Discussion of LED Models Based on Point Sources

The grid sources are useful for simulating imaging systems, e.g. finding focus point of an objective lens, but are less accurate for solving illumination problems. The arrangement of the regular grid limited the application of such a source as illumination. A scattering diffuser can be used to eliminate the effect of the grid. However, it increases the ray tracing complexity because ASAP stores all the information of the relationship between the incident ray and its split sub-rays. That information does not contribute to the simulation at this level but consumes more CPU computing power and requires more memory space.

5.4.1.4 LED Model Using a Surface Emitter

The third method to model the LED chip was using an emitting surface. Similar to the above diffuser model, a surface emitting source can be used as a set of closely spaced point sources that extend over a defined area.

A 240 μm × 240 μm plane was created as the LED emitting surface which produces a random set of rays distributed over the plane (see Figure 5-13). The author created a spatially random set of rays with an equal probability of pointing in any direction within the hemisphere. The overall intensity was then weighted according to Lambert's cosine law.

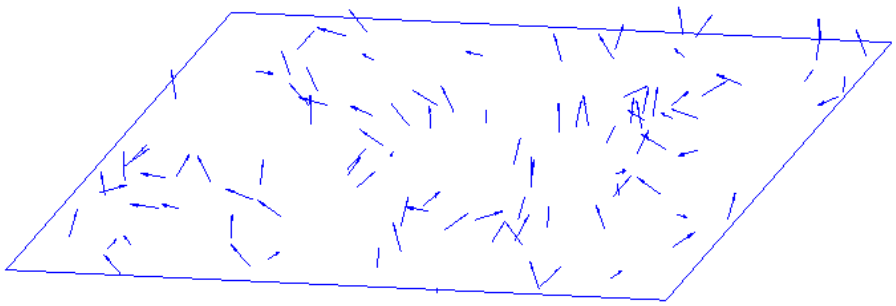

Figure 5-13 A set of random rays was created on a rectangular plane

Figure 5-14 shows the intensity position contour plot generated by a 240 μm × 240 μm emitting surface containing 25 rays. A small number of input rays was used so that light only came out from part of the surface, which resulted in irregular discrete energy patterns. The same situation existed in the angular contour map Figure 5-15, where only a few incident angles (25 arbitrary angles) were detected rather than a wide range covering the whole hemisphere.

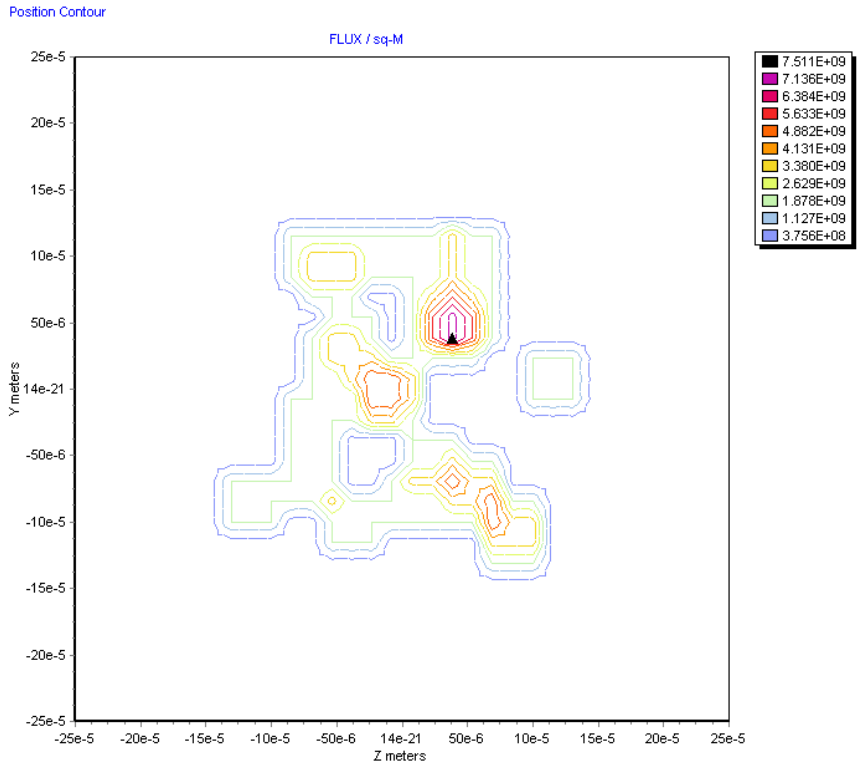

Figure 5-14 Spatial intensity distribution of an emitting surface containing 25 rays

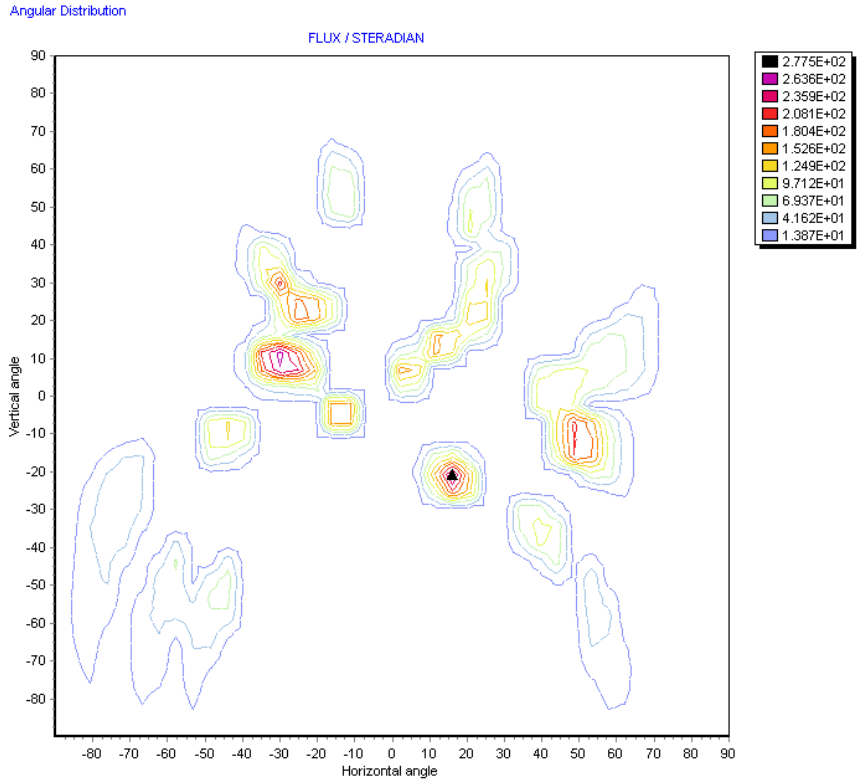

Figure 5-15 Intensity distribution as a function of angle

The angular intensity was so isolated in this example that there only two angle groups could be recognised from the following polar diagram (Figure 5-16).

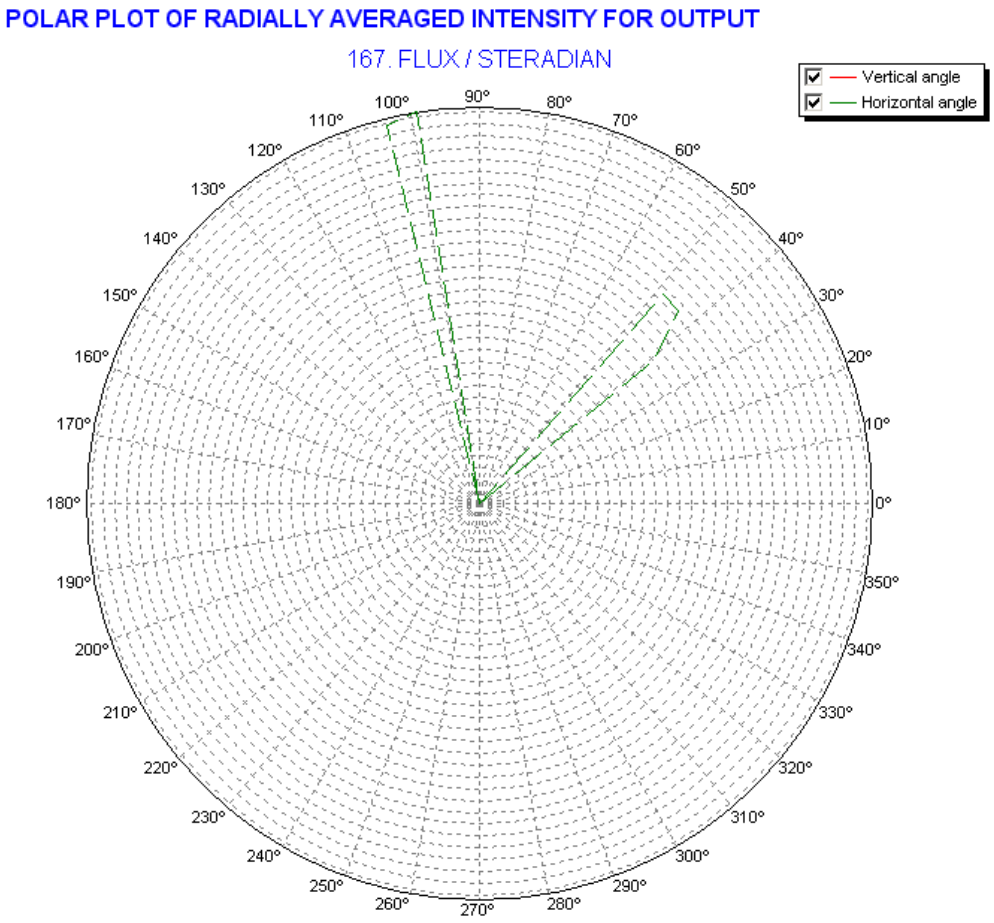

Figure 5-16 Polar diagram of the cross sections of the output intensity from emitting surface containing 25 rays

When the number of output rays was increased to 1 million, the asymmetric patterns disappeared from the space intensity contour map (as shown in Figure 5-17). The output intensity was uniformly distributed at the centre of the surface and symmetrically decreased towards the edge of the emitting surface. The output angles smoothly covered the whole hemisphere as indicated in the angular distribution contour plot in Figure 5-18 and in the angular polar diagram of the cross sections of the output intensity in Figure 5-19.

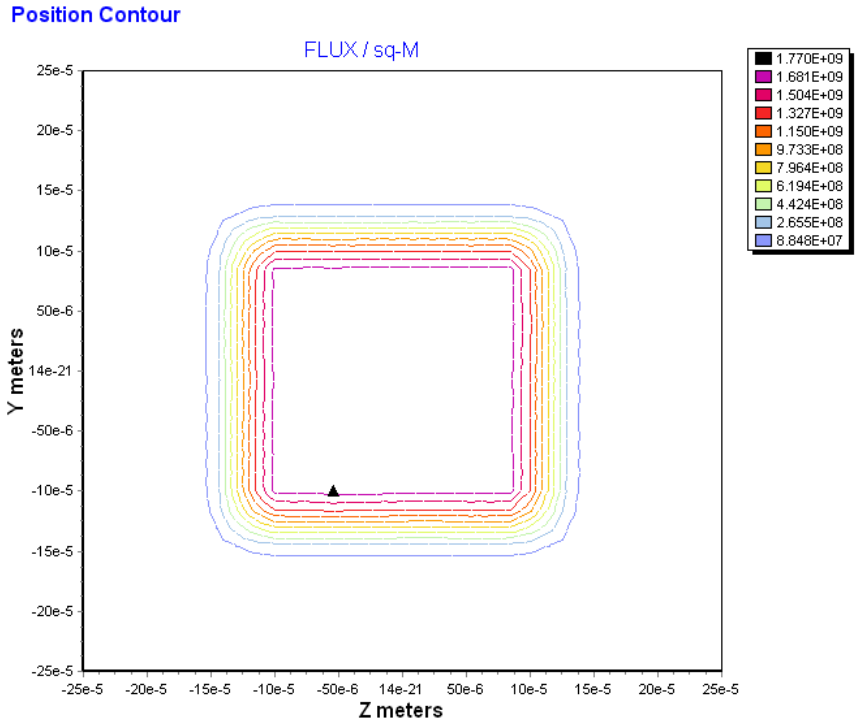

Figure 5-17 Intensity space distribution of an emitting surface containing 1 million rays

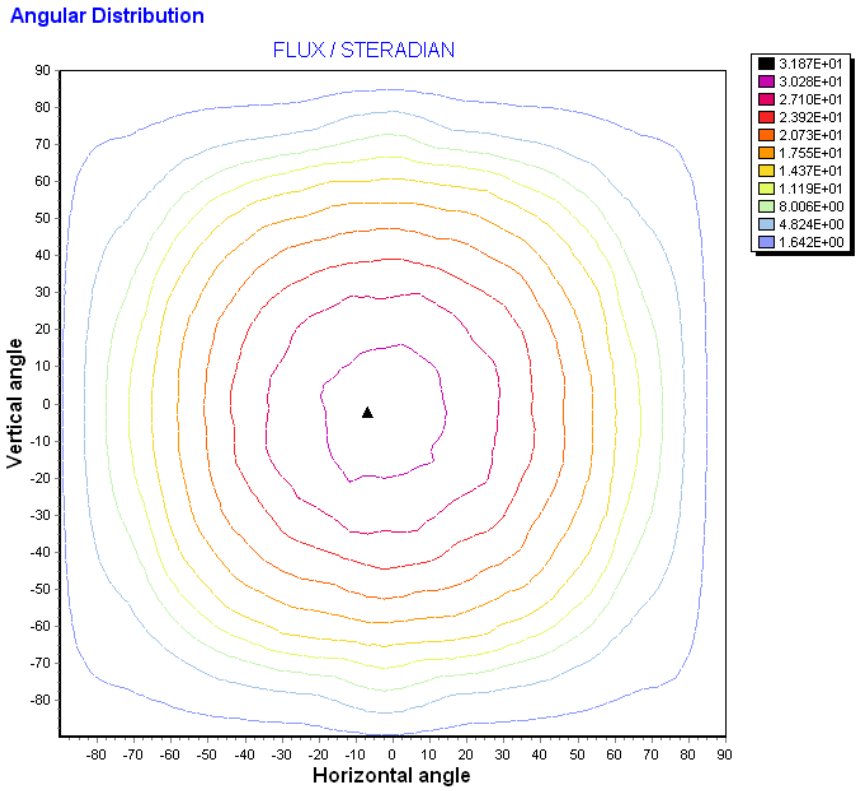

Figure 5-18 Intensity angular distribution of an emitting surface containing 1 million rays

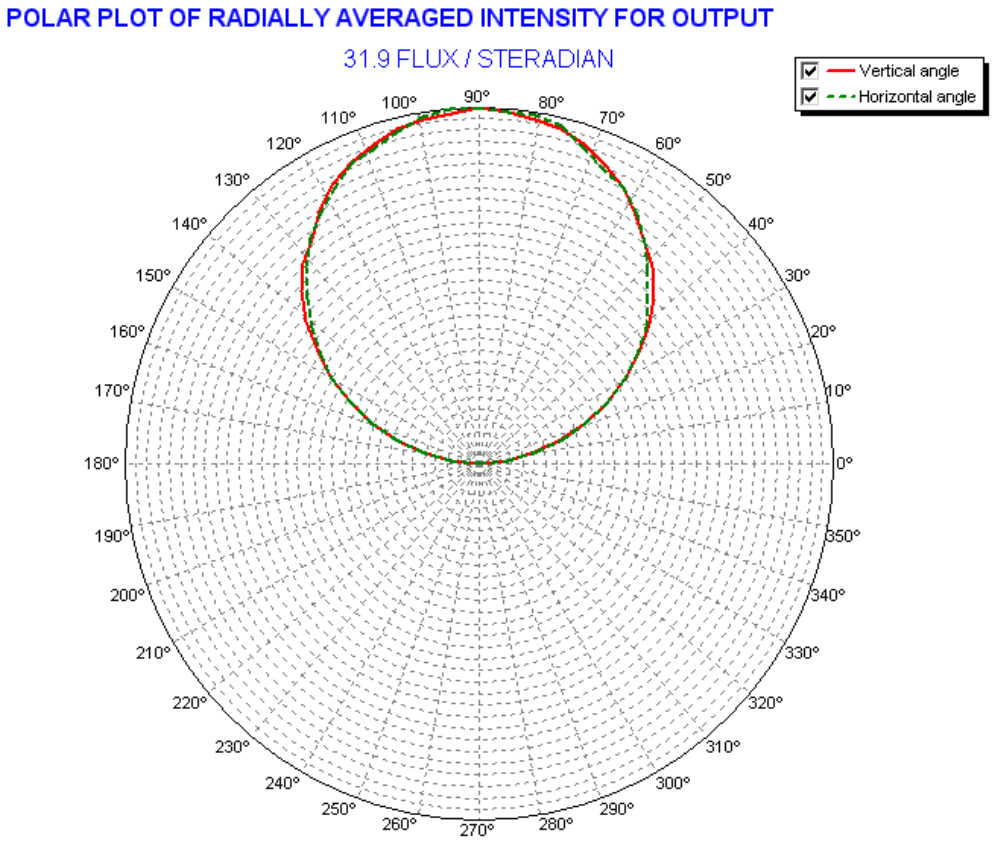

Figure 5-19 Polar diagram of the cross sections of the output intensity from emitting surface containing 1 million rays

5.4.1.5 LED with an Electrode Disc Modelled Using a Surface Emitter

The geometry design of the surface emitter model was improved to be close to that of the real chip LED by including the metal electrode in the centre of the junction. The model of the junction surface was based on the Lambertian emitting surface generating 1 million rays mentioned above. The anode was modelled by using a total absorptive circular disc placed 0.1 μm above the emitting surface and aligned with the centre.

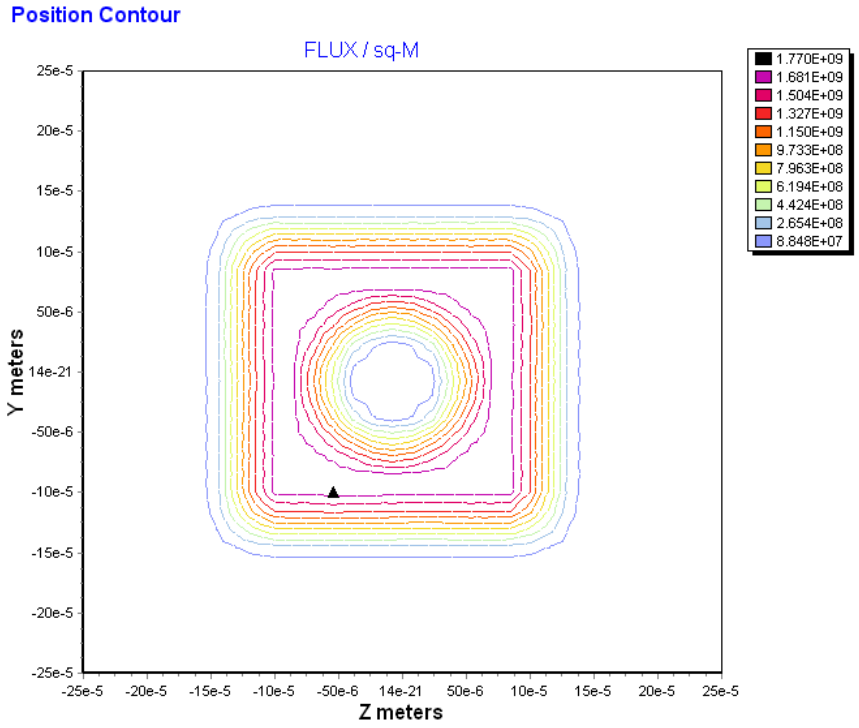

Figure 5-20 Intensity space distribution of an emitting surface with an anode containing 1 million rays

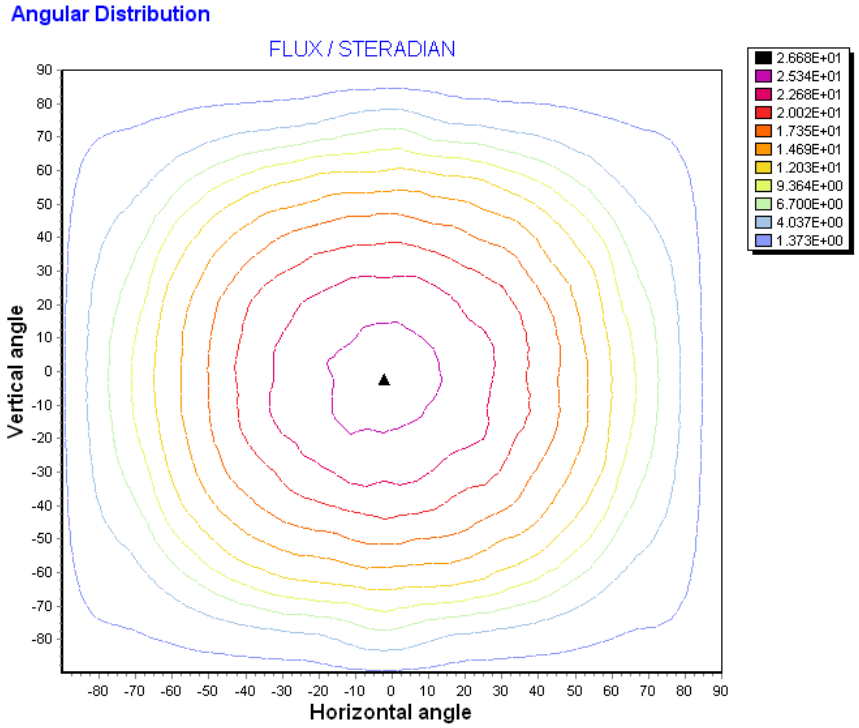

Figure 5-21 Intensity angular distribution of an emitting surface with an anode containing 1 million rays

A large (1 m × 1 m) detector was placed 1 μm away from the anode. It was close and big enough to detect all of the light that came from the emitter and to reflect the effects caused by the absorption pad. The intensity spatial distribution diagram (Figure 5-20) indicated that the power in the central area reduced to zero and the shape of the intensity pattern matched the shape of the "anode" pad, while the outer boundary of the energy pattern outlined the shape of the emitting surface. The diagram represented that the light came out over the emitting surface except where the anode pad was placed because there should not be any rays passing through the electrode. Overall, the angular intensity distribution still followed Lambert's cosine law: the angular intensity contour (Figure 5-21) proved that.

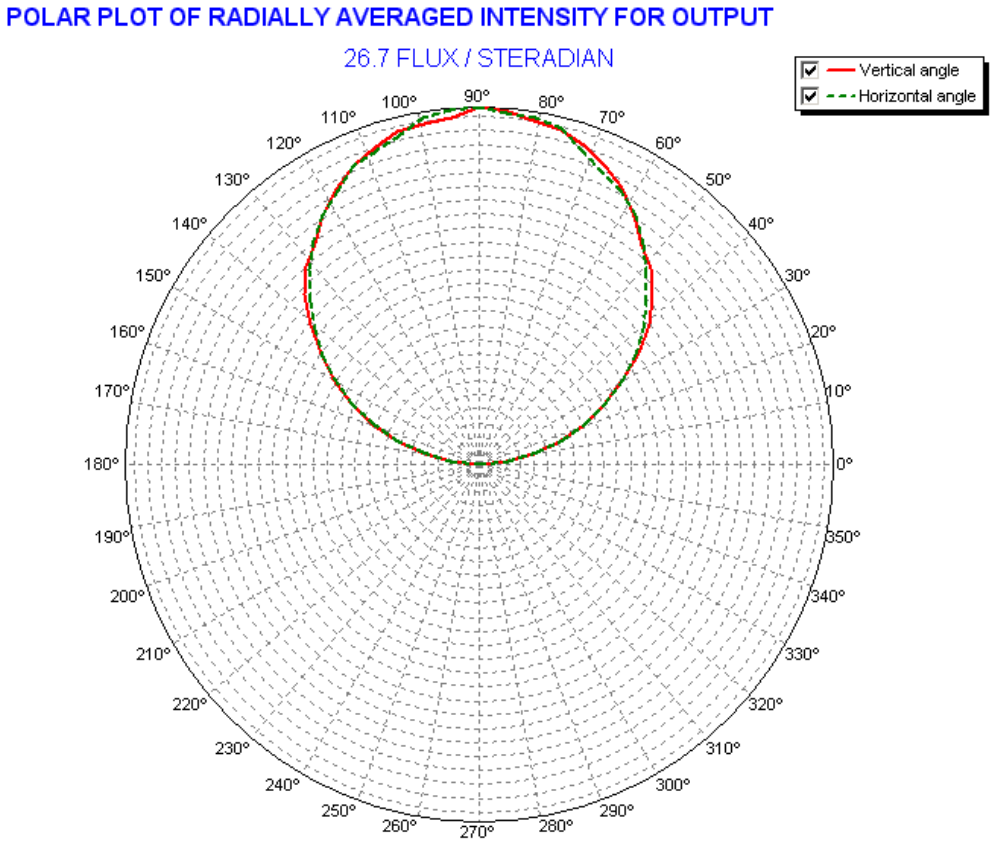

Figure 5-22 Polar diagram of the cross sections of the output intensity from emitting surface with an Anode containing 1 million rays

The polar diagram (Figure 5-22) shows that the output angular intensity distribution of the LED model with an absorption pad still follows a Lambertian distribution closely. The only major difference compared to the case without the anode was that the intensity reduced from 31.9 flux/steradian to 26.7 flux/steradian. The anode disk

reduced overall output intensity and changed the spatial near field distribution but had no impact on the angular intensity distribution.

5.4.1.6 Model of LED Array as Edge Illumination for Backlight

The surface emitter with an electrode disc aligned at the centre was chosen as a suitable light source model for a chip LED. Multiple LED source models were aligned linearly to form a single line array as edge illumination [5-26]. for the backlight system. The CREE white LED covers a wide wavelength range in the visible spectrum, it, however, has peak wavelengths at 470 nm (blue) and 525 nm (green) (a red wavelength can be generated by using phosphor plates [5-29]). A white LED model was created containing three monochromatic wavelengths, 470 nm, 525 nm and 660 nm. 1511 white LED models were used and aligned in one row as an edge illumination for a 50 mm width light guide. Figure 5-23 shows a part of (9 LEDs) a 3D model of the LEDs array. Three colours of arrows represents that each LED could emit three wavelengths of light.

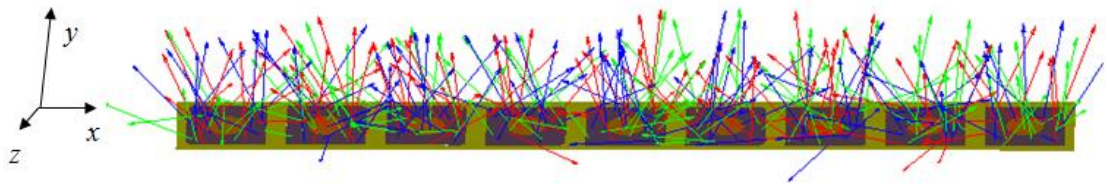

Figure 5-23 a tilted view of a 3D model of a 9-LED array each containing three wavelengths. Surface emitter with an electrode disc was used to model the LED and 1511 LED models were aligned in one row.

5.4.2 Ray Trace Model of Novel Light Guide

A light guide with dimensions of 33.00 mm × 50.00 mm × 0.99 mm (*L*×*W*×*H)* which matched the one used in the prototype was modelled in ASAP. The chosen length and width of the light guide were sufficiently large to understand the light propagation behaviour inside the guide as the optical micro-elements (one group of a grating, a microlens and three sub-pixels) repeated themselves 100 times along the guide (see Figure 5-24 for part of the light guide). The dimensions also allowed the ray tracing simulation to be performed in a reasonable length of time [5-1], which was around 40 minutes for tracing 1 million rays (the calculation time was based on a computer with Intel i5 2.5 GHz CPU and 8 GB RAM). The pitch of the microlenses was 331 μm and the thickness of the light guide was 0.99 mm. Both of the parameters matched the

specifications of the light guide used in the experiment that was conducted by David R. Selviah.

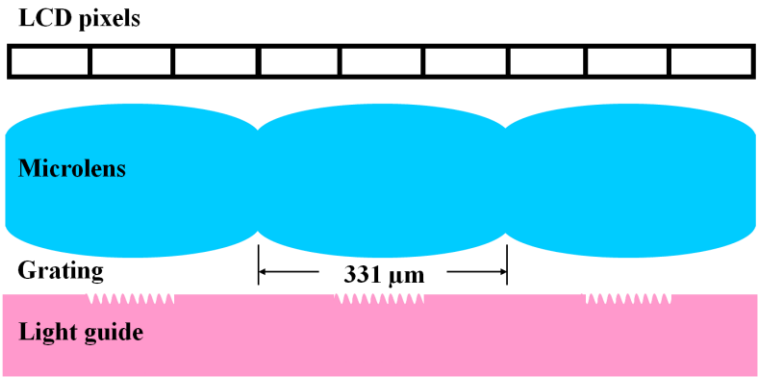

Figure 5-24 Part of the light guide shows 3 integrated gratings on top the surface of the light guide and 3 collimation micro lenses

The light guide was fabricated using a clear glass plate [5-30–32]. The refractive index of the glass was 1.50, giving a critical angle $\theta_c = 41.8°$ according to the following equations,

$$\sin\theta_c = \frac{n_i}{n_f} = \frac{1}{1.50} = 0.67 \qquad \textbf{Eq. 5-3}$$

$$\text{NA} = (n_f^2 - n_i^2)^{1/2} \qquad \textbf{Eq. 5-4}$$

where n_f is the refractive index of the light guide and n_i is the refractive index of air (see Figure 5-25).

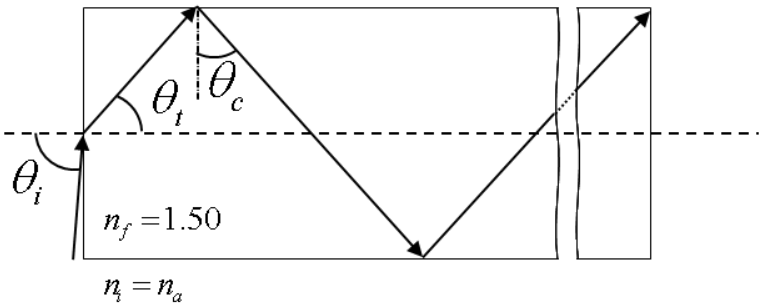

Figure 5-25 Calculation of the critical angle using Snell's Law

The numerical aperture (NA) cannot exceed 1, which means that the maximum incident angle $\theta_i = 90°$, and the light guide can totally internally reflect all light entering its entrance.

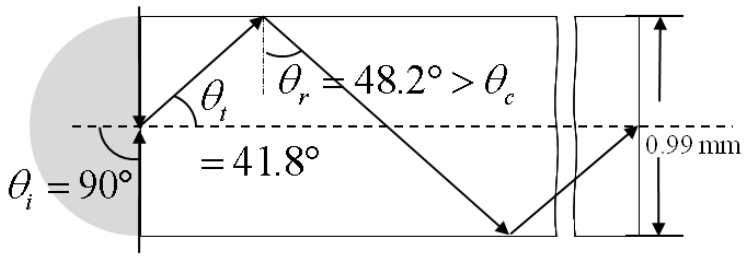

Figure 5-26 Rays in the TIR light guide

Based on $n_i \cdot \sin\theta_i = n_t \cdot \sin\theta_t$, where $\sin\theta_i = \sin 90° = 1$, here the author defined the axis normal to the light guide entrance to be 0 °. The author obtained the refraction angle $\theta_t = 41.8°$, therefore, in the lightguide the angular distribution of rays was bound within ±41.8 °. By tracing the refracted ray from the entrance face of the light guide to the guide side wall, the internal angle of the reflected ray at the side wall is $\theta_r = 90° - \theta_t = 48.2° > \theta_c$. Figure 5-26 demonstrated how the light propagated through the total internal reflection (TIR) light guide. This proved that all rays arising from the LED source (recall the chip LED radiation pattern in Figure 5-6) incident on the input face of the light guide were guided. The dimensions of the light guide are shown in Figure 5-27. A line array of 1511 white LED units were simulated and were located on one edge of the light guide and fully filled the 50 mm width.

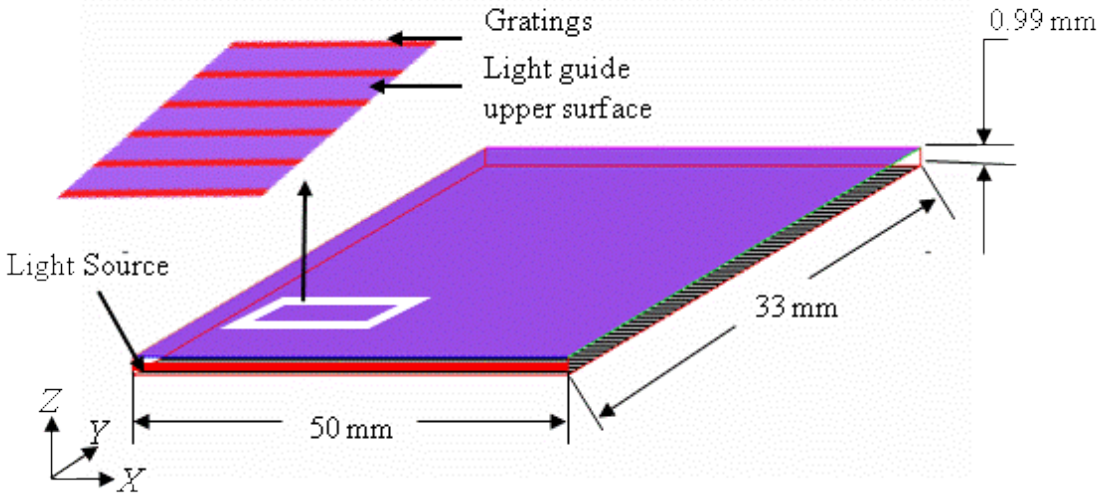

Figure 5-27 Structure of light guide

5.4.3 Model of Gratings

The most advanced feature of the light guide, as mentioned in section 5.2, was to separate three primary colours of light when they emerge from the light guide, so that

the highly lossy colour filters could be eliminated from LCDs. Diffraction gratings were the key elements to implement such a novel function of the light guide. The structure of the grating has to be designed accurately so that the three wavelengths of the incoming light are diffracted to the central diffraction orders, -1^{st}, 0^{th} and $+1^{st}$, of the grating. In this section, a ray tracing approach to model the near-field and far-field intensity distribution of the grating is reported. The advantage of this model is to provide an integrated solution which analyzes the light source, light guide and gratings as a single system, and, therefore, improves the overall performance of the colour separation light guide.

A periodic array of discrete diffraction grating apertures with 70 μm width was holographically fabricated previously by David R. Selviah on the upper surface (light emerging surface) of the light guide [5-33], [34]. The grating was in the form of parallel sine wave notches so that when light emerges at the grating it would be diffracted into different orders.

.

A ray trace technique based on the scalar diffraction theory [5-32] was used to calculate the directions of propagation of the various reflected and transmitted principal orders of a beam after interacting with the diffractive grating. The direction of the diffraction orders were modelled by calculating the direction cosines of the exiting beams [5-35]. The author included the centre 3 diffractive orders, -1^{st}, 0^{th} and $+1^{st}$ in the simulation. Even though more orders are physically present, the author assumed that most of the diffracted energy remained in these three orders. A ray trace model of a transmission grating is shown in Figure 5-28 below. We applied 3 different wavelengths, 470 nm, 525 nm and 660 nm, to represent the three colours of LEDs, blue, green and red respectively and to simulate a combined white light source. The incident multi chromatic light is diffracted into 3 orders, the 0^{th} order (normal to the grating surface) is in the middle and was a combination of three wavelengths (the blue and green were overlaid by red in the 2D diagram in Figure 5-28. The 1^{st} and -1^{st} order beams are at either side of the 0^{th} order. Due to the different behaviour of the three wavelengths according to the grating equation, the grating angularly separates the red, green and blue beams in both of the $\pm 1^{st}$ orders. Therefore, the $\pm 1^{st}$ order diffracted rays can be used to achieve colour separation in the light guide.

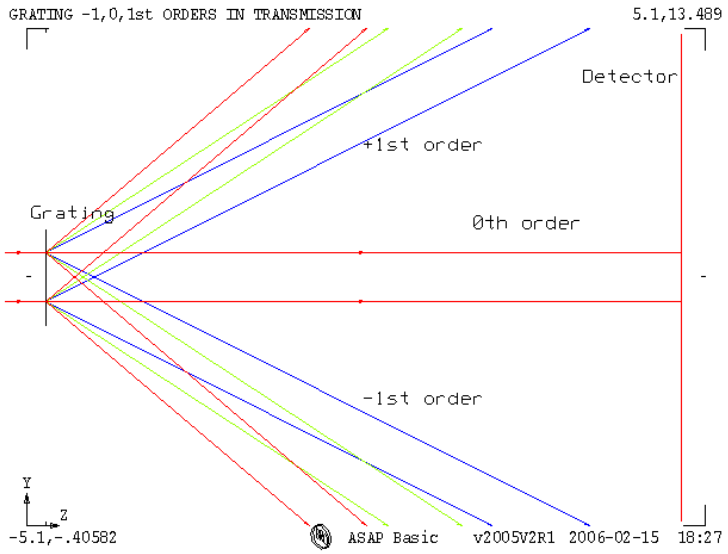

Figure 5-28 Diffraction orders from a Transmission Grating

The computer model of the structure of the light guide with the diffractive grating array is shown in Figure 5-29. The width of the grating aperture was set at 70 μm: the same as the one used in the prototype. We used different colours in the figure to distinguish the grating elements from its substrate, while the grating actually has the same refractive index as the light guide.

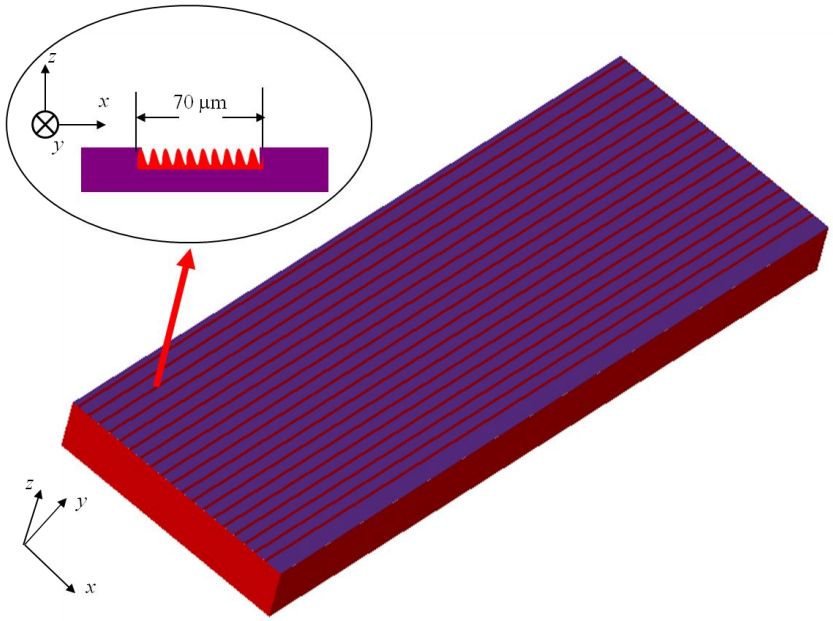

Figure 5-29 Light guide with a periodic discrete grating array on its upper surface

The novelty of the backlight, as mentioned earlier, is to separate the red, green and blue beams when they exit from the gratings. An additional microlens layer is employed to collimate the output beams, so that they are parallel to each other when

they arrive at their corresponding sub-pixels and normal to the display to maximize contrast (see Figure 5-30). Ideally the three colours of beams need to be spatially separated without overlap areas when they reach the microlens.

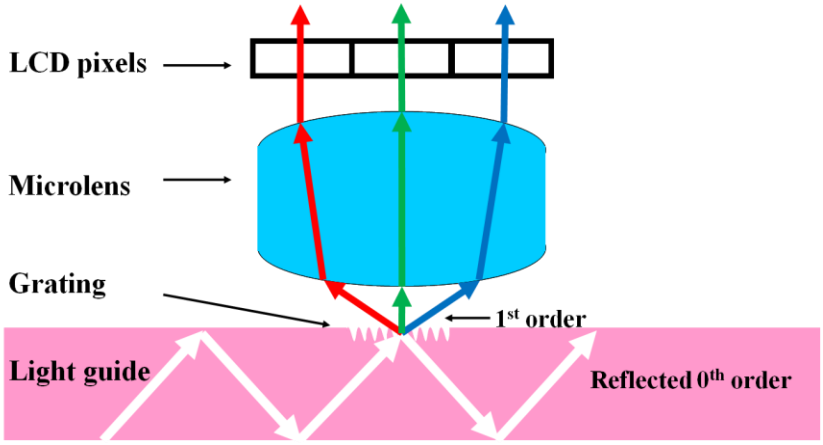

Figure 5-30 Backlight illumination system with cylindrical micro-lens array (1 pixel)

We assumed the grating to be a sine wave and designed the grating to extract the 1st order of the green beam close to the vertical axis or normal to the grating surface from the light guide, and to extract the 1st orders of the other two wavelengths on either side of it (the author defined 0 degrees as the horizontal level and counted anti clockwise for other angles, see Figure 5-31), i.e. red light emerges between 90° and 180° degrees, and blue light emerges between 0° and 90° degrees. The 0th order diffracted beam reflects most of the light back into the light guide and continuously propagates along the guide until it encounters the next grating.

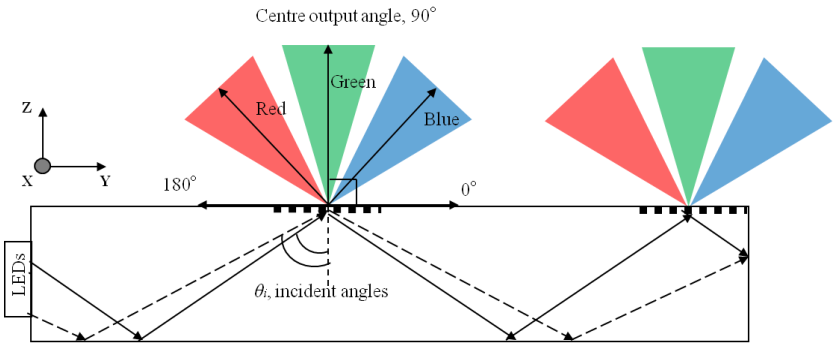

Figure 5-31 Green light comes out normal to the display

We varied the pitch of the gratings in 5 nm increments, and ray traced the propagation direction of each output ray of each wavelength at the grating surface. The pitch of the grating was chosen when the output angles of green light exited close to 90° as the

author desired (here the author refer to the same coordinate system shown in Figure 5-31). Figure 5-32 shows the average value of the output angles of the three wavelengths as a function of the grating pitch. We are interested in the range of grating pitches which diffracted the 1st order green beam vertically, so that the author only showed the grating pitch from 300 nm to 400 nm in the figure. We obtained the mean of output angle of green light from 82° to 108° within the designed range of the grating pitches. The figure showed that the angle of green light increases as the grating pitch becomes finer. The critical grating pitch was 363.1 nm where the mean of the 1st order diffraction angles of the green beam was 90°, while the mean of the 1st order of the red and the blue beam diffracted at 107° and 81° respectively.

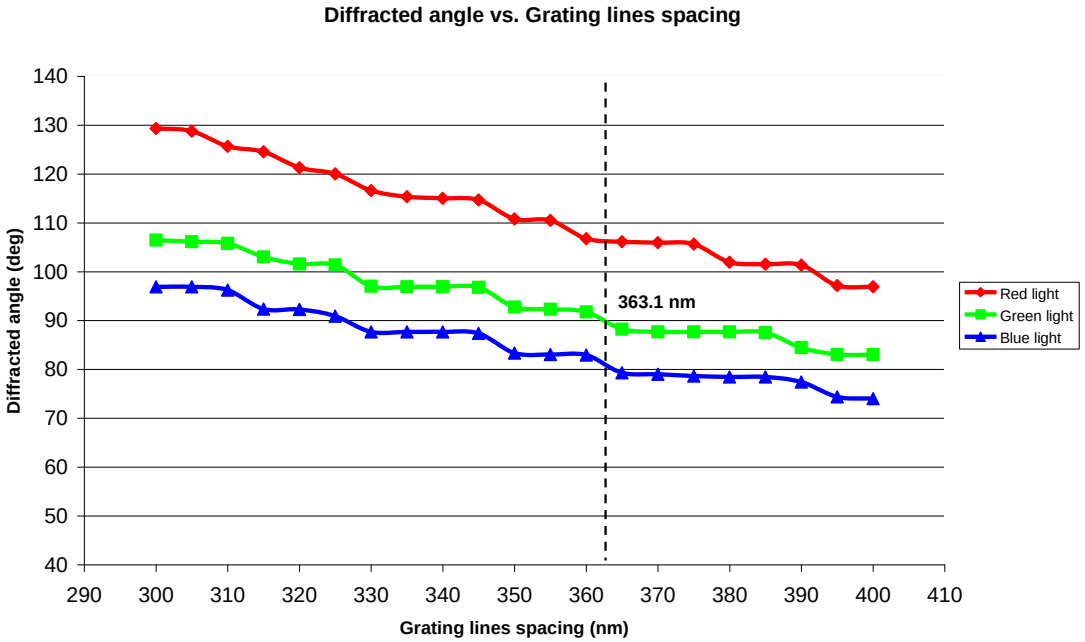

Figure 5-32 the mean of diffractive angles of each wavelength vs grating pitch

We recorded the simulated results of the angular divergence of the three wavelengths at the exit of each grating surface when the pitch of the grating was set at 363.1 nm (see Table 5-2).

Table 5-2 the output diffractive angular range for three wavelengths

Colour	The angular range in degrees
Red	108.4 ° ± 0.5 °to 103.9 ° ± 0.5 °
Green	94.6 ° ± 0.5 °to 86.3 ° ± 0.5 °
Blue	85.3 ° ± 0.5 °to 79.6 ° ± 0.5 °

There was no overlap between any colours according to this table, which meant the three colours were efficiently separated by the grating array (Figure 5-33).

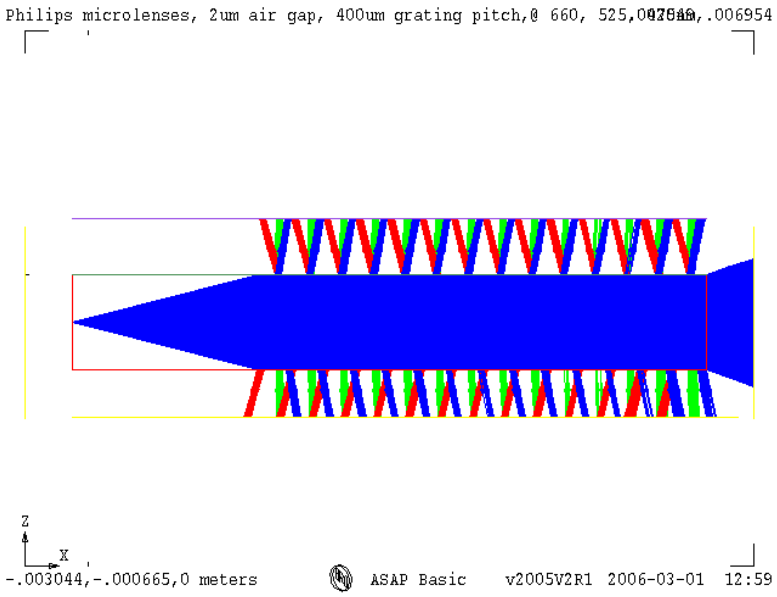

Figure 5-34 Model of a colour separating light guide

We observed that some light escaped from the bottom of the light guide, due to the 1st order reflection at the grating. The reflected beam is the major cause of light loss in the light guide. The last part of this chapter proposes a novel solution to overcome this problem.

5.4.4 Model of Internal Mirrors

Around 60% of the 1st order beams are reflected at the grating surface and travel downwards at a steep angle into the guide and then directly out of the lower surface of the guide as they are larger than the critical angle (41.8 °, according to Figure 5-26 and Table 5-2) of the guide. Figure 5-35 shows the behaviour of the rays encountering the gratings.

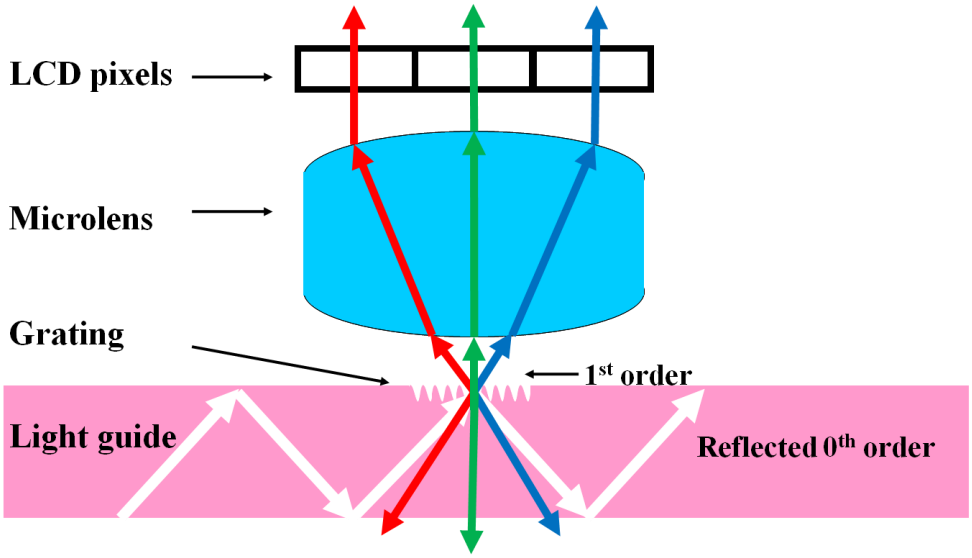

Figure 5-35 Backlight Illumination System with Reflected Diffraction Orders

This loss can be avoided by a novel design of an array of micro-mirrors which are embedded within the light guide, parallel to and beneath each grating to reflect these beams back through the grating apertures with the 1st order transmitted beams. To the best of our knowledge (at the time of submission of the thesis), these internally embedded micro-mirrors have never been used before except on the lower surface of a light guide to improve uniformity [5-36] of such a backlight. The micro-mirrors are shown schematically in Figure 5-36.

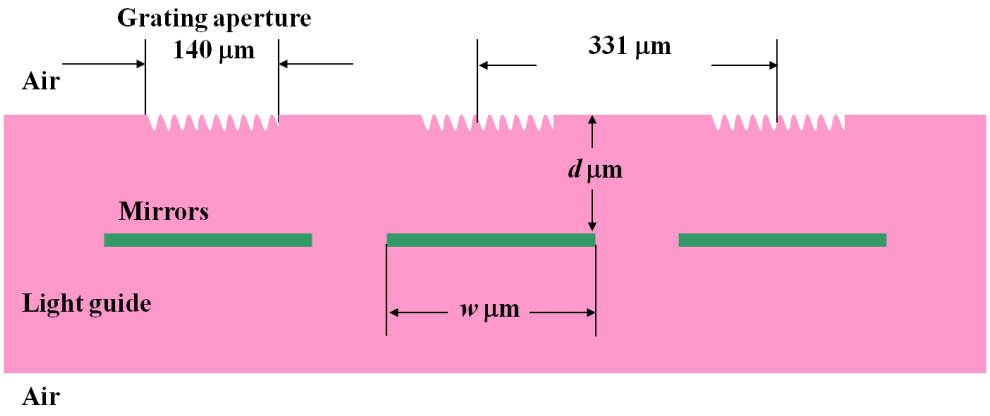

Figure 5-36 Position and width of micro-mirror array

The micro-mirrors are designed to be an array of thin, non-transparent and highly reflective metallic elements. Their positions inside the light guide and the width of each individual mirror have direct effects on the output efficiency of the light guide.

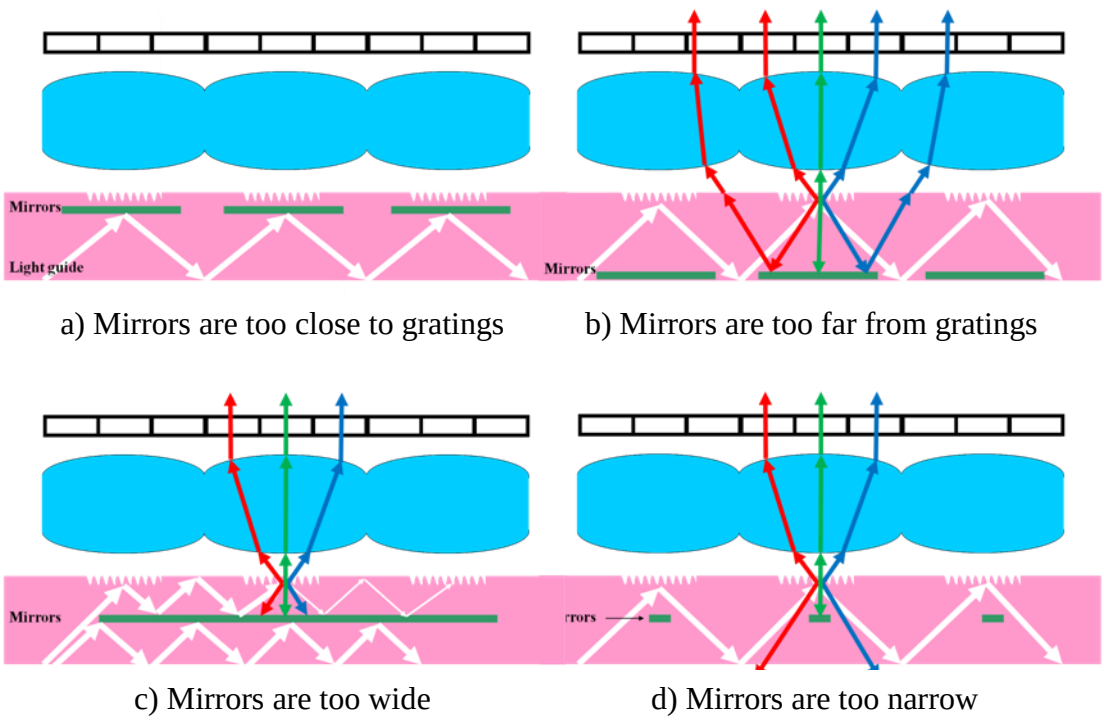

a) Mirrors are too close to gratings b) Mirrors are too far from gratings

c) Mirrors are too wide d) Mirrors are too narrow

Figure 5-37 the depth and width of the mirror layer effects the output efficiency and accuracy of the backlight illumination

Figure 5-37 illustrates how the positions of the micro-mirror layer inside the light guide and the width of each individual mirror affects the output of the light guide. In Figure 5-37a) if the mirror layer is too close to the grating apertures it will block most, or even all, of the rays inside the light guide reaching the grating and will eventually cause no output from the light guide. In Figure 5-37b) if the mirror is too far from the grating, some light exited the light guide at the top surface but outside the desired grating region. This makes the proper design of the multiple micro-lens subsystem difficult as the top surface effective source becomes extended. These beams will enter the adjacent lenses and will be directed into incorrect pixels of the display, so that the concept of the filter-less colour separation light guide is destroyed. In Figure 5-37c) if the mirror is too wide it will block part of the rays from the light source reaching the grating and so reduce the rays reaching the LCD and decrease the brightness and efficiency of the backlight unit. However, in Figure 5-37d) if the width is set too small, the mirror will not effectively reflect the first order reflected light. Some of the reflected light passes through the gaps between the micro-mirrors and exits the lower surface of the guide because its incident angle is much sharper than the critical angle of the light guide.

The author used a ray trace model to investigate the effects of the position (*d*) and width (*w*) of the micro-mirrors individually and to optimise each of them in order to improve the overall output efficiency of the light guide.

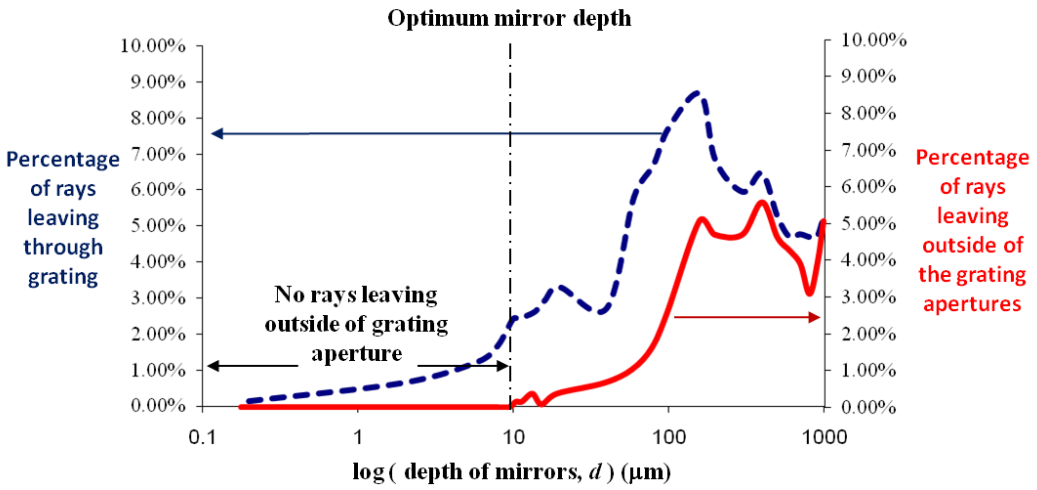

Figure 5-38 Percentage of rays leaving through the grating apertures (blue dashed line) and leaving outside of the grating apertures (red solid line) as a function of micro-mirror depth

In order to find the optimum position of the micro-mirrors, the author fixed the width of the mirrors and varied the depth and assumed the width of the mirror to be 70 μm: the same as the grating aperture to start with. Figure 5-38 shows the percentages of rays leaving through the grating apertures and leaving outside of the grating apertures as a function of micro-mirror depth (*d*) on a logarithmic scale. As the author moved the mirrors from the upper surface to the lower surface of the light guide, the number of rays leaving the guide at the grating increased because more light enters the channel between the mirror layer and the grating (the blue dashed line in Figure 5-38). When the micro-mirrors were placed deeper than 10 μm, some light exited the light guide at the top surface but outside the grating apertures. We need to have a depth where the number of rays leaving through the grating aperture is maximised and the number of rays leaving outside of the grating aperture is minimised. So the best position was found, according to the percentage of rays leaving outside of the grating apertures as a function of micro-mirror depth (red solid line) in Figure 5-38, to be 10 μm. This conveniently small simulation figure and the design parallel to the top surface of the light guide mean it can be fabricated using realistic fabrication procedures, e.g. photolithographic techniques, for this newly invented embedded micro-mirror array layer.

The author then fixed the mirror depth at the optimum of 10 μm below the upper surface of the light guide and varied the width from the minimum of 0.1 μm to the maximum of 331 μm which is the pitch of the microlens mentioned previously in the model of light guide section.

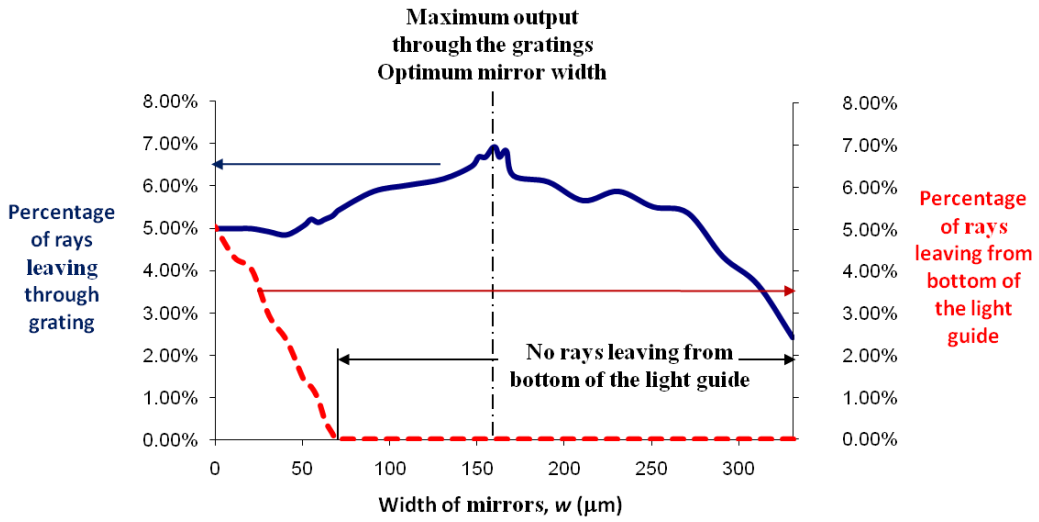

Figure 5-39 Percentage of rays leaving through the grating apertures and leaving from bottom side of the light guide as a function of micro-mirror width

Figure 5-39 reveals the ray trace result of the percentages of rays leaving through the grating apertures and leaving from the bottom of the light guide as a function of micro-mirror width (w). While the author increased the mirror width in increments of 5 μm, the number of rays leaving from the bottom of the light guide decreased as the mirror started to reflect the 1st order reflected beams back to the grating (the red solid line in Figure 5-39). If one choose a sufficiently wide mirror, 69 μm, there will be no light travelling through the bottom of the light guide. The percentage of rays leaving through the grating apertures increased with the mirror width before reaching its peak when the width of the mirror was set to 160 μm (the blue dash line in Figure 5-39). The number of rays leaving through the gratings gradually declined when the width of the mirror was wider than 160 μm, as the mirrors started to prevent light passing through the gaps between them and reaching the grating. We found that the optimum mirror width is $w = 160 \pm 2$ μm.

In fact, the micro-mirror depth and width are coupled in their effects and so cannot be considered separately. So the author calculated the effects from both of the depth and width of the micro-mirrors by varying the depth from 0 to 90 μm and width from 0 to

210 μm and plotted the output energy in a 2D contour map (Figure 5-40) showing their relationship. Figure 5-38 and Figure 5-39 provided to us a very good indication of the region where the optimum of the depth and width should occur. We varied the depth (d) from 0 μm to 90 μm away from the grating and the width (w) from 90 μm to 210 μm. The maximum output occurs at the marked point in the figure at $d = 10 \pm 2$ μm, $w = 160 \pm 2$ μm. The light exiting from the light guide with the embedded micro-mirror layer increased by 38.2% compared to the case without the internal mirror array.

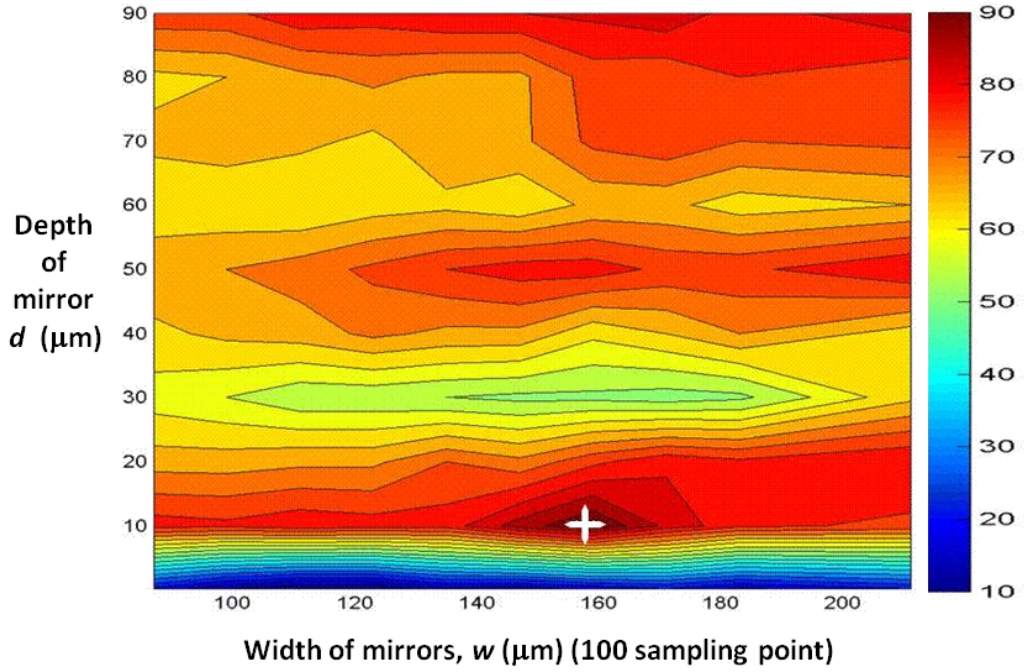

Figure 5-40 Contour plot of the number of output rays as a function of both depth and width of micro-mirrors

5.5 Conclusion

A novel colour-separating light guide for liquid crystal displays (LCDs) was modelled using non-sequential ray-tracing techniques. Several types of light sources were modelled using the ray trace method. A surface emitter was identified as a suitable model to represent a chip LED. 1511 LED models were aligned in a one dimensional array which was used as the edge illumination for the backlight. A uniform thickness light guide was designed instead of the wedge-shape one so that it could easily integrate multiple light sources at either or both sides of the light guide. Periodic, limited length, discrete gratings were used for the 1st time on the surface of the backlight unit. The novel design has clear advantages over a conventional continuous

grating. It allowed us to control the strength of each grating aperture individually by varying the modulation depth of the grating, thereby, obtaining better uniformity. An array of double convex cylindrical lenses was designed which gave more design variables to enable optimization of collimation normal to the display at the centre of each pixel of red, green and blue respectively. The author invented the horizontal micro-mirror array inside the light guide and with the help from David R. Selviah a ray trace model was used to optimise the design and to improve the overall luminous efficiency of the backlight. The depth (d) and width (w) of the mirror layer were optimised at $d = 10 \pm 2$ μm beneath the grating and $w = 160 \pm 2$ μm for each mirror respectively. The light exiting from the light guide, when the mirror was employed and optimised, increased by 38.2% compared to the case without the embedded mirror array.

Chapter 5 References

[5-1] D. R. Selviah and K. Wang, "P-64: Modeling of a Color-Separating Backlight with Internal Mirrors," *SID Symp. Dig. Tech. Pap.*, 2004.

[5-2] W. den Boer, "Active matrix liquid crystal displays," Elsevier, 2005, p. 239.

[5-3] D. J. R. Cristaldi, S. Pennisi, and F. Pulvirenti, "Liquid Crystal Display Drivers: Techniques and Circuits," Springer, 2009, p. 295.

[5-4] D. Perard and J. Beyerer, "Three-dimensional measurement of specular free-form surfaces with a structured-lighting reflection technique," *Three-Dimensional Imaging Laser-Based Syst. Metrol. Insp. III*, vol. 3204, pp. 74–80, 1997.

[5-5] N. Raman and G. J. Hekstra, "Dynamic contrast enhancement of liquid crystal displays with backlight modulation," *2005 Dig. Tech. Pap. Int. Conf. Consum. Electron. 2005. ICCE.*, pp. 197–198, 2005.

[5-6] H. S. Kim, P. D. Byrne, A. Facchetti, and T. J. Marks, "High performance solution-processed indium oxide thin-film transistors.," *J. Am. Chem. Soc.*, vol. 130, no. 38, pp. 12580–1, Sep. 2008.

[5-7] L. S. Chou and I.-H. Lin, "Design of White LED Light Source for Noble LCD Backlight Module," *Mol. Cryst. Liq. Cryst.*, vol. 495, pp. 80–96, Nov. 2008.

[5-8] S.-J. Kim, B.-H. Kim, S.-W. Kim, S.-J. Shin, A. Salleo, S. Ready, and R. Street, "Study of Ink Jet Printing Parameters to Fabricate LCD Color Filter," *J. Imaging Sci. Technol.*, vol. 54, no. 5, p. 050307, 2010.

[5-9] C.-C. Sun, W.-T. Chien, I. Moreno, C.-T. Hsieh, M.-C. Lin, S.-L. Hsiao, and X.-H. Lee, "Calculating model of light transmission efficiency of diffusers attached to a lighting cavity," *Opt. Express*, vol. 18, no. 6, pp. 6137–6148, 2010.

[5-10] Nghia Nguyen-Huu, Y.-L. Lo, Y.-B. Chen, and T.-Y. Yang, "Realization of integrated polarizer and color filters based on subwavelength metallic gratings

using a hybrid numerical scheme," *Appl. Opt.*, vol. 50, no. 4, pp. 415–426, 2011.

[5-11] H.-F. Lin, K.-Y. Huang, and K.-Y. Lin, "Fabrication the high transmittance TFT-LCD displays using photosensitive low-k spin on glass (SOG) films."

[5-12] R.-J. Xie, N. Hirosaki, and T. Takeda, "Wide Color Gamut Backlight for Liquid Crystal Displays Using Three-Band Phosphor-Converted White Light-Emitting Diodes," *Appl. Phys. Express*, vol. 2, pp. 022401–1–3, Jan. 2009.

[5-13] B.-Y. Joo and D.-H. Shin, "Design guidance of backlight optic for improvement of the brightness in the conventional edge-lit LCD backlight," *Displays*, vol. 31, no. 2, pp. 87–92, Apr. 2010.

[5-14] S. Hsia and J. Kuo, "Cost Effective Design and Implementation of Scanning-Based LED Backlight for LCD Module," *IEEE Trans. Consum. Electron.*, vol. 56, no. 4, pp. 2037–2042, 2010.

[5-15] M.-H. Huang, Y.-C. Tsai, and K.-H. Chen, "Energy-Recycling (ER) Technique for a Direct-Lit Intelligent Power Management Backlight Unit (BLU)," *IEEE Trans. Power Electron.*, vol. 25, no. 10, pp. 2588–2598, Oct. 2010.

[5-16] C.-Y. Chen, T.-Y. Hsieh, Q.-L. Deng, W.-C. Su, and Z.-S. Cheng, "Design of a novel symmetric microprism array for dual-view display," *Displays*, vol. 31, no. 2, pp. 99–103, Apr. 2010.

[5-17] D. R. Selviah, K. Wang, and X. Mo, "Modelling New Backlight Technologies," in *"Lighting and Backlighting" Seminar*, 2005, Bletchley Park, UK.

[5-18] G. Harbers and C. G. A. Hoelen, "High Performance LCD Backlighting using High Intensity Red, Green, Blue Light Emitting Diodes," *SID Symp. Dig. Tech. Pap.*, pp. 702–706, 2001.

[5-19] P. Ludwig, K. Gerhard, S. Winfried, and S. Andreas, "High efficient LEDs for LCD backlight," *ITG-Fachbericht*, vol. 183, pp. 293–296, 2004.

[5-20] M. Gebauer, P. Benoit, P. Knoll, and M. Neiger, "P-9: Ray Tracing Tool for Developing LCD-Backlights," *SID Symp. Dig. Tech. Pap.*, vol. 31, no. 1, pp. 558–561, 2000.

[5-21] Y. Fan, Y. Lee, and Y. Liao, "Improvement and Optimal Design of RGB LED Backlight Unit Using a Genetic Algorithm," *Nov. Opt. Syst. Des. Optim. XIII*, vol. 7787, 2010.

[5-22] Y. Martynov, H. Konijn, N. Pfeffer, S. Kuppens, and W. Timmers, "High-efficiency Slim LED Backlight System with Mixing Light Guide," *SID Dig.*, no. 5, pp. 1259–1261, 2003.

[5-23] C. Han, Y. Tak, and B. Ahn, "15-in. RGBW panel using two-stacked white OLED and color filters for large-sized display applications," *J. Soc. Inf. Disp.*, vol. 19, no. 2, pp. 190–195, 2011.

[5-24] J.-R. Yan, Q.-H. Wang, D.-H. Li, and J.-D. Zhang, "Edge-Lighting Light Guide Plate Based on Micro-Prism for Liquid Crystal Display," *J. Disp. Technol.*, vol. 5, no. 9, pp. 355–357, Sep. 2009.

[5-25] "CREE Optpelectronics: G-SiC Technology MegaBright LEDs CxxxMB290-S0100, CRP3BE Rev. C," *Cree, Inc* ., 2005.

[5-26] R. S. West, H. Konijn, W. Sillevis-Smitt, S. Kuppens, N. Pfeffer, Y. Martynov, Y. Takaaki, S. Eberle, G. Harbers, T. W. Tan, and C. E. Chan, "High brightness direct LED backlight for LCD-TV," *SID Dig.*, pp. 1262–1265, 2000.

[5-27] I. Moreno, "LED intensity distribution," *Int. Opt. Des. Conf. Opt. Soc. Am.*, no. June, p. TuD6, 2006.

[5-28] Yoichi Taira, H. Numata, D. Nakano, K. Sueoka, F. Yamada, M. Suzuki, M. Noguchi, R. Singh, and E. G. Colgan, "Color Filterless Liquid Crystal Display Illuminated with LEDs," *SID Dig.*, pp. 1250–1253, 2003.

[5-29] H. Gerard, "White LED for Backlight with Phosphor Plates," Patent number: JP20072739982007.

[5-30] J. F. Van Derlofske, "Computer modeling of LED light pipe systems for uniform display illumination," *Proc. SPIE*, pp. 119–129, 2001.

[5-31] E. Hecht, "Optics," in *Optics*, Addison Wesley, U.S, International 4th Edition, 2002, p. 121.

[5-32] H. Dammann, "Color separation gratings," *Appl. Opt.*, vol. 17, no. 15, pp. 2273–2279, 1978.

[5-33] GODWIN, DP, SELVIAH, DR, CAREY, and CD, "THE SELF-FOCUSING FRESNEL-DAMMANN GRATING AND THE FRESNEL BINARY CGH FOR COMPACT 2-D LIGHT SPOT ARRAY GENERATION," no. 379, pp. 147–152, 1993.

[5-34] S. Tao, Z. H. Song, and D. R. Selviah, "Bragg-shift of holographic gratings in photorefractive Fe:LiNbO3 crystals," *Opt. Commun.*, vol. 108, no. 1–3, pp. 144–152, May 1994.

[5-35] B. R. Organization, "Diffraction Gratings and DOEs," in *ASAP Technical Guide*, Breault Research Organization, Inc., 2002.

[5-36] H. J. B. Jagt, H. J. Cornelissen, D. J. Broer, and C. W. M. Bastiaansen, "Linearly polarized light-emitting backlight," *J. Soc. Inf. Disp.*, vol. 10, no. 1, pp. 107–112, 2002.

Chapter 6. Ray Trace Model of Liquid Crystal on Silicon Display -- Modelling the Angular Variation of the Reflected Light from the Nematic Liquid Crystal in an LCOS Rear Projection TV System

6.1 Introduction

It has been demonstrated in the previous chapter that ray tracing is efficient and is a low cost design solution for the detailed design of optical components for illumination and display systems. However, in some cases, for example, when modelling the liquid crystal (LC) component in displays, an accurate director model [6-1], [6-2] is necessary to describe the LC layer throughout the switching. Normally, one need a stack of at least 100 birefringent layers to model the optics of the LC layers properly [6-2]. Ray tracing recognises every incident polarized beam as an electric field and splits it into two orthogonal field components traversing each birefringent layer, therefore, the total number of split components or rays increases by a factor of 2 at each birefringent layer. It is impractical to trace all of the rays and to calculate phase relationships between them. Ray trace modelling alone becomes inefficient to model light propagating through an LC component. Dr. F.A. Fernández, Dr. Sally E. Day and author developed a novel technique to model a projection system incorporating a liquid crystal on silicon (LCOS) modulating device by combining a non-sequential ray tracing program with an in-house LC director model and a model of the optics of the LCOS chip [6-2], [6-3].

In this chapter, section 6.2 describes the configuration of a single panel (one reflective LCOS chip) integrated optical engine (OE) for a Rear Projection TV (RPTV) system. section 6.3 explains the modelling strategy and the combined simulation results.

6.2 LCOS Display System Configuration

LCOS displays have attracted widespread attention also because of their better performance versus cost than large area LCD and plasma displays while delivering high resolution (1920 × 1080 pixels), which comes about due to the combination of the two established technologies, Integrated Circuits/Chips (IC) and Liquid Crystals (LC). The RPTV system investigated here is based on LCOS technology. It uses a colour wheel to provide time sequential colour illumination that illuminates the panel

sequentially with the three primary colours: red, green and blue. Figure 6-1 depicts the Optical Engine (OE) architecture which uses an Ultra High Performance (UHP) mercury arc lamp as its light source.

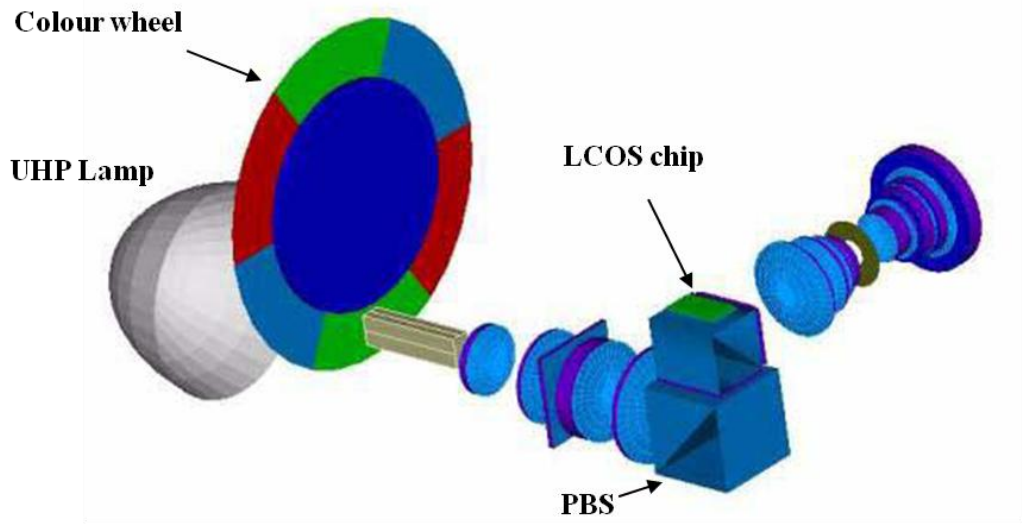

Figure 6-1 The optical engine architecture for use with a single LCOS panel (designed by the project partner, Thomson Multimedia R&D, France)

The modulating device (a LCOS chip) is illuminated with a narrow cone of light via a polarizing beam splitter (PBS), which delivers the incident light onto the chip. The light reflected by the chip is redirected towards the projection lens. The modulated light reflected from the LCOS device is then conveyed via high specification projection optics which magnified the image for display with negligible distortion.

In this OE architecture, the LCOS is operated as a binary modulator in colour time sequential mode where fast switching is essential. A full colour image being refreshed at 50 Hz comprising equal illumination segments of red, green and blue has less than 7 ms ($\frac{1}{50\times3} = 6.66 \times 10^{-3}\ s$) to display each colour's image while meeting the high contrast specification at the projection screen.

While liquid crystal on silicon (LCOS) projection systems have a very narrow illumination cone [6-1] emerging from the liquid crystal (LC) device compared to direct view displays, one of the key requirements is for a very high contrast ratio which is obtained by dividing the bright-state intensity by the dark-state intensity in a

display system [6-4], so that it is crucial to achieve a very good dark state to maximise this ratio.

6.3 Simulation of a LCOS Display System

Figure 6-2 is an enlarged schematic of the Optical Engine (OE) showing the behaviour of light inside the polarizing beam splitter (PBS).

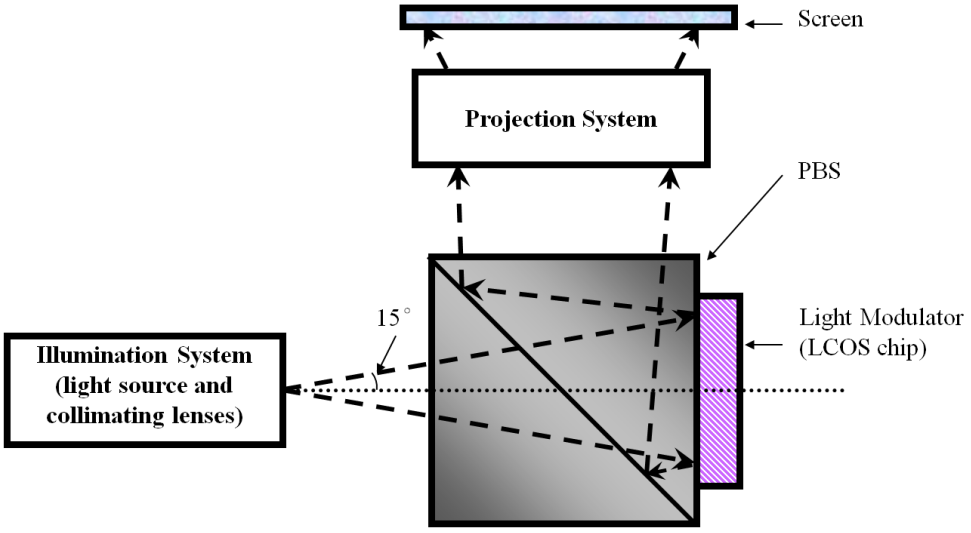

Figure 6-2 Schematic of optical engine system

The schematic configuration diagram also highlights the author's computer model in three parts (see Figure 6-3).

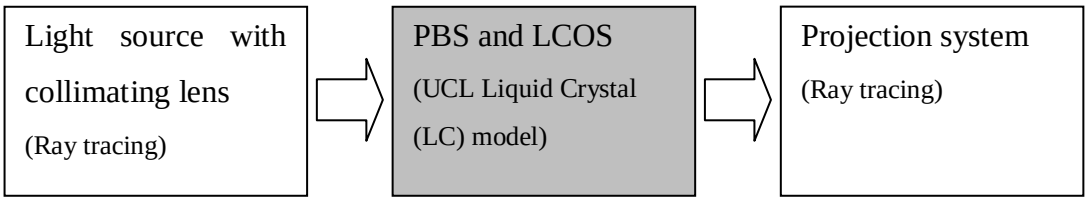

Figure 6-3 Flow chart of computer model

Firstly, the light source generates unpolarized light via an array of collimating lenses in a narrow viewing cone. Most of the energy remains within a small divergent angle. The author considered rays going out within + and - 15 degree and ray traced the illumination up to the PBS, to determine the illumination information of the position, propagation direction and intensity of each ray incident on the birefringent optical device, LCOS. Next, the illuminating rays were polarized by the PBS and were incident on the LCOS chip. Here the author integrated a polarizer (polarizes the incident rays) and an analyzer (changes the polarization of the reflected rays by the

LCOS) into the LCOS model instead of using a PBS to reduce the complexity of ray tracing. The author extracted the illumination information from the ray tracing program and employed a three dimensional model of the dynamic liquid crystal behaviour in the LCOS device [6-4] developed at the Optical Devices and Systems Research Laboratory in UCL to find the director distribution of the LC layer upon switching. Then, from this, the author calculated the reflected intensity profiles using an extended Jones matrix method [6-5] to predict the performance of the optical engine for the designed projector system. Finally, the modulated rays from the LCOS chip were imported back to the projection system for ray tracing of the return path yielding the light field to be projected onto the screen.

The mixed twisted nematic (MTN) [6-6] mode was used. It is frequently used in LCOS devices because of its short turn-on and turn-off times with good contrast and reasonably high reflectivity [6-7]. The director profile model used in the LCOS simulation works by finding a dynamic variational solution for the LC director and electric potential distributions based on the Oseen-Frank free energy formulation. The full dynamic liquid crystal director model (developed by Dr. R. James and modified by the author) uses three elastic constants and a vector representation for the director (see Figure 6-4).

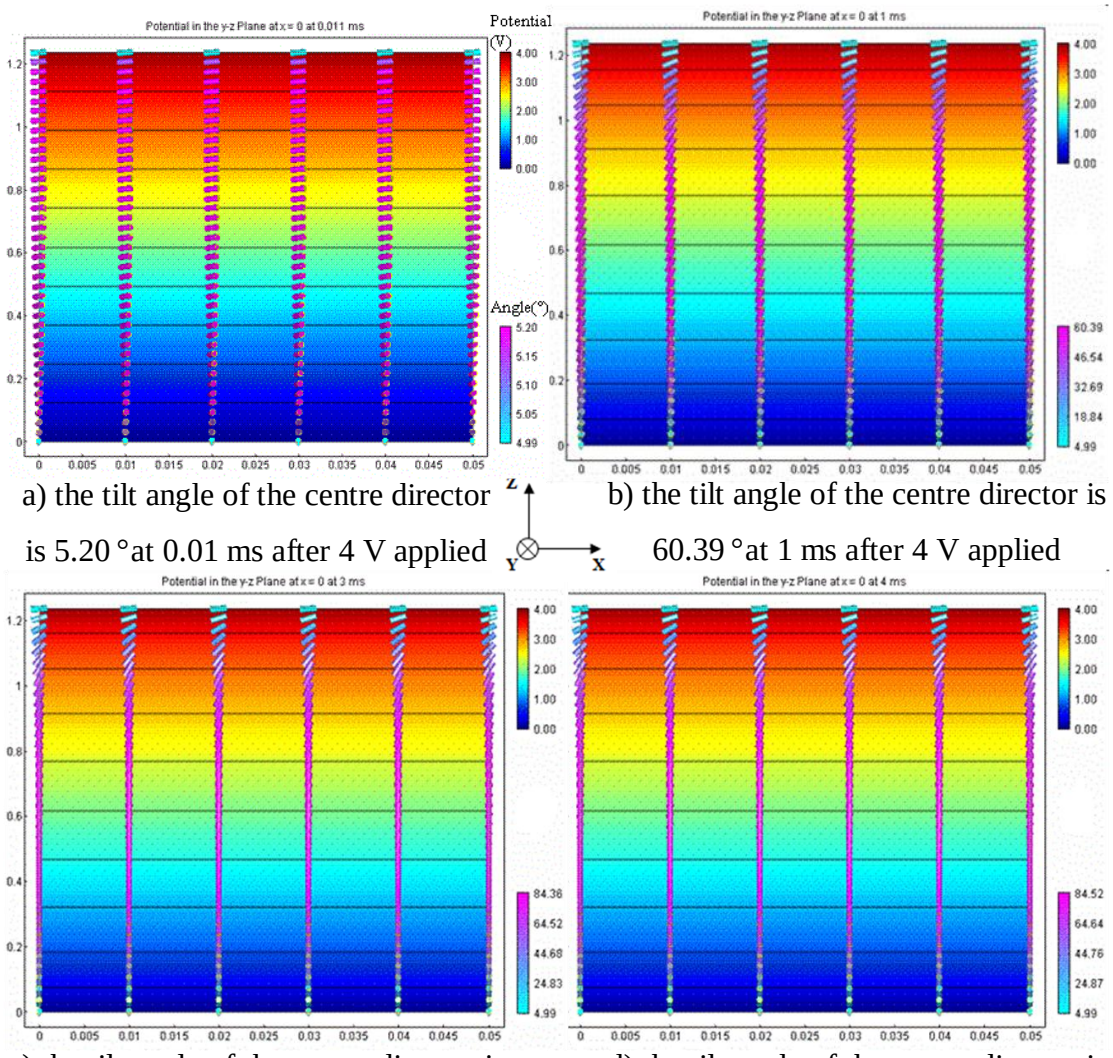

a) the tilt angle of the centre director is 5.20 °at 0.01 ms after 4 V applied

b) the tilt angle of the centre director is 60.39 °at 1 ms after 4 V applied

c) the tilt angle of the centre director is 84.36 °at 3 ms after 4 V applied

d) the tilt angle of the centre director is 84.52 °at 4 ms after 4 V applied

Figure 6-4 The model of liquid crystal directors. The tilt angle of the director increases with time when a 4 V voltage is applied across the top and bottom electrodes

The liquid crystal layer is sandwiched between two electrode layers. The rods represent the LC directors and the colour of the rods indicates the tilt angle (the tilt angle colour bar is located at the bottom right in each sub-figure). At the beginning, there is a 90 degree twist horizontally across the LC layers and the vertical pre-tilt of the LC alignment layer is 4.99 degrees, as shown in Figure 6-5.

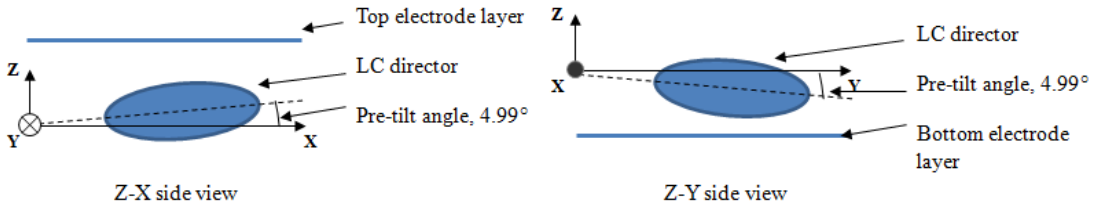

Figure 6-5 Schematic side-view of the LC director model

The tilt angle of the director increased with time, when the author applied 4 V across the electrodes. The graded background colour represents the potential difference (the potential colour bar is located at the top right of each sub-figure). The four sub figures indicate the change in the director tilt profile from 0 to 4 millisecond after application of the switching voltage. At 4 ms, the nematic cell is switched with a mid-director tilt angle of about 85 °. This model is used to determine the reflectivity across the pixels of the LCOS chip. In this 90 ° twisted, reflective mode, the LC thickness is set to $0.45\lambda/\Delta n$, and the polarizer and analyser axes are set to 20 ° and 110 ° to the front director respectively. A birefringence, Δn, of 0.19 at 550 nm was used. This configuration is chosen to match the optical properties of the LCOS chip supplied by Thomson Multimedia R&D. The simulation presented in this chapter proved that good contrast ratio can be achieved using these parameters.

The modelling results to be presented concentrate on the contrast ratio and uniformity of the LCOS chip and are represented by a contour plot in polar coordinates which is related to viewing angles. In section6.3.1, results are presented of a simulation of the contrast ratio using the LC optics model (developed by Dr. M. Gardener and modified by the author for integration with the ray trace model) on its own. An angularly uniform light source is applied over a regular array of polar and azimuthal angles to cover the incident angles of interest with sufficient density to provide a smooth contour plot. In section 6.3.2, the liquid crystal simulation model is interfaced with the OE ray tracing model. Ray tracing is used to simulate the light from the illumination system and its output propagation parameters (i.e. spatial position, incident angle and intensity) over the area of the LCOS device are used to calculate the light reflected from the LCOS layer. Finally, in section6.3.3, consideration is made of the non-uniform illumination over different areas of the LCOS device and the resulting reflectivity from the LCOS device is presented.

6.3.1 Optical Modelling of LCOS Chip in Angularly Uniform Illumination

The LC director profiles at various applied voltages were used to calculate the intensity of the light incident on the LCOS chip over a range of ±15 °. For a single panel RPTV system, which requires a single Digital Light Processing (DLP) chip to process all three colours (red, green and blue) during a single frame time, one of the most demanding requirements is achieving high contrast. The contrast ratio is

obtained by dividing the bright-state intensity I_{off} (no voltage) by the dark-state intensity I_{on} (voltage applied). These calculations are made with the display in the full-screen bright and dark states (0 V and 4 V) respectively.

The curves in Figure 6-6 indicate the director tilt profile at various switching times after applying a voltage of 4 V. The tilt angle of the director increases as a function of the switching time. 3 ms after applying 4 V to the LCOS device, the nematic cell is virtually fully switched with a mid-director tilt angle of about 85 °.

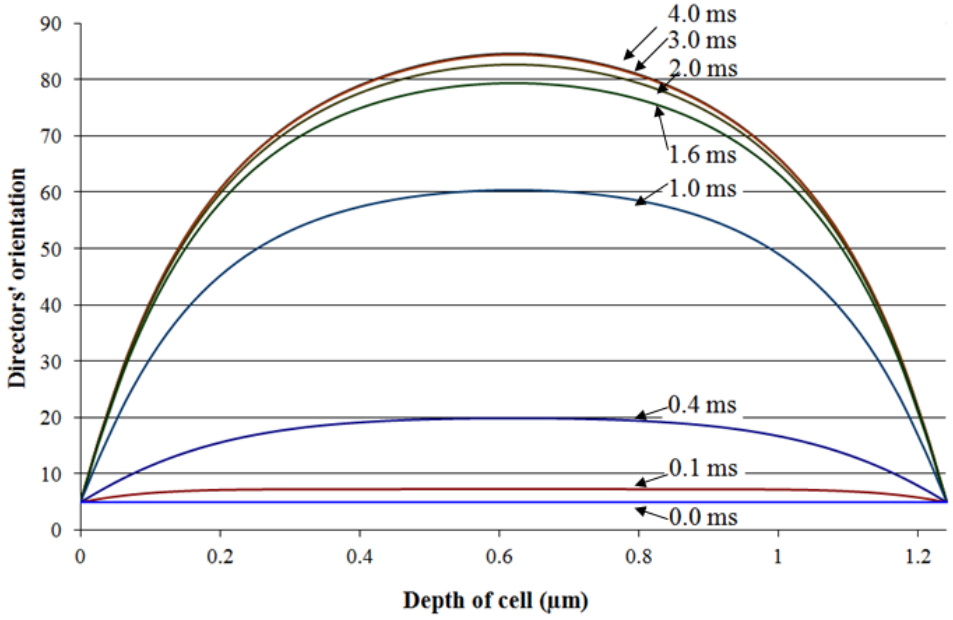

Figure 6-6 Director tilt profile vs. distance into LC layer at different response times (applied voltage: 4 V)

For a given wavelength, λ = 550 nm, and applied voltage, it is possible to display the reflected intensity as a function of incident angle $I = (\theta, \emptyset)$ in polar form by using contour plots. An angularly uniform point light source was created and was applied to the LC optics model to simulate the reflected light from the LCOS chip at the polar angle between 0 ° and 15 ° at 1 ° intervals, and at the azimuth angle between 0 ° and 360 ° with azimuth intervals of 1 ° to assess the contrast ratio at reflected angles from the LCOS chip.

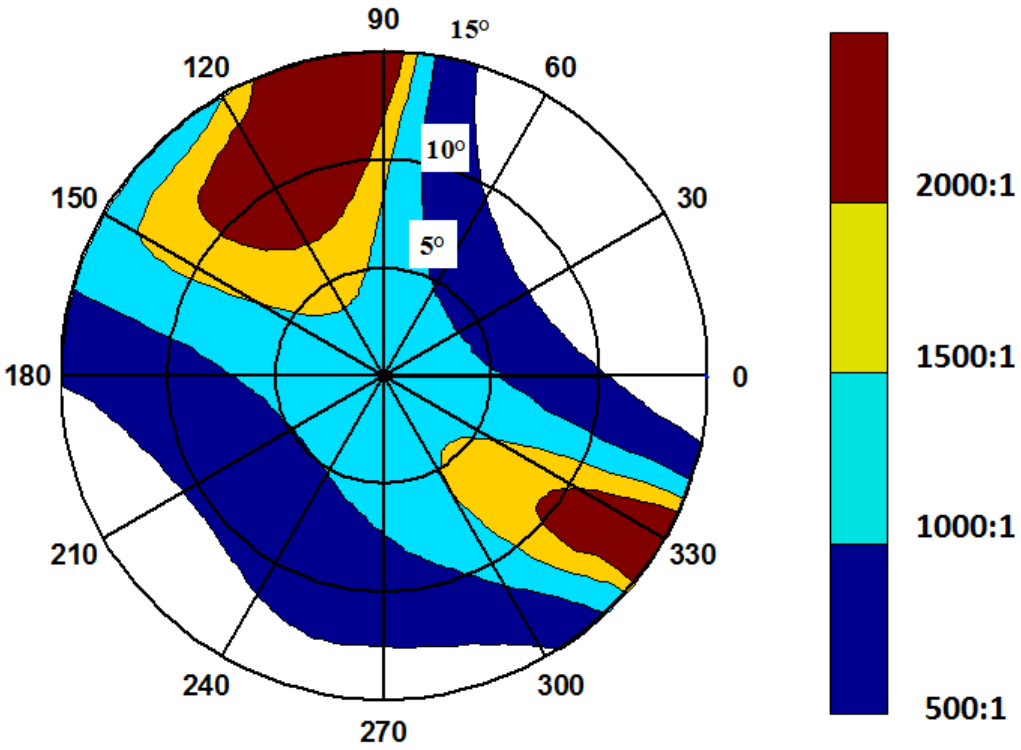

Figure 6-7 Contrast Ratio of one pixel at 3 ms after 4 Volts is applied. The polar angle varies radially between 0 ° and 15 °, while the azimuthal angle varies between 0 ° and 360 ° along the circumference. Uniform illumination (λ = 550 nm) is applied at all angles

Figure 6-7 shows the contrast ratio contours of one pixel in a polar diagram for the LCOS device without considering the illumination and projection components. The contrast ratio was calculated 3 milliseconds after the switching voltage was applied because the LC is already switched enough to give a high contrast (higher than 1000:1 and higher than 5000:1 at some areas). The contour was divided into 4 bands: 500:1, 1000:1, 1500:1 and > 2000:1 for clarity of presentation. The contrast ratio degrades towards the larger polar angles in the 30 ° and 210 ° azimuth directions but increases near the 90 ° and 330 ° directions. This trend was caused by the alignment of the polarizer and analyzer, where axes are set to 20 ° and 110 ° to the front director, respectively. The contrast ratio is higher than 1000:1 between 0 ° to 5 ° polar angles and the ratio remains almost consistent at all azimuth angles indicating the better contrast uniformity in this region.

The intensity of normal incident angle versus LC director switching time curve (Figure 6-8) indicated a switching time of 0.74 ms calculated between the intensity falling to 90% of I_{off} at 0.46 ms and 10% of I_{off} at 1.2 ms.

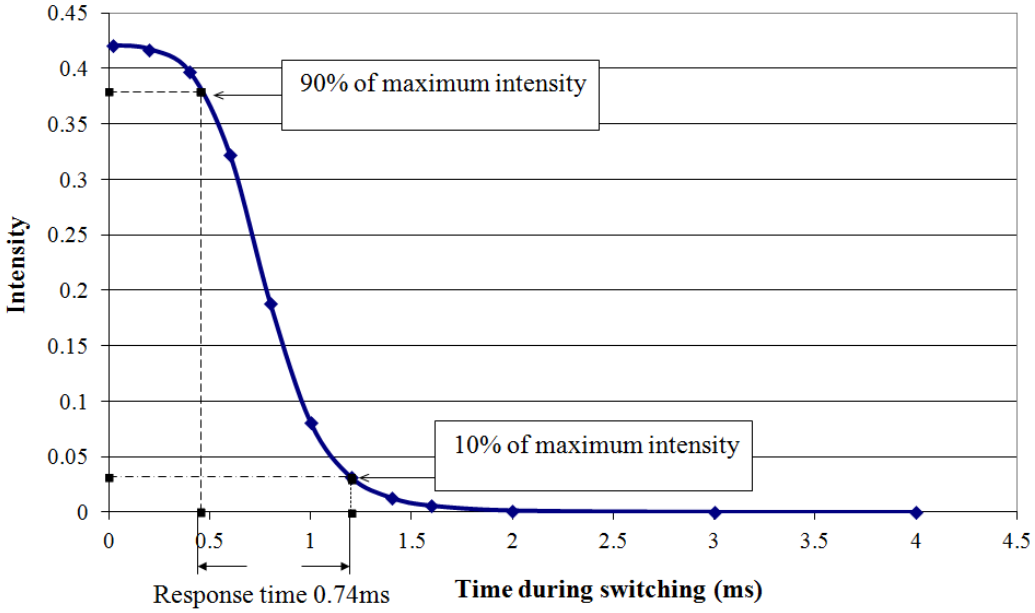

Figure 6-8 LCOS reflected intensity vs. time during switching

The evolution of contrast ratio (CR) during switching can be studied using the author's model. Figure 6-9 shows the CR at normal incidence angle and the average CR as a function of time for a range of angles of incidence averaged over the ±15° viewing cone.

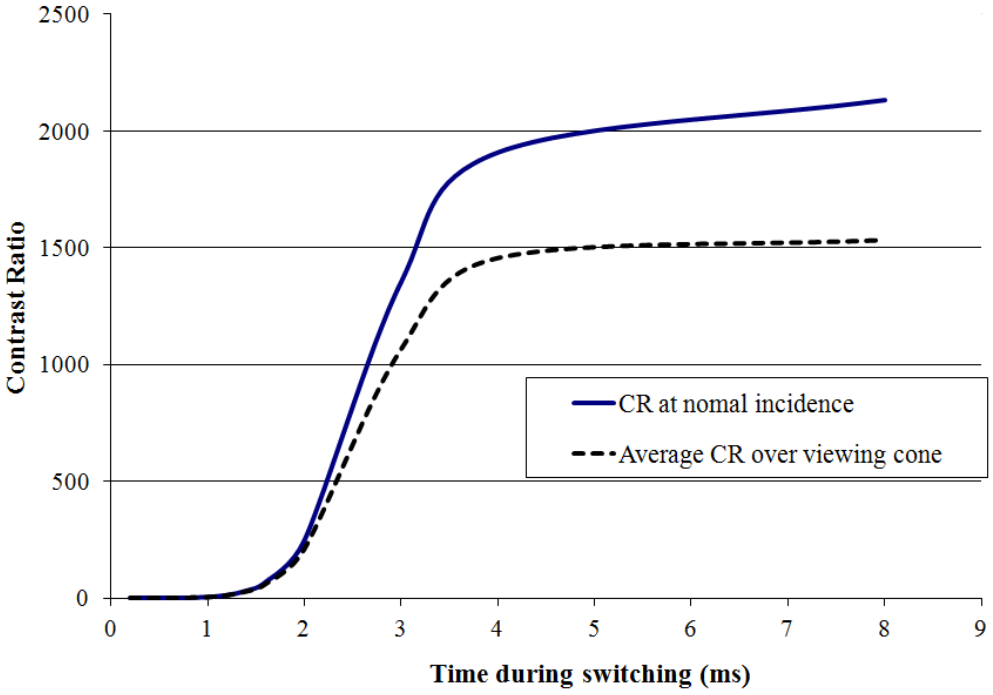

Figure 6-9 Contrast ratios vs. time during switching

The overall steady state contrast ratio (dash curve in the figure) is still within the designed range (higher than 1000:1) at 3 ms after 4 V is applied. Although the cell is considered fully switched at 3 ms, as mentioned previously, the CR curve continues to increase due to the residual on-state intensity (the denominator in the CR) continuing to change, though imperceptibly in the intensity vs. time curve. Recall that the reflected intensity has fallen to just 10% of the off value by 1.2 ms, hence, the curve in Figure 6-8 indicates a CR of 10 at 1.2 ms, but continues to grow considerably.

6.3.2 Combined Illumination and LCOS Panel Modelling

The simulation of the LCOS on its own applies rays of angularly uniform intensity on a regular array of polar and azimuth angles, where the model integrating the ray tracing with the LC model has incident rays of varying intensity and polarization as well as at irregular polar and azimuth angles. In order to compute useful results over the full space of incident angles and compare the results with the LCOS model using the angularly uniform illumination, the incident ray data from the ray tracing simulation is interpolated onto the regular array of polar and azimuth angles before being processed in the normal way as mentioned in the previous section.

Figure 6-10 represents the ray tracing of the illumination system. A volume light emitter is used to simulate a 1.0 mm arc gap in an elliptical reflector. The light is focused into a rectangular light pipe to get a spatially uniform rectangular light source at the end of the hollow light pipe. That output is then imaged by 4 collimation lenses which deliver light within a $\pm 15^\circ$ angular distribution onto a plane where it couples with the LCOS model. The modulated rays reflected from the LCOS chip can be re-applied to the projection system for further simulation.

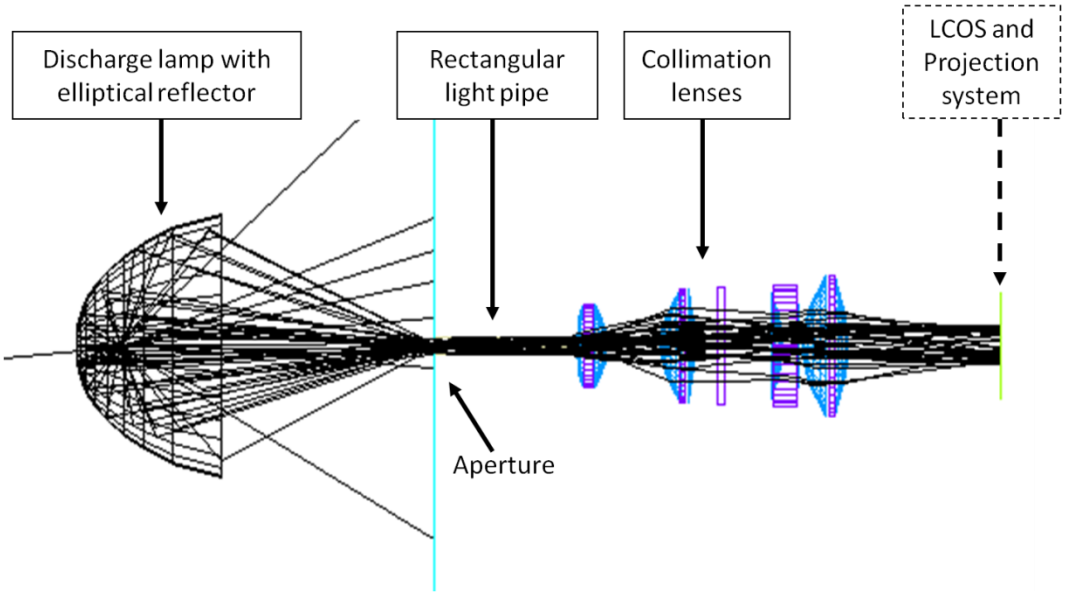

Figure 6-10 Part of simulated projection system with realistic models for light pipe and collimation lenses (designed by Thomson Multimedia R&D, France and modified at UCL for coupling with LCOS model)

The following figure shows the results of the ray tracing model of the light distribution on the detection plane in Figure 6-10, which is also the entrance surface of the LCOS chip.

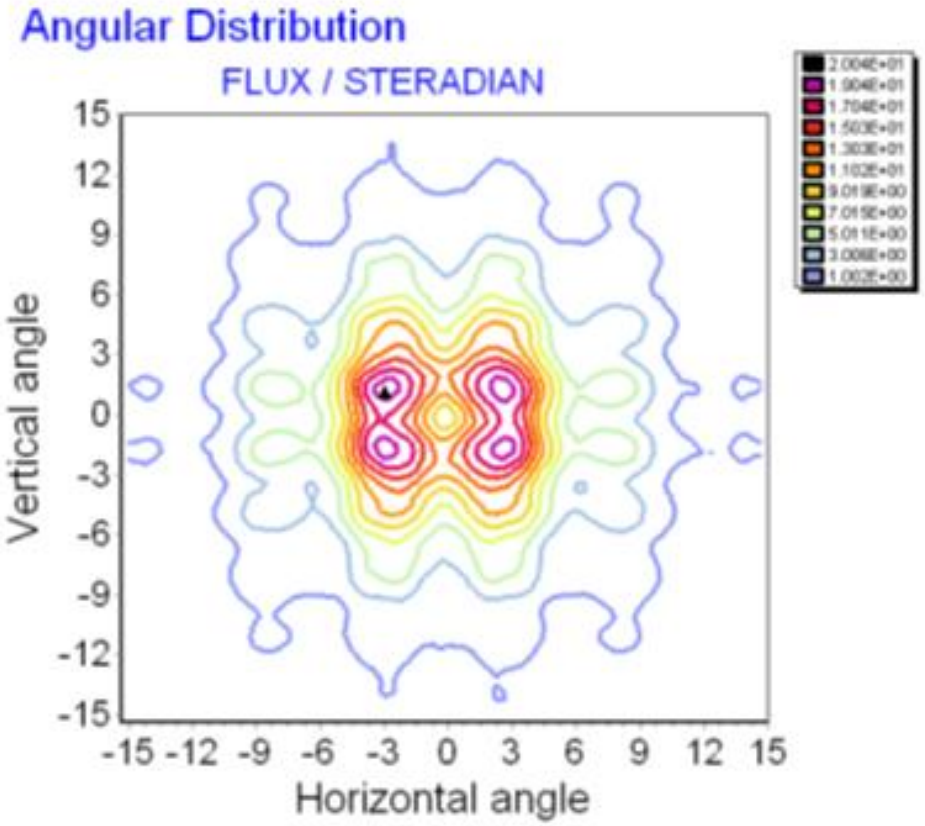

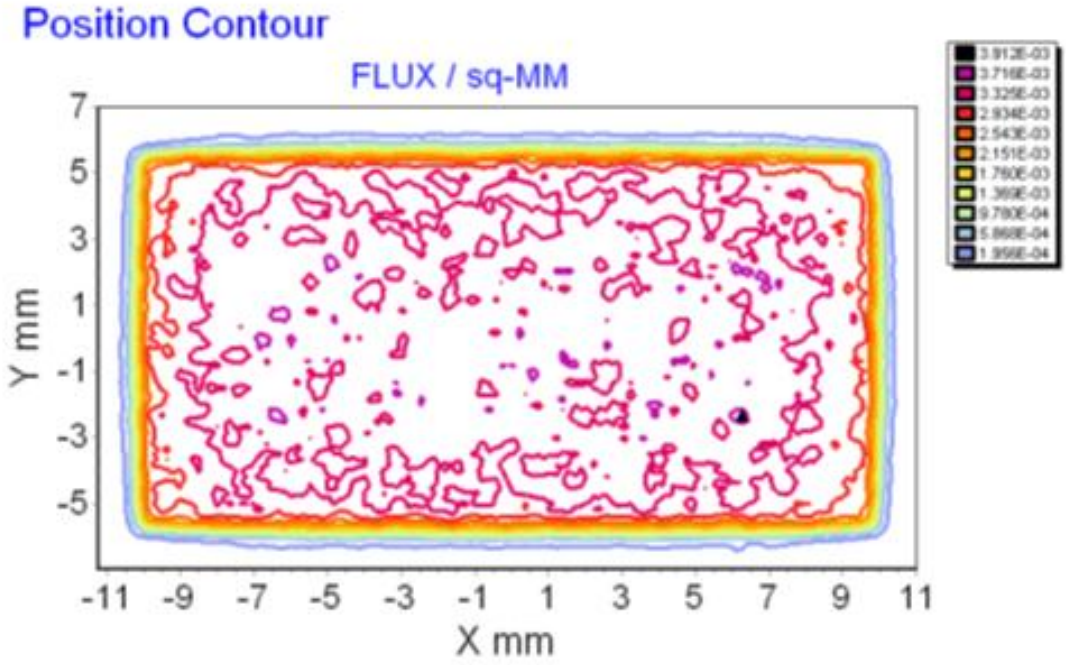

Figure 6-11 Angular distribution and flux distribution across the LCOS chip

Ideally, with the design of the illumination system, the output illumination is spatially uniform over the area of the LCOS device and the angles of the rays are as close to normal as possible to achieve high contrast ratio and good intensity uniformity. The left hand side diagram shows the angular distribution of the rays for the LCOS chip. The author included the illumination within ±15°. The intensity is lower at larger angles, as expected. The right hand side diagram is the intensity spatial distribution across the LCOS chip. The illumination is designed to produce approximately a 0.9 inch diagonal image with 16 to 9 aspect ratio. The results of the ray-tracing up to the LCOS chip determine the position on the chip, propagation direction and intensity of each incident ray and they are then used as the input to the extended Jones matrix model of the LCOS device for subsequent light modulation.

The author included a dichroic surface of a polarizer in the LCOS model to polarize the incident light so that the polarizations of the incident rays on the LCOS chip were calculated. Figure 6-12 shows the average contrast ratio of the LC model at 3 ms after 4 V is applied. The results are shown for the one pixel of the LCOS chip after combining the ray traced illumination optics and LCOS simulation. 100,000 rays were generated in ray tracing to illuminate the whole area of the LCOS chip.

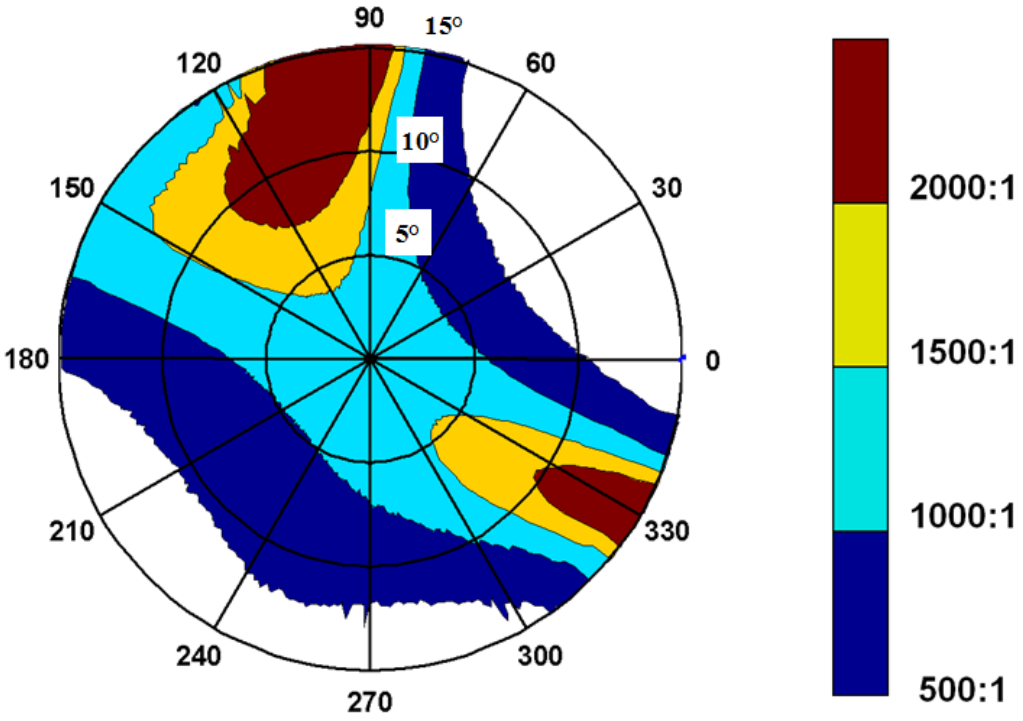

Figure 6-12 Contrast Ratio from LCOS model interfaced with ray tracing 3 ms after applying 4 Volts using 100,000 rays

The growing contrast towards large polar angles in the 90 ° & 330 ° directions is preserved, as is the significant drop in contrast in the 45 °& 225 °azimuth directions.

6.3.3 Illumination Non-uniformity over the Area of LCOS Chip

The LC model alone can only calculate the reflected light in one pixel on the LCOS chip. In order to simulate the illumination over the whole area of LCOS chip, the modulated rays from the LCOS director model are put back into the ray tracing program for simulating the projection system. The light intensity distribution to be projected onto the screen is presented below.

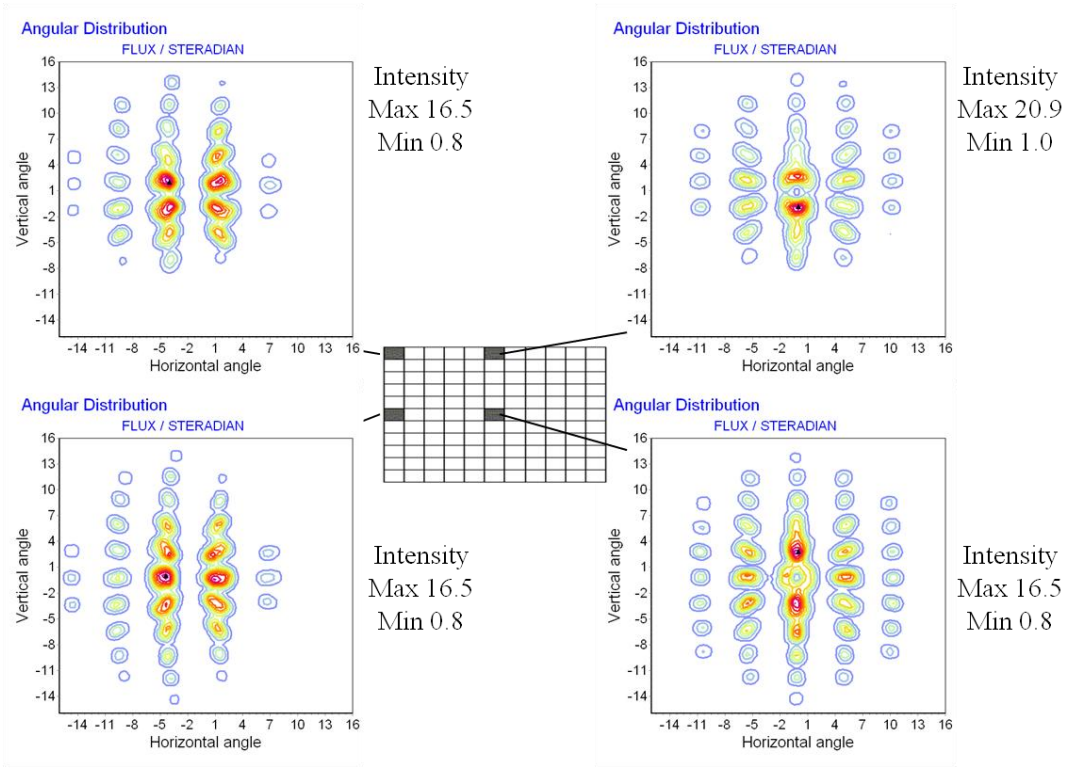

Figure 6-13 Reflected intensity contour plots for 4 different regions of the LCOS panel area, no voltage is applied, Reflected intensity distribution non-switched (bright) state

An important aspect of the display performance is the uniformity across the LCOS chip. One can use ray tracing to assess the uniformity only if there are large numbers of rays (1 million) incident on the LCOS chip, because ray tracing relies on a sufficient number of rays to produce useful results. However, it is very time consuming to trace large number of rays across the whole area of the LCOS chip and import them into the LCOS model. The author divided the LCOS area into 121 (11×11) smaller areas (Figure 6-13) and illuminated each of the sub-region by 10,000 rays. The reflected intensity in the bright state, when the LC is switched, of four individual areas in the centre, top-left corner, middle of the top edge, and middle of the left edge of the display, each occupying 1/121 of the total display area, are examined separately and significant variation between regions is revealed.

Figure 6-14 shows the reflected intensity in the dark state, when the LC is switched. One can see that the middle left region has the highest intensity. That means there are more rays leaking from this area than the others. A more collimated illumination is required to solve this problem. Combining these results with the previous reflected

intensity in the bright state, one can calculate the contrast ratio for individual regions of the LCOS chip, as listed in Figure 6-14.

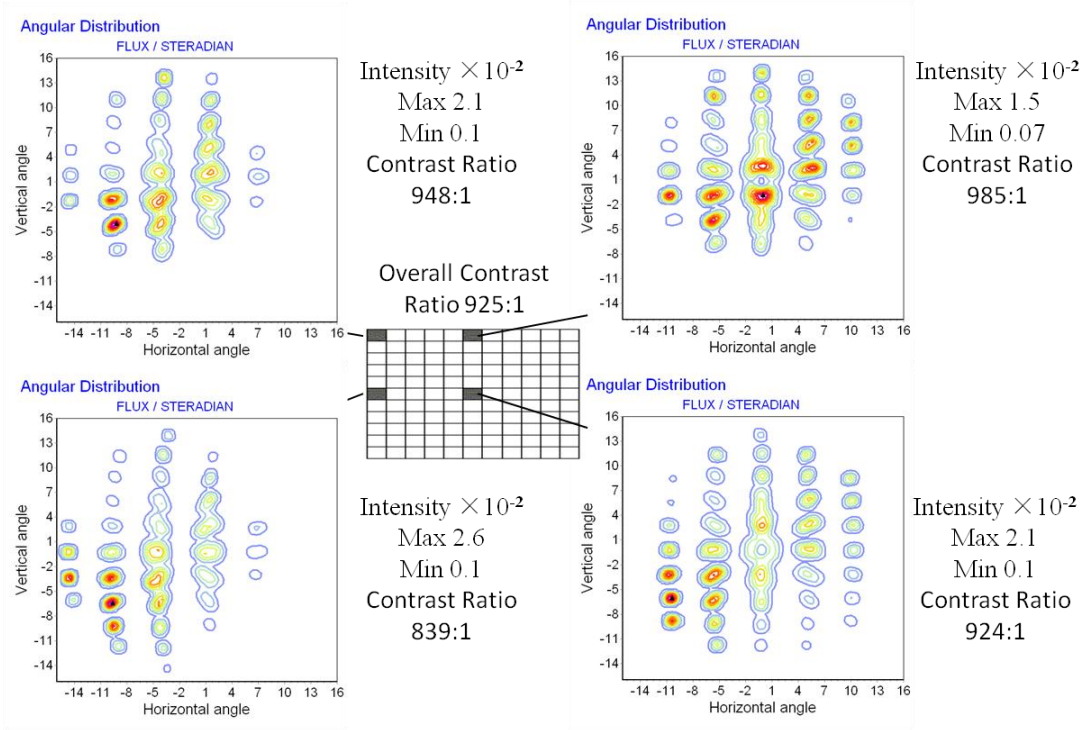

Figure 6-14 Reflected intensity contour plots for 4 different regions of the LCOS panel area, 3 ms after 4 V is applied, Reflected intensity distribution switched (dark) state

For all the regions, rays incident within 5° of normal show contrast ratios of approximately 1000 or higher. Clearly, the lowest contrast ratio appears at the middle of the left edge region because of the poor darkness in the dark state in this area. The system the author have modelled here is not perfect for a projection TV system, but the author have shown an efficient method for predicting the performance and so allowing improvement using modelling.

6.4 Summary and Discussion

The work described in this chapter combines a ray-tracing program, a full dynamic liquid crystal director model and a LC optics model to simulate the performance of a Rear-projection television (RPTV) system using an LCOS panel. Detailed simulation of the system performance is required because of the necessity to maintain very high contrast ratios and intensity uniformity in such systems and because of the variable viewing angle characteristics of LCDs. We have demonstrated how combined ray tracing and LC modelling can reveal useful information about viewing angle variation over the LCOS panel area, which would not be apparent from LC modelling alone.

The effects of non-uniform illumination over different areas of the LCOS chip on the contrast ratio and reflectivity are shown.

The dynamic LC director simulation allows accurate calculation of the reflection from the LCOS device. The optical results of the LC simulation can be imported into the ray-tracing software for tracing back through the projection optics and redirection to a projection screen. Thus, the work described here can be used to simulate the whole light path from illumination to the display screen using both ray-tracing and Liquid Crystal dynamic modelling.

These results were presented for the mixed twisted nematic (MTN) case, but the director model can be easily applied to other operating modes used in Rear-projection television (RPTV), such as vertically aligned nematic (VAN). In addition, the method can be applied to the full pixel level performance including electric fringe field effects etc., using the three dimensional capability of the model for the director structure. While the results presented are for a single LCOS panel, the method could equally well be applied to multiple panel systems.

Future work will be to use full 3D dynamic capabilities of the liquid crystal director model of the LCOS structure combined with ray-tracing program and also to use a full range of visible wavelengths for further modelling. Other work is to improve the polarization calculation in the LCOS model. One can include a compensator birefringent layer in the Extended Jones model during LC simulation. It is expected that the inclusion of a compensator layer would improve the uniformity of contrast for all the regions [6-8].

Chapter 6 References

[6-1] J. Chen, M. G. Robinson, and G. D. Sharp, "General methodology for LCoS panel compensation," *J. SID*, vol. 12, no. 4, pp. 423–428, 2004.

[6-2] M. C. Gardner, S. E. Day, F. A. Fernandez, and K. Sarayeddine, "6 . 3 : Three-Dimensional Modelling of a Projection TV System by Dynamic Liquid-Crystal Simulation and Ray Tracing," *SID Symp. Dig. Tech. Pap.*, vol. 35, pp. 68–71, 2004.

[6-3] F. A. Fernandez, S. E. Day, P. Trwoga, H. F. Deng, and R. James, "Three-Dimensional Modelling of Liquid Crystal Display Cells using Finite Elements," *Mol. Cryst. Liq. Cryst.*, vol. 375, pp. 291–299, 2002.

[6-4] M. F. Bone and M. Flynn, "Measurement methods for LCoS displays," *J. Soc. Inf. Disp.*, vol. 11, no. 1, p. 225, 2003.

[6-5] P. Yeh and C. Gu, "No Title," in *Optics of Liquid Crystal Displays*, A Wiley Interscience Publication. U.S., 1999, pp. 306–356.

[6-6] S. T. Wu and C. S. Wu, "Mixed-mode Twisted Nematic Liquid Crystal Cells for Reflective Displays," *Appl. Phys. Lett.*, vol. 68, no. 11, pp. 1455–1457, 1996.

[6-7] S. T. Wu and C. S. Wu, "Mixed-Mode Twisted-Nematic Cell for Transmissive Liquid Crystal Display," *Displays*, vol. 20, no. 5, pp. 231–236, 1999.

[6-8] M. G. Robinson, J. Chen, and G. D. Sharp, "22 . 1 : Wide Field of View Compensation Scheme for Cube Polarizing Beam Splitters Skew ray depolarization PBS compensation solution," *SID Symp. Dig. Tech. Pap.*, vol. 34, pp. 874–877, 2003.

Chapter 7 Ray Trace Modelling and Experimental Measurement of Optical Loss and Crosstalk in Multimode Step-index Photolithographically Fabricated Polyacrylate Polymer Waveguide Crossings

7.1 Introduction

In this chapter, the optical loss and crosstalk of multimode step-index photolithographically fabricated polyacrylate polymer (Truemode^{TM}) waveguide crossings, with refractive indices of the core and the cladding of 1.5560 and 1.5264 respectively, are characterised by ray tracing simulation and experiment. The aim is to find the dependence of optical loss and crosstalk on the angle between the two crossing waveguides (Figure 7-1).

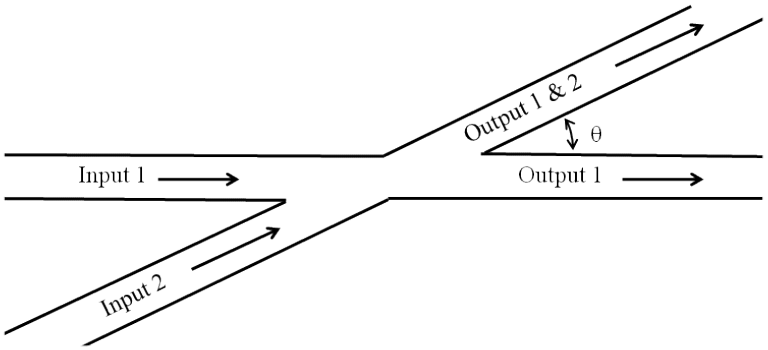

Figure 7-1 Top schematic view of a waveguide crossing with crossing angle θ

The optical loss and crosstalk measurements of waveguide crossing components at a range of crossing angles from 10 °to 90 °and crossings after bends are reported in this chapter for the first time [7-1].

Simulation of waveguide crossing using wave optics, such as the beam propagation method (BPM), has some limitations, in particular with respect to the crossing angle (up to 20) [7-2]. Therefore, the optical loss caused by waveguides crossing at a range of crossing angles was simulated using a ray tracing method. The simulation followed the experimental configuration where a multimode optical fibre was used as the light source and the output of a VCSEL was coupled into the fibre, as explained in the later

section 7.3. Five ray trace models of light sources for models of multimode polymer waveguides were investigated. The parameters used in the models were obtained from experimental measurements of far field and near field energy distributions at the output of a 10 cm long straight waveguide. A best match light source to the experimental one was found by comparing the rms and standard deviation values of the far-field intensity profiles of modelled light sources with the measured one. A general method for modelling a light source for multimode waveguides is given. In addition to a square cross section waveguide model, a ray tracing model of non-rectangular waveguides based on the waveguide shape of the cross-section of a photolithographically fabricated polyacrylate step index polymer waveguide is reported for the first time. The influence of the cross sectional shape of the waveguides on the optical loss is analyzed by the modelling method.

The optical loss due to waveguide crossings and splitters has been characterised by experiments and simulations and the research in this area was reviewed in Chapter 3. However, most of the previous research is silicon based [7-3–5], e.g. hydrogen silsesquioxane resist, waveguides with small cross sections, normally less than 6 μm x 6 μm. There are only a few people T. Ishigure, et al,, W. Ni, et al.and G. L. Bona, et al. [7-6–8] have reported the optical loss due to the waveguide crossing by both simulation and experiment and explained the factors causing the loss. The most relevant work about simulation of crossing waveguides using ray tracing and beam propagation methods was first reported by Hadi Baghsiahi in his PhD thesis [7-2] in the Optical Devices and Systems laboratory of the Photonics Research Group at UCL supervised by Dr David R. Selviah. However, a geometric model, detailed light source models and the optical loss affected by the waveguide shape are described in this thesis for the first time.

The waveguides which were measured and modelled had an approximately 50 micron width and 50 micron thickness and were fabricated photolithographically from polyacrylate Truemode^{TM} polymer by Exxelis.

7.2 Computer Modelling and Simulation

7.2.1 Geometric Model

Optical loss at waveguide crossings can be explained by geometrical optics, as shown in Figure 7-2. The optical power in the rays will be lost at the waveguide intersection part because the total internal reflection (TIR) condition is no longer satisfied, when some of the internally reflected light in the main waveguide reaches the waveguide branch, where the incident angles α to the waveguide branch internal wall are larger than the critical angle θ_c of the waveguides, All waveguide branches are made of the same core and cladding materials and have the same TIR condition, therefore, the light that enters the branch waveguide at incident angles less than the critical angle of the waveguides will propagate along the branch waveguide and may cause crosstalk if the light is received by a photo detector attached to the crossed waveguide at an angle, θ, to the main one.

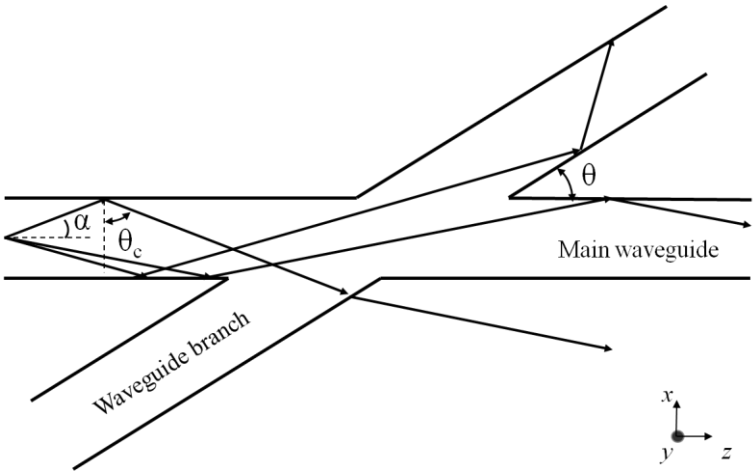

Figure 7-2 Top schematic view of a geometrical optics model for a waveguide with crossing angle θ, critical angle, θ_c, and light incident angle, α,

David R. Selviah suggested that if each light beam inside the waveguide is considered to be formed by two vector components, one in the vertical plane, *y* (perpendicular to the waveguide substrate), and only reflected at the top and bottom surface of the waveguide, and the other in the horizontal plane, *x*, and only reflected at the two side walls of the waveguide, a geometric model based on TIR can be built. The vertical component has no optical loss because the TIR condition is constant along its propagation path. However, the horizontal component will have a fraction of loss at the waveguide crossing intersect point.

The following equations were derived by the author to calculate the total optical loss, L (dB), of the two wave components.

When $\theta_c \leq \theta$

$$L = 10 \times \log_{10}(1 + \frac{\cos(2 \times \theta_c) - 1}{8 \times \theta_c \times \sin\theta}) \quad \textbf{Eq. 7-1}$$

When $\theta_c > \theta$

$$L = 10 \times \log_{10}(\frac{3}{4} - \frac{\sin(2 \times \theta_c)}{8 \times \theta_c} + \frac{\alpha}{4 \times \theta_c}) \quad \textbf{Eq. 7-2}$$

Where

$$\theta_c = \frac{\pi}{2} - \sin^{-1}\frac{n_{cd}}{n_{cr}}$$

is the critical angle, $n_{cd} = 1.5264$ and $n_{cr} = 1.5660$ are refractive index of waveguide cladding and core respectively. θ, is the waveguide crossing angle. All angles are in radians.

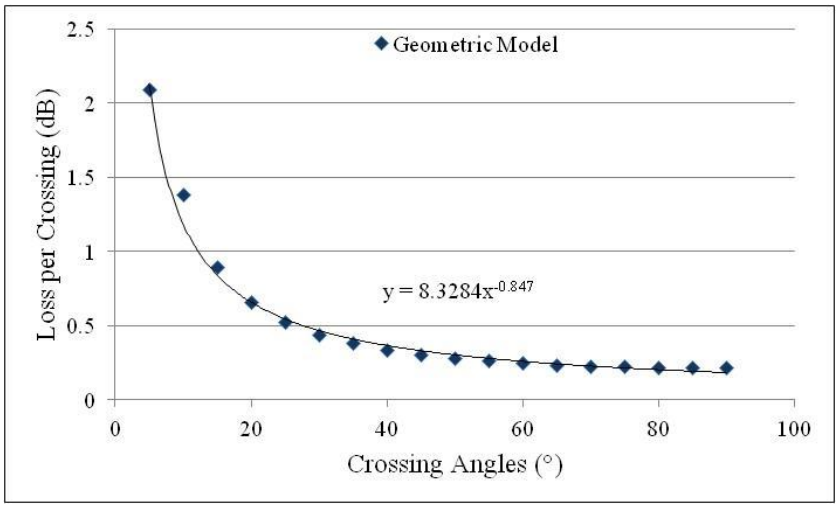

Figure 7-3 Calculated loss per crossing as a function of crossing angle (in degree) using the geometrical model

Crossing angles, θ, were simulated from 10 ºto 90 ºin increments of 5 º. The calculated loss per waveguide crossing as a function of crossing angle (in degrees) is shown in

Figure 7-3. This simulation assumed that the waveguide walls were smooth, the optical power was equally distributed in the two components and the light distribution profile was angularly uniform in the vertical and horizontal planes, respectively. This simple model predicts the trend (best fit curve in Figure 7-3) of the optical loss as a function of waveguide crossing angles. The comparison of the modelled and measured resulted is reported in section 7.4 in this chapter.

7.2.2 Ray Tracing Model

Simulation of waveguide crossing using wave optics has some limitations, in particular with respect to the crossing angle. The amount of memory and calculation time required is significantly increased if one was to solve Maxwell's equations in full vectorial mode. Ray tracing programs require less memory and are much faster (a calculation which takes 2 days in BPM takes 10 minutes in ray tracing (using a computer with Intel i5 2.5 GHz CPU and 8 GB RAM) and there is no limitation on the crossing angle [7-2]. Ray tracing modelling considers light as rays rather than waves and the rays are traced through the system starting from the light source and change direction and intensity distribution [7.6] when they travel through an object with a different refractive index, e.g. a lens or a diffusion surface, e.g. a grating surface. The ray tracing method uses total internal reflection and Fresnel equations to trace the rays and calculates the number of rays and flux that are detected at a desired plane [7-9].

In this chapter the ray tracing modelling was carried out using advanced systems analysis program (ASAP®), although many of the features are commonly found in other ray tracing software such as ZEMAX, and CODE V. Ray tracing models can include waveguide sidewall roughness scattering, but they often do this by increasing the number of rays after each sidewall scattering. This results in an exponential increase in the number of rays and a dramatic slowing down in calculation speed and an increase in memory requirement. Therefore, in this chapter we do not include sidewall roughness but instead modify the divergence of the modelled light source. The waveguide end facet roughness also increases the number of rays, although the effect is not as severe as the waveguide sidewall roughness as rays only scatter once from the end facet. However, as the experimental measurements used refractive index matching fluid at the end facets this effectively removes the end facet roughness and

so it was not necessary to include this in the modelling. It is advisable to round the waveguide corners of the geometry model (a radius of curvature equal to 0.5% of the width of the waveguide was used for the model simulated in this chapter) in ray tracing, as shown in Figure 7-4. The rays will exit from the waveguide side wall intersection because the ray tracing program cannot find a correct medium interface to calculate reflections. The round corners provide a continuous medium interface for the program to conduct calculations according to Snell's law.

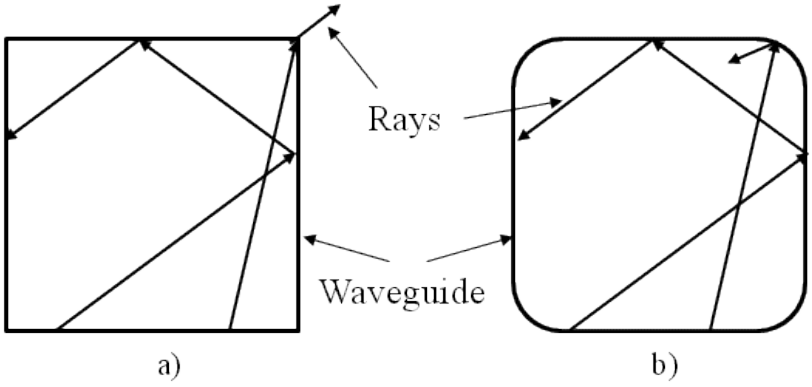

Figure 7-4 Schematic of ray tracing in a waveguide: a) light exiting from a corner of a waveguide with square cross section, b) light reflected at a corner of a waveguide with rounded corners (not to scale)

7.2.2.1 Light Source

The light source used in the experimental measurement was a graded index multimode fibre with a core diameter of 50 μm and numerical aperture NA= 0.22. The output of a VCSEL with centre wavelength 853 nm was coupled into the fibre. The divergence angle had been previously measured at ±7.5 º [7-10] (the detailed measurement is reported in chapter 8). ±7 ºwas chosen to be the divergence angle for all of the light sources. This figure is close to the measured divergence of fibre ±7.5 ºand matched the 7 º ± 1 ºfar-field half divergence angle measured (explained in the section below) from a 10 cm long waveguide. There are 5 different types of light sources (I - V) been modelled using the ray tracing technique. The detailed optical loss measurement of waveguide and waveguide crossings are described in section 7.3.

I. Semi-Empirical Sources

When the NA (0.22) is fully filled in a multimode fibre, the light output profile from the fibre should be Gaussian in angle [7-2]. According to the numerical aperture formula for a waveguide [7-11].

$$NA = nsin\theta = \sqrt{n_{core}^2 - n_{clad}^2} \quad \textbf{Eq. 7-3}$$

$$sin\theta_c = \frac{n_{clad}}{n_{core}} \quad \textbf{Eq. 7-4}$$

Where n is the refractive index of the medium outside the waveguide/fibre and θ_c is the critical angle of the waveguide/fibre. The waveguide had NA = 0.30, which means all the light coupled from the fibre will be guided inside the waveguide. However, the light intensity profile is complicated in a multimode waveguide [7-12]. In order to create a light source model having the best match to the light intensity profile inside the waveguide, David R. Selviah suggested that the far field and near field intensity of the output from a waveguide should be captured by a CCD camera and imported into the ray tracing software for use as the intensity profile of the input source. This technique has never been used before to model a light source in ray trace modelling.

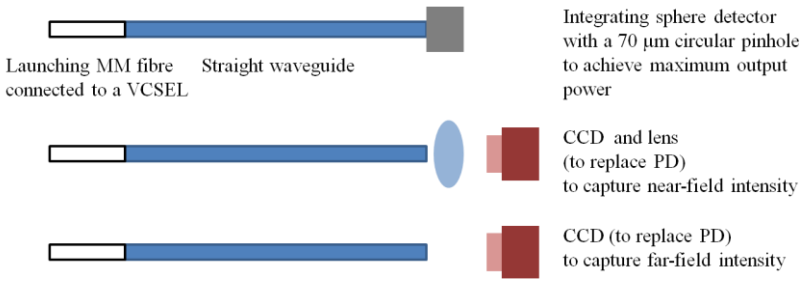

Figure 7-5 Experiment arrangement for far-field and near-field measurement

The experiment arrangement shown in Figure 7-5 was used to capture the output intensity from the waveguide. Index matching fluid (n = 1.5694 ±0.0005 at 589.3 nm) was applied to both ends of the waveguide end facets. The input fibre, waveguide and an integrating sphere photodetector were manually aligned with the aid of translation stages to obtain the maximum output power. When the fibre was aligned with the waveguide and the peak power obtained, the photodetector was replaced by a 25× magnification and NA_{lens}: 0.45 objective lens to image the near field distribution at the exit facet of the waveguide to a CCD camera which was placed after the objective lens

to capture the near field image. According to equitation Eq. 7-5 the resolution of a microscope lens [7-11] is:

$$R = \frac{1.22\lambda}{NA} \qquad \textbf{Eq. 7-5}$$

Where λ is the wavelength of light, R is the resolution of the lens and NA is the numerical aperture of the lens. Therefore, the resolution of the chosen lens was 2.30 μm when NA=0.45 and λ=850 nm were substituted into the equation. This means that any points spaced more than 2.30 μm can be viewed by the 25× microscope lens, which is sufficient for viewing the waveguide cross section 50 μm × 50 μm.

For the far field measurement, the objective lens was removed and the CCD camera was placed 20 mm away from the exit facet of the waveguide. The 20 mm distance between the CCD camera and the waveguide end facet was much larger than the aperture of the waveguide, which was 50 μm, so the field captured was the far field distribution. The sensor sizes of the camera are: horizontal pixel pitch is 8 mm (sensor width) / 720 pixels = 11.1 μm, vertical pixel pitch is 6 mm (sensor height) / 576 pixels = 10.4 μm. A Neutral Density Filter with an optical density of 0.6, refractive index of n=1.51, and thickness of 2 mm was placed in front of the CCD to prevent saturation of the camera. The effective size of the CCD camera was sufficient to capture the whole profile of the output energy field at this point, as 7 degrees divergence at 20 mm away gave 2.45 mm semi radius of an image which was less than the 6 mm height (the shorter side) of the CCD chip. The output from the multimode fibre was set as 0 dBm. Figure 7-6 shows pictures of the far-field and near field profile. The intensity of each pixel of the picture could be represented by a light beam generated from the light source.

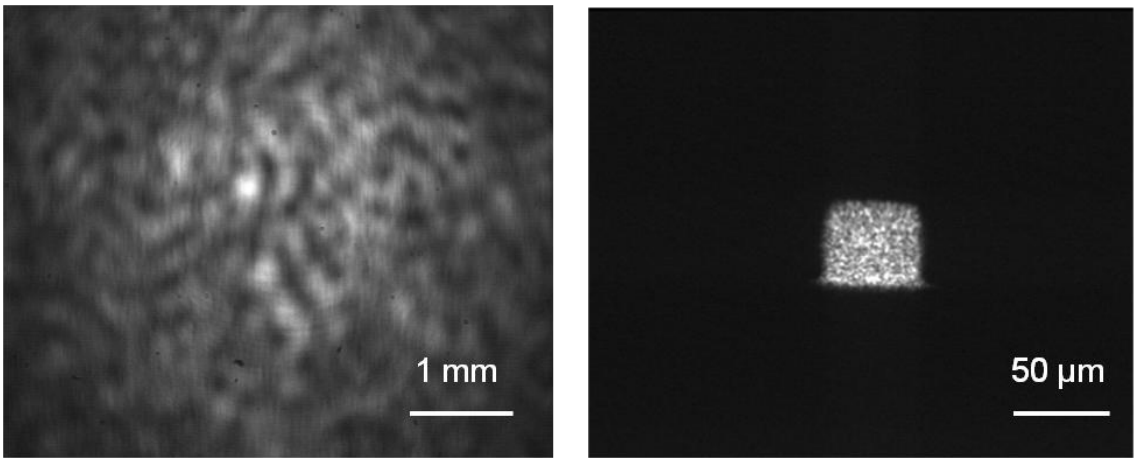

Figure 7-6 (left) Far-field intensity distribution captured using a CCD camera where the silicon sensor of the camera was 20 mm away from the exit facet of a 10 cm, 50 µm × 50 µm straight waveguide; (right) near-field intensity at the exit facet of the waveguide imaged on the CCD camera using a 25× microscope objective lens. NA_{lens}: 0.450 > NA_{wvg}: 0.302

The far-field picture in Figure 7-6 shows speckle, which is due to the interference of multiple overlapping coherently related laser beams in a volume of space such that they add constructively and destructively to give random patterns of bright and dark spots [7-13]. The speckles will be recognized by the ray trace model as discrete high intensity spots after importing the picture to a ray tracing model to create a light source and will consequently reduce the accuracy of the modelling results. It is therefore, important to remove the speckle from the captured intensity profile before importing into the ray tracing model. The technique was to apply a 2D fast Fourier transform (FFT) to the far-field picture and then to apply a suitable filter in the Fourier domain to remove speckle but keep the underlying intensity distribution of the beam undamaged.

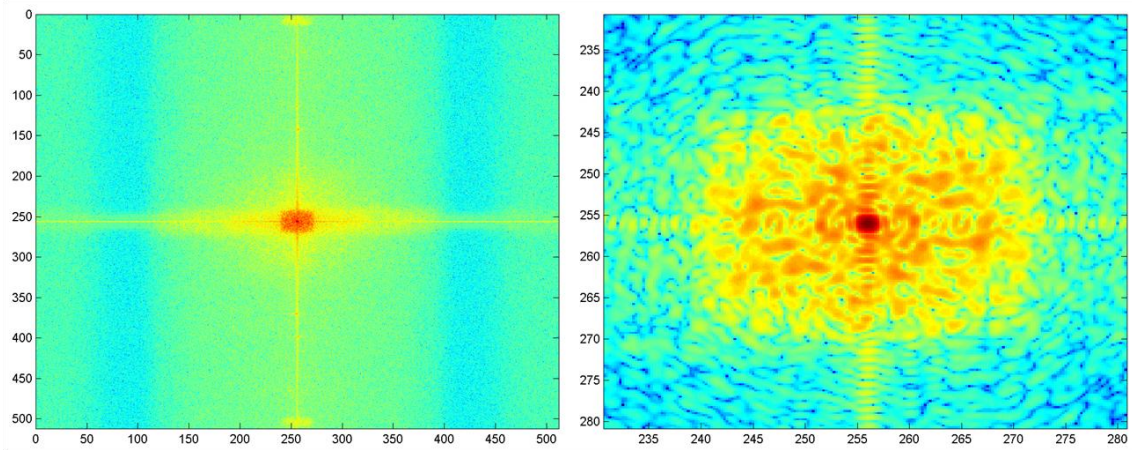

Figure 7-7 FFTed and zero-frequency component shifted far-field image in logarithmic scale (left), zoomed in plot (50 × 50) of the central region of the Fourier domains (right)

Figure 7-7 shows the fast Fourier transformed far-field image after shifting the zero-frequency component to the centre of spectrum. The spacing between speckle spots is about 80 pixels in the spatial domain in Figure 7-6 left and Figure 7-8 left; therefore, the inverse 1/80 is taken to work out the frequency where it appears in the Fourier domain. Similarly, the width of the whole bright region (including most bright speckles) is about 300 pixels. This should appear at 1/300 in the Fourier domain. The centre of the Fourier transformed image corresponds to the sampling frequency and relates to the far-field image width (and height) in spatial domain. The width of the picture in the space domain is 512, so that it should be 1/512 in the Fourier domain. Using the speckle spacing and the diameter of the bright region divided by the image width in the Fourier domain, one is able to work out that the bright region is 1.7 units (number of cycles across the original image width) from the centre and the speckle appears at 6.4 units from the centre. A circular filter was applied between the two values at 2.25 units from the centre to separate out the speckle.

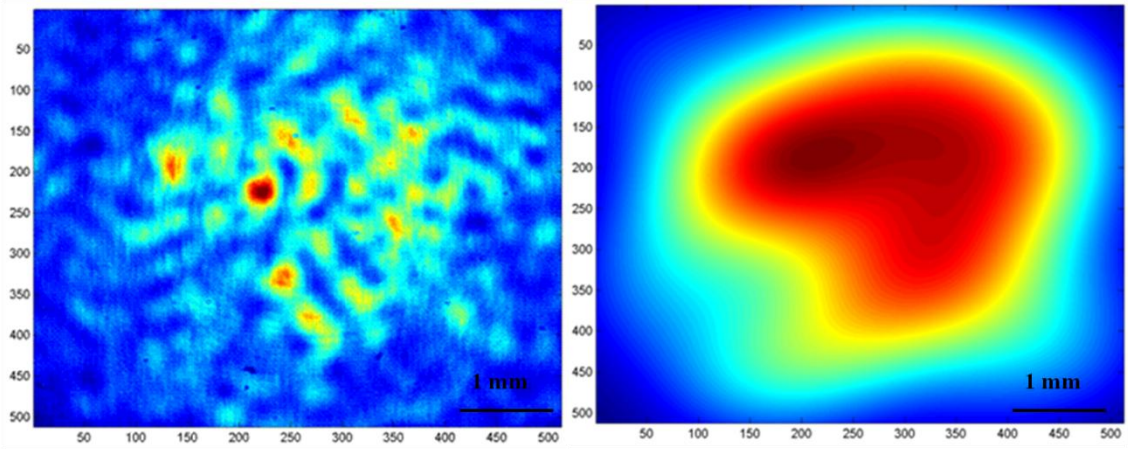

Figure 7-8 Far-field image at 512 × 512 pixels (left) for further image processing; low pass filtered intensity profile applied using a Fourier domain filter.

Figure 7-8 shows the original far-field image at 512 × 512 pixels (left) and the smoothed out speckles in the far-field distribution (right) in which the frequency component of the speckle is filtered out in the Fourier domain and inverse FFTed to get a low frequency intensity profile. The angular divergence of the light exiting from the waveguide was calculated by performing the following two steps: Firstly, the distance from a pixel to the centroid pixel in the far field image was calculated using Eq. 7-6

$$d_{i,j} = \sqrt{\left(i_c - i_p\right)^2 + \left(j_c - j_p\right)^2} \quad \textbf{Eq. 7-6}$$

where $d_{i,j}$ is the distance between the centroid point (i_c, j_c) and a pixel position (i_p, j_p).

Secondly, the divergence angle can be calculated according to Eq. 7-7.

$$\theta_{i,j} = \tan^{-1}\left(\frac{d_{i,j}}{D}\right) \quad \textbf{Eq. 7-7}$$

Where *D* is the distance between the CCD camera sensor and the exit facet of the waveguide. The angular profile calculated from the processed far-field image was used in ASAP to define the propagation directions of the light source. A square shape near-field profile was created in the computer model and weighted the intensity of each ray according to the angular profile to match the measured far-field profile. Figure 7-9 shows the intensity profile of the light source created in ASAP using the filtered far-field intensity profile.

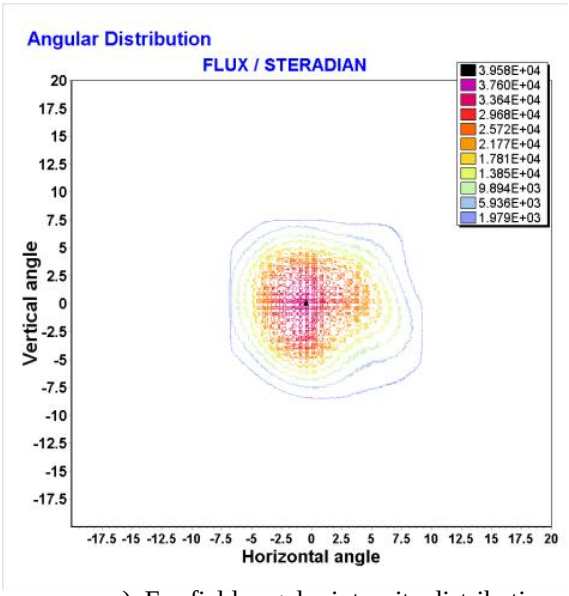

a) Far-field angular intensity distribution

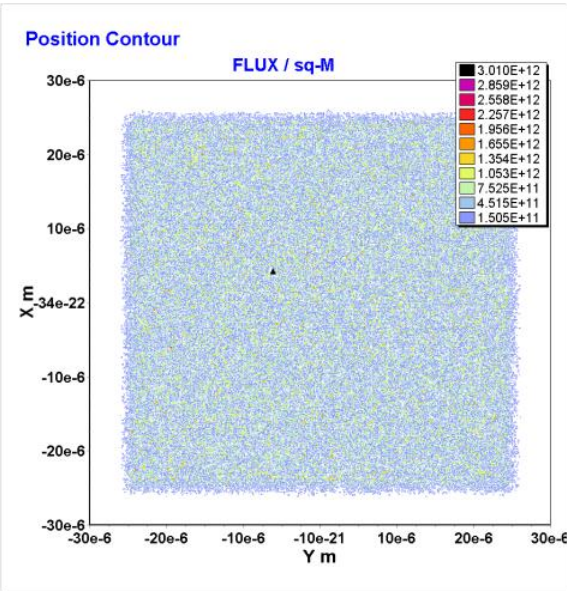

b) Near-field spatial intensity distribution

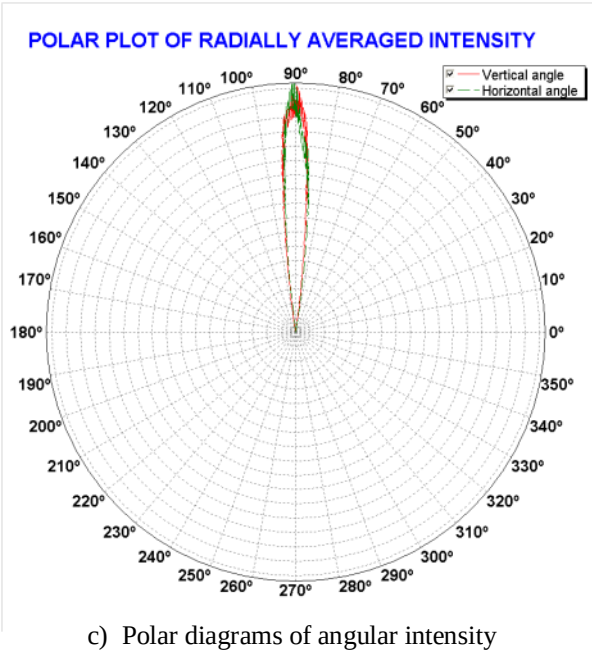

c) Polar diagrams of angular intensity distribution of the centre cross-sections on vertical and horizontal directions

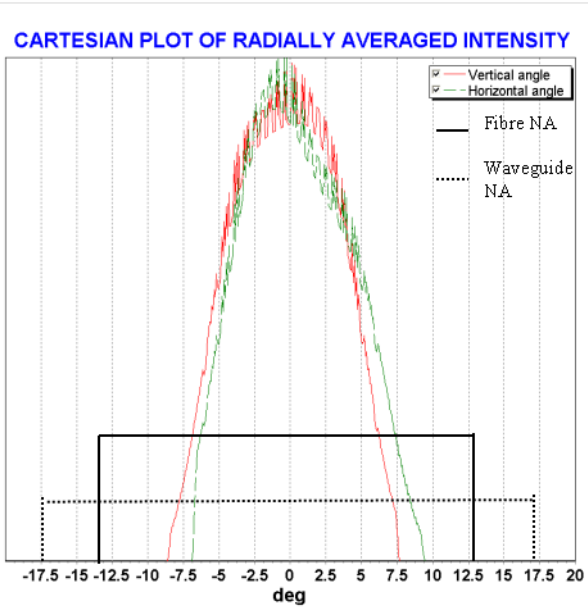

d) Cartesian diagrams of angular intensity distribution of the centre cross-sections on vertical and horizontal directions

Figure 7-9 Intensity profile of a ray trace simulated light source using the data from the capture near-field and far-field intensity. 0 °corresponding to the centroid of the far-field angular profile

Figure 7-9d is far-field of the 0.3 NA waveguide used in the experiment with an input of an 850 nm VCSEL launched via a graded index 50/125 μm fibre. The 7 °± 1 °far-field half divergence angle of the waveguide was measured at $1/e^2$ of the maximum value.

Three simpler alternative light source models were investigated, in order to find a general method for modelling the light source for multimode waveguides.

II. Point source

A point source emits light from a point which passes through a uniform spacing grid. This point source and grid combination define a set of rays that generally has a uniform distribution in 2D space. The grid could be either circular or rectangular and was divided into small square sub-areas depending on the designed resolution, i.e. number of rays. Each sub-area on the grid defines the spatial coordinates of a ray generated from the emitting point. Figure 7-10 shows the side view and top view of a 5×5 point source structure.

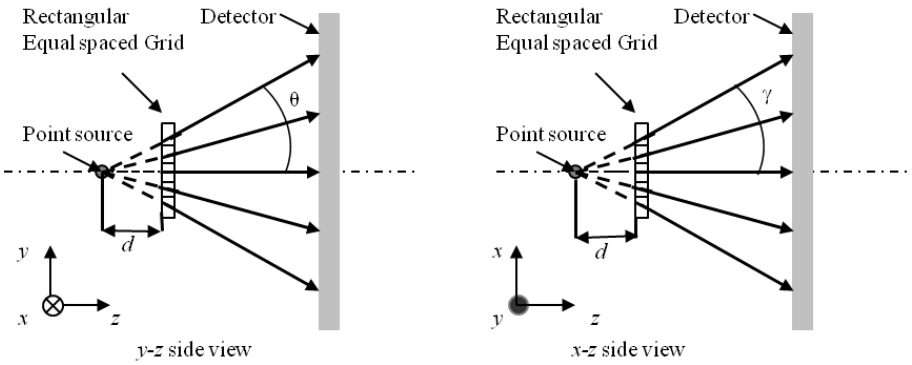

Figure 7-10 Schematic structure of a point source

The distance, d, between the point source and the grid was calculated so that the angular divergences θ and γ along the y and x axes, respectively were 7 º. Figure 7-11 shows the intensity contour plots, polar and Cartesian diagrams of the point source. Figure 7-11a and Figure 7-11b are the angular and spatial intensity distribution of the point source with ±7 º divergence. Figure 7-11c and Figure 7-11d are the angular intensity distribution of the centre cross-sections of vertical and horizontal directions and are shown in both the polar and in the Cartesian diagrams. The angular intensity distributions along the two directions were identical; therefore, the intensity plots were overlaid in both of the polar and Cartesian diagrams.

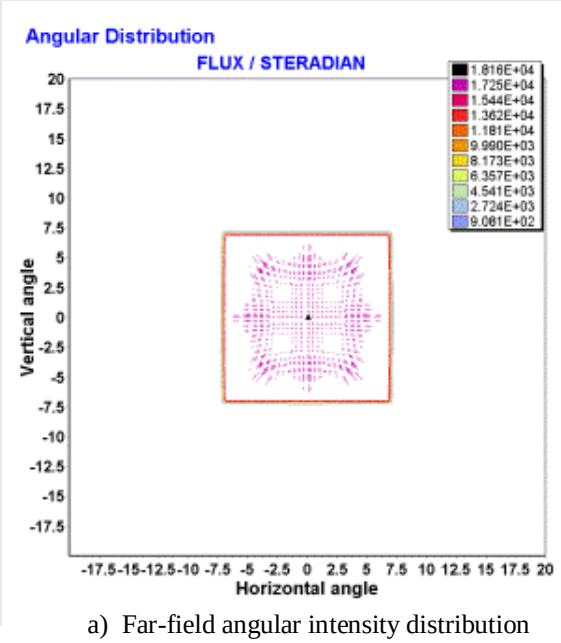

a) Far-field angular intensity distribution

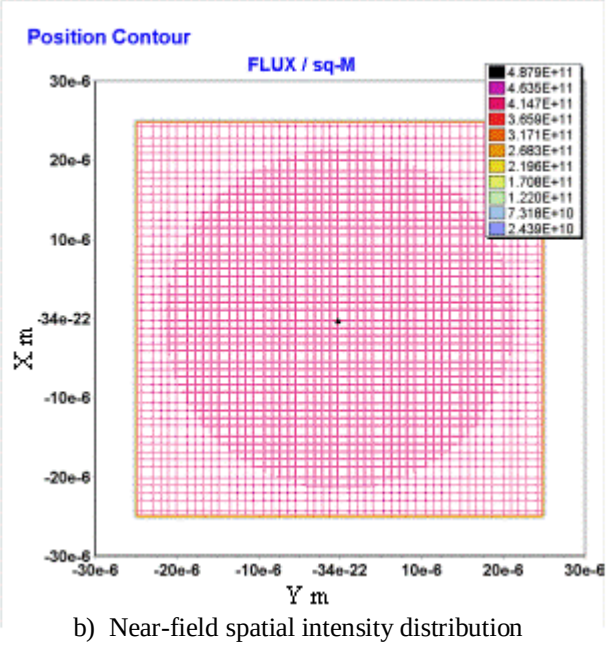

b) Near-field spatial intensity distribution

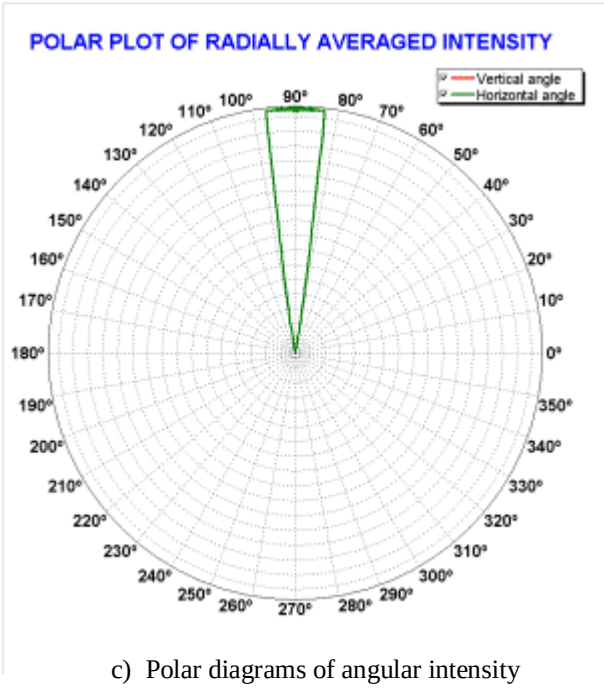

c) Polar diagrams of angular intensity distribution of the centre cross-sections on vertical and horizontal directions (overlaid)

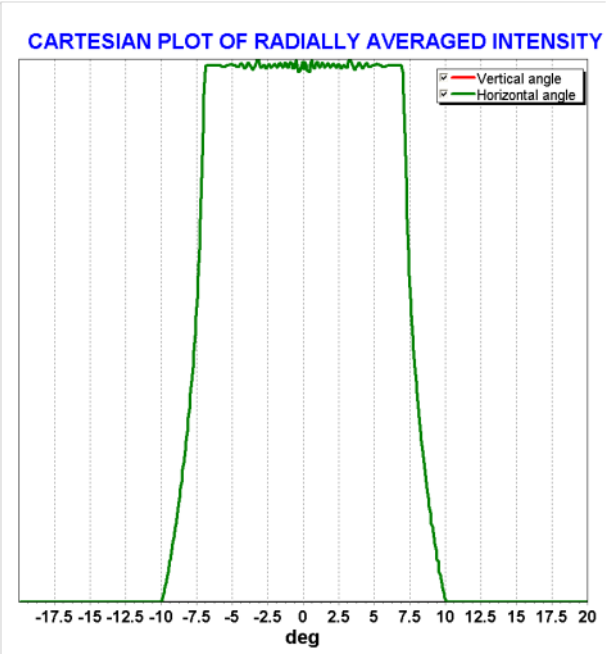

d) Cartesian diagrams of angular intensity distribution of the centre cross-sections on vertical and horizontal directions (overlaid)

Figure 7-11 Intensity profile of a point light source with ±7 °divergence

III. Emitting Surface Source

An emitting surface produces a random set of rays distributed over an arbitrary plane. Figure 7-12 shows a set of rays with an equal probability of pointing in any direction and keeps almost constant intensity within ±7 º. The intensity drops sharply from 98% of the maximum level to 0 between 7 ºto 7.5 º.

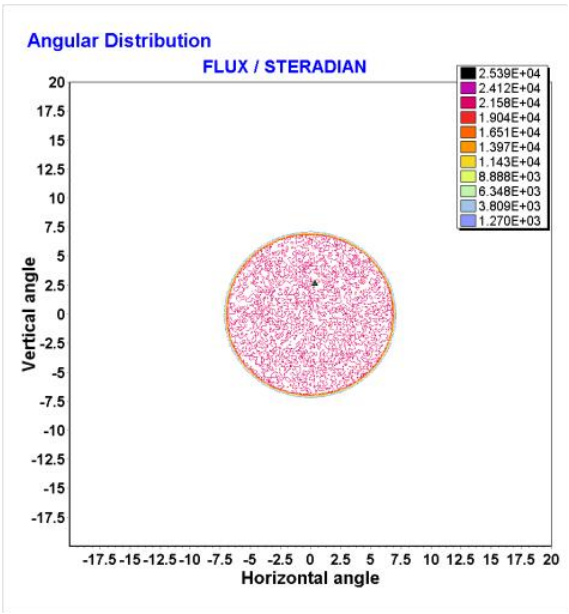

a) Far-field angular intensity distribution

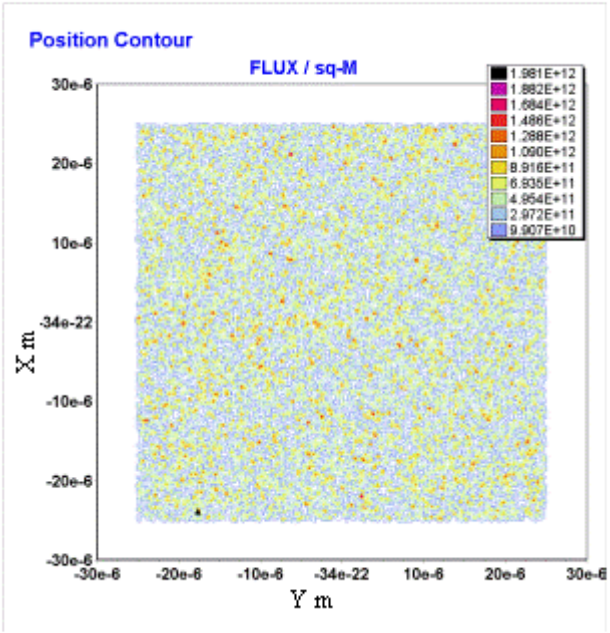

b) Near-field spatial intensity distribution

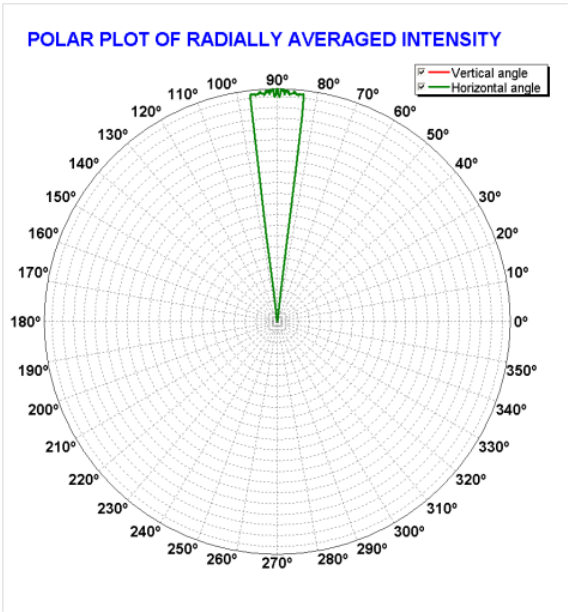

c) Polar diagrams of angular intensity distribution of the centre cross-sections on vertical and horizontal directions

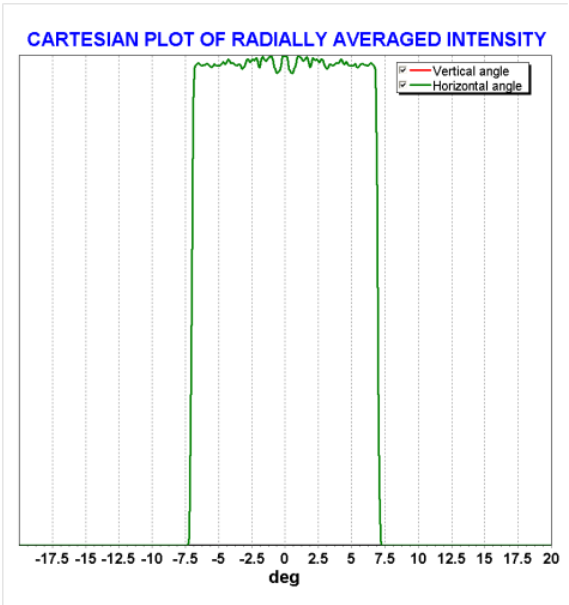

d) Cartesian diagrams of angular intensity distribution of the centre cross-sections on vertical and horizontal directions

Figure 7-12 Intensity profile of an emitting surface

IV. Gaussian Source

Both the point source and emitting surface sources are nearly angularly uniform and have flat top intensity profiles which decease from the maximum value to the minimum sharply at around 7 º. Such an intensity profile does not closely match the measured output from the waveguide, as shown in Figure 7-9. A Gaussian distributed source with a 7 ºangular half divergence (Figure 7-13) was created.

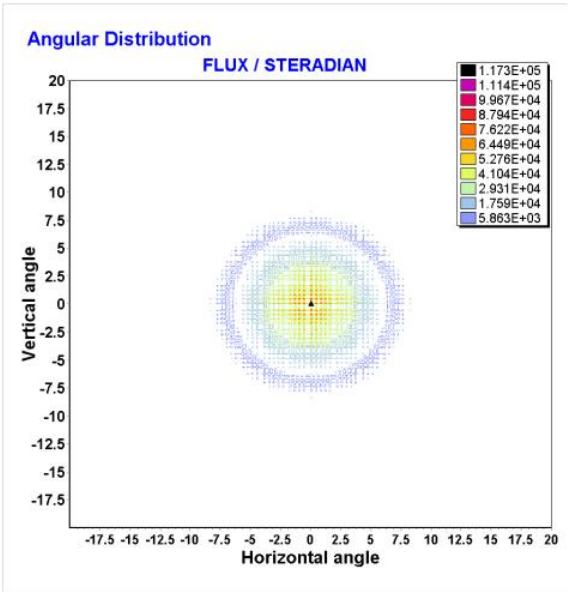

a) Far-field angular intensity distribution

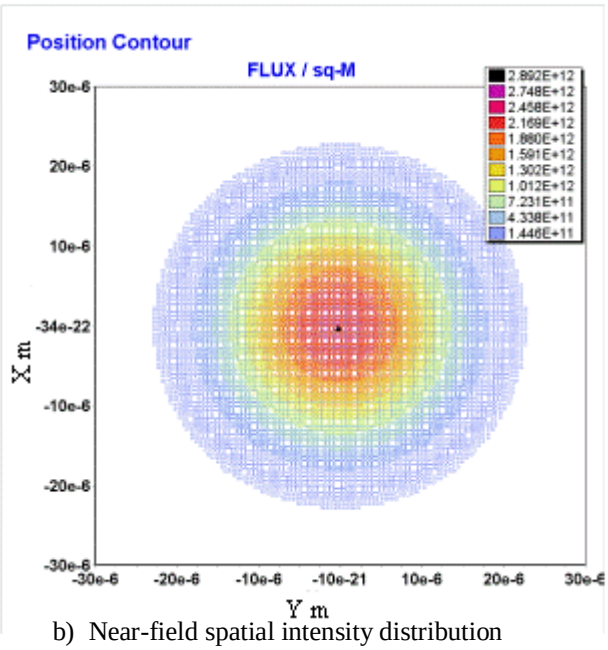

b) Near-field spatial intensity distribution

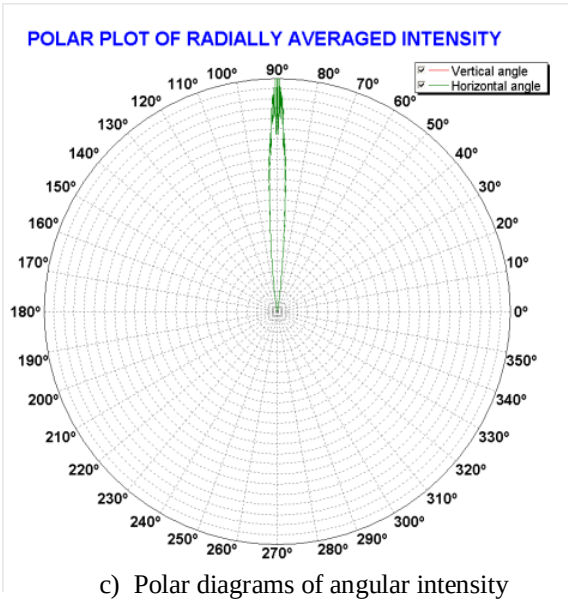

c) Polar diagrams of angular intensity distribution of the centre cross-sections on vertical and horizontal directions

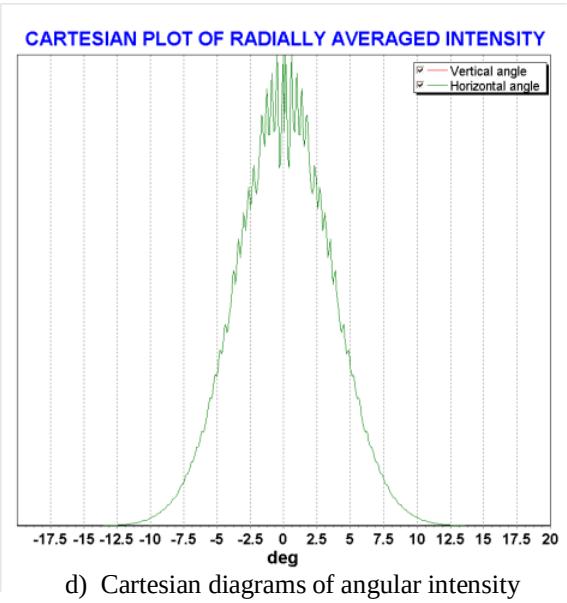

d) Cartesian diagrams of angular intensity distribution of the centre cross-sections on vertical and horizontal directions

Figure 7-13 Intensity profile of a Gaussian source

V. Diagnostic Sources in Modelled Waveguide with Realistic Cross Section Shape

The captured CCD image of the near-field Figure 7-6 shows that the shape of the waveguide is not square, but is close to a trapezium shape with triangular tails at the bottom two corners and rounded top two corners, as shown in Figure 7-14. The non square shape of the waveguide may have an influence on the optical loss of the waveguide and light distribution inside the waveguide. A waveguide model with the real cross section shape of the measured waveguide was created in ray trace model by digitising the outline of the waveguide shape from the near-field picture to analyze the influence caused by the waveguide shape.

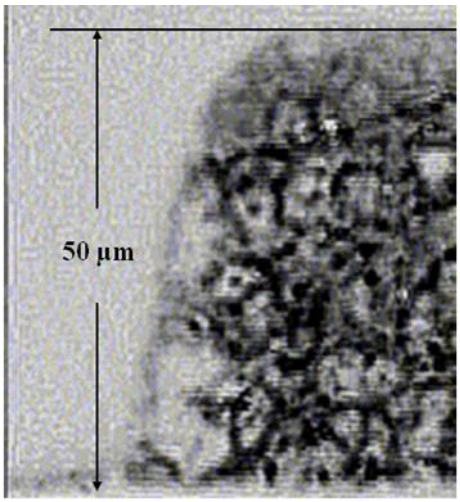

a) Picture of one side wall of a waveguide

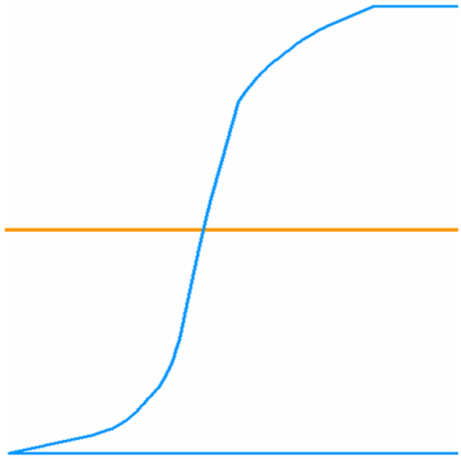

b) Realistic cross section shape Waveguide model matches the shape of the waveguide

Figure 7-14 Computer model of cross-section of the waveguide

Two diagnostic sources were created; one has only horizontal divergence (Figure 7-15) and the other has only vertical divergence (Figure 7-16). The horizontal source only reflects from the two sloped side walls of the waveguide in order to diagnose the light propagation behaviour affected by the shape of the waveguide. The vertical source only reflects from the top and bottom flat parallel surfaces of the waveguide and should not deflect much on the side walls for the vertically angular source, in order to diagnose the light reflected between two flat surfaces. It gives us a much deeper understanding of the physics of propagation of light in polymer waveguides by using two diagnostic sources.

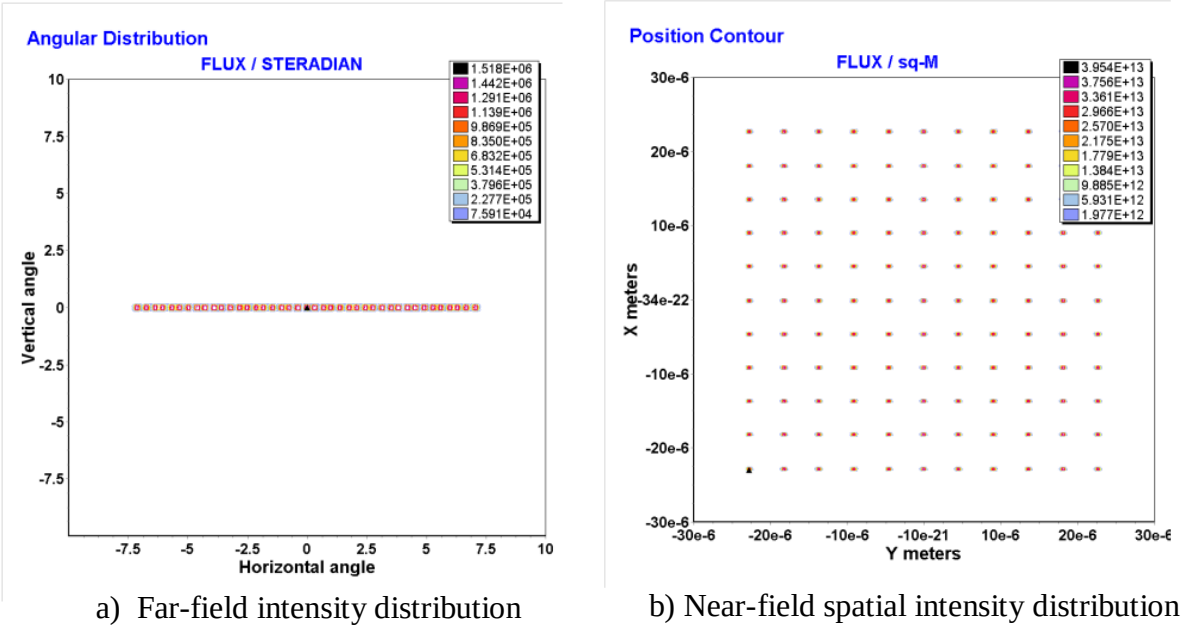

a) Far-field intensity distribution b) Near-field spatial intensity distribution

Figure 7-15 Intensity profile of a diagnostic source has horizontal divergence at the entrance of waveguide

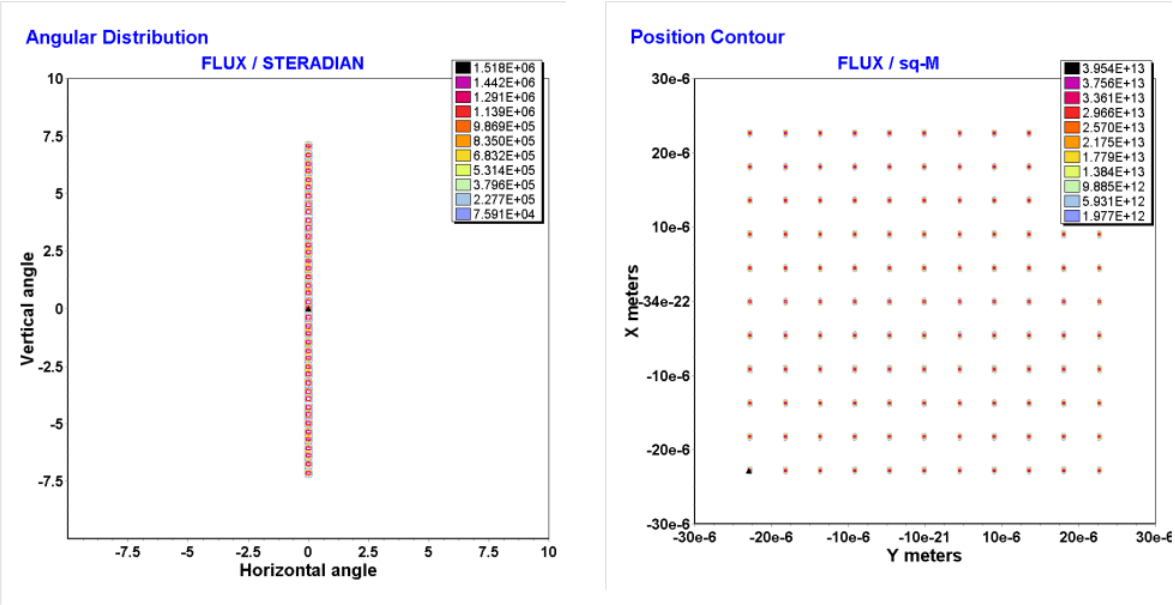

a) Far-field intensity distribution b) Near-field spatial intensity distribution

Figure 7-16 Intensity profile of a diagnostic source with vertical divergence at the entrance of the waveguide

The diagnostic source with horizontal divergence and vertical divergence were put at the input of a 10 cm long waveguide respectively and the simulated output far-field and near-field intensity profile are shown in Figure 7-17 and Figure 7-18.

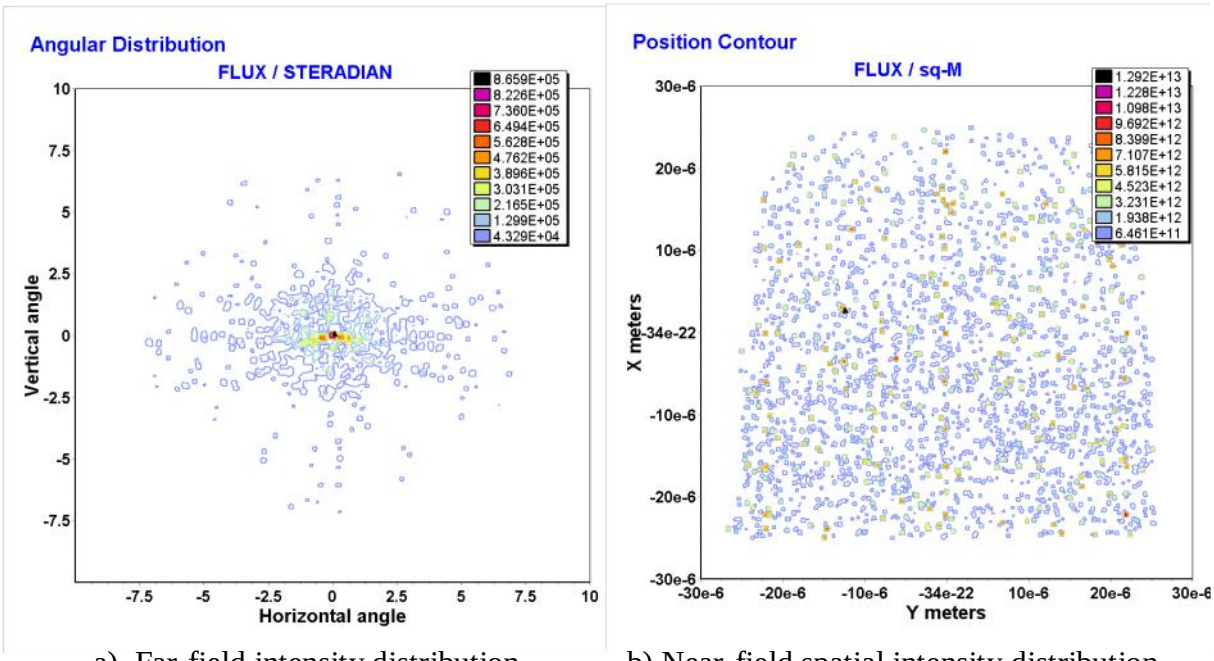

a) Far-field intensity distribution b) Near-field spatial intensity distribution

Figure 7-17 Simulated intensity profile at the exit of a 10 cm long waveguide using the horizontally divergent diagnostic source as input

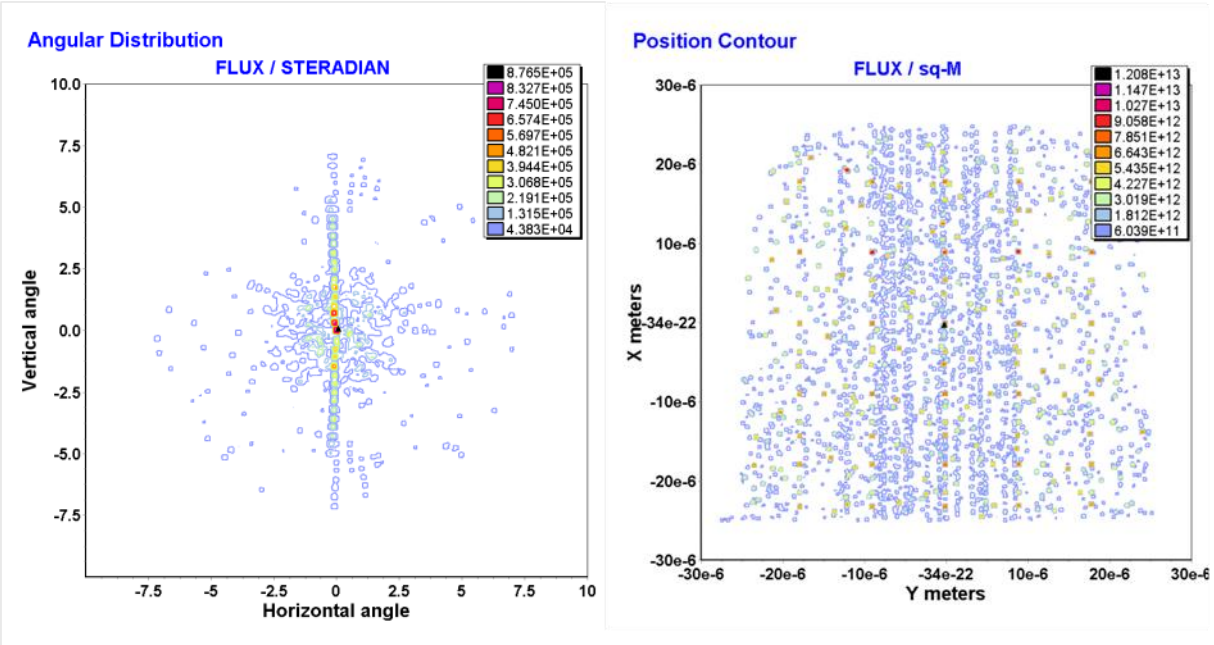

a) Far-field intensity distribution b) Near-field spatial intensity distribution

Figure 7-18 Simulated intensity profile at the exit of a 10 cm long waveguide using the vertically divergent diagnostic source as input

As shown in Figure 7-17a, the angular intensity contour plot shows the angle of the horizontal angular intensity which shows that higher than 20% of the maximum flux/steradian has reduced to ±2.5 º. A number of radial lines can be seen along which

there is higher intensity indicate that some light has changed its propagation direction due to the sloped waveguide side wall. A few high intensity spots can be seen close to the centre horizontal line aligned along a slightly curved line with two ends pointing to the bottom of the waveguide. It can also be noticed in Figure 7-17b that most of the light is trapped towards the bottom of the waveguide. The shape of the tapering region at the bottom of the waveguide where its sidewalls meet the top of the lower cladding is clearly shown. Due to the shape of the waveguide light could reflect repeatedly, moving towards the bottom of the waveguide and the tapering tip on each side where it would then escape, leading to propagation loss.

As shown in Figure 7-18a, the far field plot shows that most of the light maintained the vertical angular distribution but slightly weakened towards the top and bottom, causing the divergence angle to reduce to $\pm 5^{\circ}$. The light should reflect from the top and bottom flat surfaces of the waveguide and not deflect much to impinge on the side walls for the vertically angular source. However, the size of the input source is 50 µm $\times$ 50 µm the same as the size of the cross section of the waveguide. Any light reflected from the two curved top corners will be deflected to a different direction. There are a number of high intensity spots, 4 on each side along the original line of the source, with a horizontal divergence about $\pm 2^{\circ}$. In the near field plot Figure 7-18b, the power has concentrated in the central region between the top and bottom waveguide flat surfaces, as expected, due to multiple reflections between the two parallel surfaces.

7.2.2.2 Comparison of Modelled Light Sources

We simulated the behaviour of the light sources from I to IV modelled in section 7.2.1.1 after they propagated through a 10 cm long square cross section and a 10 cm long realistic shape cross section waveguide, respectively. The far-field intensity profile from waveguides obtained from measurement was processed using 2D FFT to smooth out the speckle and was used to define the angular divergence of a ray trace light model. The angular profiles of each modelled light source were compared with the captured far-field image to calculate the RMS and standard deviation in 2 dimensions to find the best matched light source to the measured one.

Table 7-1 Angular distribution profiles of measured and modelled light sources after propagation through waveguide

	Cross section	Full angular divergence (degrees)						
Intensity level relative to the maximum point		**20 dB**	**1/e^2**	**1/e**	**3 dB**	**1 dB**	**std**	**rms**
Measured output from a straight waveguide	x	15.9	14.1	11.7	10.4	7.3		
	y	15.8	14.7	11.9	10.4	5.6		
Ray trace light source through a square cross section waveguide								
Point	x	21.0	19.1	16.6	15.5	12.6	0.18496	0.3325
	y	21.0	19.1	16.6	15.5	12.7		
Surface emitter	x	19.6	17.6	15.2	14.0	11.0	0.15693	0.22616
	y	19.6	17.6	15.2	14.0	11.0		
Gaussian	x	23.0	14.8	10.4	8.7	4.9	0.12031	0.21776
	y	23.0	14.8	10.4	8.7	4.9		
Semi-empirical	x	18.8	15.1	11.5	9.8	5.8	0.10487	0.10986
	y	19.2	15.2	11.5	9.8	5.8		
Ray trace light source through a realistic cross section waveguide								
Point	x	21.3	19.0	16.3	14.9	11.2	0.17974	0.30760
	y	21.0	19.0	16.6	15.4	12.7		
Surface emitter	x	19.1	17.1	14.6	13.2	9.9	0.14730	0.21350
	y	19.0	17.3	14.9	13.8	11.0		
Gaussian	x	23.2	14.1	10.1	8.4	4.8	0.12075	0.14539
	y	20.7	14.7	10.7	8.9	5.2		
Semi-empirical	x	19.2	15.3	11.6	9.8	5.9	0.10609	0.10893
	y	19.2	15.4	11.6	9.9	5.9		

Table 7-1 shows the angular full width at different intensity levels of each light source after propagating through two types of waveguides (square and realistic cross section). The semi-empirical source created by using the intensity profile from the captured image offers the smallest divergence at all of the 5 intensity levels and has the lowest RMS and standard deviation errors, which indicate that it is the best match to the measured light source. The Gaussian source with a 7 °angular semi-divergence has the lowest angular divergence in most of the intensity levels with nearly 90% (column for $1/e^2$) of the total energy confined in a maximum 14.8 °cone. The point source has the widest divergence and least match to the measured one.

7.2.3 Waveguide Crossing Simulation Using Ray Trace Method

The simulated structure is a channel waveguide with a cross-section of 50 μm × 50 μm. The wavelength of the source is 853 nm and the refractive indices of the core and the cladding are 1.5560 and 1.5264 respectively [7-14]; the simulation parameters were chosen to be as close as possible to the manufactured waveguide for comparison with the experimental results. Figure 7-19 shows a schematic of a waveguide with a crossing and a straight reference waveguide which was used to calibrate the loss caused only by the crossings.

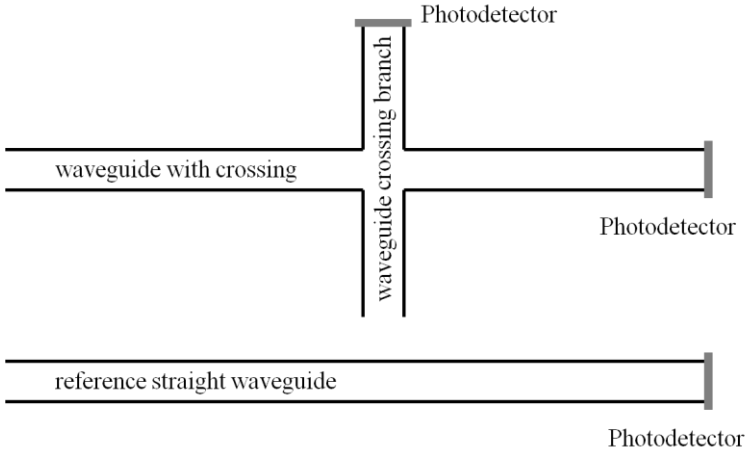

Figure 7-19: Schematic of a waveguide with a crossing and a straight reference waveguide

The modelled light sources (I to IV) were used individually to simulate the optical loss due to the waveguide crossing and to verify the performance of each source. The length of the modelled waveguides was 10 cm and the source was touching the entrance of the waveguide. The crossing waveguide branch intersected at the centre of

a straight waveguide. Three photo-detectors were modelled: two were placed at 1 μm away from the exit surfaces of each of the reference straight waveguide and the waveguide with a crossing to capture the output optical power; one was placed at the exit surface of the waveguide crossing branch to monitor the crosstalk. The power was calculated by counting the total flux of rays absorbed by the detector. The input flux of each type of the source was set to be 1000 and around 1,000,000 rays were generated from each source. The waveguide crossings were simulated at crossing angles in a range from 10° to 90° in steps of 10 °.

7.2.3.1 Simulation of Waveguide Crossing Loss in the Waveguide with Square Cross Section

Figure 7-20 shows the results of the ray tracing simulation of the waveguide crossing loss at various crossing angles through the square cross section waveguide. The angular divergence of each light source was chosen to be ±7 °and the optical loss per crossing was calculated by subtracting the output flux of the waveguide with crossing and the reference straight waveguide for every crossing angle.

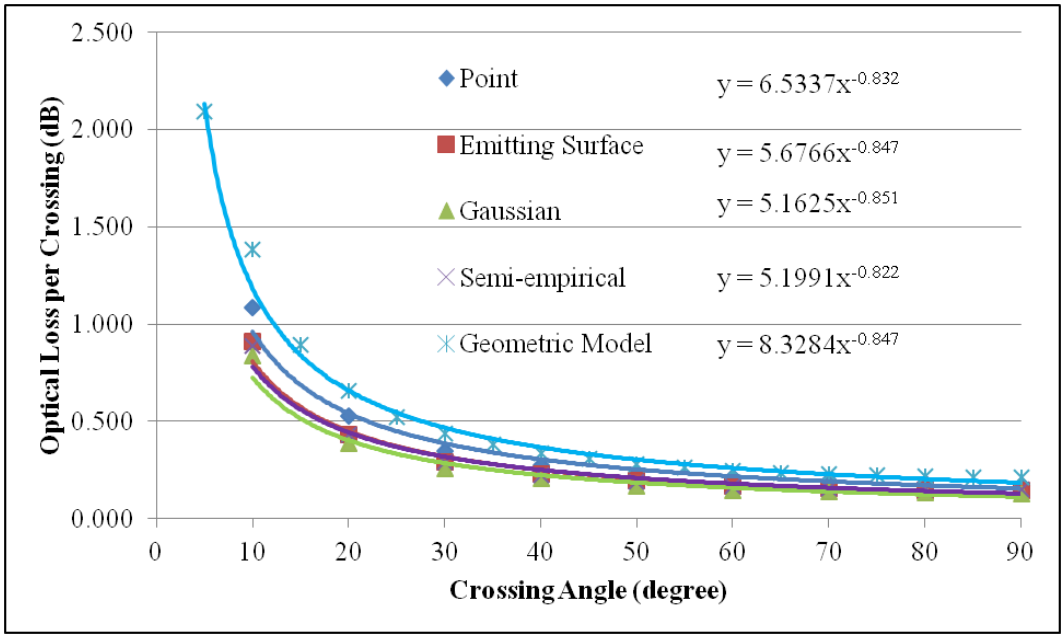

Figure 7-20: Ray tracing results of crossing loss of square crossing waveguides with different crossing angles

The Gaussian light source had the lowest loss per crossing at all angles. This was expected, as the Gaussian source had the lowest divergence according to Table 7-1,

therefore, fewer large angle rays representing higher order modes could escape from the waveguide when travelling through a crossing. The results from the emitting surface and the semi-empirical sources were quite close to each other and were just on average 0.03 dB higher than the Gaussian one. The point source gave the highest loss per crossing with 1.08 dB loss at 10 ºand 0.17 dB at 90 º.

7.2.3.2 Simulation of Waveguide Crossing Loss in the Waveguide with Realistic Cross Section

A waveguide model with realistic cross section shape of the experimentally measured waveguide was created (Figure 7-21) to assess the crossing loss.

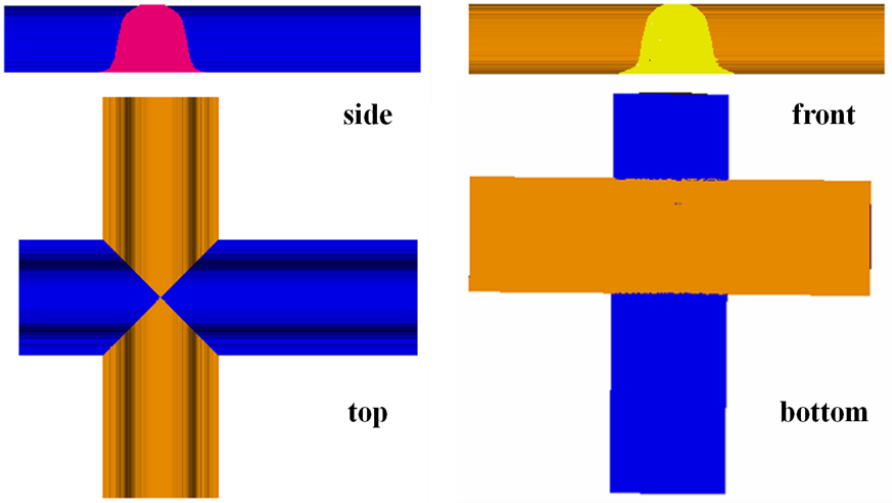

Figure 7-21 Different viewing angles of a realistic cross sectional shape waveguide model

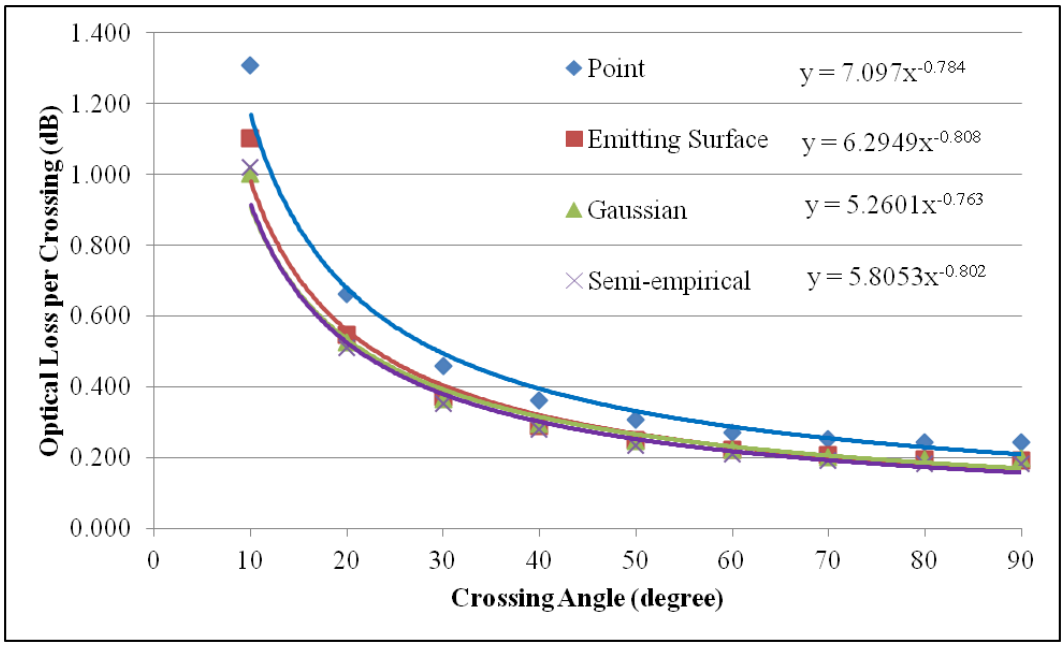

Figure 7-22: Ray tracing results of crossing loss of realistic cross section shape crossing waveguides with different crossing angles

Figure 7-22 shows the simulated results of waveguide crossing loss of the realistic cross section shape waveguide at various crossing angles. The simulation conditions were kept the same as the ones used for the square waveguide simulation. The optical loss at each crossing angle was higher than that obtained from the square waveguide. The loss simulated using the Gaussian light source gave the lowest loss per crossing at all angles. The results from the emitting surface started to match with them after 30 º. The point source still had the highest loss per crossing compared to other light sources.

7.2.3.3 Simulation of Crosstalk from the Waveguide Crossing Branch

The flux of any rays propagated through the waveguide crossing branch was calculated as well. According to Table 7-2, the simulated optical loss per crossing from realistic cross section shape waveguides is slightly lower than that calculated from the square waveguides at 10 ºcrossing. However, crosstalk had also appeared at 20 ºcrossing in the realistic cross section shape waveguide, although they were below, 35 dB in all light source cases. The simulated crosstalk was only detected at 10 º crossing in the square waveguide. The simulated results indicated that the realistic cross section shape waveguide had higher crossing loss and more crosstalk at 20 º crossings.

Table 7-2 Simulated crosstalk using 4 types of light sources

	Crossing angle (degree)	Crosstalk (dB)			
		Point	Emitter	Gaussian	Semi-empirical
Square waveguide	10	-9.427	-9.777	-10.038	-10.026
Realistic cross section waveguide	10	-9.015	-9.243	-9.800	-9.808
	20	-39.358	-36.212	-36.275	-38.914

7.3 Experimental measurement

An ST connectorized VCSEL laser (STVXCEL-850 supplied by Access Pacific Limited) was connected to a 10 m standard 50/125 μm grade index multimode fibre with NA_{fibre}: 0.200 less than the waveguide NA_{wvg}: 0.302. All the light exited from the fibre should be coupled into the waveguide when they are aligned to each other, therefore, the coupling loss should be minimal. Both the input source and PD were mounted on high precision motorized translation stages for accurate alignment and sub-micron step adjustment to maximize the light through the waveguide. The fibre was then butt-coupled to one of the waveguides to be measured. A 70 μm pinhole was used in front of an integrating sphere photo-detector to exclude much of the light travelling through the cladding. The large area integrating sphere PD was placed after the output pinhole to measure the integrated output optical power so avoiding inconsistencies due to laser speckle and spatial variation of efficiency across the photodiode detector. Index matching fluid (n = 1.5694 ± 0.0005 at 589.3 nm) was applied to both MM fibre to waveguide and waveguide to pinhole interfaces to reduce coupling loss. Crossing angles were measured from 10° to 30° in increments of 5°, and 40° to 90° in increments of 10°, giving 11 crossing angles in total.

Figure 7-23 shows a schematic of a waveguide, *I*, with a set of 6 crossings at a crossing angle, θ, and a reference waveguide, *II*, which was used to exclude all the optical losses from the experiment results by subtracting the total insertion loss from the two waveguides *I* and *II* to leave the optical loss caused by the crossings only. The

design of the layout allows us to measure crosstalk from the crossing branches and stops the light in the cladding getting to the photodetector. This was a new layout never used before designed by a former team member, Guoyu Yu, in the Optical Devices and Systems laboratory of the Photonics Research Group at UCL and was measured by Guoyu and the author.

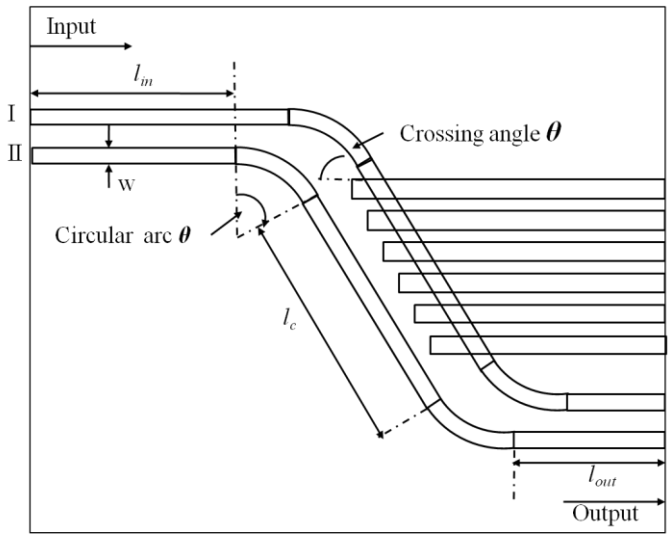

Figure 7-23: Schematic of a waveguide with a set of 6 crossings and a straight reference waveguide

The reference waveguide had the same shape, i.e. same circular arc, θ, and radius, and the same total length as the waveguide with crossings. Therefore, the optical power loss (in dB) detected at the end of the waveguide with crossings subtracted from the optical loss detected at the end of the waveguide without crossings was purely caused by the 6 waveguide crossings. The optical loss for each crossing angle was measured 50 times to reduce the error bar by averaging 50 measurements. The mean value of the optical loss for each crossing angle in the 50 measurements was divided by 6 to find the optical loss per crossing. This assumed that the loss was caused equally by each of the waveguide crossings. Figure 7-24 shows the measured optical loss per crossing versus the crossing angles.

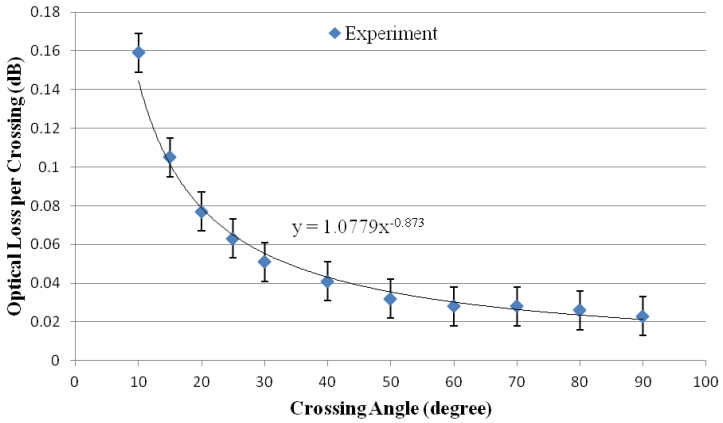

Figure 7-24: Experiment results for the optical loss per crossing for different crossing angles

The power output from all 6 crossings was measured in a similar way: the large area integrating sphere PD attached the 70 μm circular pinhole in the front was placed at exit facet of the waveguide crossing branch to measure and assess crosstalk. Index matching fluid was also applied at the waveguide-PD interface. We could only detect output from the waveguide branch at 10 ° intersect angle by using the PD with -55 dBm sensitivity. The measured crosstalk from the 6 waveguide crossing branches along the light propagation direction is shown in Figure 7-25 below.

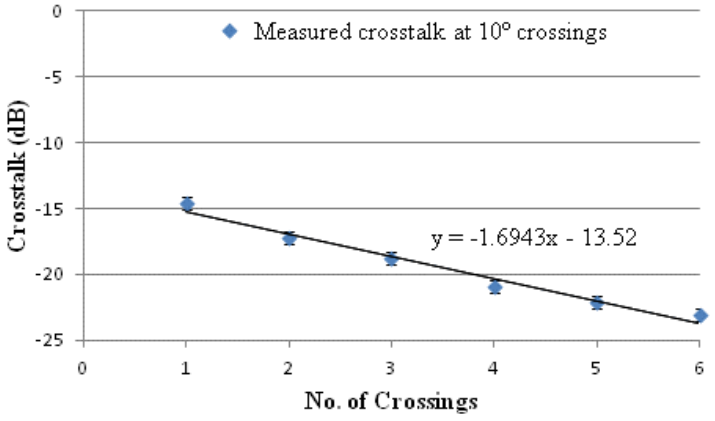

Figure 7-25 Measured crosstalk from 6 crossing branches at 10 degree crossing, a linear line is fitted within the error bar of the measurement

The measured crosstalk decreased linearly from -14.6 dB at the 1st crossing to -23.1 dB at the 6th crossing as the light propagated along the main waveguide.

7.4 Comparison between ray tracing results and experiments

Figure 7-26 and Figure 7-27 show the ray tracing simulation results and the experimental results. The simulation results predict a higher optical loss for all crossing angles.

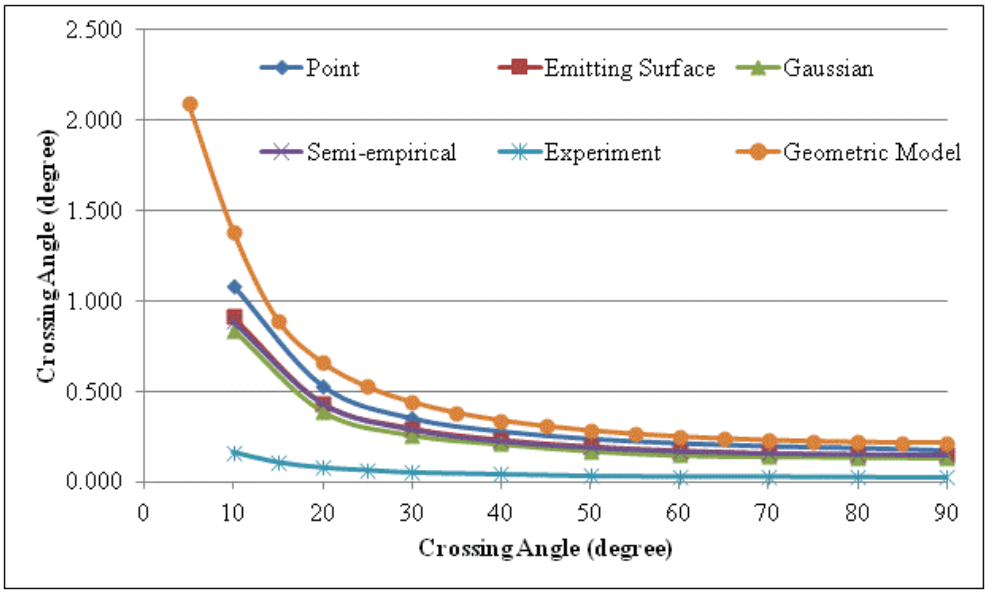

Figure 7-26: Optical crossing loss as a function of the angle of the crossing for ray tracing models with different light sources compared to the experimental result of a square cross-section waveguide

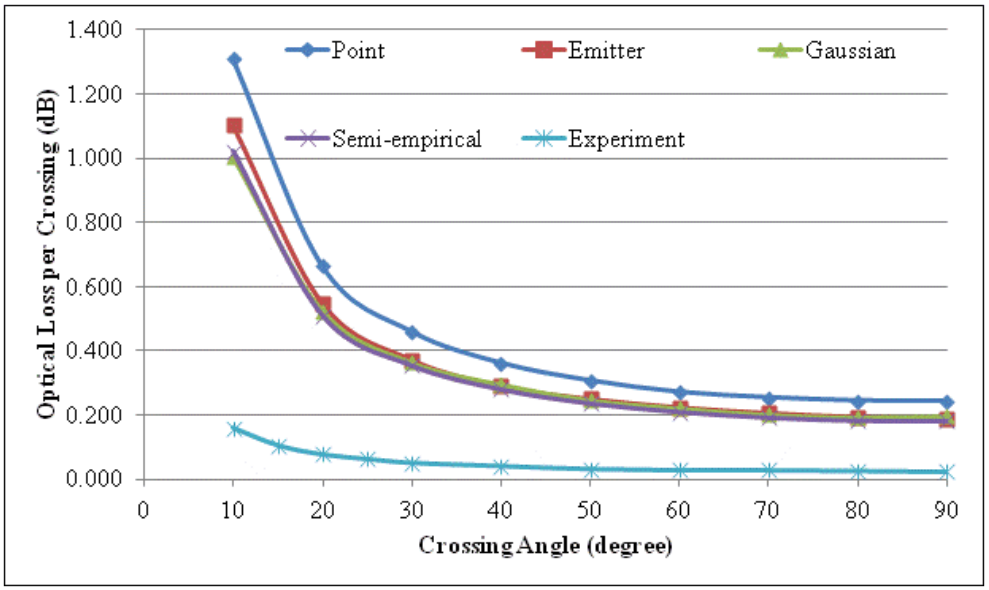

Figure 7-27: Optical crossing loss as a function of the angle of the crossing for ray tracing models with different light sources compared to the experimental result of a realistic cross-section waveguide

There were some differences between the simulations and the experiments; for example the actual waveguide shape. However, the modelled results indicated that the irregular shape of the waveguide would cause more loss. The existence of wall roughness in the fabricated waveguides would cause scattering to radiation modes which were at angles less than the critical angle of the waveguide with respect to the normal on the waveguide sidewalls and were lost. Therefore, only rays with low order modes propagate through the waveguide.

To simulate the low order mode inside the waveguide the divergence of the source was reduced to find the best match to the experiment results. A Gaussian source was chosen to perform the test and the divergence angle needed to be as low as ±2.86 ºin order to achieve the match. The results are shown in Figure 7-28 where the simulated loss is of the same magnitude as the experiment results when the crossing angle is larger than 50 ºif the experimental error is taken into account.

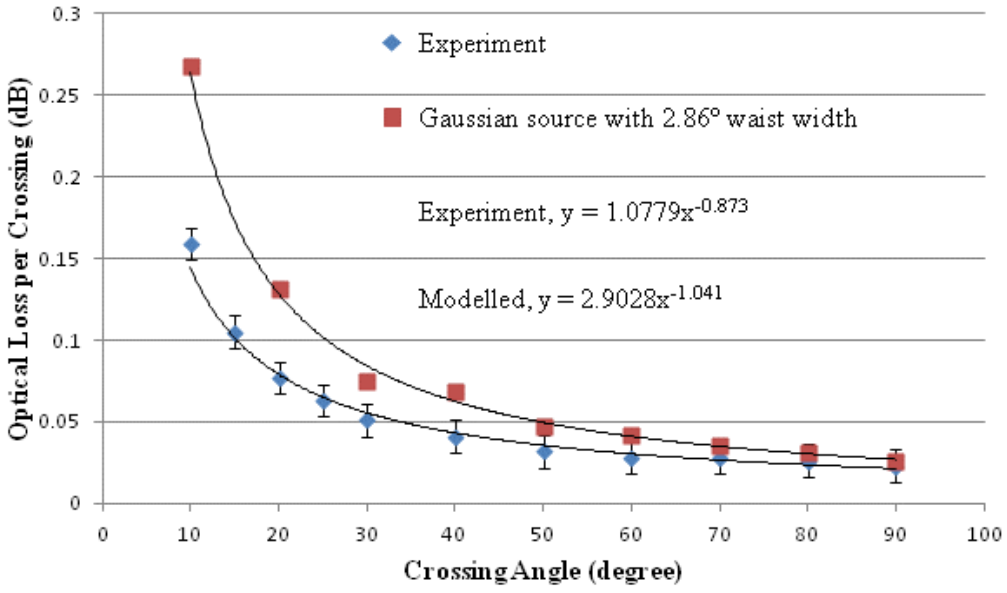

Figure 7-28: Experimental results and the ray tracing results for the source with NA=0.05.

Unfortunately the 2.86 ºhalf divergence angle was too low to be accepted as a suitable light source, because it was far below the measured half divergence 7 º±1 º from the output of the waveguide.

Table 7-3 Measured crosstalk compared with the simulated ones from 4 types of light sources

	Crossing angle (degree)	Crosstalk (dB)				
		Point	Emitter	Gaussian	Semi-empirical	Measured
Square waveguide	10	-9.427	-9.777	-10.038	-10.026	-14.6
Realistic cross section shape waveguide	10	-9.015	-9.243	-9.800	-9.808	
	20	-39.358	-36.212	-36.275	38.914	NA

Table 7-3 shows the measured crosstalk at 10 º crossing angle compared with simulated ones using 4 types of light sources. The results showed that simulated waveguides had higher crosstalk than the measured one at 10 º crossings and the realistic cross section shape waveguide had higher crosstalk at 20 º crossings than the one simulated with square cross section shape.

7.5 Conclusions

In this chapter, the optical loss caused by waveguide crossings was calculated using the ray tracing method for a range of crossing angles and the simulation results were compared with the experiment results. For the first time, the detailed models of light sources for modelling of multimode polymer waveguides were investigated. The parameters, i.e. divergence and intensity profiles, used in the light source models were obtained from experimental measurements of far field and near field energy distributions at the output of a 10 cm long straight waveguide. A best match semi-empirical source light source was found by comparing the 2D RMS and standard deviation values of the results of modelled light sources with the measured one. However, it was time consuming to create the semi-empirical source in ray trace and was only best match to a particular mode of waveguide. A Gaussian light source with the matching angular divergence to the measured light profile is recommended as a general method for modelling the light source for multimode waveguide. In addition to the square cross section waveguide model, a ray trace model of non-rectangular waveguides based on the waveguide shape of the cross-section of a photolithographically fabricated polyacrylate polymer waveguide is reported for the first time. The simulated results indicated that the realistic cross section shape

waveguide had higher crossing loss and more crosstalk at 20 ° crossings than the one with square cross section shape.

Chapter 7 References

[7-1] K. Wang, D. R. Selviah, H. Baghsiahi, I. Fernández, F.A., Papakonstantinou, and G. Yu, "Design Rules for Polymer Waveguides and Measurement Techniques," in *2nd International IEEE Symposium on Photonic Packaging Electrical Optical Circuit Board and Optical Backplane,IEEE-CPMT and IEEE-LEOS Messe München Munich, co-located with Electronica, Germany, 13th November 2008*.

[7-2] H. Baghsiahi, "Multimode Optical Waveguides and Lightguides for Backplane Interconnection and Laser Illuminated Display Systems," *PhD Thesis*, pp. 137–158, 2012.

[7-3] P. J. Bock, P. Cheben, J. H. Schmid, J. Lapointe, A. Delâge, D.-X. XU, S. Janz, A. Densmore, and T. J. Hall, "Subwavelength grating crossings for silicon wire waveguides," *Opt. Express*, vol. 18, no. 15, pp. 16146–16155, 2010.

[7-4] Y. Zhang, S. Yang, A. E.-J. Lim, G.-Q. Lo, C. Galland, T. Baehr-Jones, and M. Hochberg, "A compact and low loss Y-junction for submicron silicon waveguide.," *Opt. Express*, vol. 21, no. 1, pp. 1310–6, Jan. 2013.

[7-5] K. Inoshita, H. Kishikawa, Y. Makimoto, N. Goto, and S. Yanagiya, "Proposal of Optical Waveguide Circuits for Recognition of Optical QAM Codes," *J. Light. Technol.*, vol. 31, no. 13, pp. 2271–2278, Jul. 2013.

[7-6] T. Ishigure, K. Shitanda, T. Kudo, S. Takayama, T. Mori, K. Moriya, and K. Choki, "Low-loss design and fabrication of multimode polymer optical waveguide circuit with crossings for high-density optical PCB," *2013 IEEE 63rd Electron. Components Technol. Conf.*, pp. 297–304, May 2013.

[7-7] W. Ni, J. Wu, and X. Wu, "Crossing and branching nodes in soft-lithography-based optical interconnects.," *Opt. Express*, vol. 15, no. 20, pp. 12872–81, Oct. 2007.

[7-8] G. L. Bona, B. J. Offrein, U. Bapst, C. Berger, R. Beyeler, R. Budd, R. Dangel, L. Dellmann, and F. Horst, "Research Report:Characterization of Parallel Optical-interconnectWaveguides Integrated on a Printed Circuit Board," *Math. Phys.*, vol. 99555, pp. 8–17, 2004.

[7-9] D. Izquierdo, I. Salinas, V. Cadarso, A. Llobera, J. Ignacio, G. De Tecnolog ás, F. Instituto, D. Investigación, I. De Aragón, and U. De Zaragoza, "Hollow waveguides ray-tracing analysis," *Proc. SPIE*, vol. 6992, no. 16, pp. 1–8, 2008.

[7-10]R. C. A. Pitwon, K. Wang, J. Graham-Jones, I. Papakonstantinou, H. Baghsiahi, B. Offrein, R. Dangel, D. Milward, and D. R. Selviah, "FirstLight: Pluggable Optical Interconnect Technologies for Polymeric Electro-Optical Printed Circuit Boards in Data Centers," *J. Light. Technol.*, vol. 30, no. 21, pp. 3316–3329, 2012.

[7-11] E. Hecht, "Optics," in *Optics*, Addison Wesley, U.S, International 4th Edition, 2002.

[7-12] I. Papakonstantinou, R. James, and D. R. Selviah, "Radiation- and Bound-Mode Propagation in Rectangular , Multimode Dielectric , Channel Waveguides With Sidewall Roughness," *J. Light. Technol.*, vol. 27, no. 18, pp. 4151–4163, 2009.

[7-13] H. Baghsiahi, "Multimode Optical Waveguides and Lightguides for Backplane Interconnection and Laser Illuminated Display Systems," *PhD Thesis*, pp. 34–42, 2012.

[7-14] I. Papakonstantinou, K. Wang, D. R. Selviah, and F. A. Fernández, "Transition, radiation and propagation loss in polymer multimode waveguide bends," *Opt. Express*, vol. 15, no. 2, pp. 669–679, 2007.

Chapter 8. Development of Design Rules for Polymer Optical Waveguides

8.1 Introduction

In this chapter, the earlier research measuring the transmission insertion loss of key waveguide components including straight waveguides of various widths, novel tapered bends, crossings between two waveguides at a range of angles and bends of a range of radii is extended. The measured optical loss of each waveguide structure has been analysed so that one can establish waveguide design rules [8-1] and incorporate these into a commercial automatic design rule checker and constraint manager layout software for PCBs. PCB designers can then easily include optical connection layers without detailed knowledge of the optics involved. The optical board for high data rate (>10 Gbs) communication can then be optimised to minimise the waveguide loss and optical cross talk. Design rules were fed back to Cadence to be embedded in the future generation of E-CAD for the first time for integrated design and layout software for electronic and photonic interconnects. Cadence was used to layout optical waveguide interconnections for an OPCB for the first time. The design was the most compact and complex design to date for a data storage system. It should be noted that all the experiment measurements were carried out by the author with Dr. Ioannis Papakonstantinou.The extended analysis of the measured results to derive design rules for optical PCB layout was done by the author.

The waveguide samples investigated in this chapter had been photolithographically fabricated (samples fabricated using other techniques are being investigated and will be reported in the near future). They were fabricated by Exxelis Limited using Truemode® polyacrylate polymer [8-2], [8-3]. The refractive index of the core was 1.5560; slightly higher than the cladding 1.5264, giving a theoretical numerical aperture (NA) of 0.302. Waveguides analyzed and reported in this chapter had 50 μm thick cores unless otherwise stated, and the pitch between two adjacent waveguides was 250 μm. The Truemode® polyacrylate polymer has been measured previously by Dr. Ioannis Papakonstantinou using 1 metre spiral waveguides and had a propagation loss of 0.08 ± 0.01 dB/cm at 850 nm [8-4].

8.2 Optical Loss Measurement Technique

The measurement of optical loss is strongly dependent on the choice of optical source, the roughness of the end facets of the waveguides, the type of light source (two types of laser sources were used), the type of output photo detector (PD) and, more importantly, the relative positions of all sources, detectors and waveguides, particularly for multimode optical waveguides.

8.2.1 Arrangement of Measurement Platform

Both the input source and PD were mounted on high precision (minimum increment of 0.1 μm) motorized translation stages for accurate alignment and sub-micron step adjustment to maximize the light through the waveguide.

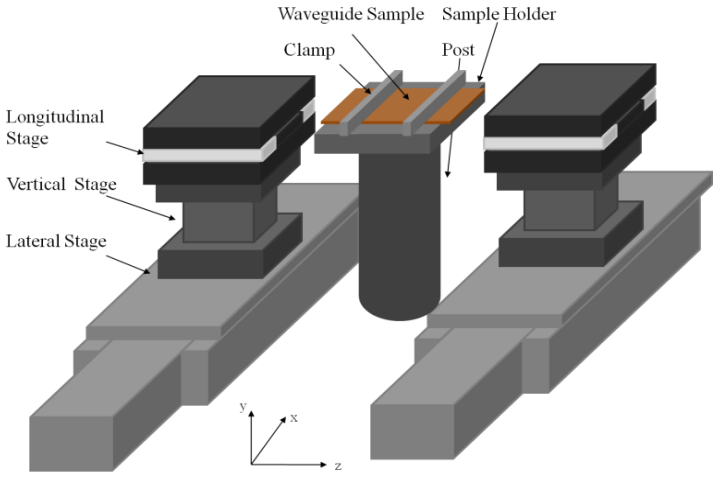

Figure 8-1 Schematic of the measurement arrangement

Figure 8-1 shows the schematic of the author's measurement arrangement, including the design of stages. The lighter and smaller stages (*y* vertical stage and *z* forward and backward stage) are mounted on top of a heavier and larger stage (x lateral stage). The order of the stages was calculated to allow the group of stages to support the maximum load within their specifications (see Table 8-1).

Table 8-1 Specifications of the Selected Translation Stages

Stage Position	Manufacturer	Model	Driver	Travel Range (mm)	Resolution (μm)	Bi-directional Repeatability (μm)
X	Newport	GTS150	XPS-DRV01	150	0.05	0.2
Y	Newport	GTS30V	XPS-DRV01	30	0.05	0.2
Z	Newport	VP-25XA	XPS-DRV03	25	0.1	0.2

Note: Both the integrated control software and an in-house developed Labview program were used to control the stages.

A translation stage which is symmetric to the vertical axis was chosen as the *y*, up-down stage, so that when all of the stages are mounted along the vertical axis (perpendicular to the optical table) the weight of the upper stages is balanced. The 3-axis stages were orthogonally assembled by the manufacturer within an off-axis error of ± 25 μrad, according to the calibration certificate from the stage manufacturer.

The waveguide sample needs to be held securely to prevent unexpected movement during the measurement and to be parallel to the optical table to align with the light launching axis, *z*. Some flat metal plates were made in different lengths to support the variety of sizes of waveguide samples, which ranged in length from 20 mm to 120 mm. The plates were cut 2 to 5 mm shorter than the length of their corresponding samples. This is because if the holder plate is longer than the waveguide sample it will prevent the light source and the PD approaching the waveguide, causing higher optical loss [8-4]; if the holder is cut too short and leaves a large proportion of the waveguide sample without sufficient support, the waveguide will vibrate during the measurement and will cause the results to fluctuate. Two clamps with rubber clamping surfaces are used to secure the waveguide sample flat to its holder and to avoid damage to the polymer surface.

8.2.2 Measurement Arrangement

A VCSEL TOSA (transmission optical sub-assembly) with TO-46 housing and ball lens and ST receptacle (STVXCEL-850, Access Pacific Ltd) was used as one laser source for most of the measurements. It was connected to a standard 50/125 μm graded index multimode (MM) fiber with NA_{fibre}: 0.2; less than the waveguide NA_{wg}: 0.302. The VCSEL TOSA was connected to a digital power supply and was powered up for at least 30 minutes (1800 seconds) to stabilize the optical output before carrying out any measurement. Figure 8-2 shows the VCSEL wavelength and output power as a function of operating time.

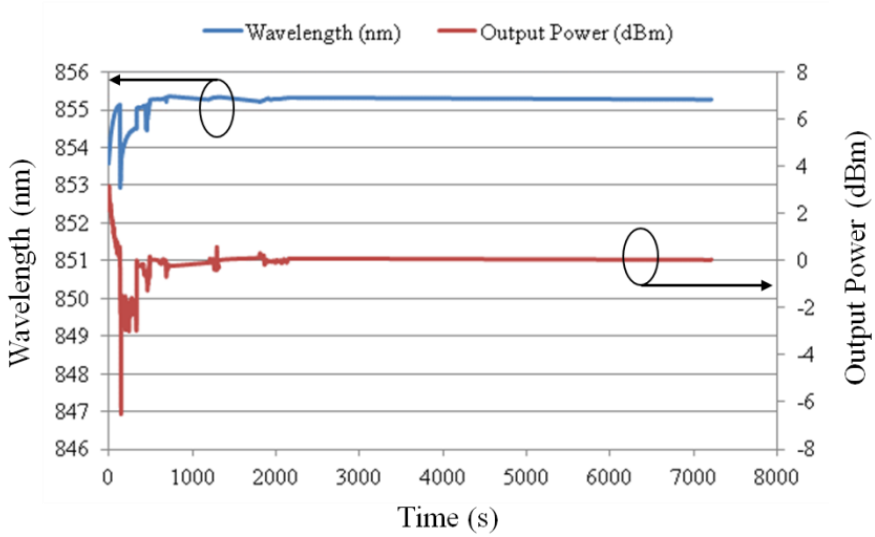

Figure 8-2 VCSEL output wavelength and power as a function of time

The power supply should ideally have an output monitor loop, which could automatically adjust the drive current and hence supply a consistent optical output. The author manually measured the output from the MM fibre periodically at one-hour intervals to calibrate the output variation against temperature of the VCSEL chip.

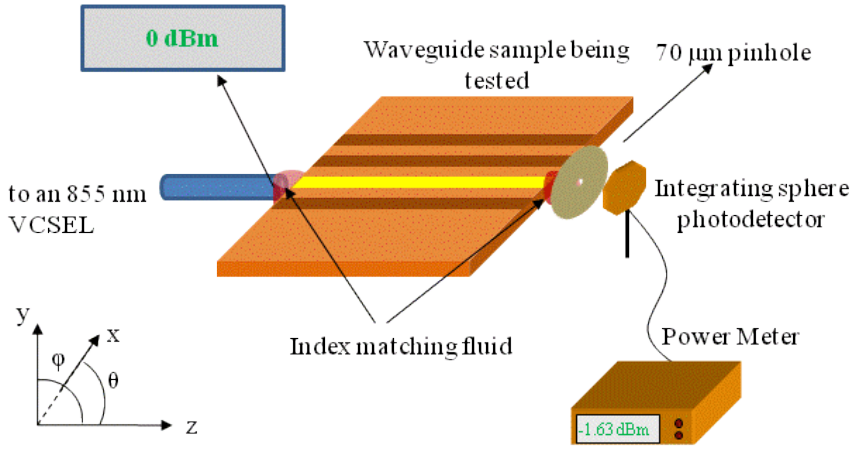

Figure 8-3 One 850 nm VCSEL was connected to a 50/125 µm MM fibre via an ST connector and was set to provide an output optical power of 0 dBm at the output end of the fibre.

Figure 8-3 shows a schematic of an optical insertion loss measurement using an 855 nm (840 nm minimum and 860 nm maximum) light source launched via a 10 m long MM fibre. Similar methods have been widely used by other researchers [8-5–8]. The fibre has ST and FC/PC connectors and was wound 20 times around a 38 mm diameter mandrel to fill the NA_{fibre}. The output from the fibre was measured to check the NA of the fibre was fully filled with a large number of transverse modes [8-9] (as shown in Figure 8-4).

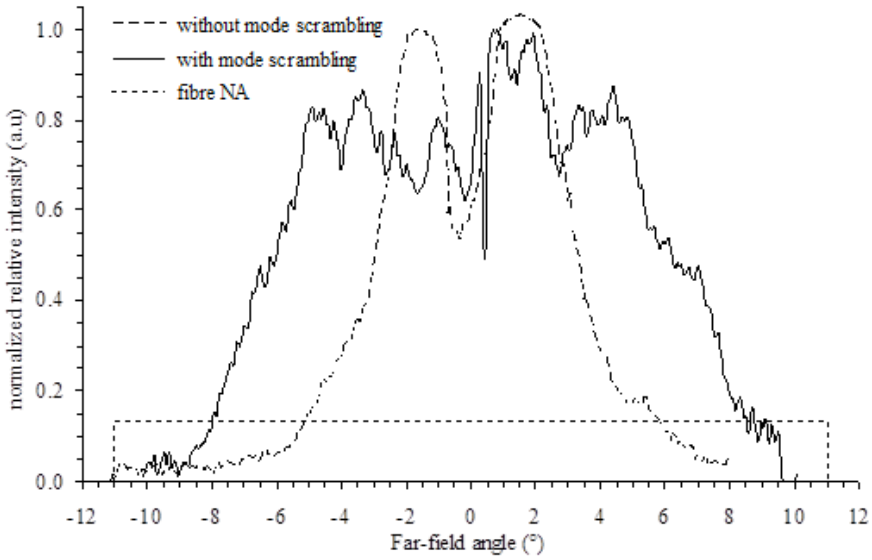

Figure 8-4 Far-field intensity of the 50/125 µm fibre used in the experiment with and without wounding around a mandrel. The far-field intensity was normalized to unity maximum value

The FC/PC end of the fibre was then aligned and butt-coupled to one of the waveguides on a waveguide sample to be tested (as shown in Figure 8-5).

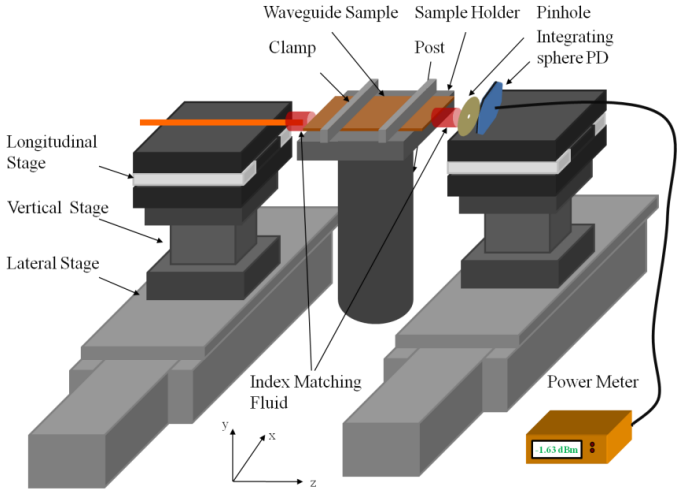

Figure 8-5 Schematic of the measurement arrangement. One 850 nm VCSEL was connected to a 50/125 µm MM fibre via an ST connector and was set to provide an output optical power of 0 dBm at the output end of the fibre.

A 70 µm pinhole was placed in front of a large area integrating sphere PD to spatially filter much of the light travelling through the cladding and to simulate the aperture of the PD used in the current demonstrator [8-10]. The large area integrating sphere PD was placed after the output pinhole to measure the integrated output optical power. Compared to other results obtained using photodiode detectors, this measurement technique avoided inconsistencies of measured optical power due to laser speckle and

spatial variation of efficiency across the active area of the optical power sensor. Index matching fluid (n = 1.5433 ± 0.0005 for 840.0 nm at 25 ℃), which was close to the refractive index of the waveguide core; 1.5560 ± 0.0005 at 850 nm) was applied to the MM fiber-waveguide interfaces to reduce coupling loss and to the waveguide-pinhole interface to reduce loss due to the scattering occurring at the rough entry and exit facets of the waveguide.

8.2.3 Measurement Procedures

The light source, the waveguide and the PD need to be properly aligned; the author followed the following procedure to do so.

1) All of the optical devices were securely placed onto an optical table, so that they were parallel to the optical table.

2) The bearing slide of each of the translation stages was positioned to its centre position in order to leave sufficient travelling distance in all directions.

3) A MM fibre with FC/PC connector was used as the light source input. An FC/PC fibre connector has a screw type metal casing which make it very easy to engage to an appropriate adapter and the fibre ferrule provides good protection to the fibre core.

4) One end of the MM fibre was manually aligned to one of the waveguides on a sample and moved close, but not pushing too hard, to the waveguide end facet to prevent the fibre ferrule scratching the waveguide end facet.

5) The other end of the fibre was connected to a 650 nm Class 2 red laser via a standard FC/PC fibre connector for the aid of visual alignment between the fibre and the waveguide. A white surface projector screen, e.g. a piece of non-reflective white paper, was placed on the output side of the waveguide sample to observe the changes of the output. The position of the fibre might need to be adjusted by using the motorized stages until a bright spot is observed on the paper screen, hence, the input was roughly aligned with a waveguide.

6) The PD with a pinhole attached to the front was moved close to the waveguide output end facet and aligned to the bright spot.

7) The red laser was replaced by the infrared VCSEL.

8) The position of the input fibre and the PD were precisely adjusted until the maximum output power from the waveguide was recorded.

9) A camera was used to visually examine the angular rotation of the input fibre, the waveguide and the PD about the *z* axis.

In the case of using the VCSEL chips as a light source, step 2) and 6) were omitted. All of the measurements were carried out in similar environment conditions: room temperature 25.7 ℃ – 27.2 ℃ and air humidity 35% - 40%.

8.3 Design Rules of Photolithographically Manufactured Waveguides

8.3.1 Crosstalk in Chirped Width Straight Waveguides Array

The choice of the width of waveguides was based on evidence from measurements of insertion loss, cross-talk and misalignment tolerance in an array of 15 waveguides with a range of widths from 10 μm to 150 μm with an increment of 10 μm. The lateral centre-to-centre separation between two neighbouring waveguides was 250 μm. Optical input power was measured using an integrating sphere PD to be 0 dBm. Figure 8-6 shows a photograph of a chirped width waveguide array. A 50 μm x 150 μm waveguide was illuminated by the VCSEL light source. Light can be observed from the adjacent waveguides, indicating the existence of crosstalk.

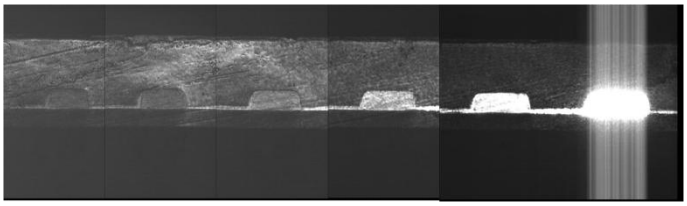

Figure 8-6 Photograph showing a photolithographically fabricated chirped width waveguide array (widths from left to right are 100 μm to 150 μm). Light launched from a VCSEL is imaged via a GRIN lens into the 50 μm x 150 μm waveguide. (Photo mosaic with increased camera gain towards left)

In order to find a suitable waveguide for an optical backplane, the optimised cross-section dimensions are needed to be identified. After the optimised optical power coupled into the waveguide under investigation was measured, the author fixed the position of the PD and laterally moved the input by 250 μm to the left and then by 250 μm to the right of this waveguide and recorded the power at the two positions respectively, which defined as crosstalk to the waveguide. In this way, the author measured the signal to cross-talk ratio (SCR) that the reference waveguide would experience from one waveguide on its left and one waveguide on its right in a real system. The author then moved the PD and input to the next waveguide, repeated the

same measurements, and continued in the same way to cover all of the 15 waveguides in the array. The results are presented in Figure 8-7. The insertion loss was minimized for the waveguides with widths in the range between 50 µm – 80 µm. The maximum SCR was exhibited by the 70 µm – 80 µm wide waveguides.

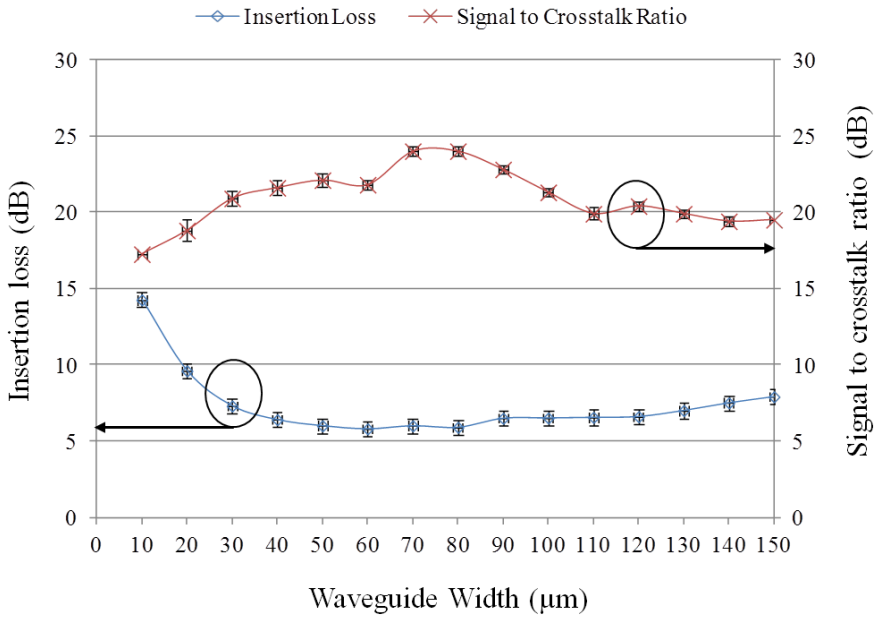

Figure 8-7 Insertion loss and signal to noise ratio (SCR) measured for an array of 15 waveguides with chirped widths varying from 10 µm to 150 µm. For a given waveguide, the SCR shown corresponds to the mean signal to cross-talk value due to one waveguide on its left and one waveguide on its right. The maximum value of the error bar corresponds to the SCR resulting from the crosstalk from the left while the minimum value to the SCR resulting from the right waveguide.

Optical connections between the light source and the waveguide have to tolerate misalignments, and therefore, the insertion losses as a function of the three possible translational misalignments *x*, *y* and *z* at the waveguide interface were measured. The measurement technique is similar to the crosstalk measurement, but this time the author focused on the waveguide widths from 30 µm to 100 µm and scanned continuously across each waveguide. If one defines the position of maximum coupling efficiency of each waveguide to correspond to $x = 0$, $y = 0$, $z = 0$, then by scanning along x by ± 100 µm at 0.5 µm intervals and monitoring the power at the waveguide output one can generate the graph shown in Figure 8-8 of normalised insertion loss due to the input lateral misalignment. Figure 8-9 shows that the lateral misalignment tolerance increases when the width of waveguides increases.

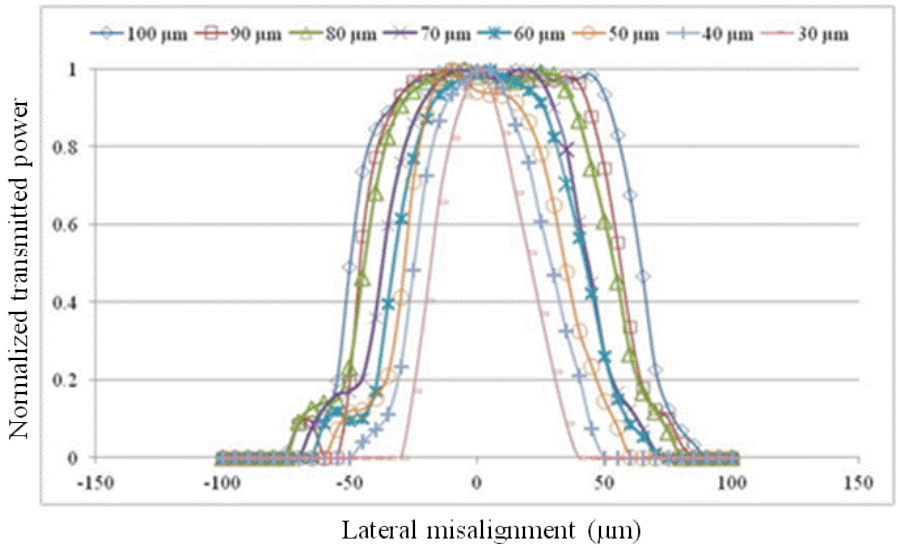

Figure 8-8 Normalized transmitted power as a function of lateral misalignment of the waveguides with different width when the input is at the position z= 0 scanning along x from -100 µm to +100 µm. Figures normalised to the maximum value

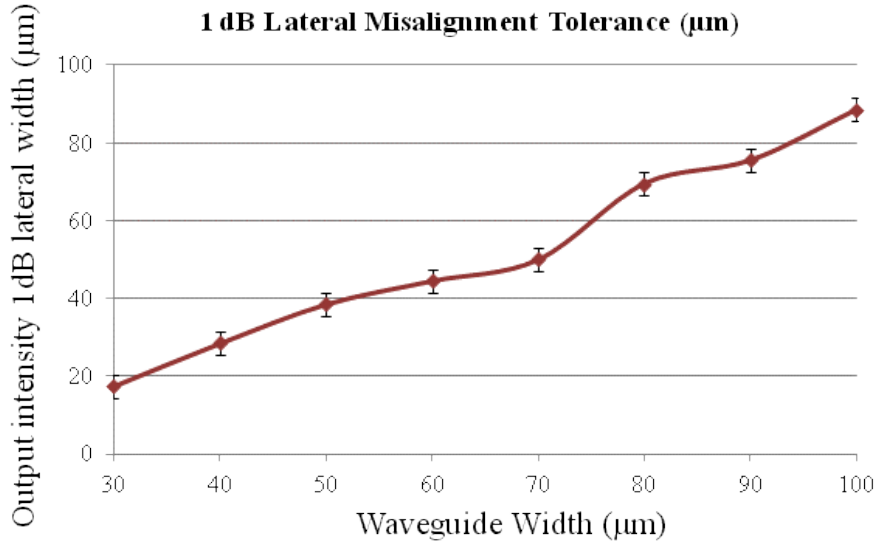

Figure 8-9 Maximum coupling efficiency and the width of 1 dB lateral misalignment tolerance as a function of the width of waveguides

To investigate the effect of longitudinal, *z*, misalignment, the author performed an additional set of experiments where the author repositioned the input to the origin (x = 0, y = 0 and z = 0) while at the other end the PD was returned to the position where the maximum output was received. The power at the waveguide output was monitored as the input fibre was moved axially away from the waveguide $0 < z < 900$ µm with a 100 µm increment step and the results are presented in Figure 8-10.

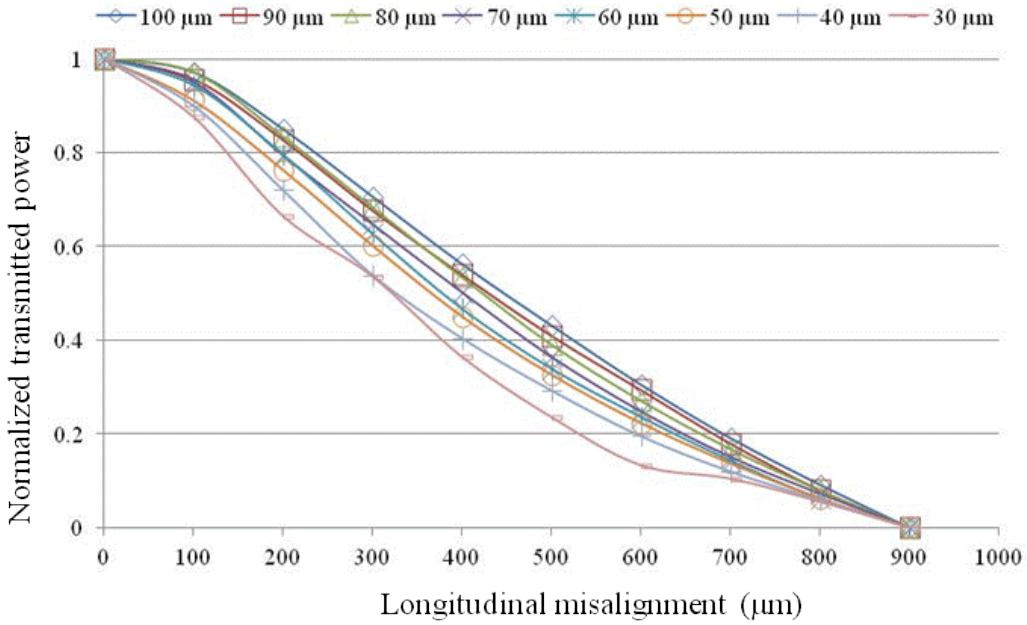

Figure 8-10 Normalized transmitted power as a function of longitudinal misalignment of the waveguides with range of widths when the input fibre is at the position z= 0 scanning along z from 0 µm to 900 µm.Figures normalised to the maximum value of intensity

Table 8-2 shows that when the input fibre is 200 µm away from the waveguide entrance surface, for a loss less than 1 dB (20% of the relative insertion loss), the waveguides with widths in the range between 60 µm -100 µm offer the highest coupling efficiency.

Table 8-2 Permitted input fibre movement along *z* axis at different loss level

Input fibre misalignment along *z* (µm)	Loss level (dB)	Qualified waveguide width (µm)
100	0.1	80 and 100
	0.5	All widths except 30
	1	All widths
200	0.1	No waveguide qualified
	0.5	No waveguide qualified
	1	60 to 100

Therefore, the waveguides that showed minimum insertion loss (50 µm – 80 µm width), maximum SCR (70 µm – 80 µm width), maximum longitudinal (z) misalignment tolerance (60 µm – 100 µm width) and relatively high lateral (x) misalignment tolerance, were found in the range between 70 µm – 80 µm. This prompted the author's selection of 70 µm width waveguides in the prototype demonstrator [8-11], [8-12].

8.3.2 Crosstalk between Straight Waveguides

Optical crosstalk between neighbouring waveguides is critical to multi-channel optical interconnection design because it could increase the bit error rate in high data rate communication. –30 dB crosstalk from the adjacent channel is a desirable target [8-12]. A sample containing an array of straight waveguides with 70 µm × 70 µm cross-section was used to characterize insertion loss and crosstalk [8-4]. In the crosstalk measurement, an array of 844 nm vertical cavity surface emitting lasers (VCSELs) (ULM photonics, ULM850-10-TT-C010104U) was used and was aligned to a Gradient Index lens (GRIN-lens) array via a mechanically transferable (MT) connector. The GRIN-lens was used to image the incident light from the VCSEL chip onto the centre of the waveguide entrance facet to increase the coupling efficiency and to protect the bond wires on the VCSEL chip by preventing them being knocked off by the waveguide facet. The GRIN-lens has flat entry and exit surfaces, which are perpendicular to its optical axis, making it a better choice than the conventional microlens' curved surfaces for the direct butt coupling. The air gap between the GRIN-lens and the waveguide is minimized and index-matching material can be easily applied when required, therefore, the loss caused by Fresnel reflection and surface scattering can be reduced. The VCSEL chip was the same model as the one used in the Storlite demonstrator [8-4], [8-13] mentioned in chapter 4. The schematic of the crosstalk measurement system is illustrated in Figure 8-11. Two types of loss occur in all of the waveguide components: input and output coupling and propagation loss.

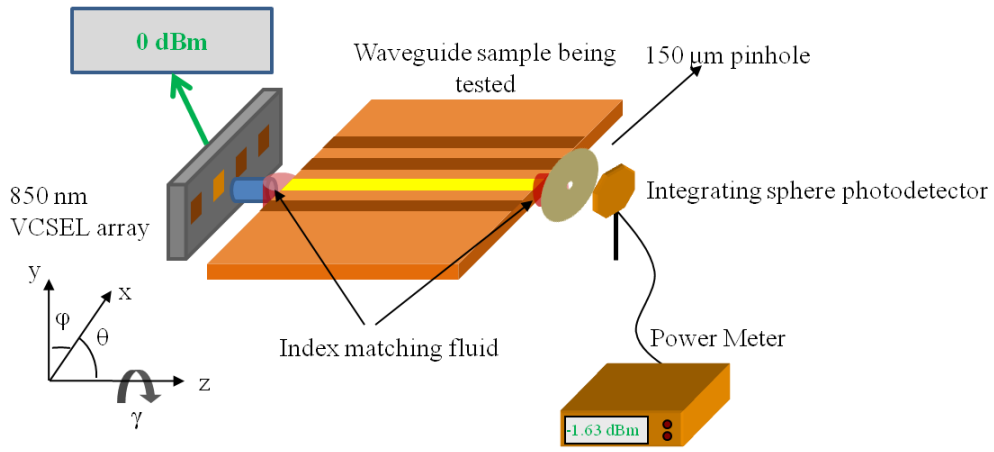

Figure 8-11 Schematic of crosstalk measurement. One VCSEL of the 850 nm VCSELs array was activated and was set to provide an output optical power of 0 dBm.

Input and output coupling loss (CL) occurs between an incoming multimode fibre and the waveguide and also between the waveguide exit and a photodetector. It is caused by:

a. Fresnel reflection loss due to reflection at the interface between different refractive index media with a magnitude that depends strongly on whether an air gap exists between the waveguide and adjacent external components.
b. Scattering loss caused by a rough waveguide end face which scatters light forwards and backwards into a wide range of angles.
c. Mode mismatch loss due to the circular cross section input waveguide meeting the rectangular cross section waveguide.
d. Offset misalignment between the light source and the waveguide in the Cartesian coordinate, x, y and z and rotation axes θ, φ and γ.

Propagation loss (PL) is caused by the scattering of energy from propagating to radiating modes due to the rough waveguide sidewalls, and also direct loss due to material absorption. The core layer is spun as a liquid onto the wafer so the upper and lower surfaces of the waveguide are flat. However, the vertical sidewalls are formed by lithographic UV exposure using an e-beam mask. This causes sidewall roughness, which may be the main reason for the measured total propagation loss [8-14]. The scattering of guided modes at the rough side walls not only causes loss by radiation but also redistributes energy between guided modes [8-15].

One VCSEL of the 850 nm VCSEL array was activated and the output optical power imaged via the GRIN-lens was 0 dBm, measured using an integrated sphere PD. The light was incident onto a waveguide at $x = 0$, $y = 0$, $z = 0$ (named the 0^{th} waveguide in Figure 8-13). The position of the integrating sphere PD was optimized to receive maximum transmitted power. The VCSEL was laterally scanned across the waveguides from –500 μm to 1600 μm in 1 μm increments along the x axis, while the power at the end of the 0^{th} waveguide was monitored at every step. The power detected by the PD simulated the crosstalk originating from the neighbouring VCSELs of the same array that would be coupled into the 0^{th} waveguide (Figure 8-12).

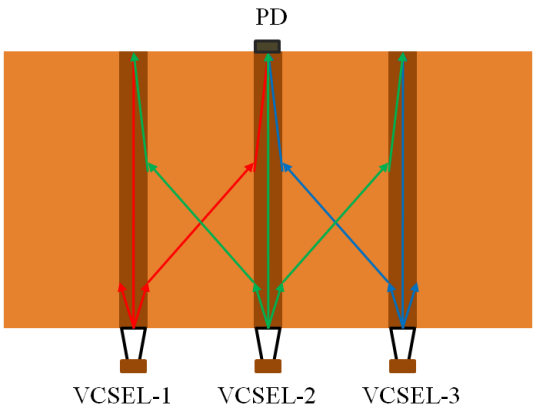

Figure 8-12 A photo detector will receive signal from neighbouring active waveguides. The bit error rate might increase due to the cross talk.

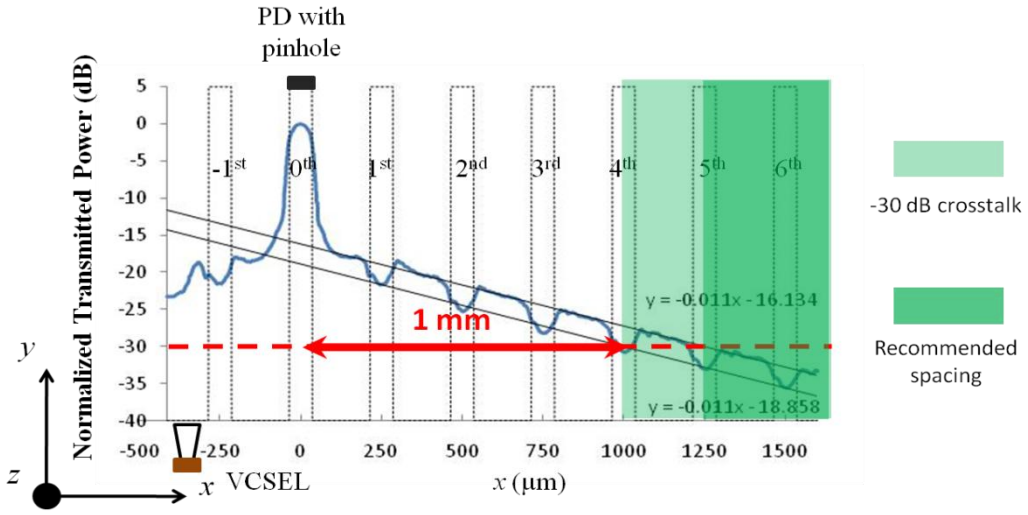

Figure 8-13 Optical crosstalk between straight waveguides. The curve might shift up or down by 0.5 dB due to the measurement error. The waveguides cross-section size is 70 μm × 70 μm square and the aperture of the pinhole is 150 μm.

The columns in Figure 8-13 represent the appearance of waveguides on the sample and the curve is the normalized transmitted power detected at the output end at the 0th waveguide. When the VCSEL is completely misaligned with the waveguide, light emits into the cladding, the power drops almost linearly along *x* at a rate of 0.011 dB/μm, as its distance increases from the boundary of the 0th waveguide (Eq. 8-1, the upper line in Figure 8-13). It means that the power in the cladding will drop 2.75 dB at every 250 μm away from the 0th waveguide. The valleys in the curve show that the lowest crosstalk levels were achieved when the VCSEL aligned to the centre of the waveguides. The power drop means that the power is confined in the waveguide core

area. In this case, the waveguide power valley minima have a linear relationship given by Eq. 8-2.

$$y = -0.011x - 16.134 \quad \textbf{Eq. 8-1}$$

$$y = -0.011x - 18.858 \quad \textbf{Eq. 8-2}$$

According to the equations, if a system is designed to achieve –30 dB crosstalk between the optical interconnections, the centre-to-centre spacing needs to be wider than 1 mm (shaded region in Figure 8-13) for the 70 µm × 70 µm square waveguides and 150 µm detector aperture. However, the crosstalk is reduced if the aperture of the detector is smaller (Figure 8-14).

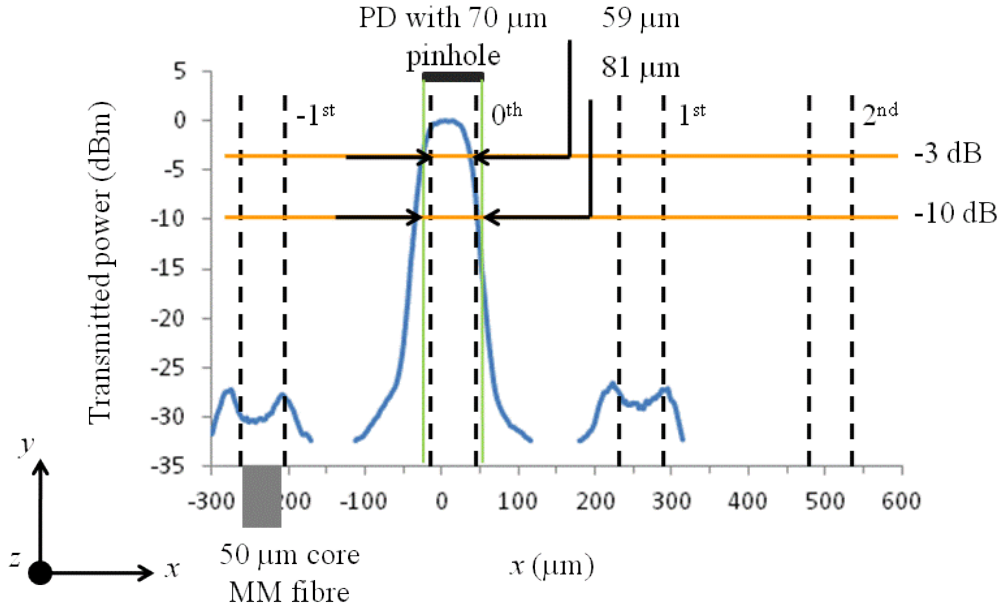

Figure 8-14 Optical crosstalk between straight waveguides. The waveguides cross section size is 70 µm × 70 µm square and the aperture of the pinhole is 70 µm.

The crosstalk measurement was repeated again and all the measurement conditions were kept the same, but the 150 µm pinhole was replaced with a 70 µm one. The measured result was shown in Figure 8-14. The maximum transmitted power was -4.36 dBm and the crosstalk could only be detected from the adjacent waveguides (1st and -1st) at maximum -28.16 dB or -32.52 dBm. There was no detectable optical power from the 2nd waveguide onwards using the PD with -37 dBm sensitivity. The 70 µm pinhole is the same as the aperture of the photodiodes used in the two demonstrators (StorLite [8-4] and FirstLight [8-12], mentioned in chapter 4). According to Figure 8-14 the waveguide centre-to-centre spacing could reduce to 0.5

mm to achieve –30 dB crosstalk between the optical interconnections if using a photo detector with a 70 μm aperture.

8.3.3 Waveguide Crossing Angles

The layout of the waveguide crossing sample was introduced in the section 7.3 in chapter 7. The author used the same technique as the author did for the crosstalk measurement to access the crossing loss. The crossing angles were 10°, 15°, 20°, 25°, and from 30° to 90° in increments of 10° giving a total of 11 different crossing angles. The optical power detected at the end of the waveguide with crossing, *I* in **Error! Reference source not found.**, subtracted the power detected at the end of the waveguide without crossings, *II*, to calibrate out the cascaded effects of waveguide bends and crossings. However, the calibrated power was quite low; the author had to measure each waveguide 50 times and use the average value to minimise the error due to power fluctuations, which may also have been exacerbated by an unstable hunting stage. 0.023 ± 0.03 dB losses were achieved at a 90° crossing. The arithmetic mean of the calibrated transmitted power at each crossing as a function of the crossing angle is shown in Figure 8-15. The vertical axis is the calibrated loss per crossing, which is defined as the power measured at the end of waveguide I containing 6 crossings, P_I, minus the power measured at the end of the waveguide II, P_{II}, in the same group divided by 6 (see Eq. 8-3).

$$L_c = 10 \cdot \log\left(\frac{P_I - P_{II}}{6}\right) \qquad \textbf{Eq. 8-3}$$

Since the radius, angle of the arc and the total length of straight sections are the same in both curved waveguide *I* and *II*, this calibration step removes all the additional losses.

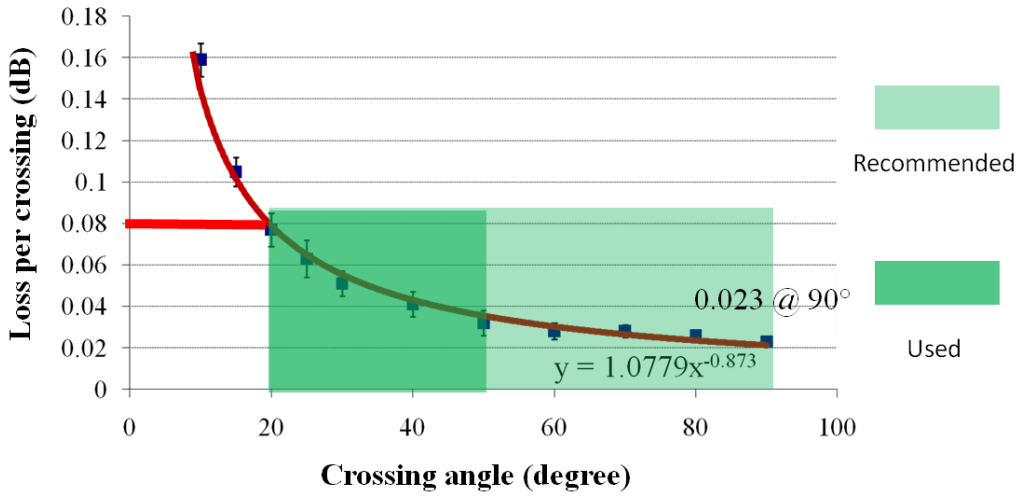

Figure 8-15 Loss per waveguide crossing as a function of crossing angles. The waveguides cross section size is 50 μm × 50 μm square and the aperture of the pinhole is 70 μm.

Figure 8-15 shows that the loss per waveguide crossing (L_c) decreases as the crossing angle (θ) increases. A trend-line was fitted in the figure and the author achieved:

$$L_c = 1.0779 \cdot \theta^{-0.8727} \qquad \textbf{Eq. 8-4}$$

If one accepts 0.08 dB loss at each crossing, then one can include twelve 20 °crossings in one waveguide before the power drops more than 1 dB. According to Eq. 8-4, any crossing angles larger than 20 ° are valid for the design. Eq. 8-4 can be used as a design curve to establish the loss for the link power budget calculation.

8.3.4 Waveguide Bends

The modes in waveguide bends have their power shifted towards the outside of the bend and are inherently high loss. More importantly, bends are usually attached to other waveguide elements, for example, to a straight waveguide. The modes in straight waveguide are different to the modes in bends, so that straight waveguides result in a modal mismatch and additional loss at the transition point. The relative strengths of the various types of loss must be found so that other waveguides on the backplane can be arranged to reduce crosstalk and optimise the layout of an optical data link. Therefore, carefully arranged experiments must be designed to separate the total bend loss from the input and output coupling loss.

Three sets of waveguides with the same thickness, 50 µm, but different widths, w = 50 µm, 75 µm, and 100 µm were measured. All of them were fabricated at the same time by the same procedure on the same 6-inch circular FR4 PCB wafer.

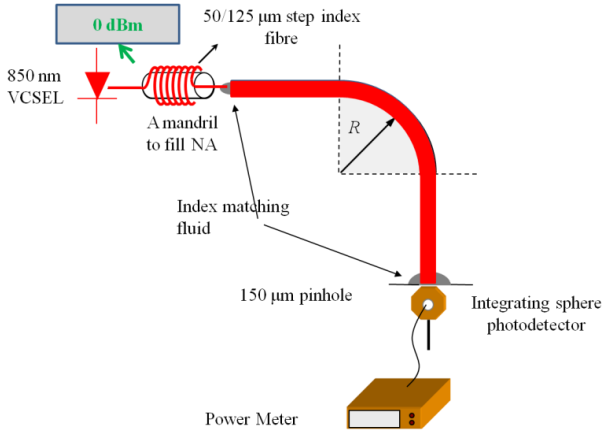

Figure 8-16 Schematic of bend insertion loss measurement. One 850 nm VCSEL was connected to a 50/125 µm MM fibre via an ST connector and was set to provide an output optical power of 0 dBm at the output end of the fibre.

The waveguide bend with a uniform width starts from a minimum radius, R = 5.5 mm and increases in radius in increments of 1 mm, to a maximum radius of R = 34.5 mm giving a total number of waveguide bends N = 30 in each width set. Figure 8-17 shows a picture of a group of nested waveguide bends. A straight waveguide was fabricated on the same sample to calibrate out the input and output coupling loss.

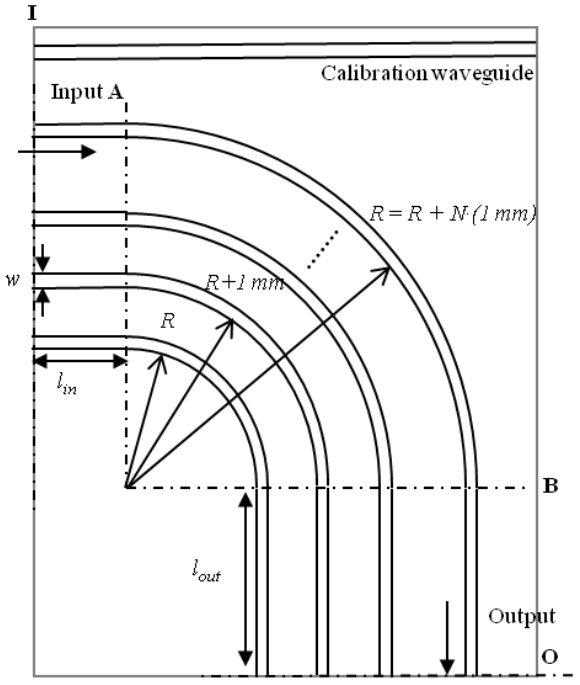

Figure 8-17 Schematic of one set of nested waveguide bends

Waveguide bends suffer from bend radiation loss (*RL*) and waveguide transition loss (*Trans*) as well as coupling losses at the input (*CouplI*) and output (*CouplO*) facets. Figure 8-18 illustrates all of the loss components in a waveguide bend.

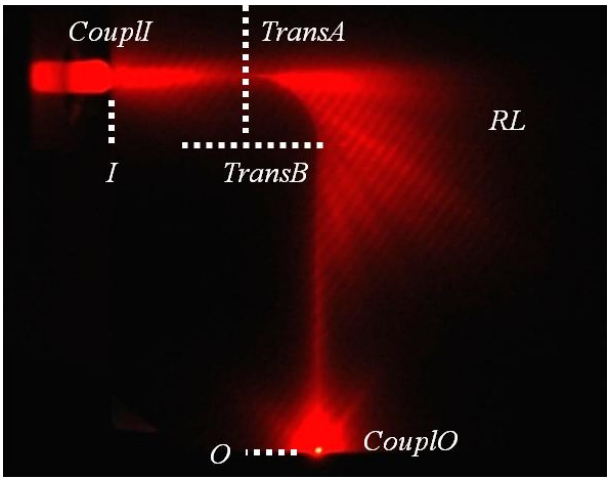

Figure 8-18 Light through a waveguide bend of *R* = 5.5 mm. Light lost due to scattering (*CouplI*) at the waveguide entrance, transition loss (*TransA and TransB*), radiation loss (*RL*), reflection and back-scattering (*CouplO*) at the end of the waveguide and propagation loss (*PL*). Waveguide was butt-coupled to a 50/125 MM fibre illuminated with a red laser.

Bend radiation loss exists because waveguide bends cannot support perfectly bound modes, but instead they host leaky modes, which radiate energy continuously around a bend, causing radiation loss, *RL*. Each propagating mode loses power at a unique rate determined by its mode number and waveguide parameters such as numerical aperture, physical dimensions and radius of curvature [8-16], [8-9].

Waveguide transition loss or joint loss or mode mismatch loss occurs at the junction between waveguide structures supporting different modes when the field across the waveguide cross section emerging from the first waveguide or incident externally from a fibre cannot be expanded and fully represented as a weighted combination of only the propagating modes of the waveguide into which the light travels. The modal field expansion must also include radiation modes to match the field distribution fully. In Figure 8-18, transition loss occurs along the plane *I*, since the fibre modes do not match those of the waveguide, and this loss is assumed to be included with the coupling loss in the term, *CouplI*. Transition loss also occurs along line A, at the interface between the straight and the curved waveguides, *TransA* and along line B at the interface between the curved waveguide and the straight waveguide, *TransB*

The total bend insertion loss, *TL*, in this sample can be described by the following equation:

$$TL = CouplI + TransA + RL + TransB + CouplO + PL \quad \textbf{Eq. 8-5}$$

Where *CouplI* and *CouplO* are the input and output coupling loss, *TransA* and *TransB* are the waveguide transition loss, *RL* is the bend radiation loss and *PL* is the Propagation loss. These loss components can be clearly identified in Figure 8-18, which shows red 632.8 nm light from a helium-neon laser passing through an input standard 50/125 μm multimode fibre butt-coupled to one waveguide of Figure 8-17. A small bend radius was chosen to give a high loss so that the directions of the lost light can be clearly seen. The light from the glowing input fibre can first be seen to scatter forward and backward at the rough input face (the roughness depends on the cutting technique) of the waveguide after which it traverses the straight waveguide and emerges as a narrow beam due to transition loss at the joint between the straight waveguide and the waveguide bend. As the light travels around the bend tangentially, emitted light due to bend radiation loss can be discerned. Finally, as the light exits the waveguide light backscattered from the rough waveguide output face can be seen. The slanted fringes are due to scattering from the top surface of the PCB below the lower cladding of the waveguide due to the weave and weft of the FR4 material. Although Figure 8-18 was obtained for red light for convenience, similar results occur for infra red light (850 nm) more often used in optical backplanes. This is the first time the optical loss in bends has been analyzed and broken down into components and shown using a visible light source.

After the author removed the coupling loss by subtracting the measured total insertion loss from the straight waveguide fabricated on the same sample, the author plotted bend loss as a function of the radius of curvature in Figure 8-19 for the three sets of waveguides. The transmitted power increases significantly as the radius of curvature increases when $R < 12$ mm in all three cases, because of the dominance of radiation and transition loss which have high dependency on radii [8-16–18]. As the radius keeps increasing, the power decreases again due to the propagation loss over the longer length. Waveguide loss vs. bend radii curves will allow engineers to choose the appropriate bend radius and to layout the waveguides to minimize bend insertion loss [8-9].

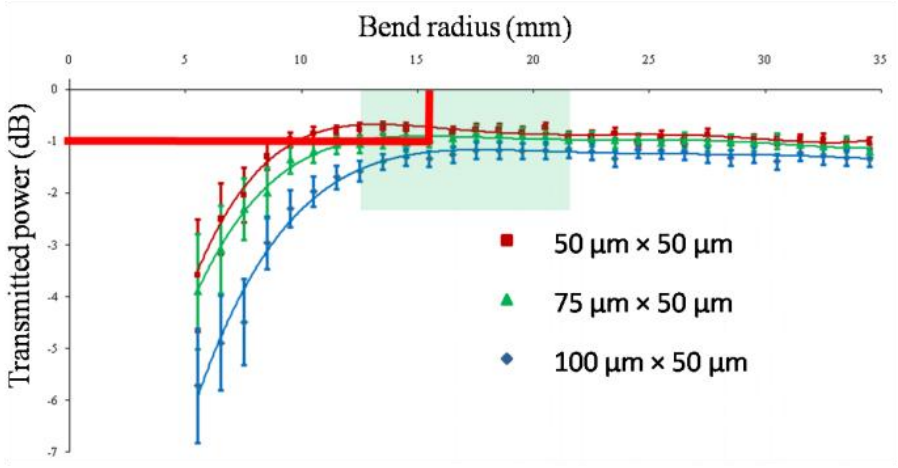

Figure 8-19 Power transmission of waveguide bends for three widths w = 50 µm, 75 µm and 100 µm

Table 8-3 Optimum radius for different waveguide widths

Width (µm)	Optimum Radius (mm)	Maximum Transmitted Power (dB)
50	13.5	-0.74
75	15.3	-0.91
100	17.7	-1.18

In the case of 75 µm × 50 µm waveguide, the output power reached a maximum at *R* = 15.3 mm as shown in Table 8-3. The wider waveguides have consistently higher insertion loss. In the range of radii 13 mm to 22 mm, the output power was close to the maximum value; hence, the author recommend these values, shown in the shaded region in Figure 8-19, for the 90 °bend design.

8.3.5 Environment Stability Test

One waveguide sample containing 24 identical 10 cm long straight waveguides with 70 µm × 70 µm cross section was separated into two pieces (see Figure 8-20). A group of 12 waveguides was subjected to testing at or beyond the section 6.2.5 High Temperature Storage Test (damp heat) in Telecordia GR-1209/GR-1221-CORE standards [8-19]. The temperature-humidity environmental test involves 85 ℃ and 85% R.H. (relative humidity) cycling up to 2000 hours. Another group of 12 waveguides was kept in a normal environment with temperature 25.5 ℃ - 27.2 ℃ and R.H. 35.4% - 40.1% and was used as a reference for measurement comparison.

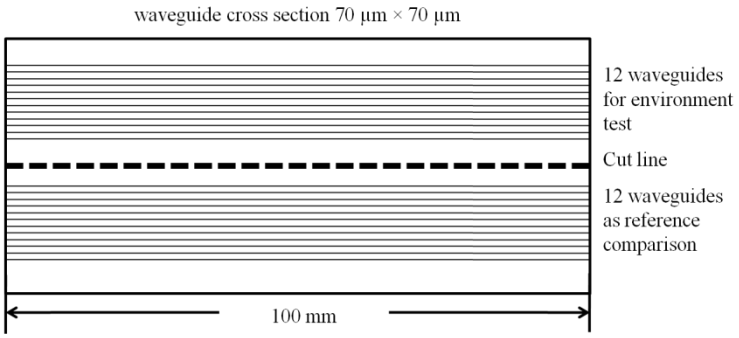

Figure 8-20 A waveguide sample repaired for environment aging test

Temperature-humidity aging cycling with 500 hours per cycle was performed in Stevenage Circuits Ltd. to assess the change in transmitted power. Figure 8-21 shows that after 1500 hours in 85%RH/85^{0}C environment, the transmitted power became too low to be detected by the PD used in the experiment.

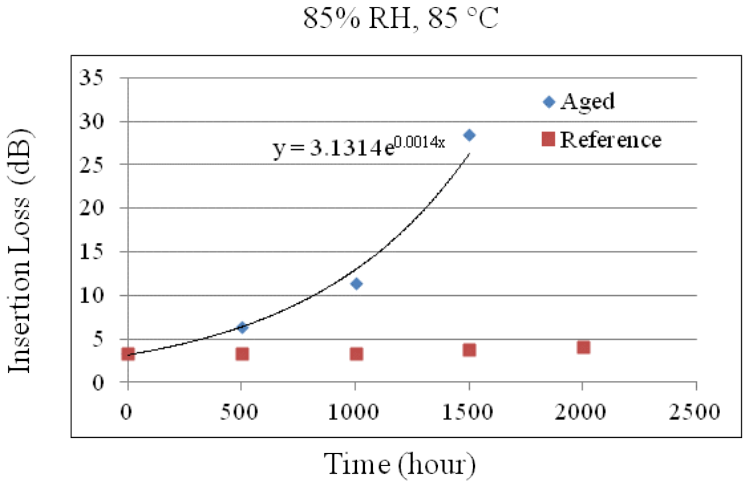

Figure 8-21 Insertion loss change after 2000 hours 85%RH/85^{0}C temperature-humidity cycling

The total insertion loss (L) after each aging cycle increased exponentially. A trend-line was fitted in the figure:

$$L = 3.1314 \cdot e^{0.0014x} \qquad \textbf{Eq. 8-6}$$

If 9.62 dB [8-12] is the designed power budget, then the waveguide could survive less than 1000 hours 85% R.H. / 85^{0}C storage test due to degradation of the waveguide material. Eq. 8-6 can be used as a design curve to predict the life cycle of the photolithographically fabricated Truemode® polymer waveguide.

8.4 Conclusions

Photolithographically manufactured buried channel multimode waveguides made from acrylate Truemode® polymer were characterized by measuring the optical transmission loss of key waveguide components, i.e. straight, bend and crossing. A detailed technique to measure the transmitted power at waveguide crossings was reported for the first time. The result of environmental tests of such polymer waveguides against temperature and humidity was reported for the first. Design rules derived from the experimental measurement could be potentially embedded in the next generation of E-CAD for integrated design and to assist optical system designers to optimise OPCB layout.

Chapter 8 References

[8-1] H. Baghsiahi, D. R. Selviah, M. Yau, and F. A. Fernandez, "Photolithographically manufactured acrylate multimode optical waveguide translation and rotation misalignment tolerances," in *2008 2nd Electronics Systemintegration Technology Conference*, 2008, pp. 617–622.

[8-2] Tetahertz-Photonics, "Truemode Backplane Enabling optical backplanes," *www.thzonline.com*, no. April, pp. 1–5, 2003.

[8-3] "Truemode™ wetfilm core datasheet," *Exxelis Limited*. [Online]. Available: http://www.exxelis.com/products/Truemode-datasheet-f.pdf. [Accessed: 01-Mar-2014].

[8-4] I. Papakonstantinou, D. R. Selviah, R. C. A. Pitwon, and D. Milward, "Low-Cost, Precision, Self-Alignment Technique for Coupling Laser and Photodiode Arrays to Polymer Waveguide Arrays on Multilayer PCBs," *IEEE Trans. Adv. Packag.*, vol. 31, no. 3, pp. 502–511, Aug. 2008.

[8-5] N. Bamiedakis, J. Beals, R. V Penty, S. Member, I. H. White, J. V Degroot, T. V. Clapp, and A. Cost-effective, "Cost-Effective Multimode Polymer Waveguides for High-Speed On-Board Optical Interconnects," *IEEE J. Quantum Electron.*, vol. 45, no. 4, pp. 415–424, 2009.

[8-6] S. Hiramatsu, K. Miura, and K. Hirao, "Optical Backplane Connectors Using Three-Dimensional Waveguide Arrays," *J. Light. Technol.*, vol. 25, no. 9, pp. 2776–2782, Sep. 2007.

[8-7] G. Sialm, D. Lenz, D. Erni, G. Bona, C. Kromer, M. X. Jungo, T. Morf, F. Ellinger, and H. Jäckel, "Comparison of Simulation and Measurement of Dynamic Fiber-Coupling Effects for High-speed Multimode Vcsels," *J. Light. Technol.*, vol. 23, no. 7, pp. 2318–2330, 2005.

[8-8] T. Ishigure, K. Shitanda, T. Kudo, S. Takayama, T. Mori, K. Moriya, and K. Choki, "Low-loss design and fabrication of multimode polymer optical

waveguide circuit with crossings for high-density optical PCB," *2013 IEEE 63rd Electron. Components Technol. Conf.*, pp. 297–304, May 2013.

[8-9] I. Papakonstantinou, K. Wang, D. R. Selviah, and F. A. Fernández, "Transition, radiation and propagation loss in polymer multimode waveguide bends," *Opt. Express*, vol. 15, no. 2, pp. 669–679, 2007.

[8-10] D. R. Selviah, A. Walker, D. Hutt, K. Wang, A. Mccarthy, F. A. Fernández, I. Papakonstantinou, H. Bagshiahi, H. Suyal, M. Taghizadeh, P. Conway, J. Chappell, S. S. Zakariyah, D. Milward, R. C. A. Pitwon, K. Hopkins, M. Muggeridge, J. Rygate, J. Calver, W. Kandulski, D. J. Deshazer, K. Hueston, D. J. Ives, R. Ferguson, S. Harris, G. Hinde, M. Cole, H. White, N. Suyal, H. ur Rehman, and C. Bryson, "Integrated Optical and Electronic Interconnect PCB Manufacturing Research," *Circuit World*, vol. 36, no. 2, pp. 5–19, 2010.

[8-11] I. Papakonstantinou, D. R. Selviah, K. Wang, R. A. Pitwon, K. Hopkins, and D. Milward, "Optical 8-Channel , 10 Gb / s MT Pluggable Connector Alignment Technology for Precision Coupling of Laser and Photodiode Arrays to Polymer Waveguide Arrays for Optical Board-to-Board Interconnects," *58TH Electron. COMPONENTS Technol. Conf. Proc.*, pp. 1769–1775, 2008.

[8-12] R. C. A. Pitwon, K. Wang, J. Graham-Jones, I. Papakonstantinou, H. Baghsiahi, B. Offrein, R. Dangel, D. Milward, and D. R. Selviah, "FirstLight: Pluggable Optical Interconnect Technologies for Polymeric Electro-Optical Printed Circuit Boards in Data Centers," *J. Light. Technol.*, vol. 30, no. 21, pp. 3316–3329, 2012.

[8-13] R. C. A. Pitwon, K. Hopkins, and D. Milward, "An optical backplane connection system with pluggable active board interfaces," *Circuit World*, vol. 33, no. 4, pp. 20–25, 2007.

[8-14] M. L. Wu, P. L. Fan, and C. T. Lee, "Completely adiabatic S-shaped bent tapers in optical waveguides," *IEEE Photonics Technol. Lett.*, vol. 9, no. 2, pp. 212–214, 1997.

[8-15] I. Papakonstantinou, D. R. Selviah, and K. Wang, "Insertion Loss and Misalignment Tolerance in Multimode Tapered Waveguide Bends," *IEEE Photonics Technol. Lett.*, vol. 20, no. 12, pp. 1000–1002, 2008.

[8-16] M. Hikita, S. Tomaru, K. Enbutsu, N. Ooba, R. Yoshida, M. Usai, T. Yoshida, and S. Imamura, "Polymeric optical waveguide films for short-distance optical interconnects," *IEEE J. Sel. Top. Quantum Electron.*, vol. 5, no. 5, pp. 1237–1242, 1999.

[8-17] S. Musa, A. Borreman, A. Kok, and M. Diemeer, "Experimental study of bent multimode optical waveguides," *Appl. Opt.*, vol. 43, no. 30, pp. 5705–5707, 2004.

[8-18] L. Dellmann, R. Dangel, R. Beyeler, C. Berger, F. Horst, B. J. Offrein, and G. L. Bona, "Polymer waveguides for high-speed optical interconnects," *Proc. EOS Top. Meet. Opt. Comput.*, pp. 131–132, 2004.

[8-19] Telecordia, "Telecordia GR-1209/GR-1221-CORE standards," in *Generic Reliability Assurance Requirements for Passive Optical Components*, 2010.

Chapter 9 Polymer Electro-Optical Printed Circuit Boards in Data Centres

9.1 Introduction

The growth in storage networks [9-1], [9-2] with more consumers using the Internet as a backup storage service, increased performance of network servers, worldwide increased dependence on the Internet and the growth of bandwidth-hungry applications, such as IPTV and video on demand (VoD) [9-3] has caused increased demand for bandwidth and capacity in data centres. The projected global digital demand will grow from 1.8 to 7.9 Zettabytes (ZBs or 1×10^9 Terabyte) from 2011 – 2015, of which the amount of available data storage will reach 3.3 ZB in 2015 [9-4].

However, the exponential increase in system bandwidth [9-4] and density of printed copper channels, e.g. on a data storage midplane or backplane, constantly push the limits of the current network and data centre infrastructure exposing the system to some of the fundamental constraints inherent to high frequency signal transmission along copper traces. Dielectric absorption and skin effect are the key loss mechanisms on a copper trace [9-5], which cause an increase in signal attenuation with frequency, while electro-mechanical connectors introduce parasitic capacitance and inductance effects, and conductive vias between layers within the printed circuit board can act as impedance stubs giving rise to partial reflections in the signal path [9-6], [9-7]. Many of these constraints can be mitigated to some degree [9-8], however, at signal data rates of 24 Gb/s and higher, additional design measures need to be taken into account, including the use of lower dielectric loss PCB substrates, skew and loss controlled electro-mechanical connectors and enhanced via control techniques such as back-drilling or buried vias [9-9–12]. All of the solutions, however, come at a mounting cost to the overall system design [9-13–16].

It is therefore proposed by many researchers [9-17–22] that using electro-optical PCB (OPCB) as the midplane incorporating optical interconnect technology is the solution to the bottleneck in data storage systems. OPCB technology offers significant performance over conventional PCBs: higher data rates (>10 Gb/s), less electromagnetic interference, reduction in power consumption and over a 50%

reduction in PCB size and weight [9-23]. There are large and rapidly growing demands for OPCB products by many industries including the IT, telecommunications, aerospace and space sectors [9-24].

9.1.1 Modern Data Storage System Architectures

One example of a data storage system is shown in Figure 9-1 (courtesy of Xyratex Ltd.), where data storage arrays, typically hard disk drives (HDDs) or solid-state drives (SSDs), are connected within systems of varying complexity and size with applications ranging from high capacity storage racks to high performance computing data storage systems. A data storage array system (Figure 9-1a) comprises an array of HDDs connected to one side of a passive midplane while controller modules and power supplies are connected to the other side. As shown, the midplane and its peripherals are connected in a mutually orthogonal geometry, which, as is described later, has advantages for incorporating optical connections.

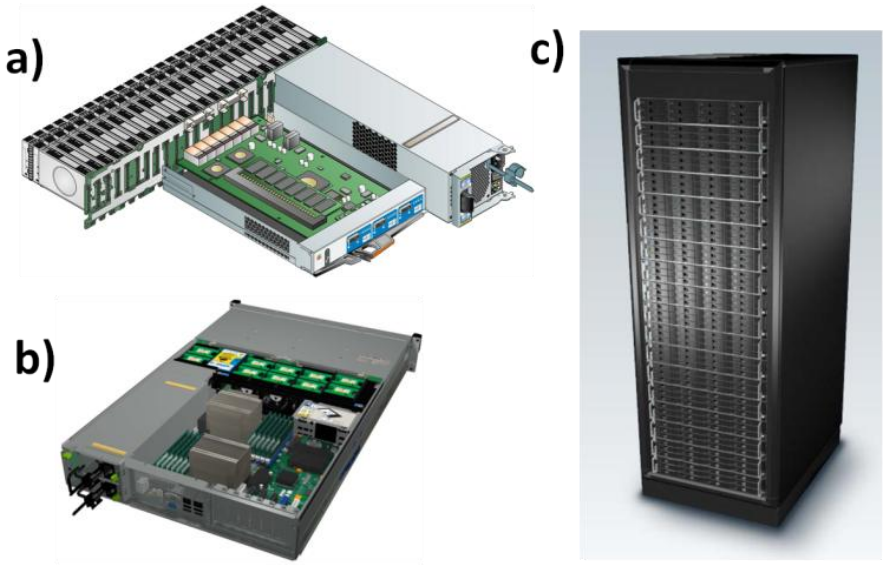

Figure 9-1 a) one example of a data storage system with storage media connected to one side of the midplane and controller modules and power supplies connected to the other b) Data storage integrated application platform c) data storage rack (courtesy of Xyratex Ltd.)

Figure 9-1b shows a data storage enclosure, which could be an application platform having desired functionality such as server hardware in a data storage system. Figure 9-1c shows a data storage rack in which assorted data storage subsystems, such as those shown in Figure 9-1a and Figure 9-1b are incorporated according to the required capacity and processing power of the rack and data centre application.

9.1.2 Data Centre Interconnect Topologies

The interconnect topology of high speed, high reliability data storage enclosures is typically defined by a passive dual star configuration (Figure 9-2), in which each data storage device supports two duplex data links on the midplane, one to each of two separate controller modules.

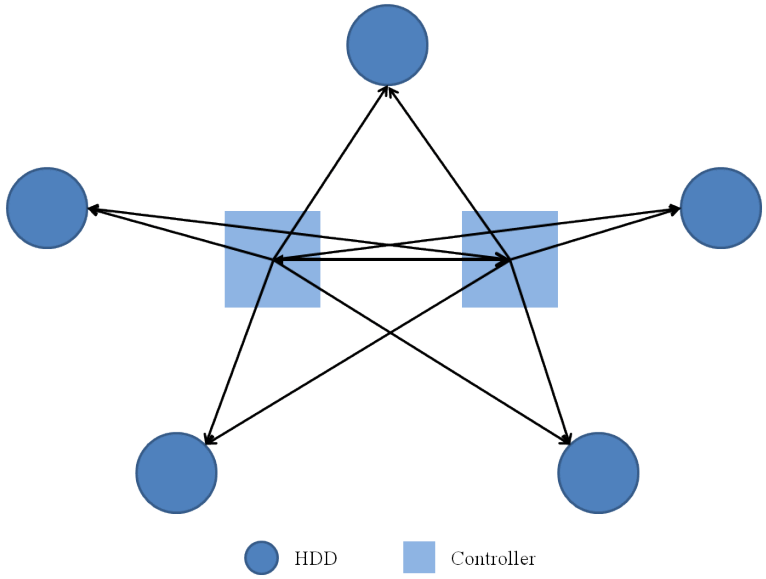

Figure 9-2 Schematic of a dual star configuration topology

As a current example, the Storage Bridge Bay (SBB) Specification [9-25], which defines mechanical, electrical and low-level enclosure management requirements for an enclosure controller slot, allows for a maximum of 48 interface lanes in a given data storage system enclosure. HDDs or SSDs in the enclosure each support two duplex links to each of the two controller modules. A further 17 duplex lanes directly connect the controllers to each other. The midplane of a 48 drive storage array would, therefore, have to accommodate 113 (2×48+17) duplex links or 226 high speed transmission links. The level of fault tolerance and scalability offered by these topologies forces increased complexity and cost into the midplane, particularly when interconnect protocols define serial data rates beyond 12 Gb/s [9-26].

9.1.3 Implementation of Embedded Optical Interconnect

In order to evaluate the viability of OPCB technology in a data centre environment, a demonstration platform (FirstLight) has been constructed, comprising 4 test line-cards, which are plugged electrically and optically into an electro-optical midplane. An OPCB has been developed incorporating conventional 10 copper layers for electrical

and electronic interconnect, and an optical interconnect layer comprising polymer optical waveguides. In addition, pluggable optical connectors have been developed incorporating high speed parallel optical transceivers and a passive alignment mechanism to ensure accurate dynamic optical engagement between the transceiver interfaces and the embedded polymer optical waveguides in the OPCB. The polymer waveguide layer includes self-alignment features to enable passive alignment and assembly of proprietary optical connector receptacle devices onto the polymer waveguides. Most of the work was carried out in close collaboration with Xyratex Technology Ltd, IBM-Zurich and Vario-print. Their contributions have been reviewed and acknowledged in chapter 4.

This chapter focuses on the author's contribution and describes the most compact and complex optical waveguide interconnections layout to date for an electrical-optical printed circuit board (OPCB) to meet exacting specifications to demonstrate how polymer waveguides would perform when subjected to the routing constraints expected within a conventional midplane form factor. Waveguide crossings at non-orthogonal angles and in bend sections were designed and used in a demonstrator for the first time.. A method for low cost, a high precision, passive optical assembly was presented. The demonstration platform with high speed optical data rate of 10.3125 Gb/s was measured through a polymer waveguide interconnect layer embedded into a 262 mm × 240 mm × 4.3 mm electro-optical midplane. A further new method for reducing the end facet roughness, and so the coupling loss, by curing a thin layer of core material at the end of the waveguide facet to cover the roughness fluctuations is presented.

9.2 Electro-Optical Midplane with Embedded Polymer Waveguides

9.2.1 Polymer Optical Waveguide Layer

A passive electro-optical midplane was designed, which included 10 electrical layers devoted to power distribution and low-speed (400 kHz to 5 MHz) bus communication and one optical polymer interconnect layer to convey high speed (10.3125 Gb/s) serial data between peripheral connectors. An optical interconnect layer was fabricated by IBM Zurich on one surface of the midplane PCB using an acrylate/polyurethane based polymer (IBM proprietary) exhibiting a propagation loss of 0.03 - 0.04 dB/cm at a

wavelength of 850 nm. The optical layer comprised a 70 µm thick core layer, a 100 µm lower cladding and upper cladding layer (as shown in Figure 9-3). The refractive index of the core material was n_{core} = 1.5600, while that of the cladding was $n_{cladding}$ = 1.5240, giving the step-index multimode waveguides a core - cladding index difference of Δn = 2.3% and a numerical aperture (NA) of 0.33.

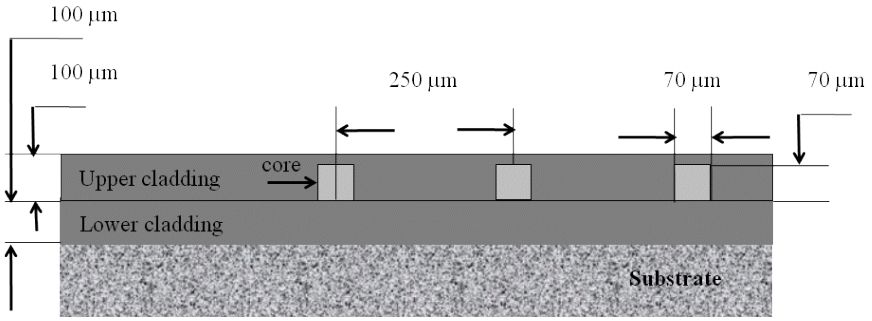

Figure 9-3 Schematic illustrating waveguide embedded in claddings, refractive index n_{core} = 1.5600 and $n_{cladding}$ = 1.5240

The waveguide core layer was patterned using a vectorial Laser Direct Imaging (LDI) writing process with a cross-section of 70 µm × 70 µm, to maximise coupling efficiency while keeping the lateral misalignment tolerance of transmitter and receiver as high as possible [9-27], [9-28], as mentioned in the previous chapter.

9.2.2 Design of an Electrical-Optical Backplane

In the demonstration platform, a complex polymer waveguide interconnect layout was designed to form the optical layer of a 262 mm × 240 mm × 4.3 mm electro-optical PCB. The design was guided by two key requirements: 1) In rack chassis systems, the peripheral cards are similarly oriented, so this was set as a constraint for the design of the system. All optical engagement interfaces of the midboard were oriented in the same direction to allow line cards to be pluggable in arbitrary slots and interchangeable. 2) The design was needed to meet the high-density requirement for a data storage system provided by Xyratex and to demonstrate the routing compactness and manoeuvrability. Therefore, waveguide structures needed to be carefully designed according to meticulously calculated optical waveguide layout design rules [9-28] described in the previous chapter to minimize the optical loss in each waveguide segment and to ensure that the total insertion loss for each waveguide channel falls within the receiver sensitivity threshold to allow bit error free (typically 10^{-12}) signal transmission.

Design rules for the photolithographically manufactured acrylate polymer multimode optical waveguide derived in the previous chapter were used in the layout of a complete set of optical interconnections on the backplane. Figure 9-4 is the optical interconnect layout the author designed using Cadence Allegro layout software for PCBs, for an electrical-optical printed circuit board (OPCB). This is the most compact and complex design to date for data storage applications. It includes parallel straight waveguide sections, cascaded 90° bends and waveguide crossing over a range of crossing angles.

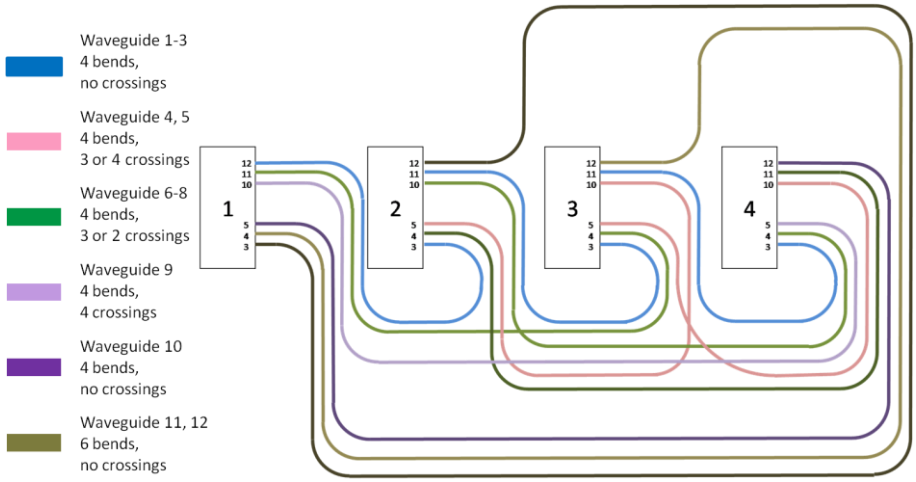

Figure 9-4 schematic of the optical waveguide interconnection layout

Figure 9-4 shows the schematic of the optical interconnect lay-out. The waveguides centre-to-centre pitch of 250 μm were arranged to match the linear arrays of 4 vertical cavity surface emitting lasers (VCSELs) and 4 photodiodes (PDs). The VCSELs are placed at the position 2-5 and the PDs are placed at 9-12, however, position 2 and 9 are currently not in use.

The design is a simplified model to simulate the midplane used in the data storage system. There are four identical rectangular optical engagement apertures in the middle of the optical board. The engagement apertures allow four line-cards. Each integrates 4 high bit rate (12.5 Gb/s) optical transceivers, to engage at right angles to the OPCB backplane. All of the four line-cards are interconnected by an any-to-any waveguide network via the 4 apertures. Each aperture has three bidirectional links (a pair of waveguides) and each connects to every other aperture, resulting in a total of 12 waveguides on the board.

There are three main advantages of this design. Firstly, all the optical interfaces were designed to face the same direction and to be identical to each other, so that the line-cards are interchangeable. Secondly, it could significantly reduce the manufacturing and maintenance costs, because any line-card can be plugged into any engagement aperture without special modification and maintenance technicians will not make a mistake in orientation and position of the board. Finally, the OPCB is very compact, as the line-cards are closely spaced to meet the design specification of a highly populated storage bridge bay (SBB). However, there were restrictions in the optical layout because of the compact design, e.g. waveguides had to bend almost immediately after the short straight sections to avoid other electrical connectors, e.g. power connectors. This would increase the total optical loss in each optical link as more waveguide bends were used.

It is worth mentioning again that the optical layout was designed and the corresponding optical insertion loss calculated based on previous experimental measurements [9-27] carried out on photolithographically fabricated polymer acrylate test waveguide [9-29] samples, which were cut using a dicing saw. The results may be different to the ones IBM obtained from their polymer material and fabrication technique. Each waveguide was designed to have an approximately square cross section 70 μm × 70 μm to minimise both insertion loss and crosstalk (Chapter 8.3.1 Crosstalk in Chirped Width Straight Waveguides Array). In chapter 8 the measurement results for waveguide bends showed that the optical loss decreased as the bend radius increased [9-27], [9-28]. However, as the bend radius increases beyond a certain point, around 17 mm in the author's measurements, propagation loss becomes more significant than the combination of transition and radiation loss since the larger radius bends have longer lengths and propagation loss is included also within the loss per bend. The least loss of 90° bends was measured for bend radii in the range of 16 mm to 22 mm. Therefore, the author chose bend radii values within this range taking the polymer waveguide fabrication techniques into account. However, IBM Zurich modified the bend radii to a range of 16.5 mm to 24.5 mm according to their internal data (commercial in confidence) when they fabricated the optical board. The modified radii are very close to the range of 16 mm to 22 mm the author has recommended.

The transmitter (VCSELs) and the receivers (PDs) on the line-card were located at the same position and pointing in the same direction. The waveguides, therefore, had to cross each other at some points to achieve full interconnection. Using design rules on crossing angles (recall chapter 8 waveguide crossing angles), the author used crossings in the range of 20 ° to 50 °. This is the first time such small waveguide crossing angles have been designed and used as optical interconnects. If one uses 5 crossings in one waveguide, the guided signal dropped only by 0.08 dB after one 20 ° crossing, in the worst case scenario, one has a maximum 0.4 dB drop after the 5 crossings at 20 °. Such a loss is very small and can be easily offset in the total power budget by adjusting other waveguide components. The author innovatively aligned the transmitters and receivers to their desired branches of a crossing to minimize crosstalk. It is more likely that a receiver will detect a proportion of a signal from the crossing branch Figure 9-5, if it aligns with a waveguide branch at an angle less than 90 ° to the propagation direction of the crossing signal; while there will be much less effect on crosstalk, if the receiver aligns with a waveguide branch that is almost oppositely directed at an angle greater than 90 degrees to the propagation direction of the crossing signal. However, in the new design the cross-coupled light instead goes into the transmitter rather than a detector, which may increase relative intensity noise, RIN, oscillations in a laser. If a further design rule is set to define that this crosstalk must be less than -30 dB it should have little effect on RIN.

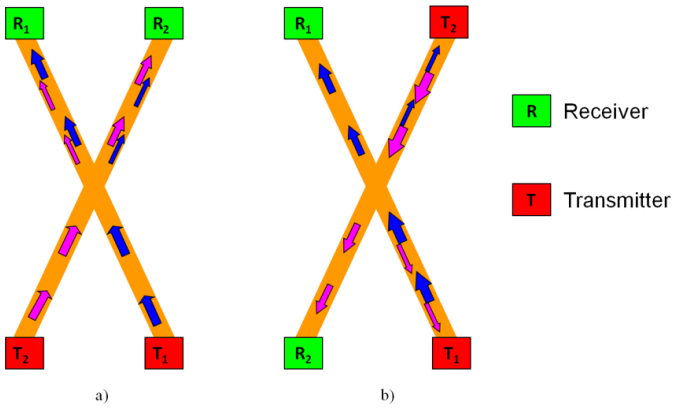

Figure 9-5 Crosstalk occurred inside waveguide crossings. a) severe crosstalk may be detected by both receivers R_1 and R_2 b) light leakage is still exist, however, most of the leaked light would be guided in the waveguide branches to transmitters so that there is much less crosstalk in both receivers R_1 and R_2

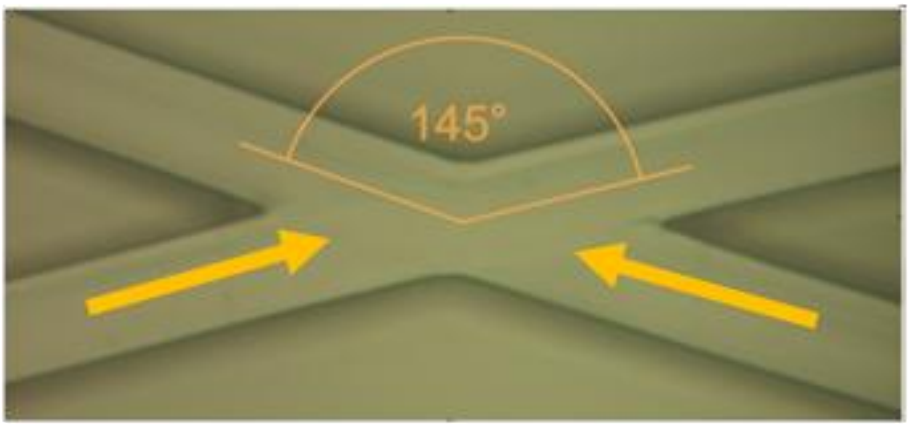

Figure 9-6 Top view micrographs showing two waveguides intersecting with a crossing angle of 145º

A number of waveguides intersect at one or more positions to accommodate space restrictions. The crossing angles chosen range from 130 ºto 160 º(see Figure 9-6, with respect to the relative propagation direction of light in the two waveguide branches) and the measured optical losses are 0.03 dB to 0.08 dB per crossing [9-28].

The test waveguide elements measured previously (Chapter 8) included 90 °bends and crossings at a range of angles. The insertion loss of each test waveguide is listed in Table 9-1. The test waveguide elements listed were deployed in the optical board layout and were used to calculate the power budget.

Table 9-1 Optical Loss of Each Waveguide Segment

Combined input/output coupling loss at both ends (dB)	90 °Bends		Propagation loss (dB/cm)	Crossing	
	Radius (mm)	Loss per bend (dB)		Crossing angle ( )	Loss per crossing (dB)
4.60 ±0.50[1]	16.5	0.94 ±0.07	0.08 ±0.01	160	0.08 ±0.03
	17.5	0.83 ±0.07		150	0.05 ±0.03
2.07 ±0.50[2]	18.5	0.85 ±0.07		145	0.05 ±0.03
	19.5	0.89 ±0.07		140	0.04 ±0.03
	20.5	0.95 ±0.07		130	0.03 ±0.03
	22.5	0.97 ±0.07			
	23.5	0.99 ±0.07			
	24.5	1.03 ±0.07			

[1] Average coupling loss without index matching fluid.

[2] Average coupling loss with index matching fluid.

The author kept the waveguide spacing at 250 μm close to the optical interfaces because the VCSELs and PDs have a pitch of 250 μm. According to the crosstalk design rules (chapter 8 Crosstalk between Straight Waveguides), the author increase the line spacing to 1250 μm (the maximum space available) once there is available space to minimize crosstalk among the neighbouring waveguides, as the optical power coupled from the adjacent waveguide reduced to -34 dB, which will cause negligible impact on the waveguides close by. The OPCB layout was optimized by incorporating design rules for the maximum output power and the minimum crosstalk.

The power budget of each optical link depends on the optical transmitter output power and on the sensitivity of the receiver used in the system. A receiver sensitivity of -11.1 dBm [9-30], matching the transceiver devices used in the demonstrator, was selected as the threshold for receiving error free signals (BER < 10^{-12}) at 10.3125 Gb/s (10G Ethernet) for the system design. The output power of the optical transmitters deployed in the system was -1.48 dBm, which limited the maximum tolerable insertion loss in each optical link to a power budget of 9.62 dB.

The division of the waveguides into straight and 90 º bends was used to calculate optical link loss. The total insertion losses on all 12 waveguides were calculated based on cascading the losses of all segments comprising a given waveguide. This neglects any mode mismatch loss occurring between different segments, which is expected to occur particularly between cascaded positive and negative bends and between straight and bend sections. The calculated results are listed in Table 9-2, which shows that all of the 12 waveguides were designed to have insertion losses lower than the error free threshold of 9.62 dB when index matching fluid (n = 1.5433 ± 0.0005 for 840.0 nm at 25 ℃) was applied on the coupling interfaces, while 10 out of 12 waveguides fell within the desired threshold when no index matching fluid was applied. The predicted optical losses of the last two waveguides exceeded the desired threshold, due to routing constraints increasing both the total length of waveguides and the number of bends in the waveguides, such that both material absorption and bend losses became prohibitive.

Table 9-2 Calculated Optical Loss in Each Waveguide Interconnect in Terms of Cascaded Loss from Every Waveguide Segment

Waveguide	No. of crossings	No. of 90 °bends	Length of straight section (cm)	Calculated optical loss (dB)	
				[1]	[2]
1	0	4	2.17	8.24	6.04
2	0	4	2.17	8.24	6.04
3	0	4	2.14	8.26	6.06
4	3	4	2.24	8.54	6.34
5	5	4	2.04	8.48	6.28
6	3	4	5.95	8.67	6.47
7	3	4	5.78	8.68	6.48
8	2	4	6.80	8.87	6.67
9	4	4	9.67	9.17	6.97
10	0	4	12.99	9.30	7.10
11	0	6	16.30	11.36*	9.16
12	0	6	20.19	11.81*	9.61

[1] calculation based on the coupling loss without index matching fluid.

[2] calculation based on the coupling loss with index matching fluid.

*insertion loss is higher than the threshold 9.62 dB due to routing constraints.

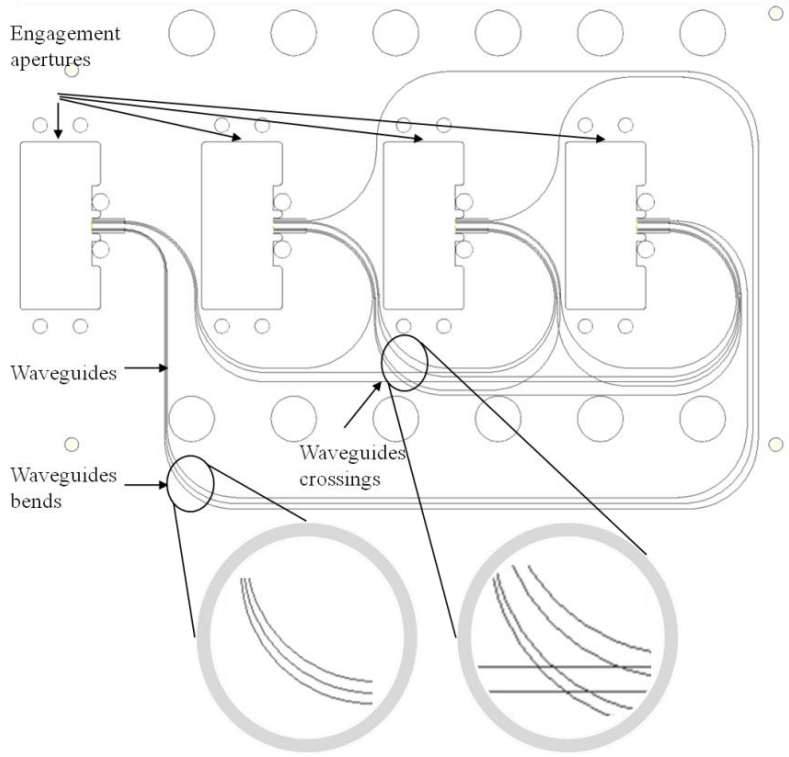

Figure 9-7 The most compact optical waveguide interconnection layout to date, including parallel waveguide straight sections, cascaded bends and non-orthogonal crossings

Figure 9-7 shows the final optical interconnection layout designed according to the design rules, including parallel waveguide straight sections, cascaded bends and non-orthogonal crossings and crossings in bends. Figure 9-8 shows a waveguide in the optical layer illuminated by 650 nm visible laser via a multimode step index fibre.

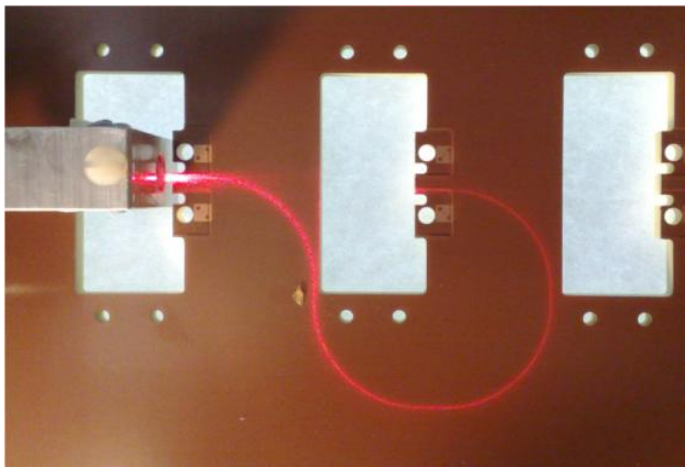

Figure 9-8 One waveguide interconnection illuminated by 650 nm visible laser via a multimode step index fibre

9.2.3 Insertion Loss Measurements for the Electrical-Optical Backplane with Polymer Waveguides

The complex optical waveguide layer designed by the author was incorporated into a hybrid passive electrical-optical PCB backplane assembly designed by Xyratex. The passive electrical-optical backplane fabricated by Varioprint and IBM Zürich to the above design was built up of 10 copper layers and one polymeric layer on the bottom side of the PCB board (Figure 9-9).

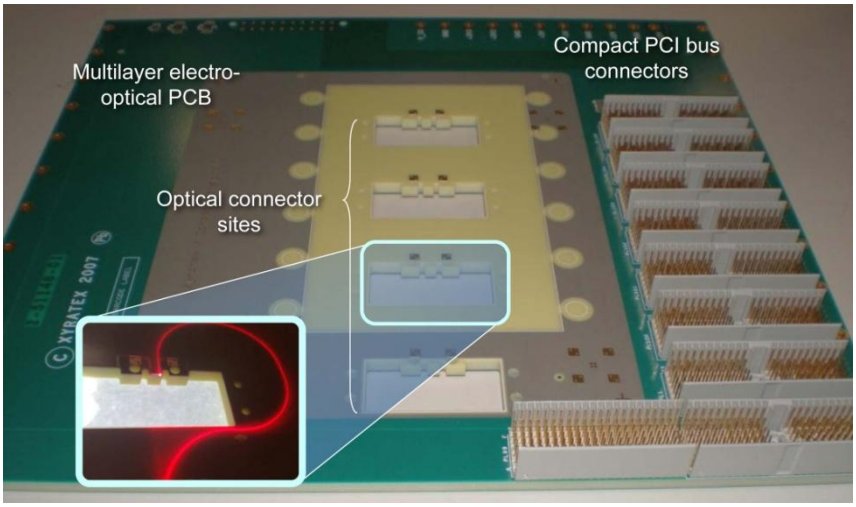

Figure 9-9 An electrical-optical backplane and a waveguide illuminated with 635 nm light exiting one of the connector slots

Initially, the optical layer was deposited directly onto the electrical PCB, but the board surface roughness caused unacceptably large variations in waveguide height of ±18 μm. The optical layer was fabricated on a separate flexible substrate to overcome this problem, and was laminated on the outer surface of the backplane PCB. This lamination technique showed significant thickness tolerances on multi electrical layer PCBs in the preliminary tests. The detailed fabrication technique has been reviewed in chapter 4.

The measurements for the optical insertion loss of the optical interconnects were conducted with Richard Pitwon from Xyratex and led by the author. The experimental configuration was the same as that for the waveguide crossings described in the previous chapter. An ST connector packaged 850 nm VCSEL was connected to a standard 50/125 μm step MM fibre with NA_{fibre}: 0.2. The fibre core cross-section area and its NA are less than the waveguide core 70 μm × 70 μm square and $NA_{\text{waveguide}}$ = 0.33 respectively. This will reduce the coupling loss when the fibre and the waveguide are perfectly aligned. The fibre was 10 m long and was wound 20 times around a 38 mm diameter circular post before it was butt coupled to a waveguide to fill the NA [9-27]. A thin (2 mm thick) silicon photo detector with an 8 mm aperture was calibrated against the light conditions in the dark room where the measurements were conducted to offset the background noise. The optical power at the output of the fibre was measured using the photodetector and was 0.00 ± 0.02 dBm. The launch fibre was mounted on a group of motorised linear translation stages with sub-micron step resolution in 3 axes, *x*, *y* and *z*, to accurately align the fibre to the waveguide and to maximize the light through the waveguide. The photodetector was put through one of the apertures on the backplane and was aligned to the output of the waveguide to measure insertion loss. An index matching fluid (n = 1.5694 ± 0.0005 at 589.3 nm) was also applied to the fibre-waveguide interface and waveguide output facet to reduce scattering loss caused by the roughness of the waveguide end facets. The loss measured for each interconnect included coupling losses at the fibre-waveguide interface, absorption by the propagation medium, transition losses due to modal mismatch between waveguide bend and straight segments and losses incurred at crossing junctions.

Though the FirstLight board contained 12 waveguides in total, the longest 3 waveguides were excluded from experimental characterization due to damage during assembly. Insertion loss measurements were made on the remaining 9 waveguides both with and without index matching fluid applied. The measurement results are shown in Figure 9-10 along with the original calculated values. The height of each column represents the total insertion loss in dB and the colours represent the conditions of measurement (with or without index matching fluid) and methods (calculation or measurement). The results highlight the strong dependence of loss on end facet roughness. The waveguides in the optical interconnect layout were designed to never exceed an insertion loss of 9.62 dB, the threshold required to achieve communication at a bit error rate (BER) of less than 10^{-12}.

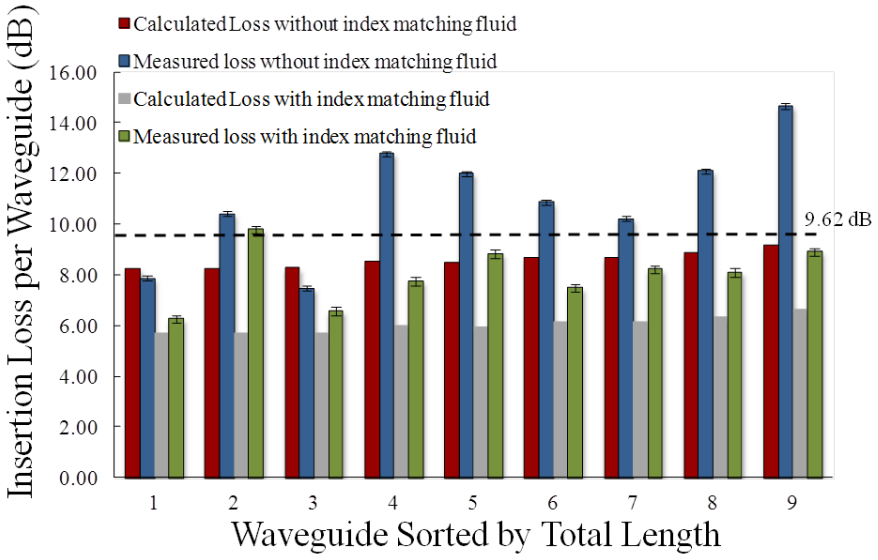

Figure 9-10 Calculated and measured values for insertion loss of a group of 9 waveguides on the OPCB. The plots are arranged in order of increasing waveguide length, starting from the shortest waveguide 1, as listed in Table 9-2. The longest 3 waveguides were excluded from experimental characterization due to damage during assembly. The dashed line shows the 9.62 dB threshold.

Figure 9-10 includes the comparison of the calculated optical losses without index matching fluid (red column) and the measured insertion losses of waveguides without index matching fluid applied (blue column) which are on average 2.36 dB higher than the calculated predictions. The insertion losses of waveguides 2, 4, 5, 6, 7, 8 and 9 without index matching fluid are in excess of the 9.62 dB error free threshold. The higher insertion losses are partially due to the higher scattering losses at the waveguide end facets, which depend on the surface roughness of the end facet in

question. The surface roughness in turn depends on how the end facets were cut and polished. In this case, the waveguide end facets are located at the edges of the milled midboard optical engagement apertures. Though the end facet roughness of these waveguides could not be measured without damaging the OPCB, waveguides cut using similar milling techniques to those deployed on this board exhibit RMS surface roughness values ranging from 183 nm to 350 nm [9-31]. The grey columns represent the calculated insertion losses with index matching fluid, the values for which are 2.57 dB lower than the waveguide losses calculated without index matching fluid applied. The green columns represent the measured insertion losses with index matching fluid applied. All of the measured insertion losses were less than or equal to the 9.62 dB design target to within experimental error. The measured insertion losses of the 9 waveguides were on average 2.93 dB lower than those measured without applying the index matching fluid (blue columns). This reduction is close to 2.53 dB (4.60 dB - 2.07 dB) reduction shown in measured results in Table 9-1. In both cases the measured loss was higher than the calculated loss with and without index matching fluid. This may be because the author ignored any mode mismatch loss occurring between different waveguide segments. The variations in insertion loss shown in Figure 9-10 (both calculated and measured) between waveguides with and without index matching fluid applied highlight the strong dependence of loss on end facet roughness.

9.2.4 Waveguide End Facet Roughness Treatment

Index matching fluid, however, is not a practical means of reducing the roughness of waveguide end facets in applications involving repeatable connection to the waveguides as the fluid tends to dry out gradually and may accumulate dust, which in turn will cause the end facet scattering losses to increase in an unpredictable manner. Over time, the index matching fluid evaporates, resulting in increased insertion loss. The insertion loss of waveguide samples with 61 nm and 910 nm RMS roughness increased to 3.9 dB and 8.1 dB two days after applying index matching fluid at both ends of the waveguides [9-31]. Therefore, a more durable method using waveguide core polymer to smooth the end facets was invented and demonstrated to permanently reduce the end facet roughness. The deployment of this technique improved waveguide transmissivity by 0.49 dB on average compared to waveguides with index matching fluid applied [9-31]. It should be noted that this technique was jointly

invented by David R. Selviah in UCL and Richard Pitwon in Xyratex and the experimental work was led by the author and conducted with Hadi Baghsiahi in in UCL and Richard Pitwon in Xyratex.

The waveguide samples cut by the milling router and dicing saw were also polished in order to examine its effect and to determine the challenges of manual polishing. Three types of silicon carbide grinding paper were used from coarse to fine grain. Polishing was carried out using a sequence of operations with progressively finer grains, these were, 20 μm grit sand cloth, 3 μm aluminum oxide polishing cloth, 1 μm fine grit aluminum oxide polishing cloth. Cerium Oxide 'Jewellers' Rouge' could also have been used in which the grain size reduces with use giving a progressively finer surface structure. The samples were rubbed on the surface of polishing paper in a figure of eight-shaped path when the polishing paper was held in a fixed position. Two people operated on each sample in two-minute sessions with 1-2 sessions for smoothing and 2-4 sessions for polishing. Each sample was held perpendicularly to a sanding table mounted and fixed on the floor. The sample was flipped 180 °around the vertical axis every 5-6 seconds to minimize polishing error caused by sample orientation and rotation speed of the hand. This type of error results in the surface not being flat but instead being tilted at different angles with deviations up to a few degrees to the horizontal direction. This is because the sample was tilted during polishing or can be due to the differing hardness of different materials such as FR4 and polymer. A jig could have been used to maintain the waveguides at right angles to polishing paper. Nevertheless, hand polishing is not a reliable method of reducing roughness as the finished surface quality is dependent on the ability of the polishing operative, the force applied and other human factors. Moreover, it is not suitable for mass production as a mechanical arm is needed to do the polishing which increases the cost and the results are inconsistent for a given type of board for several reasons. Firstly, the copper layer must be removed otherwise there will be a lot of copper dust contamination on the waveguide surface. Secondly, and more importantly, polishing removes some of the waveguide material so the polished end facet of the waveguide will not be exactly where it was cut, thus, increasing the gap between the laser source and the waveguide or the waveguide and the photodetector if the alignment method assumes the end surface to be at the cut position. Any gap results in increased

coupling loss and increasing laser beam diameter due to divergence unless the amount of material polished away is taken into account so that the optical source is moved that much closer to the waveguide to compensate.

Therefore, a new technique was developed to smooth the end facets of the cut waveguide. In this method, uncured liquid waveguide core material is coated on each of the end facets of the waveguide and cured to reduce the effect of end facet roughness. This actually acts like refractive index matching fluid without its evaporation drawback. The fabrication procedure is shown in Figure 9-11. Firstly, a small amount of liquid waveguide core polymer is applied using a dropper onto one end of the waveguide core when the waveguide is held vertically. The polymer droplet also covers the cladding too in the experiment reported here without observable detrimental effects. Secondly, a release agent, Silicone Lubricant Aerosol (CP1051, CRC Industries UK Ltd) is spayed on one side of a glass microscope slide (made by Menzel-Glaser) and this coated microscope slide is pushed against the waveguide end facet to flatten and spread uniformly the liquid core polymer droplet. Care was taken to make sure the waveguide was held perpendicular to the microscope slide. A clamp was used to apply force to the microscope slide of approximately 1.3 kPa, which gave a layer thickness of 10 ± 2 μm. It may be better to use a flatter surface such as an optical interferometer mirror with $\lambda/20$ or $\lambda/40$ or better but in the experiment reported a microscope slide was used. The surface roughness of the microscope slide was 9 ± 3 nm (measured using AFM by Hadi Baghsiahi) about twice that of a silicon wafer. The microscope slide was used to achieve a flat surface at the end of the waveguide and to be transparent to allow ultraviolet light to pass through it to cure the polymer.

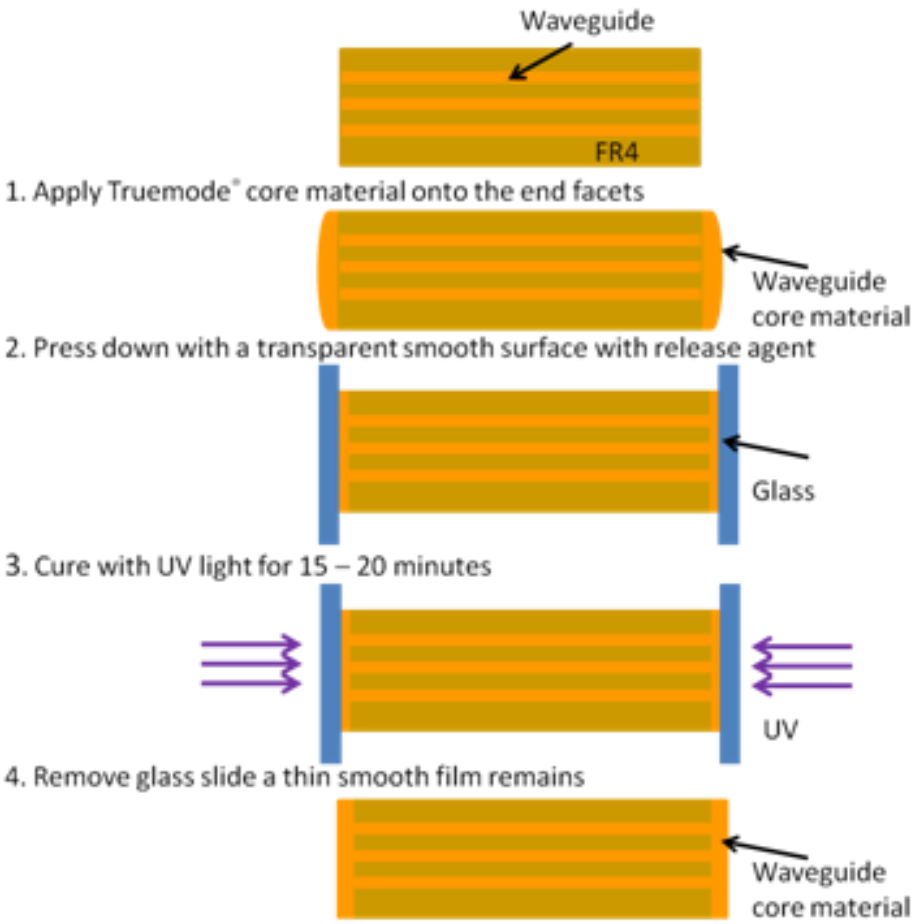

Figure 9-11 New technique for coating the ends of an array of cut waveguides with core polymer and curing to leave a flat smooth surface

UV light was then used to cure the polymer through the glass slide and the glass slide was removed. The result was a flat surface as smooth as the microscope slide. Both end facets were treated in the same manner.

The nine waveguides were measured before and after applying refractive index matching fluid, before and after applying core polymer and curing it according to the procedure described. All of the waveguides were cut with the same milling router and had similar roughness profiles. The optical loss measurement procedure was the same as that shown in Figure 9-10 and the same photodiode with a small form factor to fit inside the apertures [9-12]. The results for insertion loss are shown in Figure 9-12 where the waveguide number is arbitrary but relates to the same number as in reference [9-12].

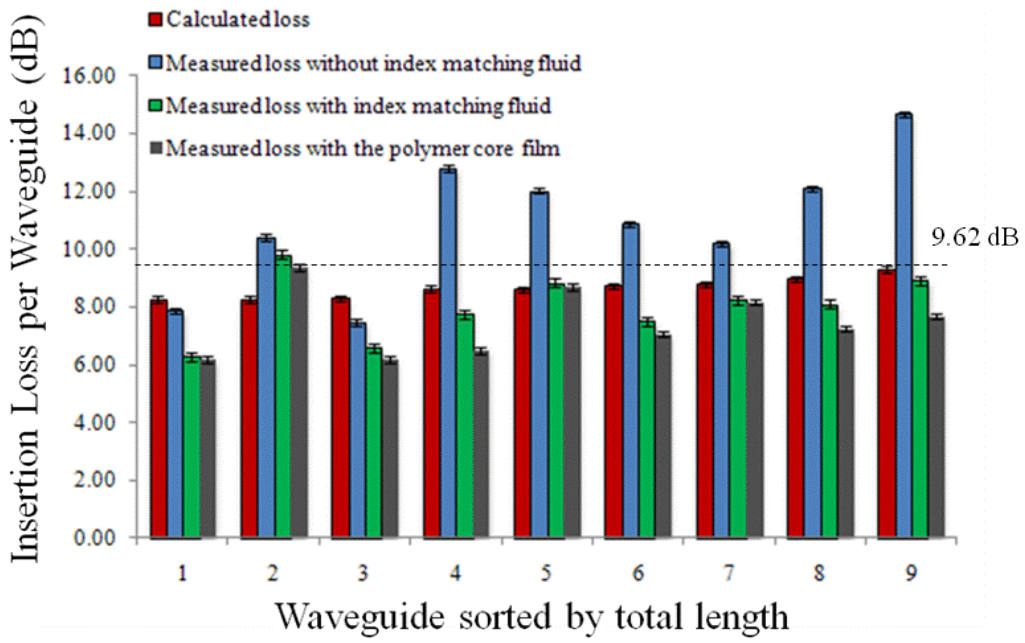

Figure 9-12. The insertion loss of a range of 9 waveguides with the same RMS roughness. The improvement of the coupling loss after applying index fluid matching on average is 2.23 ± 1.2 dB and after applying Truemode™ acrylate polymer is 2.60 ± 1.3 dB. There is an error bar on each column in the figure

Figure 9-12 shows that the insertion loss of the waveguides is reduced by on average 2.23 ± 1.2 dB after applying index matching fluid compared with the untreated case whereas the insertion loss was reduced on average by 2.60 dB ± 1.3 dB after applying the waveguide core polymer and curing it as described. Moreover, every waveguide had less loss with the new method compared to index matching fluid so the method is consistent and works correctly for many different lengths and types of waveguide having different numbers of bends and crossings, which affect the modes present in the waveguide. In conclusion, the core polymer results in even more improvement than the index matching fluid and is far more robust as it is solid and does not evaporate nor collect dust. The 0.37 dB improvement over index matching fluid may be because the closest available index matching fluid differed by a possible 0.9 % in refractive index from the core polymer refractive index, whereas using the core polymer itself produced a perfect match. No adverse effects were noticed due to the thin layer of core polymer over the surrounding cladding polymer. The error bars in Figure 9-12 for both the index matching fluid and core polymer were very small in all cases showing an improvement in loss reproducibility across samples which is important in a manufacturing environment.

9.2.5 Passive Alignment Method

One crucial requirement for the commercial deployment of optical PCB technology is a low-cost technique for the high-yield assembly of optical interface components onto the optical layers. In order to enable high volume assembly it is preferable that such techniques be passive and repeatable. David R. Selviah in UCL and Richard Pitwon in Xyratex jointly invented a low loss, low cost and high accuracy self alignment, mechanically transferable (MT) connector to butt-couple VCSELs to the end of waveguides to maximize light throughput [9-32]. The experimental measurement was carried out with Ioannis Papakonstantinou in UCL.

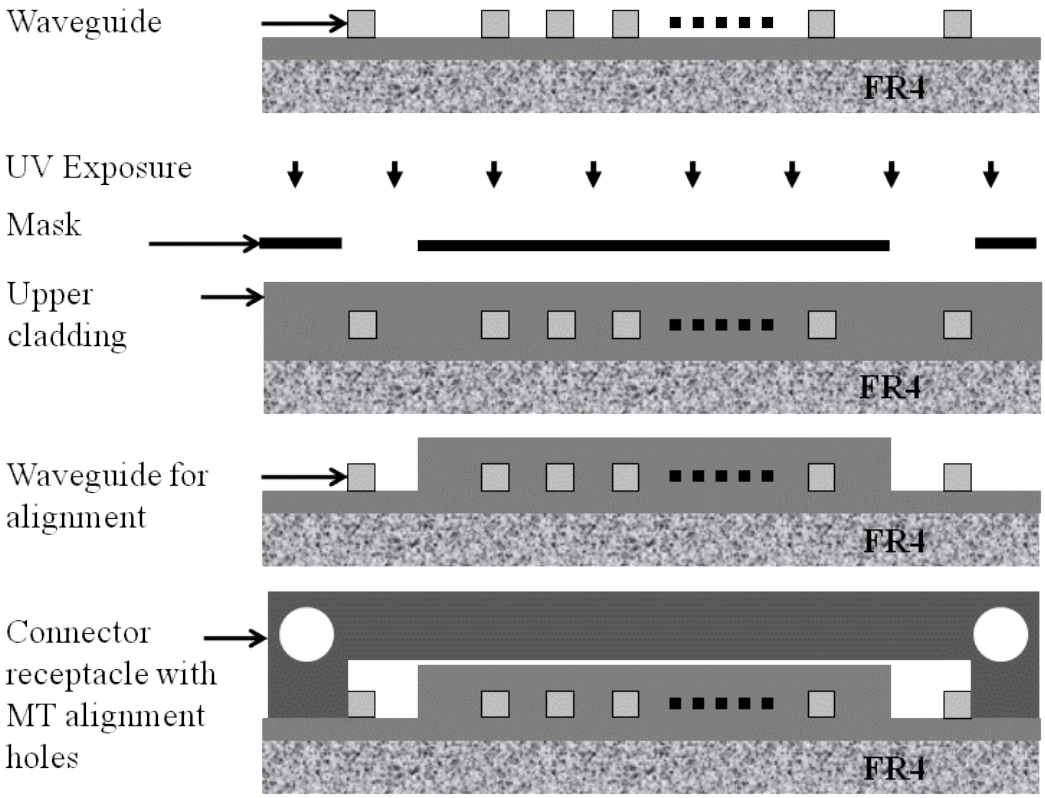

Figure 9-13 Fabrication process for the passive alignment features on the optical layer

The complete fabrication process for the passive alignment features on the optical layer is outlined in Figure 9-13. The procedure involves the fabrication of passive mechanical registration features in the core layer during the same process step in which the waveguide cores themselves are patterned. For the OPCB presented in this chapter, IBM Zurich used the LDI technique, in which a 372 nm CW GaN ultraviolet laser diode was moved across the uncured wet film core layer to selectively cure the waveguide core and the waveguide for alignment, which are positioned on either side of the signal waveguides. The positional accuracy of the alignment waveguide with

respect to the signal waveguides is comparable to that of the signal waveguides to each other [9-33], [9-34]. A layer of upper cladding polymer was then spun-coat over the core features. A photolithographic mask was aligned over the upper cladding, instead of uniformly curing the mask allowing all areas of the upper cladding to be cured except the mechanical registration waveguides. Thus, during the subsequent wet chemical development step, a clearance is created around the mechanical registration waveguides. This clearance allows for direct mechanical registration of arbitrary components to the waveguides. In addition, the fabrication tolerances required to pattern the upper cladding for this purpose are far lower than those required to pattern the waveguides themselves. It is only important that the outer edges of the registration waveguides be mechanically exposed to form the alignment features.

In order to measure the insertion loss as a function of the horizontal (x) and vertical (y) translational misalignments, the same system of motorized stages was used as previously. The position of maximum coupling efficiency corresponded to x=0, y=0, z=0, where z is the optical axis along the propagation direction of light. The x-y contour maps of insertion loss due to the VCSEL misalignment (Figure 9-14a) were generated by scanning the input along x and y. The insertion loss shown in the contour maps is the difference relative to the minimum insertion loss. To investigate the effect of photodiode (PD) misalignments the position of the PD and input was exchanged on the motorized stages and the experiments repeated. x-y contour maps of the relative insertion loss due to PD misalignment were generated (Figure 9-14b).

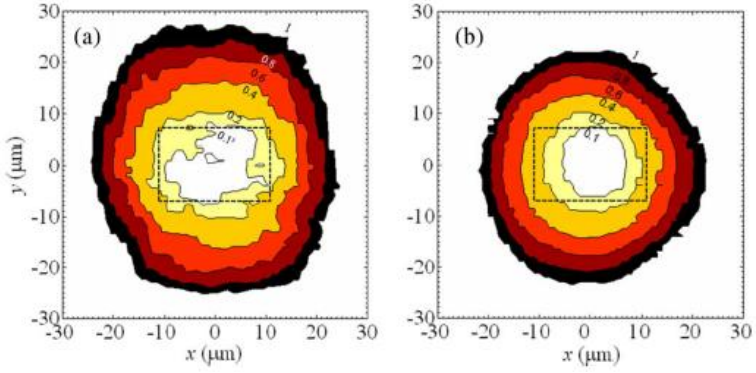

Figure 9-14 (a) Contour map of relative insertion loss compared to the maximum coupling position for VCSEL misalignment at z = 0. (b) Same for PD misalignment at z = 0. Scan resolution step was $\Delta x = \Delta y$ = 1 μm.

The dashed rectangle in the middle of the maps corresponds to the expected relative insertion loss according to the positional tolerance of the mechanical registration features with respect to each other, which has been measured to be ±3 μm for lateral misalignment in-plane and ± 4 μm normal to the PCB plane [9-33], [9-35]. The contour maps indicated a maximum of 0.2 dB due to vertical cavity surface emitting laser (VCSEL) misalignment tolerance and 0.4 dB [9-33] due to PD misalignment tolerance for the waveguides designed.

9.2.6 High Speed Data Transmission across Demonstration Platform

Peripheral test cards (Figure 9-15) were designed by Xyratex to relay external 10.3125 Gb/s 10 GbE LAN test data to each other optically across the midplane through the pluggable connectors. The 10 GbE LAN signal integrity test was carried out with, and led by, Richard Pitwon in Xyratex and bit error rate test was carried out with Richard and led by the author in UCL.

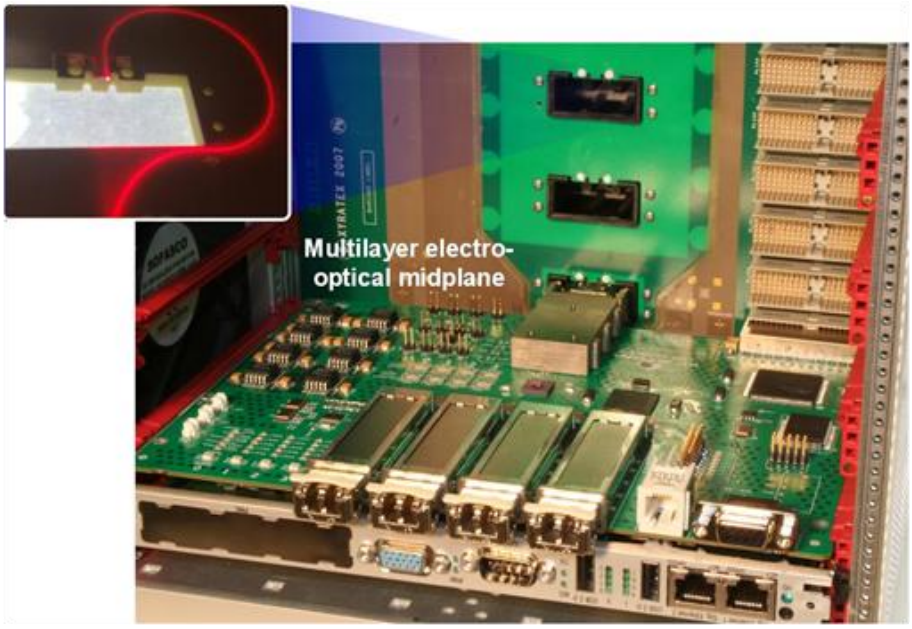

Figure 9-15 A peripheral test card and pluggable optical connector attached to an OPCB (Inset is a waveguide illuminated with 635 nm laser for aid of visualization)

Figure 9-16a shows the fully assembled demonstration platform. A Tektronix CSA8000B communications signal analyzer was used to generate proprietary 10 Gb Ethernet LAN traffic source to convey a 10.3125 Gb/s test data stream along a fiber-optic cable to one of the commercial XFP devices on the front edge of a peripheral test card in the demonstration platform.

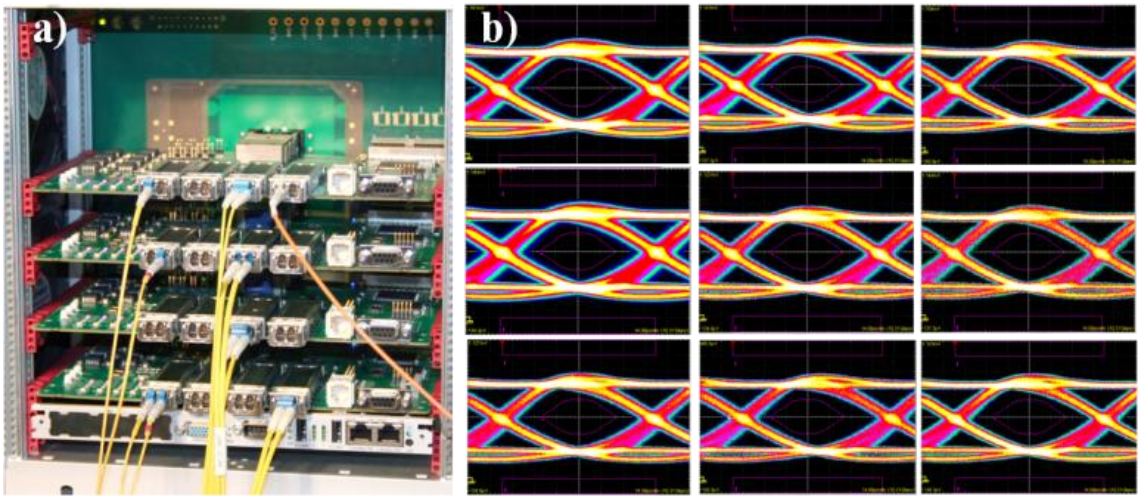

Figure 9-16 a) Demonstration platform fully assembled b) Eye diagrams showing 10.3125 Gb/s optical signals received from demonstration platform on 9 waveguide links under test

In total, 9 waveguides were tested as described and 10.3125 Gb/s test data was successfully conveyed between all test cards and their prototype connectors with an acceptable level of signal recovery. Figure 9-16b shows the eye diagrams corresponding to the nine waveguides under test. The average total peak to peak jitter on the 9 links including front end clock and data recovery through the exit XFP was measured to be 28.217 ps or 0.29 Unit Interval (UI), which is within the jitter thresholds for both transmitter input (0.61 UI) and receiver output (0.363 UI) as specified by the XFP MSA [9-36]. In addition, the author carried out bit error rate (BER) tests on the nine waveguides directly using an Anritsu signal analyzer MT1810 and a SFP+ driver and receiver unit and applied index matching fluid at both the launch and exit facets of the waveguides. The SFP+ unit [9-37] had the same sensitivity as the XFP model employed in the system, but excluded the clock recovery unit, so that the quality of the raw signal could be measured. A PRBS (Pseudorandom binary sequence) 2^{12}-1 pattern length Ethernet LAN traffic 10.3125 Gbit/s bit rate was generated by the MT1810 and was used to modulate the SFP+ transceiver. The optical signal was guided by a 50/125 μm step-index MM fiber with NA of 0.22, which was butt coupled to a waveguide channel on the prototype midplane. The output from the waveguide was captured by another MM fiber, which was connected to the receiver port of the SFP+ unit on the BER tester (BERT). Individual channels were tested with this arrangement. An error rate of less than 10^{-12} was achieved through each of the 9 waveguides under test.

9.3 Conclusion

This chapter has shown that a complex optical interconnect pattern of polymer waveguides can be deployed across a densely populated 6U board with error free transmission, BER $<10^{-12}$. The detailed characterisation studies of the insertion loss of optical embedded waveguide were given. This chapter also addressed some of the practical issues related to the adoption of this technology in real-world systems. A technique to passively align optical devices to such waveguides with high precision was developed and successfully implemented. A novel method giving a more robust waveguide end facet for use in commercial products was proposed and demonstrated, which reduces the insertion loss.

Chapter 9 References

[9-1] SearchStorage.com, "Data storage trends 2011: Predictions of hot data storage technologies," *searchstorage.techtarget.com*, 2011. [Online]. Available: http://searchstorage.techtarget.com/Data-storage-trends-2011-Predictions-of-hot-data-storage-technologies. [Accessed: 01-Jul-2014].

[9-2] C. Barrera and S. Wojtowecz, "Five storage trends for 2011," *Computer World UK*, 2011. [Online]. Available: http://www.computerworlduk.com/in-depth/infrastructure/3258578/five-storage-trends-for-2011/. [Accessed: 01-Jul-2014].

[9-3] G. Eastwood, "The Future of Digital Home Entertainment Key trends and drivers shaping devices , content and services," *Bus. Insights*, 2010.

[9-4] J. Gantz and D. Reinsel, "Extracting Value from Chaos," *IDC iView*, pp. 1–12, 2011.

[9-5] W. T. Beyene and C. Yuan, "An Accurate Transient Analysis of High-Speed Package Interconnects," *Analog Integr. Circuits Signal Process.*, no. 35, pp. 107–120, 2003.

[9-6] M. M. Pajovic, J. Yu, Z. Potocnik, and A. Bhobe, "GigaHertz-Range Analysis of Impedance Profile and Cavity Resonances in Multilayered PCBs," *IEEE Trans. Electromagn. Compat.*, vol. 52, no. 1, pp. 179–188, Feb. 2010.

[9-7] H. W. Johnson, "High-speed backplane connectors," *2011 IEEE Int. Symp. Electromagn. Compat.*, pp. 612–618, Aug. 2011.

[9-8] H. Cho, K. Koo, P. Kapur, and K. C. Saraswat, "The Delay , Energy , and Bandwidth Comparisons between Copper , Carbon Nanotube , and Optical Interconnects for Local and Global Wiring Application," *IEEE Int. Interconnect Technol. Conf.*, pp. 135–137, 2007.

[9-9] W.-T. Huang, C.-H. Lu, and D.-B. Lin, "Suppression of Crosstalk Using Serpentine Guard Trace Vias," *Prog. Electromagn. Res.*, vol. 109, pp. 37–61, 2010.

[9-10] R. Ramzan, J. Fritzin, J. Dabrowski, and C. Svensson, "Wideband Low-Reflection Transmission Lines for Bare Chip on Multilayer PCB," *ETRI J.*, vol. 33, no. 3, pp. 335–343, Jun. 2011.

[9-11] H. F. Lee, C. Y. Chan, and C. S. Tang, "Embedding capacitors and resistors into printed circuit boards using a sequential lamination technique," *J. Mater. Process. Technol.*, vol. 207, no. 1–3, pp. 72–88, Oct. 2008.

[9-12] R. C. A. Pitwon, K. Wang, J. Graham-Jones, I. Papakonstantinou, H. Baghsiahi, B. Offrein, R. Dangel, D. Milward, and D. R. Selviah, "FirstLight: Pluggable Optical Interconnect Technologies for Polymeric Electro-Optical Printed Circuit Boards in Data Centers," *J. Light. Technol.*, vol. 30, no. 21, pp. 3316–3329, 2012.

[9-13] F. Gisin and G. Dudnikov, "State of the Art of Electrical High Speed Backplanes in Industry Today and the Transition to Optical interconnects," *Biophotonics/Optical Interconnects VLSI Photonics/WBM Microcavities, 2004 Dig. LEOS Summer Top. Meet.*, vol. 1, pp. 7–8, 2004.

[9-14] W. Heirman, J. Dambre, I. Artundo, C. Debaes, H. Thienpont, D. Stroobandt, and J. Van Campenhout, "Predicting the performance of reconfigurable optical interconnects in distributed shared-memory systems," *Phot. Netw. Commun.*, vol. 15, pp. 25–40, 2008.

[9-15] J. A. Conway, S. Sahni, and T. Szkopek, "Plasmonic interconnects versus conventional interconnects: a comparison of latency, cross- talk and energy costs," *Opt. Express*, vol. 15, no. 8, pp. 1069–1071, 2007.

[9-16] K. Koo, H. Cho, P. Kapur, and K. C. Saraswat, "Performance Comparisons Between Carbon Nanotubes, Optical, and Cu for Future High-Performance On-Chip Interconnect Applications," *IEEE Trans. Electron Devices*, vol. 54, no. 12, pp. 3206–3215, 2007.

[9-17] F. E. Doany, C. L. Schow, C. W. Baks, D. M. Kuchta, S. Member, P. Pepeljugoski, L. Schares, R. Budd, F. Libsch, R. Dangel, F. Horst, B. J. Offrein, and J. A. Kash, "160 Gb/s Bidirectional Polymer-Waveguide Board-Level Optical Interconnects Using CMOS-Based Transceivers," *IEEE Trans. Adv. Packag.*, vol. 32, no. 2, pp. 345–359, 2009.

[9-18] L. Schares, J. A. Kash, F. E. Doany, C. L. Schow, C. Schuster, S. Member, D. M. Kuchta, P. K. Pepeljugoski, J. M. Trewhella, C. W. Baks, R. A. John, L. Shan, Y. H. Kwark, R. A. Budd, P. Chiniwalla, F. R. Libsch, J. Rosner, C. K. Tsang, C. S. Patel, J. D. Schaub, R. Dangel, F. Horst, B. J. Offrein, D. Kucharski, D. Guckenberger, S. Hegde, H. Nyikal, C. Lin, A. Tandon, G. R. Trott, M. Nystrom, D. P. Bour, M. R. T. Tan, and D. W. Dolfi, "Terabus: Terabit / Second-Class Card-Level Optical Interconnect Technologies," *J. Quantum Electron.*, vol. 12, no. 5, pp. 1032–1044, 2006.

[9-19] R. Dangel, C. Berger, R. Beyeler, L. Dellmann, M. Gmur, R. Hamelin, F. Horst, T. Lamprecht, T. Morf, S. Oggioni, M. Spreafico, and B. J. Offrein, "Polymer-Waveguide-Based Board-Level Optical Interconnect Technology for Datacom Applications," *IEEE Trans. Adv. Packag.*, vol. 31, no. 4, pp. 759–767, Nov. 2008.

[9-20] S. Uhlig, "Micro-Processing Applied to Optical Interconnects and High-Frequency Packaging," *Sci. Technol.*, no. 1011, 2006.

[9-21] P. Lukowicz, J. Jahns, R. Barbieri, P. Benabes, T. Bierhoff, a. Gauthier, M. Jarczynski, G. a. Russell, J. Schrage, W. Sullau, J. F. Snowdon, M. Wirz, and G. Troster, "Optoelectronic interconnection technology in the holms system," *IEEE J. Sel. Top. Quantum Electron.*, vol. 9, no. 2, pp. 624–635, Mar. 2003.

[9-22] N. Bamiedakis, J. Beals, R. V Penty, S. Member, I. H. White, J. V Degroot, T. V. Clapp, and A. Cost-effective, "Cost-Effective Multimode Polymer Waveguides for High-Speed On-Board Optical Interconnects," *IEEE J. Quantum Electron.*, vol. 45, no. 4, pp. 415–424, 2009.

[9-23] R. C. A. Pitwon, K. Hopkins, K. Wang, D. R. Selviah, H. Baghsiahi, B. J. Offrein, R. Dangel, F. Horst, M. Halter, and M. Gmür, "Design and implementation of an electro-optical backplane with pluggable in-plane connectors," *Proc. SPIE*, p. 76070J–76070J–12, 2010.

[9-24] D. R. Selviah, A. C. Walker, D. A. Hutt, K. Wang, A. McCarthy, F. A. Fernández, I. Papakonstantinou, H. Baghsiahi, H. Suyal, M. Taghizadeh, P. Conway, J. Chappell, S. S. Zakariyah, D. Milward, R. C. A. Pitwon, K. Hopkins, M. Muggeridge, J. Rygate, J. Calver, W. Kandulski, D. J. Deshazer, K. Hueston, D. J. Ives, R. Ferguson, S. Harris, G. Hinde, M. Cole, H. White, N. Suyal, H. ur Rehman, and C. Bryson, "Integrated optical and electronic interconnect PCB manufacturing research," *Circuit World*, vol. 36, no. 2, pp. 5–19, 2010.

[9-25] "Storage Bridge Bay (SBB) Specification," *Storage Bridge Bay Working Group Inc.*, 2008. [Online]. Available: http://www.sbbwg.org. [Accessed: 01-Jul-2014].

[9-26] "Serial Attached SCSI Master Roadmap," *http://www.scsita.org*, 2011. [Online]. Available: http://www.scsita.org/sas_library/6gbs-sas/roadmap-1/. [Accessed: 01-Jul-2014].

[9-27] I. Papakonstantinou, K. Wang, D. R. Selviah, and F. A. Fernández, "Transition, radiation and propagation loss in polymer multimode waveguide bends," *Opt. Express*, vol. 15, no. 2, pp. 669–679, 2007.

[9-28] K. Wang, I. Papakonstantinou, D. R. Selviah, H. Baghsiahi, and G. Yu, "Design rules for Polymer Multimode Waveguide Interconnects and Design of waveguide layout for a highly constrained Electrical-Optical Backplanes," *Opt. Express*.

[9-29] K. Wang, D. R. Selviah, I. Papakonstantinou, H. Baghsiahi, and F. A. Fernandez, "Photolithographically manufactured acrylate polymer multimode optical waveguide loss design rules," in *2008 2nd Electronics Systemintegration Technology Conference*, 2008, pp. 1251–1256.

[9-30] "Datasheet: 10 Gbps Dual Rate 850 nm Multi-Mode XFP Transceivers," *MRV Communications, Inc.*, 2010. [Online]. Available: www.mrv.com/. [Accessed: 01-Jul-2014].

[9-31] H. Baghsiahi, K. Wang, W. Kandulski, R. C. A. Pitwon, and D. R. Selviah, "Optical Waveguide End Facet Roughness and Optical Coupling Loss," *J. Light. Technol.*, vol. 31, no. 16, pp. 2659–2668, Aug. 2013.

[9-32] I. D. Johnson, R. C. A. Pitwon, D. R. Selviah, and I. Papakonstantinou, "Optical printed circuit board and manufacturing method," Patent number: WO2007/0101842006.

[9-33] I. Papakonstantinou, D. R. Selviah, R. C. A. Pitwon, and D. Milward, "Low-Cost, Precision, Self-Alignment Technique for Coupling Laser and Photodiode Arrays to Polymer Waveguide Arrays on Multilayer PCBs," *IEEE Trans. Adv. Packag.*, vol. 31, no. 3, pp. 502–511, Aug. 2008.

[9-34] I. Papakonstantinou, D. R. Selviah, K. Wang, R. A. Pitwon, K. Hopkins, and D. Milward, "Optical 8-Channel , 10 Gb / s MT Pluggable Connector Alignment Technology for Precision Coupling of Laser and Photodiode Arrays to Polymer Waveguide Arrays for Optical Board-to-Board Interconnects," *58TH Electron. COMPONENTS Technol. Conf. Proc.*, pp. 1769–1775, 2008.

[9-35] D. R. Selviah, F. A. Fernández, I. Papakonstantinou, K. Wang, H. Bagshiahi, A. Walker, A. Mccarthy, H. Suyal, M. Taghizadeh, D. Hutt, K. Williams, J. Chappell, S. S. Zakariyah, and D. Milward, "Integrated Optical and Electronic Interconnect Printed Circuit Board Manufacturing," *Circuit World*, vol. 34, no. 2, pp. 21–26, 2008.

[9-36] "10 Gigabit Small Form Factor Pluggable Module," *SFF Committee*, no. 408, 2005.

[9-37] "Datasheet: 10 Gbps 850 nm Multi-mode SFP + Transceiver," *MRV Communications, Inc.*, 2010. [Online]. Available: www.mrv.com/. [Accessed: 01-Jul-2014].

Chapter 10 Conclusions and Future Work

10.1 Conclusions

10.1.1 Colour Separating Backlight with Embedded Mirrors

A novel colour separating light guide for liquid crystal displays (LCDs) was modelled using a non-sequential ray-tracing technique. We designed a uniform thickness guide that simplified the fabrication procedure, as it was convenient for use with photolithographic techniques. Periodic, limited length, discrete gratings were used for the 1st time on the surface of the backlight unit. The pioneering design has some advantages over the conventional continuous grating: It allowed us to control the size of the exit aperture from the light guide to direct the output light normal to the display screen. It could potentially allow us to control the strength of each grating window individually by either varying the modulation depth of the grating or the length of each grating, thereby, obtaining better uniformity. We designed two cylindrical micro lens arrays which gave more design variables to enable optimization of collimation normal to the display at the centre of each pixel of red, green and blue respectively. A horizontal micro-mirror array was invented and was embedded inside the light guide to improve the overall luminous efficiency. The depth (d) and width (w) of the mirror layer were optimised at $d = 10 \pm 2$ μm beneath the grating and $w = 160 \pm 2$ μm for each mirror respectively. The light exiting from the light guide, when the mirror was employed and optimised, increased by 38.2% compared to the case without the embedded mirror array.

10.1.2 Modelling the Angular Variation of the Reflected Light from the Nematic Liquid Crystal in an LCOS Rear Projection TV System

The work described in chapter 6 combines a ray-tracing program, a full dynamic liquid crystal director model and an LC optics model to simulate the performance of an RPTV system using a liquid crystal on silicon (LCOS) panel. Detailed simulation of the system performance is required because of the necessity to maintain very high and uniform contrast ratios in such systems and because of the variable viewing angle characteristics of LCDs. The dynamic LC director simulation allows accurate calculation of the reflection from the LCOS device. The optical results of the LC simulation can be imported into the ray-tracing software for tracing back through the

projection optics and redirection to a projection screen. Thus, the work described here can be used to simulate the whole light path from illumination to the display screen using both ray-tracing and Liquid Crystal dynamic modelling. We have demonstrated how combined ray tracing and LC modelling can reveal useful information about viewing angle variation over the LCOS panel area, which would not be apparent from LC modelling alone.

10.1.3 Experimental Measurement and Ray Tracing Modelling of Optical Loss and Crosstalk in Multimode Step-index Photolithographically Fabricated Polyacrylate Polymer Waveguide Crossings

The optical loss caused by waveguide crossings was calculated using the ray tracing method for a range of crossing angles and the simulation results were compared with the experiment results. For the first time, the detailed models of light sources for modelling of multimode polymer waveguides were investigated. The parameters, i.e. divergence and intensity profiles, used in the light source models were obtained from experimental measurements of far field and near field energy distributions at the output of a 10 cm long straight waveguide. A best match semi-empirical light source, was found by comparing the 2D RMS and standard deviation values of the results of modelled light sources with the measured one. However, it was time consuming to create the semi-empirical source using ray tracing and was only the best matched to a particular mode of a waveguide. A Gaussian light source with matching angular divergence to the measured light profile is recommended as a general method for modelling the light source for a multimode waveguide. In addition to the square cross section waveguide model, a ray trace model of non-rectangular waveguides based on the waveguide shape of the cross-section of a photolithographically fabricated polyacrylate polymer waveguide is reported for the first time. The simulated results indicated that the realistic cross section shape waveguide had higher crossing loss and more crosstalk at 20 °crossings than the one with a square cross section.

10.1.4 Development of Design Rules for Polymer Optical Waveguides

Chapter 8 characterised photolithographically-manufactured acrylate polymer multimode waveguides by measuring the optical loss of key waveguide components. Photolithographically manufactured buried channel multimode waveguides made from acrylate Truemode® polymer were characterized by measuring the optical

transmission loss of key waveguide components, i.e. straight, bend and crossing. A technique to measure the transmitted power at waveguide crossings is reported for the first time. The result of environmental testing of such polymer waveguides against temperature and humidity is reported for the first time. Design rules derived from the experimental measurement could be potentially embedded in the next generation of E-CAD for integrated design and to assist optical system designers to optimise OPCB layouts.

10.1.5 Pluggable Optical Interconnect Technologies for Polymeric Electro-Optical Printed Circuit Boards in Data Centres

We have developed and successfully implemented a technique to passively align optical devices to such waveguides with high precision. The most compact and complex optical interconnects layout to date, including parallel straight waveguide sections, cascaded 90 ° bends and waveguide crossing other than 90 ° angles, has been designed using Cadence Allegro for the first time. It was tested and used in an optic-electrical demonstration platform to convey a 10.3 Gb/s data stream. Our results have shown that a complex optical interconnect pattern of polymer waveguides can be deployed across a densely populated 6U board with error-free transmission. A further new method for reducing the end facet roughness and so the coupling loss, by curing a thin layer of core material at the end of the waveguide facet to cover the roughness fluctuations, was proposed and successfully demonstrated, giving the best results reported to date. It resulted in an improvement of the insertion loss of 2.8 dB, which was better than the results obtained by using index matching fluid.

10.2 Future work

10.2.1 Design Rules for Other Fabrication Techniques

The future work for design rules would be to obtain more measured data from other waveguide manufacturing technologies – laser-writing, laser ablation and inkjet printing and waveguide materials, e.g acrylate and polysiloxane. Insertion loss, propagation loss (Figure 10-1), cross talk and misalignment tolerance on horizontal and vertical axis should be measured and compared. More measurement techniques e.g. direct butt coupling and free space coupling, should be assessed and used to measure the waveguide insertion loss.

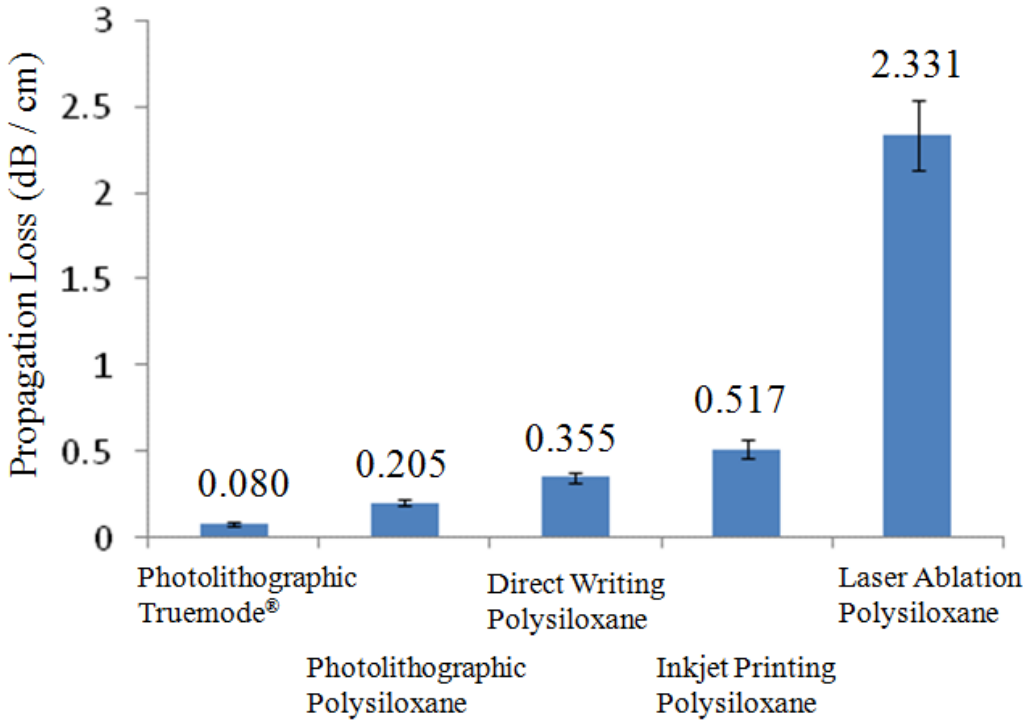

Figure 10-1 Propagation loss comparison of 4 fabrication techniques: Photolithography, laser direct writing, inkjet printing and laser ablation for the two polymer materials: polyacrylate and polysiloxane. The listed losses were mean values.

10.2.2 Ray Trace Models of Inkjet Printed Multimode Step Index Acrylate Polymer Waveguides

Ray trace models of waveguides based on the real shape of the cross-section (**Error! Reference source not found.**) of the inkjet-printed acrylate polymer waveguide should be carried out. Insertion loss as a function of space ratio (the ratio of waveguide height to its width) of the waveguide cross section should be assessed by both ray trace model and experimental measurements to optimize the ratio. Insertion loss, propagation loss, cross talk and misalignment tolerance (Figure 10-2) should be experimentally measured to assess the dependency of performance of the waveguide on the inkjet printing settings.

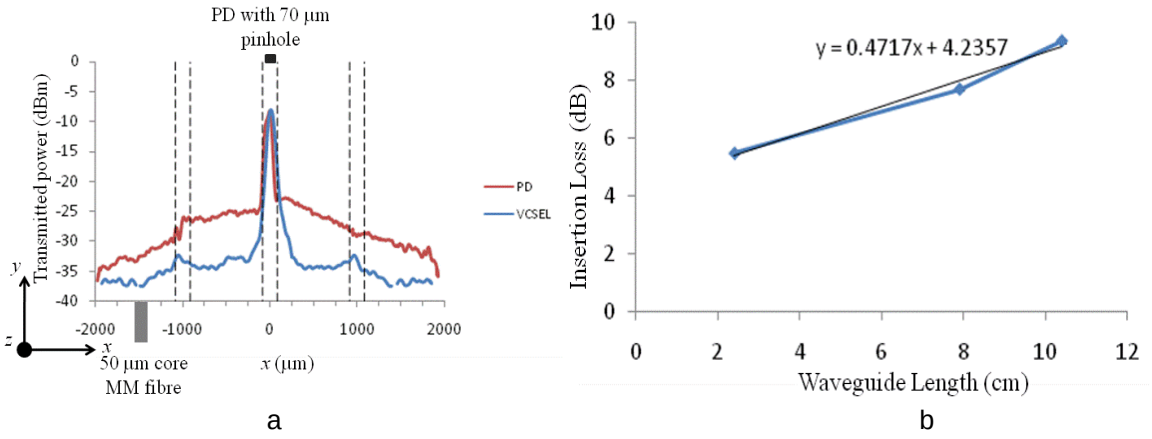

Figure 10-2 Experimental measurement of the inkjet printed samples made of Polysiloxane fabricated in Loughborough University. The sample was cut with a low speed BUEHLER ISOMET™ saw, 5 rpm, unpolished. a. **Crosstalk within straight waveguides Maximum output: -8.30 dBm and crosstalk in the adjacent waveguide: PD: -20.03 dBm, VCSEL: -25.83 dBm.** b. **Insertion loss and propagation loss measurement. Sample lengths were: 24.30 mm, 79.60 mm and 10.43 mm. Propagation loss was 0.4717 dB / cm and coupling loss was 4.24 dB.**

10.2.3 Modelling the Angular Variation of the Reflected Light from the Nematic Liquid Crystal in an LCOS Rear Projection TV System

The simulation can be improved by combining a ray-tracing program and a full dynamic liquid crystal director model to simulate the performance of an RPTV system using an LCOS panel. The results presented in this thesis are for the mixed twisted nematic (MTN) case, but the director model can be easily applied to other operating modes used in RPTV, such as vertically aligned nematic (VAN). In addition, the method can be applied to the full pixel level performance including electric fringe field effects etc., using the three dimensional capability of the model for the director structure. While the results presented are for a single LCOS panel, the method could equally well be applied to multiple panel systems.

10.2.4 Design Waveguide Structures for Bend Loss Reduction

In-plane bends are an inextricable requirement in complex waveguide layouts on OPCBs. However, bend radii as large as the minimum bend radius of 24.5 mm deployed on the FirstLight midplane would be difficult to accommodate within a high density PCB layout, especially where high numbers of optical waveguides are involved. Research into novel waveguide structures allowing a reduction in bend loss

and corresponding reduction in minimum bend radius was proposed by Xyratex to address this issue [9-39].

Appendix A. Commercial Evaluation Report of Electro-Optical Backplane Technology (FirstLight)

A.1. Introduction

This report assesses the commercial potential of the electro-optical backplane technology (OPCB, FirstLight) developed during the flagship project, Integrated Optical and Electronic Interconnect PCB Manufacturing, a 36-month Engineering and Physical Sciences Research Council (EPSRC) funded research project via the Innovative electronics Manufacturing Research Centre (I*e*MRC) grant FS/06/01/01. The work in this report was sponsored by UCL Business.

FirstLight was organised with the partners chosen on the basis of a wide range of contrasting expertises and formed a supply chain for the OPCB technology. The consortium that delivered the project output consisted of three universities, University College London (UCL), conducting optical channel characterisation and optical interconnects layout design, Heriot-Watt University (HWU), fabricating waveguides using laser direct write and Loughborough University (LU), fabricating waveguides using laser ablation and ink-jet printing, and 8 companies, three end users: Xyratex Technology (storage company), BAE Systems (military defence company), Renishaw (metrology equipment manufacturer); two polymer manufacturers: Dow Corning and Exxelis; one PCB manufacturer: Stevenage Circuits Ltd.; one E-CAD software vendor: Cadence; and one standards developing institute: National Physical Laboratory (NPL).

FirstLight provides technologies and solutions for increased demand for bandwidth in data centres, growth in storage networks with more consumers using Internet as a backup storage service, increased performance of network servers, worldwide increased dependence on the Internet and the growth of bandwidth-hungry applications, such as IPTV and video on demand (VoD), constantly push the limits of the current network infrastructure and continue to drive the need for more bandwidth from the data links. The projected global digital demand will grow from 1.8 to 7.9 Zettabytes (ZBs or 1×10^9 Terabyte) from 2011 – 2015 of which the amount of available data storage will reach 3.3 ZB in 2015 [A-1]. However, the exponential increase in system bandwidth and density required to satisfy this demand will impose unmanageable cost and performance burdens on future data center technologies. In

particular, the reduction in size and the increase in the number of high speed ports of peripheral storage devices, such as hard disk drives, will cause the density of printed copper channels on the data storage midplane or backplane to increase. The increase in data communication speeds will further expose the system to some of the fundamental constraints incurred when higher frequency data is conveyed along electronic channels. Many of these constraints can be mitigated to some degree [A-2], however, at a mounting cost to the overall system design [A-3–6]. It is, therefore, proposed by many researchers and FirstLight [A-7–12] that the projected performance bottleneck in data storage systems is mitigated by using electro-optical PCB as the midplane which incorporating optical interconnect technology. OPCB technology offers significant performance over conventional PCBs, higher data rates (>10 Gbit/s), no electromagnetic interference, reduction in power consumption and over a 50% reduction in PCB size and weight [A-13]. There are large and rapidly growing demands for OPCB product by many industries including the IT, telecommunications, aerospace and space sectors [A-14].

The commercialization report is to look at the OPCB technology from a market point of view and evaluate the future of the technology. This report is structured as following: firstly, FirstLight technology and its advantages are introduced; then the relative market sectors and potential customers are reviewed; finally, the commercialisation routes of FirstLight technology to the market are discussed.

A.2. FirstLight OPCB Technology

FirstLight aimed at designing an OPCB architecture could be used in electronic cabinets or racks that form the heart of a variety of IT systems (requested by Xyratex) and incorporate connectors to allow daughter-cards to be attached at right angles (see Figure A-1). The daughter-cards are fully interconnected via polymer waveguide optical interconnections embedded in an OPCB.

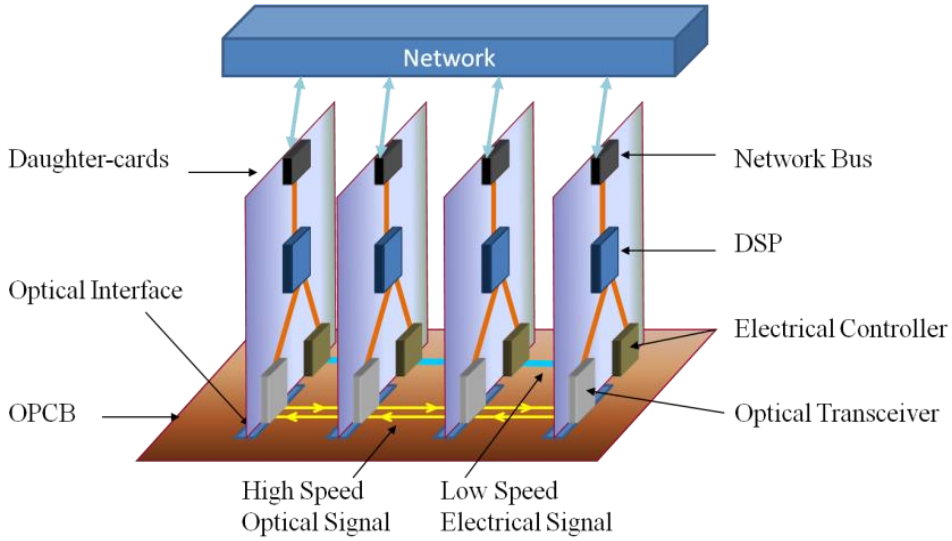

Figure A-1 Schematic system integrated electronic and optical interconnections on a backplane with 4 connected line/daughter cards

The optical waveguide research, however, has been limited to the academic sector and has not been adapted in any commercial product. A number of key challenges to the commercialization of optical PCB interconnect technology have yet to be overcome. These include the development of low-cost methods of waveguide fabrication and deposition, reduction in optical loss in optical channels, repeatable high-precision assembly methods of optically connecting line-cards to the waveguide interface of an OPCB. FirstLight was to address the following problems to exploit OPCB technologies to make it be suitable for commercial applications:

- Polymer for optical interlinks
- OPCB fabrication
- OPCB connectors
- System architecture

Although each of these problems appears at a different key point on an optical backplane value chain, all of them need to be addressed as a whole, because if there is

one problem exists in any of those points, it will break the whole value chain and therefore defer the pace of commercialisation of the OPCB technology.

A.2.1. Polymer for optical interconnect/waveguide

UCL have collaborated with several industrial companies and academy institutes and tested many types of polymer, i.e. Polyacrylate from Exxelis Ltd., Polysiloxane from Dow Corning Ltd., proprietary acrylate/polyurethane based polymer from IBM Research Zurich, polymer dry film from Hitachi. We provided the test results to companies to help them improve the formulae of their polymers and could potentially share an IP with other institutions if we could identify a material has better optical properties for waveguides.

A.2.2. OPCB fabrication

One of the FistLight objectives is to adapt commercial printed circuit board (PCB) manufacturing techniques to devise low cost fabrication methods for optical waveguides and new processes to incorporate optical transmission layers into conventional copper-based PCBs. The manufacturing processes developed will focus on high yield production, while minimising investment in new capital. UCL designed waveguide test layouts to measure key parameters such as optical loss, crosstalk and misalignment tolerance for different waveguide material and fabrication techniques. A data base was established based on the measured parameters and waveguide design rules were derived for different waveguide manufacturing techniques, e.g. photolithography, laser direct writing, laser ablation, embossing, extrusion, inkjet printing and a new technique combination of dry polymer film and liquid UV sensitive polymer materials. The data base has drawn broad interests from E-CAD software companies, such as Cadence who would like to see optical design rules incorporated into commercial automatic design rule checker and constraint manager layout software for PCBs so that PCB designers can easily include optical connection layers without detailed knowledge of the optics involved. The optical board layout can be automatically optimised to minimise the waveguide loss and optical cross-talk. Design rules are expected to be embedded in future generation of E-CAD for integrated design and layout software for electronic and photonic interconnect.

A.2.3. OPCB connectors

UCL designed a low cost, passive and high precision optical connector – *StorConn* [A-15–18] and improved during the FirstLight [A-19] project. The complete fabrication process for the passive alignment features on the optical layer is outlined in Figure A-2.

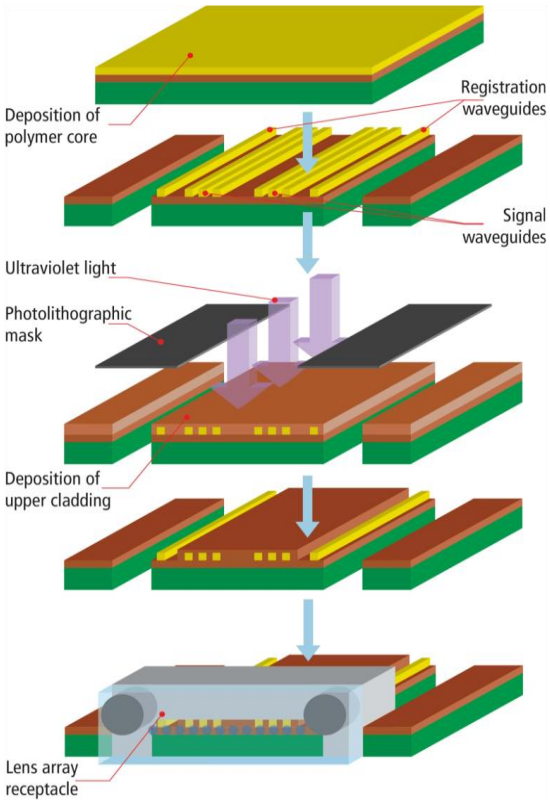

Figure A-2 Fabrication process for the passive alignment features on the optical layer

The procedure involves the fabrication of passive mechanical registration features in the core layer during the same process step in which the waveguide cores themselves are patterned using the laser direct imaging (LDI) technique, whereby, an ultraviolet laser diode was moved across the uncured wet film core layer to selectively cure the salient core features. These features included the signal waveguides as well as registration waveguides which are positioned on either side of the signal waveguides and as a result their positional accuracy with respect to the signal waveguides is comparable to that of the signal waveguides to each other. A layer of upper cladding polymer was then spun-coat over the waveguide cores, while the mechanical registration waveguides were kept exposed through an additional photolithographic process. This clearance allows for direct mechanical registration of arbitrary components to the waveguides. In addition, the fabrication tolerances required to

pattern the upper cladding for this purpose are far lower than those required to pattern the waveguides themselves. It is only important that the outer edges of the registration waveguides, which form the mechanical datum, be mechanically exposed.

The *StorConn* has the following key features:

- The connector is low cost, high precision and passive self-alignment between transceivers, i.e. arrays of lasers and photo detectors.
- The connector is pluggable with high degree of accuracy and repeatability. The positional tolerance of the mechanical registration features with respect to each other has been measured to be ±3 μm for lateral misalignment in-plane and ± 4 μm normal to the PCB plane [A-15], [A-20].
- The connector is suitable for the most of optical waveguide fabrication techniques, e.g photolithography, embossing, extrusion and laser writing.
- The connector is compatible to the commercially available MT technology for fibre ribbons and patchcord mitigating cost and development issues.
- Connector is scalable and can be easily scale up to 72 channels inputs and outputs when using a 6-row MT connector.

StorConn connector has been successfully employed in two different demonstration systems: Storlite [A-15] and FirstLight and both systems has exhibited satisfactory performance. We believe that there is good potential for the connector to be commercialized.

A.2.4. System architecture and application

FirstLight demonstrator is the first prototype to explore the design challenges of an embedded optical architecture for a modern data storage system which requested by the leading data storage company, Xyratex Technology Ltd. In a typical data storage system, a passive backplane (or midplane) and its peripherals are connected in a mutually orthogonal geometry: controller modules (or storage bridge bays) and power supplies are connected to one side of the backplane while an array of hard disk drives are connected to the other side. Due to the critical redundancy requirements in modern data storage systems, the interconnect topology essentially describes a dual star configuration, whereby each disk drive conveys a duplex data link across the

backplane to each of two separate controller modules. Each duplex link in turn comprises a pair of transmission lines. A number of additional duplex links directly connect the controller modules to each other. The Storage Bridge Bay Specification7 [A-21] allows for a maximum of 48 disk drives in an enclosure, each supporting two duplex links, with a further 17 duplex links between controller modules. The backplane of a 48 drive storage array would therefore have to accommodate 113 duplex links or 226 high speed transmission lines. The level of fault tolerance and scalability offered by these topologies is significant, however this forces increased complexity and cost into the backplane, particularly when interconnect protocols define serial data rates beyond 10 Gb/s.

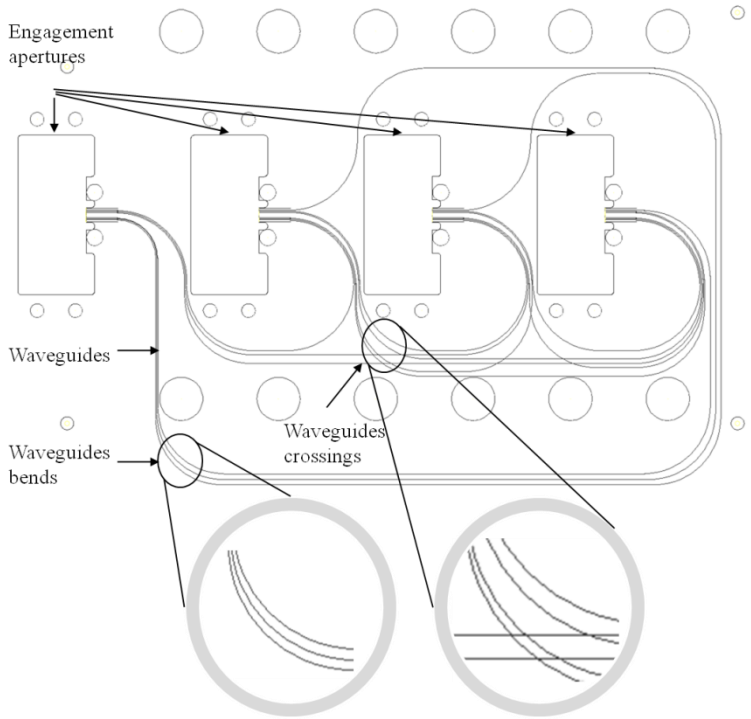

Figure A-3 The most compact and complex optical waveguide interconnection layout designed and successfully demonstrated to-date, including parallel waveguide straight sections, cascaded bends and non-orthogonal crossings

Design rules for the photolithographically manufactured acrylate polymer multimode optical waveguide derived from our optical material and fabrication techniques data bases were used in the layout of a complete set of optical interconnections on the backplane. Figure A-3 is the optical interconnects layout we designed using Cadence Allegro, commercial layout software for PCBs, for an electrical-optical printed circuit board (OPCB).

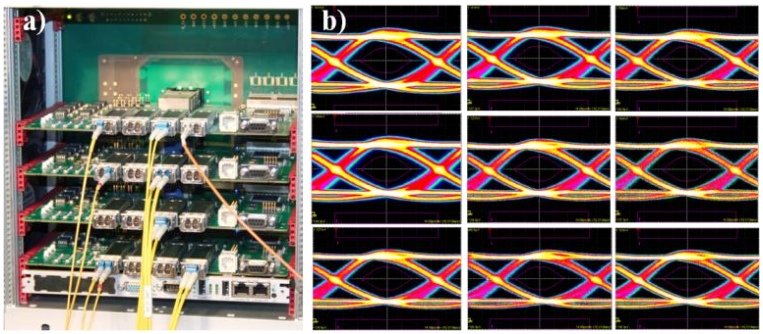

Figure A-4 a) Demonstration platform b) Eye diagrams showing 10.3125 Gb/s optical signals received from demonstration platform on 9 waveguide links under test

The demonstrator (Figure A-4) is a simplified model to simulate a data storage system. There are four identical rectangular optical engagement apertures in the middle of the optical board. There are two main advantages of this design. First, all the optical interfaces were designed to face the same direction and to be identical to each other, so that the line-cards are inter-exchangeable. We could, therefore, significantly reduce the manufacturing and maintenance costs, because any line-card can be plugged into any engagement aperture without special modification. Second, the OPCB is very compact, as the line-cards are closely spaced to meet the design specification of a highly populated storage bridge bay. Figure A-4a shows the fully assembled demonstration platform. 10 Gb/s test data was successfully conveyed between all test cards. Figure A-4b shows the eye diagrams corresponding to the nine waveguides under test.

A.3. Target Market Review

A.3.1. PCB Market

The world printed electronics market is expected to grow significantly over the next a few years with advancement in technology, commercialization of more products and entering new market according to Frost & Sullivan [A-22]. Figure A-5 shows the revenue forecasts for the world printed electronics market from 2007-16. The market size by revenue of the printed electronics market in 2009 was USD 0.53 billion and compound annual growth rate (2009-2016) was 32.5%. This is primarily constituted by printed components in devices such as gaming cards, medical disposable sensors, printed antennas in RFID and flexible displays in e-readers. Further advancements in

these devices would contribute to the steady growth of printed electronics market in the short term, i.e. over two years. The industry is expected to rapidly grow over the medium (3 to 5 years) to long term (6 to 7 years) of the forecast period, due to the introduction and commercialization of a range of products in printed lighting, printed displays, printed RFID and photovoltaic.

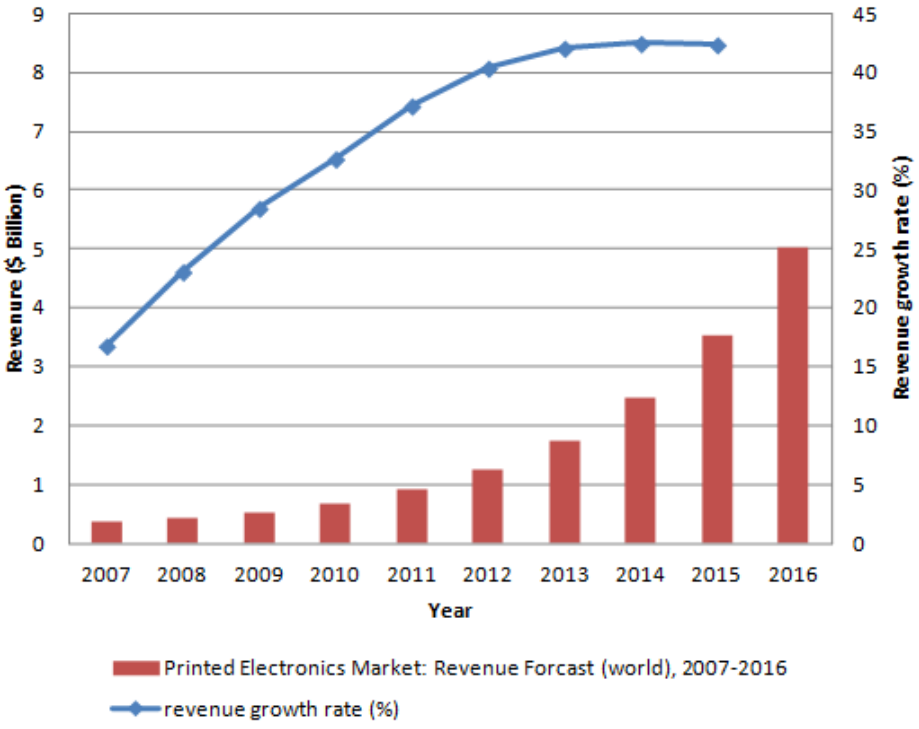

Figure A-5 Printed Electronics Market: Revenue Forecast (world), 2007-2016

Note: All figures are rounded, the base year is 2009. source: Frost & Sullivan, 6 April 2010

Table A-1 shows the regional sales of PCB from the year 2005 to 2015 where the data from 2010 were predicted ones. The sales around the world are steadily increasing after the 2009 economic downturn.

Table A-1 Regional sales of PCBs

Decision Support Database												
Table	PCB sales ($ Million)											
Region / Country	2005	2006	2007	2008	2009	2010	2011	2012	2013	2014	2015	CAGR % (2008-2015)
North America												
Canada	896.5	930.5	951.5	959.1	969.7	984.2	1001.9	1023.0	1047.5	1075.8	1108.1	2.08
US	4856.0	5003.0	5168.1	5219.8	5282.4	5388.1	5512.0	5655.3	5813.7	5988.1	6179.7	2.44
Total	5752.5	5933.5	6119.6	6178.9	6252.1	6372.3	6513.9	6678.3	6861.2	7063.9	7287.8	2.39
Asia- Pacific												
China	9400.0	11100.0	12900.0	12771.0	13409.6	14616.4	16370.4	18171.1	19988.2	21787.2	23530.2	9.12
India	540.0	660.0	838.2	1089.7	1362.1	1634.5	1879.7	2124.0	2357.7	2581.6	2801.1	14.44
Indonesia	162.0	171.0	180.0	190.0	199.0	208.0	216.9	225.0	234.6	243.3	251.8	4.10
Japan	13110.4	14068.0	14972.8	14373.9	14445.7	14590.2	14882.0	15254.0	15711.7	16261.6	16912.0	2.35
Malaysia	1798.0	1994.0	2244.0	2292.0	2323.0	2427.0	2506.0	2581.2	2650.9	2714.5	2771.5	2.75
Singapore	237.0	250.0	262.0	272.8	282.5	290.9	298.5	304.5	309.7	314.0	317.5	2.19
South korea	5100.0	6086.0	7037.0	7969.5	8168.7	8348.5	8515.4	8668.7	8807.4	8930.7	9037.9	1.81
Taiwan	5838.6	6297.1	6779.3	6745.4	6833.1	6969.8	7144.0	7358.3	7630.6	8012.1	8492.9	3.35
Total	36186.9	40626.7	45213.3	45704.2	47023.7	49085.2	51812.8	54687.7	57690.7	60845.0	64114.7	4.95
Europe												
Benelux	191.7	196.3	201.4	200.4	200.2	201.2	203.6	207.7	213.3	221.0	230.3	2.00
France	473.1	483.8	493.8	474.1	464.6	466.9	473.0	482.4	495.9	513.8	535.9	1.77
Germany	1720.0	1900.0	1979.5	1821.1	1711.9	1729.0	1754.9	1793.5	1847.3	1921.2	2013.5	1.44
Italy	411.3	419.8	427.9	406.5	400.4	402.0	406.4	414.1	425.7	441.5	461.8	1.84
Scandinavia	320.9	328.0	334.7	321.3	314.9	318.0	323.1	329.6	337.8	348.3	360.8	1.67
Spain	239.0	249.0	255.0	249.9	247.4	248.9	252.1	257.2	263.6	271.5	281.0	1.69
United kingdom	662.4	666.7	671.2	667.8	667.2	668.5	671.8	677.2	684.7	693.6	704.0	0.76
Rest of Europe	260.8	267.3	274.8	272.6	271.5	274.2	278.3	283.9	290.7	298.8	308.1	1.77
Total	4279.2	4510.9	4638.2	4413.7	4278.0	4308.7	4363.3	4445.6	4559.1	4709.7	4895.3	1.49
World Total	46218.5	51071.2	55971.1	56296.8	57553.7	59766.1	62690.0	65811.6	69110.9	72618.5	76297.8	4.44

Source: Frost & Sullivan, 6 April 2010. All figures are rounded the base year is 2008. The above figure represents sales value of PCB

Note

1 Benelux includes Belgium, Netherlands and Luxemburg

2 Scandinavia includes Denmark, Finland, Norway and Sweden

3 Rest of Europe includes Austria, Greece, Ireland and Switzerland

4 The above table shows large fluctuation in terms of year on year growth rate, these fluctuation are purely due to exchange rate. In local currency the PCB sales may have increased or decreased.

Optical printed circuit board (OPCB) market has not been established and the technology for fabricating optical printed circuits does not mature yet; however, researchers all over the world are exploring different ways to manufacture optical circuits reliably and cheaply. OPCB will certainly become one of the key elements in the printed electronics market in the medium or long term.

A.3.2. Special Polymer Market

The global chemical industry which is over USD 3 trillion in size and is closely related to the US and EU economies [A-23]. The European chemical industry is in a top position and according to Cefic (European Chemical Industry Council), chemicals form the second leading manufacturing sector (after pharmaceuticals) in terms of 'value added per employee' in Europe. Figure A-6 illustrates the sectoral breakdown of EU chemical industry sales in 2007. There are four segments in the European chemical industry:

- Base chemicals – cover basic inorganics, petrochemicals and their derivatives, are produced in large volumes;
- Pharmaceuticals – represent both basic pharmaceutical products and pharmaceutical preparations;
- Specialty chemicals – cover the auxiliaries for industry, paints and inks, crop protection, dyes and pigments;
- Consumer chemicals – includes chemicals which are sold to final consumers such as soaps, detergents, perfumes and cosmetics.

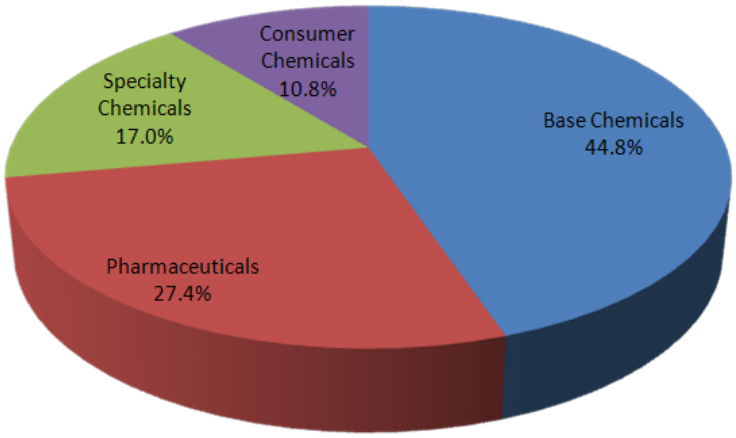

Figure A-6 Sectoral breakdown of EU chemical industry sales in 2007. Source: Cefic and Business Insight.

The global economic slowdown had an adverse effect on chemicals sales volume. One of chemical companies' growth strategies is to invest in biotechnology which holds a strong addressable market opportunity for the global chemical industry, and is expected to capture over 50% of the polymer market and 15% of the base chemical market in the next five years. Optical sensitive chemicals are within this development process.

A.3.3. Electronic Connector Market

During the last decade (2000-2010) the global connector market has been primarily dominated by four applications (Figure A-7): industrial, automotive, computer and peripherals, and telecom/data communication [A-24]. The share of the market for telecom and data communication connectors has decreased from over 26% in 2000 to little over 16% in 2010. Likewise, the share of the connector market for computer and peripherals has increased from almost 15% in 2000 to well over 20% in 2010. In 2010, these four market segments combined made up almost 69%, or more than two-thirds,

of the total global connector market. Bishop & Associates' current forecast predicts this combined share may notch up a little, to more than 71% in 2015.

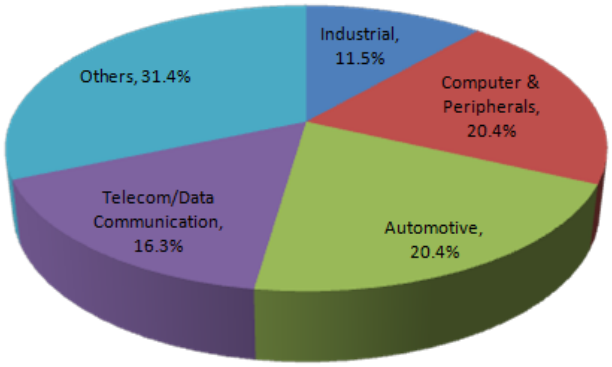

Figure A-7 Global Connector Market Segmentation 2010

A market research report, "The World Distribution Market for Connectors" by Bishop & Associates, Inc. presents a very positive picture of electronic connectors distribution [A-25] as well. The Global Electronic Connectors Market is projected to Reach USD 89.6 Billion by 2018, According to New Report by Global Industry Analysts, Inc [A-26]. The fast growth rate is primarily driven by factors such as rapid proliferation of electronic devices, technology developments, improving world GDP, growth in shipments of smart phones and other portable computing devices and emerging opportunities from non-traditional end-user industries, such as, medical and alternative energy. Telecommunications industry represents the fastest growing end-use market for electronic connectors. Growth in demand from telecom industry especially for multi fibre connectors will be driven by increase in adoption of 40/100 GbE network technologies.

A.4. Applications and Potential Market Analysis

A.4.1. Broadband Market

According to Business Insight [A-27], global IP traffic is predicted to quadruple between 2009 and 2014 to reach 767 EB (1 exabyte = 1 billion gigabytes) per year – or 64 EB per month. Global consumer fixed broadband revenues (Figure A-8) are set to grow by 42.2% between 2010 and 2015 to reach USD 233.2 billion by 2015. Digital subscriber line (DSL) technologies will account for the largest share of those revenues in 2015, at 48.6% of total revenues – this represents a fall from 58% of all consumer fixed broadband revenues in 2010. The massive market opportunity will

stimulate the development of optical components and systems to serve the demand. Research [A-27] shows that Fibre to the Home & Fibre to Building or Business (FTTH/B) will grow the fastest, with a 154% rise in revenues between 2010 and 2015, to reach USD 64.4 billion by the end of the forecast period. By 2015, FTTH/B revenues will account for 27.6% of total consumer fixed broadband revenue market share, up from 15.5% in 2010. FTTH/B

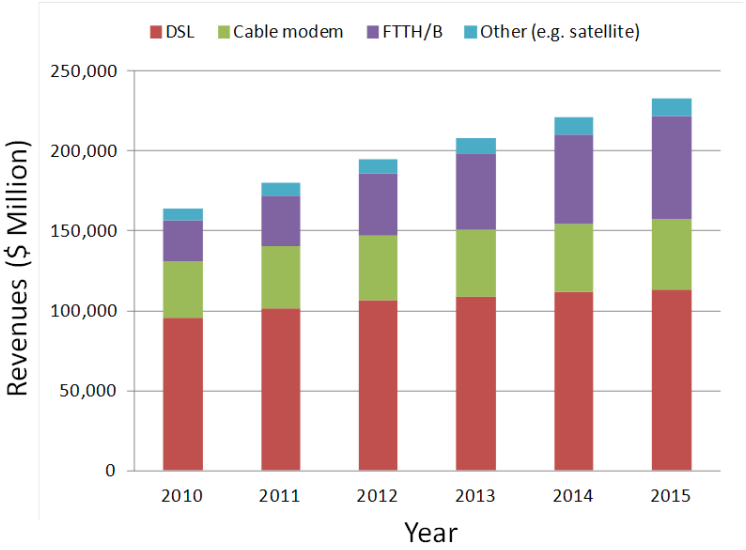

Source: Business Insights

Figure A-8 Global consumer fixed broadband revenues by technology, 2010-2015

The Photonics21 Strategic Research Agenda published in January 2010 [A-28] highlighted the need for a new generation of networks that are faster, more dynamic, more transparent and greener.

All of these different sources point to optical broadband technologies being a high growth sector, which still needs a considerable input in terms of highly focussed leading edge research and development investment. Figures from the FTTH Council suggest that homes with fibre optic broadband will drive three times the traffic of homes with DSL connections. According to research carried out by OIDA in 2008 and quoted in the Photonics21 SRA the market sizes are:

- Overall telecom market: USD 3400 billion
- Optical equipment market: USD 14 billion
- Optical component market: USD 4 billion

Business Insight estimated the market at 2009 [A-29] for IT virtualization could be worth over USD 19 billion.

A.4.2. Mobile Broadband

Business Insight carried out a research in 2011 and concluded that the global uptake of mobile broadband would overtake fixed subscriptions in 2011, and would grow from USD 152.1 million in 2008 to USD 1.9 billion by 2014 [A-27]. The popularity of mobile telephones is expected to continue to rise over the a few years. By the end of 2013, there will be over 5.6 billion mobile connections worldwide, a 68% increase over 2007 levels. Content will increasingly be accessible online, and shared between home-based and mobile devices. According to ABI Research [A-30], mobile cloud computing subscribers (Figure A-9) will increase from 42.8 million in 2008 across the world (about 1.1% of global mobile subscribers) to a little over 998 million in 2014 (close to 19% of global mobile subscribers). Location-enabled services such as navigation and maps applications will drive most of the growth in 2009 and 2010. It is expected that mobile cloud computing will be crucial to mobile application development and deployment strategies, ahead of downloadable mobile applications

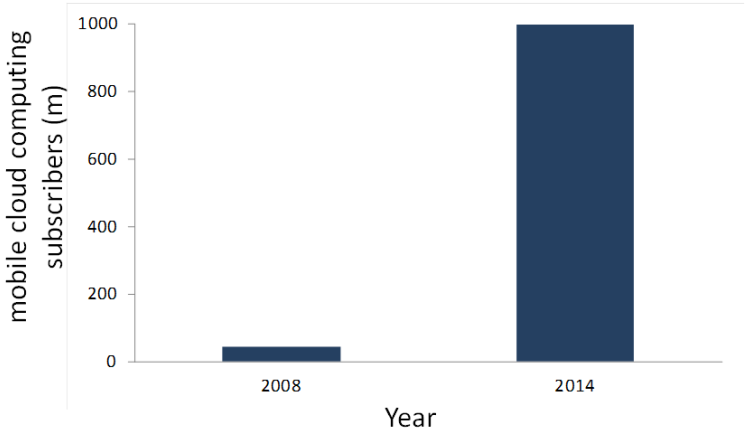

Source: ABI Research and Business Insights

Figure A-9 Global mobile cloud computing subscribers 2008-2014

Worldwide mobile operator revenue for TV and video content is forecast to grow from USD 1.87 billion in 2008 to USD 6.65 billion by 2014 [A-30], with Asia-Pacific accounting for nearly half that amount at the end of the forecast period. According to figures from market research house Ovum, Table A-2 shows worldwide mobile operator revenues for TV and video content are forecast to grow from USD 1.87 billion in 2008

to USD 6.65 billion by 2014, with Asia-Pacific accounting for nearly half that amount at the end of the forecast period.

Table A-2 Global mobile TV and video content revenues (USD m)

Region	2008	2009	2010	2011	2012	2013	2014
North America	344	448	557	674	788	905	1,026
South and Central America	37	57	81	103	124	148	164
Western Europe	541	709	867	1,028	1,191	1,353	1,516
Eastern Europe	166	247	316	377	436	500	544
Asia-Pacific	722	1,056	1,431	1,836	2,258	2,694	3,126
Middle East	41	62	83	100	118	140	153
Africa	19	30	43	59	76	100	120
Total	1,870	2,609	3,378	4,177	4,991	5,840	6,649

Source: Ovum and Business Insights

A.4.3. IPTV Market

Next-generation broadband paves the way for next-generation content, such as video-on-demand, 3D video, HD video, multiplayer advanced gaming, and so on. According to Cisco, video content will account for 57% of all internet traffic by 2014, and furthermore advanced internet video applications will account for nearly half of that traffic [A-27]. Global consumer Internet video traffic to PCs is rapidly increasing as shown in Figure A-10, from 1,112 petabytes per month in 2008 to a projected 12,442 petabytes per month in 2013 [A-31]. Approximately one-third of all consumer internet traffic was video to PCs in 2009, which not even including not including the amount of video exchanged through peer-to-peer (P2P) file sharing. Internet traffic to TV will also increase as the use of internet enabled smart TVs increases, reaching 2,594 petabytes per month in 2013, as shown in Figure A-10. There will be a forecast 64 million IPTV subscribers by the end of 2012, an almost six-fold increase over 2007 levels. IPTV subscription revenues are expected to increase at an even faster pace, reaching USD 17.5 billion in 2012, up from around USD 2 billion in 2007. The network connected devices, such as set top boxes, game consoles and Blu-ray player and improved broadband service will increase Video-on-demand (VoD) traffic which will double every two years through 2013. The sum of all forms of video (TV, VoD, Internet, and P2P) will account for over 91% of global consumer traffic by 2013. Internet video alone will account for over 60% of all consumers Internet traffic in 2013. Internet TV will represent over 4% of consumer Internet traffic, and ambient video will account for 8% of consumer Internet traffic by 2013.

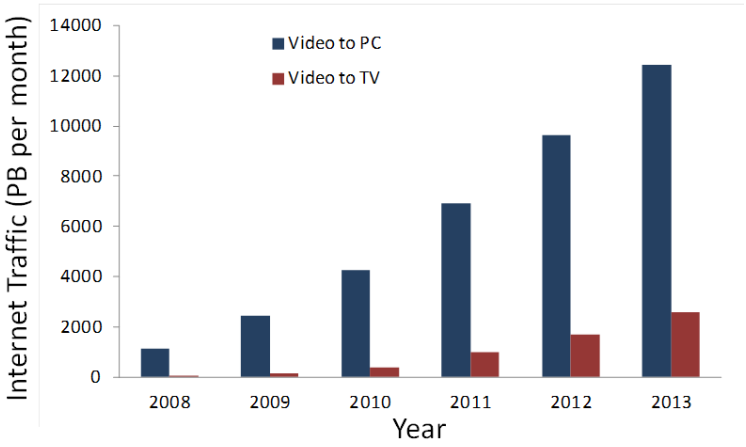

Source: Business Insights

Figure A-10 Consumer internet traffic, video to PC and TV (petabytes per month), 2008-2013

A.4.4. The future of digital home entertainment: Gaming

The global video gaming market is expected to grow at a CAGR of 8.9% for the period between 2008 and 2013 (Figure A-11), to reach USD 76.1 billion [A-32]. Business Insights forecasts that global video gaming revenues will grow at a CAGR of 5.1% during the period 2009 - 2014, to reach USD 92.5 billion in 2014.

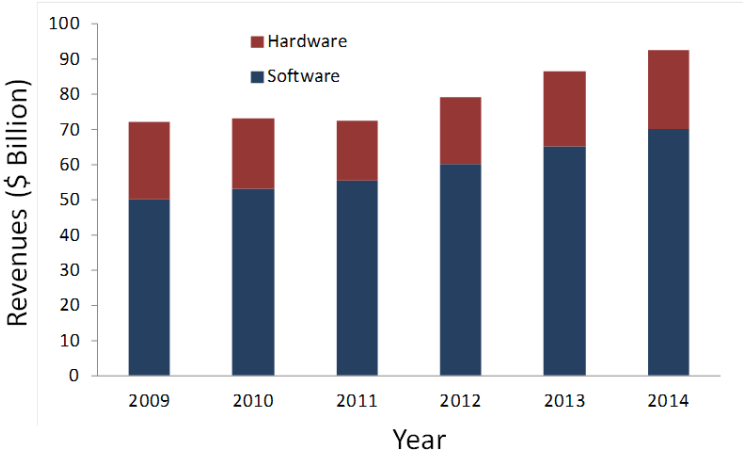

Source: Business Insights

Figure A-11 Global video gaming revenues (USD billions) 2008-2014

The online console market Figure A-12 is forecast to grow from USD 1.3 billion in 2008 to USD 12.6 billion in 2013, representing a CAGR of 57.5% over the forecast period. The online gaming market is expected to grow at a CAGR of 12.5% over the period 2008-2013 to reach USD 20.2 billion, as shown in the figure below.

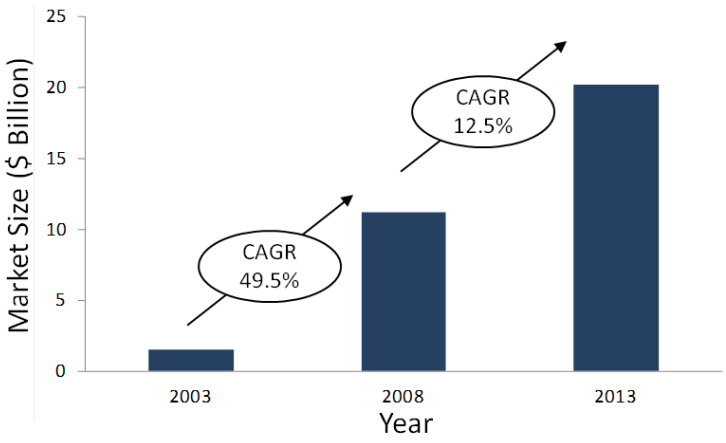

Source: Business Insights

Figure A-12 Global online gaming market (USD billions) 2008-2013

The mobile gaming market is set to be the fastest growing segment of video gaming between 2008 and 2013, growing at a CAGR of 17.6% to reach USD 15.1 billion by the end of the period. The ability to download and access games and other applications from online stores will drive the mobile gaming market forward. Gaming content will be increasingly stored, rendered and processed in the cloud network, with players only requiring a controller and broadband connection to play games.

A.4.5. The future of digital home entertainment: Music on demand

The digital music market will continue to grow at a fast pace, and is forecast to grow at a CAGR of 30% over the period 2009-2013 to reach USD 13.7 billion by 2013.

A.4.6. Digital Home Entertainment: TV and video on demand

The future TV sets will have faster screen refresh rates, and Internet connectivity, as well as a move beyond 1080p HDTV resolution to 2160p [A-33]. The number of HD-enabled TV sets in Europe (Figure A-13) has grown from 59 million households in 2008 to 116 million in 2010 – to currently represent around 51% household penetration. Figures further predict that growth of HD-enabled TV sets will continue at a rapid pace, almost doubling to reach 220 million European households by 2018.

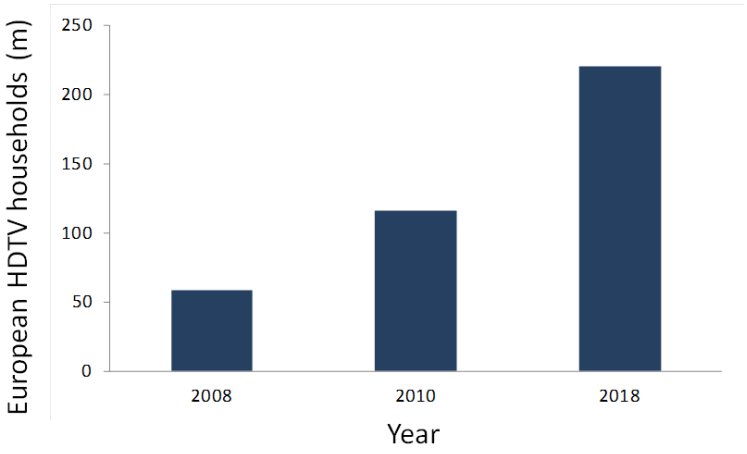

Source: FutureScience and Business Insights

Figure A-13 European HDTV households (m) 2008-2018

HD is set to become the 'standard' TV experience, in Europe at least, within 5-10 years, while 3D TV will become a mainstream technology in the home within the next 10 years. Global sales of 3D TV sets Figure A-14 are forecast to surge at a CAGR of 80% from 4.2 million units in 2010, to reach 78m units sold in 2015. Revenues will grow by a factor of nearly nine times, from USD 7.4 billion n in 2010 to USD 64.4 billion in 2015.

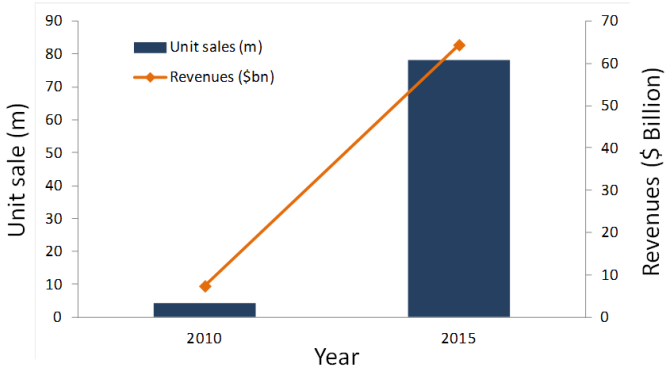

Source: iSuppli and Business Insights

Figure A-14 Global 3D TV unit sales and revenue, 2010-2015

A.4.7. Gigabit Ethernet Test Equipment Market

Media and content providers are likely to increasingly be one and the same as the broadband service provider themselves – either through merger and acquisition, or through close partnerships. Fixed broadband will enable next-generation video services to mix web content with traditional TV services. While a few trends, in terms of content consumption, will drive broadband traffic – notably short video clips, such

as those popularized by YouTube and others, and Internet TV – video-on-demand is likely to be the 'killer app', with consumers increasingly wanting to control how, when and where they consume video content.

VoD, IPTV, HDTV, social networking, voice over internet protocol (VoIP) and the availability of high-speed and high-capacity access networks such as Fibre to the x (FTTx) and WiFi have push IP traffic to grow 50% annually. The industry is quickly moving towards 40/100 GbE links and network service providers are developing the next-generation high-speed network protocols to meet the high demand of bandwidth [A-34]. However, network service providers and network equipment manufacturers find that it is very complex to map 10 GbE lines and Synchronous Optical Networking and Synchronous Digital Hierarchy (SONET/SDH) into 40 G SONET. Thus, the next imminent step for Ethernet equipment vendors is to move directly to 100 GbE.

IEEE is currently working on the standardization of 40 Gbs and 100 Gbs Ethernet under the P802.3ba task force. In addition to the existing 40 Gbs telecom standards, the Optical Internetworking Forum (OIF) and the Telecommunication Standardization Sector (ITU-T) are currently working on standardizing SDH and Optical Transport Network (OTN) telecom interfaces for long-haul transmission of 100 Gb Ethernet. Proper testing has proven to be the catalyst for success of any technology. As such, 40/100GbE brings a number of new challenges associated with it and requires testing to ensure its successful adoption. However, the components needed to support such high speeds tend to be rather expensive, e.g. transceivers, are rather expensive ranging from USD 25,000 to USD 65,000. The affordability of the components challenges the market at present which is a challenge for 100 G equipments.

Table A-3 40/100G Ethernet Test Equipment Market: Market Engineering Measurements (World, 2009)

Measurement Name	Measurement	Trend
Market age	**Nascent**	**Increasing**
Revenues	$6.1 million	Increasing
Potential revenues (maximum future market size)	**$39.1 million**	**Increasing**
Base year market growth rate	408.30%	Decreasing
Compound annual growth rate	**0.858**	**Decreasing**
Price sensitivity	Low	Increasing
Average product development time	**9 to 12 months**	**Decreasing**
Competitors (active market competitors in base year)	4	Increasing
Degree of competition	**High**	**Increasing**
Degree of technical change	High	Increasing
Market concentration (per cent of base year market controlled by top three competitors)	**0.962**	**Decreasing**

Note: All figures are rounded; the base year is 2009. Source: Frost & Sullivan

Table A-3 shows the global 40/100 GbE test equipment market reached USD 6.1 million in revenues in 2009, which was an increase of 408.3 percent from 2008.

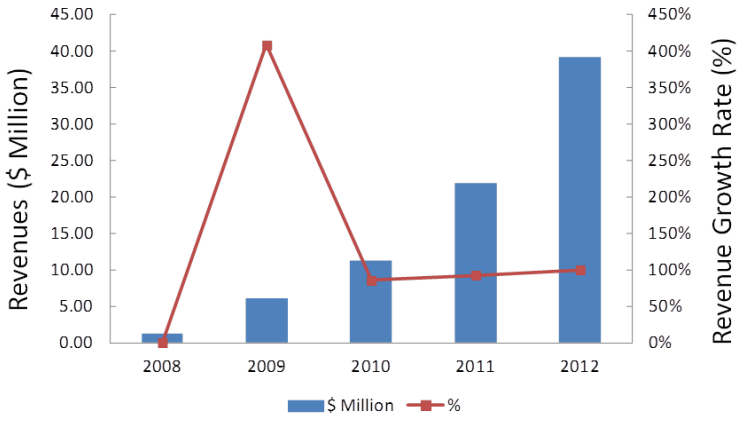

Note: All figures are rounded; the base year is 2009. Source: Frost & Sullivan

Figure A-15 40/100 Gigabit Ethernet Test Equipment Market: Revenue Forecasts (World), 2008-2012

This market is forecast to continuously grow in the future (Figure A-15). The revenues are expected to reach USD 39.1 million by 2012 with CAGR of 85.8 percent from 2010 to 2012 (Figure A-15).

A.5. Commercialization options

This section explores options for commercialization of the FirstLight technology. FirstLight covers a few key technologies for the optical PCBs, therefore, we list the potential ways for each or all of the technologies in bringing FirtLight to the market. We have mainly considered pursuing one of the following three strategies:

1) **Manufacturing:** Optical Device Group in UCL establishes a spin-out company and collaborates with UCL. We research and develop waveguide material, fabricate OPCB and design optical connectors, outsource manufacturing.

2) Collaboration: We form a company and seek collaboration with a PCB or connector company. We use our technology and expertise in exchange for a certain percentage of shares in the company.

3) Licensing: We carry out research and develop activities within UCL and licence our data base and core patents to an established connector and PCB manufacturer and CAD software vender. We receive a margin from the revenue.

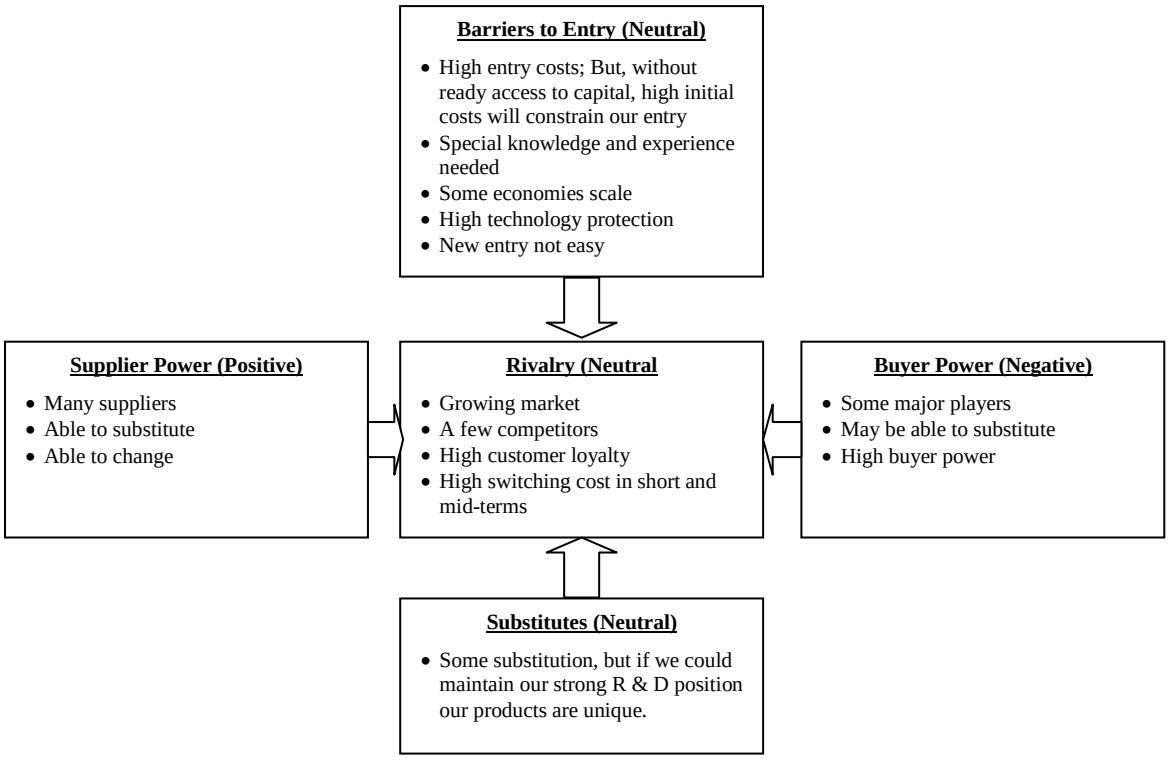

Fig. 1 Five forces analysis for FirstLight

Five forces analysis [A-35] for our new technology venture is given in Fig. 1

- **Supplier Power:** Here we assess how easy it is for suppliers to drive up prices and we consider supplier power to be the positive force in our industry. There are plenty of suppliers who can provide polymer material, we only need to apply appropriate formulae and mix the polymer compounds to produce the correct products for our customers. The *StorConn* connector is compatible to the commercially available MT technology for fibre ribbons and patchcord. We may

need an OEM company to customaries the connector for us, but there is no difficulty to outsource manufacturing and the fabrication cost will reduce exponentially when the demand for the products increases.

- **Buyer Power:** We don't think buyers could drive prices down for the optical backplanes in short term. There are currently no industrial standards for optical waveguides and optical connectors. Most of optical PCBs are tailored for customers which increases switching costs for buyers to other optical PCB vendors. However, buyers' power will increase when the whole optical PCB supply chain becomes more mature and more big players jump into the market.
- **Competitive Rivalry:** Optical PCBs especial waveguide embedded PCBs are not widely commercially available, high fabrication cost limit number of customers. Therefore, big connector companies and PCB companies are not focusing on developing waveguide material and connectors. It is very good opportunities for us to step into the market and use our expertise to build a health IP portfolio. We could explore more options, e.g. licensing or collaboration, when the optical PCBs market becomes more attractive in mid- or long-term.
- **Threat of Substitution:** The optical PCB market is not established yet, most customers who need optical integrated PCBs are for their own demonstrator or trial products in small scale. There are not many companies in the world could fabricate reliable waveguides embedded backplane and provide high precision optical connectors for waveguides. This situation limits the ability of our customers to find a different way or a provider in short term.
- **Threat of New Entry:** We consider the threat of new entrants in the optical backplane and optical connector for backplane industry to be neutral in the short- and mid- term. This is because capital requirements for research, equipments and production lines, set a high barrier for new companies to enter; and more importantly, we have knowledge, experience and protected key technologies. However, we expect more competitions in the industry in long-term when optical waveguide technology becomes more mature.

A.5.1. Manufacturing

This option would include raising capital and acquiring laboratory site. The UCL Optical Device team lacks knowledge about the non-technical aspects of the business. Moreover, the time and infrastructure costs involved make this a relatively difficult option for commercializing a technology. However, manufacturing will likely be viable if UCL could let the team access UCL's research facilities.

Advantages

- Potentially significant revenue opportunity
- Could collaborate with UCL to rent research and fabrication facilities in the university to reduce initial investment

Risks

- Large initial investment
- Limited market in short-term
- No distribution network
- No reliable connections with suppliers product quality may be varied
- Requires raising capital; significant delay for plant setup
- Speed of R & D may be limited by man power and facilities.

A.5.2. Collaboration

We could seek an industrial partner who can offer to create and manage the entire manufacturing value chain, including mechanical design and engineering, procurement, assembly, marketing and post-sales. We obtain some shares of the company as a technical partner and we receive margin from sales and license fee.

Advantages

- Capture good value from technology
- Quick time to market
- Don't need initial investment
- Less risk as the commercialisation is managed by expertise

Risks

- Unclear whether the firm have long term plan to partner
- Requires venture capital investment for long-term R & D; this will solely depend on the firm's business plan
- Less or even no control to our own business
- Turns manufacturing partner into a single powerful supplier

A.5.3. IP Licensing

We recommend licensing as the preferred method of commercialization for the FirstLight. This option has the least risk and, unlike the other options, guaranteed profits. Potential licensing partners include end users, PCB manufacturers, connector manufacturers and PCB CAD software vendors.

Advantages

- Low risk
- Quick time to market, since companies already possess infrastructure to implement FirstLight
- Guaranteed profits return

Risks

- Other optical backplane innovations on the horizon may provide similar benefit, which would significantly reduce bargaining power.
- Companies license in a lot of technology, but mainly through cross-licensing; they may be unwilling to pay for licensing.
- Lack knowledge about future, difficult to assess true value of a patent when a company ask to purchase the patent.

A.5.3.1. Potential Licensing Partners

- ***End Users:*** Attractive licensing partners, e.g. Xyratex, Huawei. They have full knowledge about the advantages that would result from optical PCB but they have direct contacts to PCB manufacturers and connector manufacturers and are engaged in optical PCB research and development activities. We had a shared patent ownership with Xyratex on *StorConn*.
- ***PCB Manufactures:*** The PCB manufacturers are the beneficiaries of the FirstLight, because they are able to fabricate optical enabled PCBs without heavily invest their existing production lines. Moreover, they are the ones that would have to make changes to their manufacturing process in order to integrate optical interlinks in the traditional PCBs. However, this group's activities are driven by customers' demands, they will unlikely to adapt the new technology before the market is well established.

- ***Connector Manufacturers:*** Preferred licensing partners because they in the business of mass-producing a specialist technology. They already possess the tools to quickly produce the *StorConn*, without additional capital expenditure. In fact, we have already taken this step and we have collaborated with the US connector manufacturer Samtec.
- ***CAD software vendors:*** There are numerous players in this area, e.g. Cadence. There are no optical layout tools available in the market. Cadence already expressed interests in incorporating optical waveguide design rules into their electrical PCB packages.

A.5.3.2. Licensing Arrangements

- ***Exclusive Licensing:*** Research shows that the world's top 100 connector manufacturers recorded shipments of USD 42.307 billion for 2011 [A-24]. This represented 87.5% of the worldwide connector market. The Top10 of the connector manufacturers (see Table A-4) for 2010 achieved a 31% increase in sales, outperforming the overall market growth of 28.4%.

Table A-4 Connector Manufacturers Ranking 2010/2011 – Industrial Markets

1	TE Connectivity
2	Amphenol
3	Molex Inc.
4	Yazaki
5	Foxconn (Hon Hai)
6	FCI
7	JST
8	Delphi Connection Systems
9	Hirose
10	JAE

The market is highly concentrated among a small number of companies. Therefore, profits from the exclusive licensing may become attractive if it involves partnership with major manufacturers, e.g TE connectivity. Customers might be willing to pay premium for a technology that enables them to expand sales dramatically or consolidate their market positions. If we were to choose exclusivity (or if licensing partners preferred this arrangement) a good way to capture the full value of the innovation would be to use an auction. A bidding mechanism would help give manufacturers the incentive to

reveal greater information about the benefit. Nevertheless, this is not typical industry practice.

- ***Multi-License:*** We would recommend this option because the profit potential is likely higher, since more companies can take advantage of technology.

A.5.3.3. Composition of Licensing Arrangement

- ***Per Unit Licensing:*** A per unit manufactured arrangement is attractive for a licensing partner because it is low risk (i.e. component is a variable rather than fixed cost). This could easily be arranged as a percentage of the wholesale price of each unit. A percentage (as opposed to a fixed per-unit cost) would mean that the deal automatically prices in the sliding cost of the unit over time.
- ***Flat Fee:*** **Licensing** partners more likely to take a per-unit fee in order to limit risk and gain greater flexibility.

A.6. Financial Analysis of IP Licensing

We created a financial model to assess the financial potential presented by the StorConn connector in the FirstLight technology portfolio, because we already filed a patent for it. The model is based on the information we had about our target market, connector manufacturers and we assumed TE connectivity is one of our partners and our license fee is based on TE connectivity's net sales revenue.

The model begins with the 2011 revenue for TE connectivity, which was USD 14,312 million [A-36]. We made assumptions about the percentage of the waveguide connector market we are able to capture, and the percentage license fee we will charge. We created three scenarios, with a "Best", an "Average", and a "Worst". The following spreadsheet (Table A-5) highlights the "worst", "average" and "best" cases. The average gives us values of USD 286,240 per year licensing fee, more than USD 1.4 million for the best case.

Table A-5 Licensing finance model

	Worst	Average	Best
Net Sales	14,312,000,000	14,312,000,000	14,312,000,000
Waveguide Connector Market	1%	2%	2%
Net Sales of Waveguide Connector	143,120,000	286,240,000	286,240,000
License Fee	0.10%	0.10%	0.50%
Profit	143,120	286,240	1,431,200

The potential profit is huge if we could just capture a faction of the market share owned by TE connectivity only.

A.7. Conclusions

We assessed the commercial opportunity of the FlightLight technology which includes: polymer formulae and waveguide guide design rules database and optical waveguide connector, *StorConn*. Market research underlines the fact that the optical polymer, PCB and connectors market are all attractive and growing quickly. Meanwhile, it also highlights rapid changing in those markets, with high demand of new innovations to lower costs and high data speed and wide bandwidth. A transition from the electronic to the optical technology will be unavoidable in the next a few years to confront the electronic interconnection bottleneck. The quick pace of change underlines the need for rapid commercialization of the FirtLight through patent licensing.

Market analysis showed that the demand for optical enabled products will be high in the very near future caused by exponentially increased demand for high data rate from broadband, digital entertainment, data-communication and high speed test equipment industries. Fortunately, the optical PCB market is far from mature, big players are not focus on developing the whole optical ECO system. It is a right time for new players to enter the market. Our expertise and inventions covers major elements in the optical PCB supply chain, from raw material, design rules, optical connectors to design of optical integrated system architectures. We can find our position in the OPCB market if we are willing to take risks and found a company to continue the R & D.

Our low risk recommendation is to pursue a multi-licensing approach to take advantage of the various players in the market. Ideally this would be negotiated on a percentage per-unit basis, so that the risk and reward of the innovation would be shared between the patent holder and the licensee. We already licensed the *StorConn* patent to a US connector manufacturer Samtec and UCL have received a revenue stream as an agreed percentage of sales, which is a good example to show the advantages of our inventions.

While the financial model we have created lacks accurate data, it still underlines the significant potential offered by the technology. The innovation has clear commercial potential. How the benefit is divided between the licensee, the patent holder, and the end-user will depend on market and competitive developments that arise over the coming months.

Appendix A References

[A-1] J. Gantz and D. Reinsel, "Extracting Value from Chaos," *IDC iView*, pp. 1–12, 2011.

[A-2] H. Cho, K. Koo, P. Kapur, and K. C. Saraswat, "The Delay , Energy , and Bandwidth Comparisons between Copper , Carbon Nanotube , and Optical Interconnects for Local and Global Wiring Application," *IEEE Int. Interconnect Technol. Conf.*, pp. 135–137, 2007.

[A-3] F. Gisin and G. Dudnikov, "State of the Art of Electrical High Speed Backplanes in Industry Today and the Transition to Optical interconnects," *Biophotonics/Optical Interconnects VLSI Photonics/WBM Microcavities, 2004 Dig. LEOS Summer Top. Meet.*, vol. 1, pp. 7–8, 2004.

[A-4] W. Heirman, J. Dambre, I. Artundo, C. Debaes, H. Thienpont, D. Stroobandt, and J. Van Campenhout, "Predicting the performance of reconfigurable optical interconnects in distributed shared-memory systems," *Phot. Netw. Commun.*, vol. 15, pp. 25–40, 2008.

[A-5] J. A. Conway, S. Sahni, and T. Szkopek, "Plasmonic interconnects versus conventional interconnects: a comparison of latency, cross- talk and energy costs," *Opt. Express*, vol. 15, no. 8, pp. 1069–1071, 2007.

[A-6] K. Koo, H. Cho, P. Kapur, and K. C. Saraswat, "Performance Comparisons Between Carbon Nanotubes, Optical, and Cu for Future High-Performance On-Chip Interconnect Applications," *IEEE Trans. Electron Devices*, vol. 54, no. 12, pp. 3206–3215, 2007.

[A-7] F. E. Doany, C. L. Schow, C. W. Baks, D. M. Kuchta, S. Member, P. Pepeljugoski, L. Schares, R. Budd, F. Libsch, R. Dangel, F. Horst, B. J. Offrein, and J. A. Kash, "160 Gb/s Bidirectional Polymer-Waveguide Board-Level Optical Interconnects Using CMOS-Based Transceivers," *IEEE Trans. Adv. Packag.*, vol. 32, no. 2, pp. 345–359, 2009.

[A-8] L. Schares, J. A. Kash, F. E. Doany, C. L. Schow, C. Schuster, S. Member, D. M. Kuchta, P. K. Pepeljugoski, J. M. Trewhella, C. W. Baks, R. A. John, L. Shan, Y. H. Kwark, R. A. Budd, P. Chiniwalla, F. R. Libsch, J. Rosner, C. K. Tsang, C. S. Patel, J. D. Schaub, R. Dangel, F. Horst, B. J. Offrein, D. Kucharski, D. Guckenberger, S. Hegde, H. Nyikal, C. Lin, A. Tandon, G. R. Trott, M. Nystrom, D. P. Bour, M. R. T. Tan, and D. W. Dolfi, "Terabus: Terabit / Second-Class Card-Level Optical Interconnect Technologies," *J. Quantum Electron.*, vol. 12, no. 5, pp. 1032–1044, 2006.

[A-9] R. Dangel, C. Berger, R. Beyeler, L. Dellmann, M. Gmur, R é Hamelin, F. Horst, T. Lamprecht, T. Morf, S. Oggioni, M. Spreafico, and B. J. Offrein, "Polymer-Waveguide-Based Board-Level Optical Interconnect Technology for Datacom Applications," *IEEE Trans. Adv. Packag.*, vol. 31, no. 4, pp. 759–767, Nov. 2008.

[A-10] S. Uhlig, "Micro-Processing Applied to Optical Interconnects and High-Frequency Packaging," *Sci. Technol.*, no. 1011, 2006.

[A-11] P. Lukowicz, J. Jahns, R. Barbieri, P. Benabes, T. Bierhoff, a. Gauthier, M. Jarczynski, G. a. Russell, J. Schrage, W. Sullau, J. F. Snowdon, M. Wirz, and G. Troster, "Optoelectronic interconnection technology in the holms system," *IEEE J. Sel. Top. Quantum Electron.*, vol. 9, no. 2, pp. 624–635, Mar. 2003.

[A-12] N. Bamiedakis, J. Beals, R. V Penty, S. Member, I. H. White, J. V Degroot, T. V. Clapp, and A. Cost-effective, "Cost-Effective Multimode Polymer Waveguides for High-Speed On-Board Optical Interconnects," *IEEE J. Quantum Electron.*, vol. 45, no. 4, pp. 415–424, 2009.

[A-13] R. C. A. Pitwon, K. Hopkins, K. Wang, D. R. Selviah, H. Baghsiahi, B. J. Offrein, R. Dangel, F. Horst, M. Halter, and M. Gmür, "Design and implementation of an electro-optical backplane with pluggable in-plane connectors," *Proc. SPIE*, p. 76070J–76070J–12, 2010.

[A-14] D. R. Selviah, A. C. Walker, D. A. Hutt, K. Wang, A. McCarthy, F. A. Fernández, I. Papakonstantinou, H. Baghsiahi, H. Suyal, M. Taghizadeh, P.

Conway, J. Chappell, S. S. Zakariyah, D. Milward, R. C. A. Pitwon, K. Hopkins, M. Muggeridge, J. Rygate, J. Calver, W. Kandulski, D. J. Deshazer, K. Hueston, D. J. Ives, R. Ferguson, S. Harris, G. Hinde, M. Cole, H. White, N. Suyal, H. ur Rehman, and C. Bryson, "Integrated optical and electronic interconnect PCB manufacturing research," *Circuit World*, vol. 36, no. 2, pp. 5–19, 2010.

[A-15] I. Papakonstantinou, D. R. Selviah, R. C. A. Pitwon, and D. Milward, "Low-Cost, Precision, Self-Alignment Technique for Coupling Laser and Photodiode Arrays to Polymer Waveguide Arrays on Multilayer PCBs," *IEEE Trans. Adv. Packag.*, vol. 31, no. 3, pp. 502–511, Aug. 2008.

[A-16] I. D. Johnson, R. C. A. Pitwon, D. R. Selviah, and I. Papakonstantinou, "Optical printed circuit board and manufacturing method," Patent number: WO2007/0101842006.

[A-17] R. C. A. Pitwon, D. R. Selviah, and I. Papakonstantinou, "Optical wavelength division multiplexed multiplexer/demultiplexer for an optical printed circuit board and a method of manufacturing the same," Patent number: US8,007,9652011.

[A-18]I. Papakonstantinou, D. R. Selviah, K. Wang, R. A. Pitwon, K. Hopkins, and D. Milward, "Optical 8-Channel , 10 Gb / s MT Pluggable Connector Alignment Technology for Precision Coupling of Laser and Photodiode Arrays to Polymer Waveguide Arrays for Optical Board-to-Board Interconnects," *58TH Electron. COMPONENTS Technol. Conf. Proc.*, pp. 1769–1775, 2008.

[A-19] R. C. A. Pitwon, K. Wang, J. Graham-Jones, I. Papakonstantinou, H. Baghsiahi, B. Offrein, R. Dangel, D. Milward, and D. R. Selviah, "FirstLight: Pluggable Optical Interconnect Technologies for Polymeric Electro-Optical Printed Circuit Boards in Data Centers," *J. Light. Technol.*, vol. 30, no. 21, pp. 3316–3329, 2012.

[A-20] D. R. Selviah, F. A. Fernández, I. Papakonstantinou, K. Wang, H. Bagshiahi, A. Walker, A. Mccarthy, H. Suyal, M. Taghizadeh, D. Hutt, K. Williams, J.

Chappell, S. S. Zakariyah, and D. Milward, "Integrated Optical and Electronic Interconnect Printed Circuit Board Manufacturing," *Circuit World*, vol. 34, no. 2, pp. 21–26, 2008.

[A-21] "Storage Bridge Bay (SBB) Specification," *Storage Bridge Bay Working Group Inc.*, 2008. [Online]. Available: http://www.sbbwg.org. [Accessed: 28-Feb-2012].

[A-22] "World printed electronics market," *Frost & Sullivan*, no. April, 2010.

[A-23] "Global Growth Strategies for Chemical Companies," *Bus. Insights*, 2010.

[A-24]"2012 Top 100 Connector Manufacturers," *Bish. Assoc. Inc.*, no. August, 2012.

[A-25] "The World Distribution Market for Connectors," *Bish. Assoc. Inc.*, no. April, 2012.

[A-26] "Electronic Connectors - a Global Strategic Business Report," *Glob. Ind. Anal. Inc*, no. March, 2012.

[A-27] G. Eastwood, "Next-generation broadband delivery: Global opportunities and challenges for high speed fixed consumer internet services," *Bus. Insights*, no. August, 2011.

[A-28] P. R. Boyce, "Lighting: The way ahead," *Prop. Manag.*, vol. 1, no. 4, pp. 333–343, 2010.

[A-29] V. Furness, "The Future of Virtualization - Emerging trends and the evolving vendor landscape," *Bus. Insights*, 2009.

[A-30] E. Seka, "The Future of PC / Mobile Convergence," *Bus. Insights*, 2010.

[A-31] M. Sasso and R. Absalom, "The Future of TV," *Bus. Insights*, 2010.

[A-32] "The Video Gaming Industry Outlook," *Bus. Insights*, no. May, 2011.

[A-33] G. Eastwood, "The Future of Digital Home Entertainment Key trends and drivers shaping devices , content and services," *Bus. Insights*, 2010.

[A-34] "World 40 and 100 Gigabit Ethernet Test Equipment Market," *Frost & Sullivan*, no. February, 2010.

[A-35] John W. Mullins, *The New Business Road Test: What Entrepreneurs and Executives Should Do Before Writing a Business Plan*. London: FT Prentice Hall, 2003.

[A-36] "TE Connectivity 2011 Annual Report," 2012.

Appendix B. Publication List

1. Baghsiahi, H; Wang, K; Kandulski, W; Pitwon, RCA; Selviah, DR; (2013) Optical Waveguide End Facet Roughness and Optical Coupling Loss. Journal of Lightwave Technology , 31 (16) 2959 – 2968

   Contribution 40%: the author led the measurement of optical insertion loss after applying the waveguide end facet coating.

2. Pitwon, RCA; Wang, K; Graham-Jones, J; Papakonstantinou, I; Baghsiahi, H; Offrein, BJ; Selviah, DR; (2012) FirstLight: Pluggable Optical Interconnect Technologies for Polymeric Electro-Optical Printed Circuit Boards in Data Centers. Journal of Lightwave Technology, 30 (21) 3316 - 3329.

   Contribution 40%: the author designed and measured the optical PCB.

3. Pitwon, R; Smith, C; Wang, K; Graham-Jones, J; Selviah, DR; Halter, M; Worrall, A; (2012) Polymer optical waveguides with reduced in-plane bend loss for electro-optical PCBs. In: Proceedings of SPIE - The International Society for Optical Engineering. (pp. 82640Z-1-82640Z-10)

   Contribution 30%: the author analyzed the measured data.

4. Pitwon, R.C.A.; Hopkins, K.; Wang, K.; Selviah, D.R.; Baghsiahi, H.; Offrein, B.J.; (2010) Design and implementation of an electro-optical backplane with pluggable in-plane connectors. Optoelectronic Interconnects and Component Integration IX. (pp. 76070J-1-76070J-12).

   Contribution 20%: the author measured and analyzed the optical performance of the in-plane connector.

5. Pitwon, RCA; Hopkins, K; Milward, D; Muggeridge, M; Selviah, DR; Wang, K; (2010) Passive assembly of parallel optical devices onto polymer-based optical printed circuit boards. Circuit World, 36 (4) 3 - 11.

   Contribution 10%: the author measured the optical performance of the optical PCB.

6. Selviah, DR; Walker, AC; Hutt, DA; Wang, K; McCarthy, A; Fernandez, EA; Bryson, C; (2010) Integrated optical and electronic interconnect PCB manufacturing research. Circuit World, 36 (2) 5 – 19.

   Contribution 10%: the author provided measured results and analysis of the waveguide samples delivered during the cause of the OPCB project.

7. Papakonstantinou, I., Wang, K., Selviah, D.R., Fernandez, F.A. (2008). Transition, radiation and propagation loss in polymer multimode waveguide bends. Optics Express 15(2), 669-679. ISSN: 1094-4087

Contribution 20%: Papakonstantinou, I and the author measured the waveguide bends experimentally that resulted in separating out the various loss components involved for the 1st time in the world and thus in identifying the most severe ones.

8. Baghsiahi, H., Selviah, D.R., Yu, G., Wang, K., Yau, W.Y.M., Fernández, F.A. (2008). Photolithographically Manufactured Acrylate Multimode Optical Waveguide Translation and Rotation Misalignment Tolerances. 2nd Electronics System-Integration Technology Conference (ESTC) Greenwich, UK, 1st-4th September 2008, Session We-A-1,

   Contribution 30%: Yu, G., Yau, W.Y.M and the author build the measurement stages and measured the waveguide translation misalignment tolerances.

9. Milward, D., Selviah, D.R., Hutt, D., Walker, A., Wang, K., Chappell, J., Baghsiahi, H., McCarthy, A. (2008). Optical Printed Circuit Board Flagship. 3rd Annual IeMRC Conference,Innovative electronics Manufacturing Research Centre, Henry Ford College, Loughborough University, Friday, July 4th 2008

   Contribution 15%: the author investigated the commercial and technological benefits of four polymer waveguide manufacturing technologies – photolithography, laser-writing, laser ablation and inkjet printing – for high data rate printed circuit boards. Insertion loss, cross talk and misalignment tolerance on horizontal and vertical axis were measured for each waveguides fabricated by the four manufacturing technologies.

10. Papakonstantinou, I., Selviah, D.R., Wang, K. (2008). Insertion Loss and Source Misalignment Tolerance in Multimode Tapered Waveguide Bends. IEEE Photonics Technology Letters 20(12), 1000-1002. ISSN: 1041-1135

    Contribution 20%: Papakonstantinou, I and the author measured the measured translation misalignment tolerances and the optical transmission loss of waveguide tapered bends for the 1st time in the world.

11. Papakonstantinou, I., Selviah, D.R., Wang, K., Pitwon, R.A., Hopkins, K., Milward, D. (2008). Optical 8-Channel, 10 Gb/s MT Pluggable Connector Alignment Technology for precision coupling of laser and photodiode arrays to polymer waveguide arrays for Optical Board-to-Board Interconnects. IEEE 57th Electronic Components and Technology Conference, ECTC '08, Florida, USA

    Contribution 15%: Papakonstantinou, I and the author experimentally measured the waveguide translation misalignment tolerances.

12. Selviah, D.R., Fernández, F.A., Papakonstantinou, I., Wang, K., Baghsiahi, H., Walker, A.C., McCarthy, A., Suyal, H., Hutt, D.A., Conway, P., Chappell, J., Zakariyah, S.S., Milward, D. (2008). Integrated Optical and Electronic Interconnect Printed Circuit Board Manufacturing. Circuit World 34(2), 21-26. ISSN: 0305-6120

    Contribution 15%: the author investigated the commercial and technological benefits of four polymer waveguide manufacturing technologies for high data rate

printed circuit boards. Insertion loss, cross talk and misalignment tolerance on horizontal and vertical axis were measured for each waveguides fabricated by the four manufacturing technologies.

13. Selviah,D.R., Walker,A.C., Hutt,D.A., Milward,D., Wang,K., Papakonstantinou,I., Baghsiahi,H., McCarthy,A., Suyal,H., Chappell,J., Zakaraiah,S.S. (2008). Innovative Optical and Electronic Interconnect Printed Circuit Board Manufacturing Research. 2nd Electronics System-Integration Technolgy Conference (ESTC) Greenwich, UK, 1st-4th September 2008.

    Contribution 20%: the author investigated the commercial and technological benefits of four polymer waveguide manufacturing technologies for high data rate printed circuit boards was developed and compared. Insertion loss, cross talk and misalignment tolerance on horizontal and vertical axis were measured for each waveguides fabricated by the four manufacturing technologies. the author made the presentation slides.

14. Selviah,D.R., Wang,K., Baghsiahi,H, Papakonstantinou,I., Fernández,F.A. (2008). Invited Paper: Design Rules for Polymer Waveguides and measurement techniques. IEEE LEOS International Symposium on Advanced Packaging, Munich, 22nd November 2008,

    Contribution 70%: the author designed the most compact and complex multimode waveguide layout in the world, experimentally measured waveguide components: straight waveguides, crossings at non-orthogonal angles and tapered bends and derived waveguide design rules.

15. Selviah,D.R., Wang,K., Baghsiahi,H., Pitwon,R., Milward,D. (2008), ECOC, Brussels, 22nd-24th September 2008, Xyratex Stand 151.

    Contribution 40%: the author prepared posters, presentations and worked in the exhibition stand.

16. Wang, K., Selviah, D.R., Baghsiahi, H., Fernández, F.A., Papakonstantinou, I., Yu, G. Invited Paper: Design Rules for Polymer Waveguides and Measurement Techniques. 2nd International IEEE Symposium on Photonic Packaging Electrical Optical Circuit Board and Optical Backplane Sponsored by Fraunhofer IZM, VDI/VDE, IEEE-CPMT and IEEE-LEOS, Messe München, Munich, 13th November 2008.

    Contribution: the author designed the world most compact multimode waveguide layout, experimentally measured waveguide components: straight waveguides, crossings at non-orthogonal angles and tapered bends and derived waveguide design rules for the photolithographically manufactured acrylate multimode optical waveguide.

17. Wang, K., Selviah, D.R., Papakonstantinou, I., Yu, G., Baghsiahi, H and Fernández, F.A (2008). Photolithographically Manufactured Acrylate Multimode

Optical Waveguide Loss Design Rules. 2nd Electronics System-Integration Technolgy Conference (ESTC) Greenwich, UK, 1st-4th September 2008, Session Th-P-9 Optoelectronics: Interconnect Design and Applications.

Contribution: the author experimentally measured waveguide components: straight waveguides, crossings at non-orthogonal angles and tapered bends and derived waveguide design rules for the 1st time in the world. The author made slides and presented the work in the conference.

18. Selviah,D.R, Wang,K. (2007), Patent System and Method for Vehicular real time synthetic imaging.

    Contribution 60%: the author developed programs using Matlab to implement the method.

19. Selviah,D.R., Wang,K., Richards,M. (2007). The AutoEye Mark 1 Vehicle Rear View Camera Vision system. Displays and Lighting on the Move, Willams Formula 1 Centre, UK Displays and Lighting (UKDL)

    Contribution 80%: the author designed and assembled the first functional prototype,

20. Papakonstantinou,I., Wang,K., Selviah,D.R., Fernández,F.A. (2006). Experimental Study of Bend and Propagation Loss in Curved Polymer Channel Waveguides for High Bit Rate Optical Interconnections. IEEE/LEOS 17th Annual Workshop on Interconnections with High Speed Digital Systems, Santa Fe, New Mexico, USA, 14-17 May 2006:IEEE

    Contribution 20%: Papakonstantinou, I and the author investigated the waveguide bends experimentally that resulted in separating out the various loss components involved and thus in identifying the most severe ones.

21. Pitwon,R., Hopkins,K., Milward,D., Selviah,D.R, Papakonstantinou,I., Wang,K., Fernández,F.A. (2006). High speed pluggable optical backplane connector. Fraunhofer IZM and VDI/VDE-IT International Symposium on Photonic Packaging: Electrical Optical Circuit Board and Optical Backplane, Munich, Germany, 16th November 2006:Fraunhofer IZM and VDI/VDE-IT

    Contribution 30%: the author designed the multimode waveguide layout design, experimentally measured waveguide components: straight waveguides, crossings at non-orthogonal angles and bends and derived waveguide design rules.

22. Selviah,D.R., Wang,K., Xia,M. (2005). Invited Paper: Modelling New Backlight Technologies. UKDN, UK Displays Network "Lighting and Backlighting“ Seminar, Bletchley Park, UK:UKDN

    Contribution 80%: the author modelled a novel colour separation backlight for LCDs using ray tracing method. The author invented embedded metallic mirrors in

the light guide and the modelled result proved that the efficiency of the backlight improved by 38.2%.

23. Wang, K., Gardner, M.C., Day, S.E., Fernandez, F.A., Sarayeddine, K., Benoit, P. (2005). Modelling the effect of angular variations of the optical properties of a nematic liquid crystal in an LCOS rear projection TV system. Eurodisplay 2005, 25th International Display Research Conference, Edinburgh, UK, 20-22 Sept. 2005, 120-123

    Contribution: the author modelled the optical properties of a nematic liquid crystal in an LCOS rear projection TV system using a novel technique which combined a model of the liquid crystal director model and a LCOS optics model with ray tracing.

24. Wang, K., Selviah, D.R. (2005). Invited Paper: Modelling of a Colour Separating Backlight for Liquid Crystal Displays. SID annual general meeting 2005, Optics of Displays, Knebworth House, Stevenage, UK

    Contribution: the author modelled a novel colour separation backlight for LCDs using ray tracing method. The author invented embedded metallic mirrors in the backlight and the modelled result proved that the efficiency of the backlight improved by 38.2%.

25. Selviah,D.R and Wang,K. (2004). Modelling of a Colour-Separating Backlight with Internal Mirrors. SID, Society of Information Display International Symposium Digest of Technical Papers, XXXV (1), pp. 487-489

    Contribution: the author modelled a novel colour separation backlight for LCDs using ray tracing method. The author invented embedded metallic mirrors in the backlight and the modelled result proved that the efficiency of the backlight improved by 38.2%.

26. Selviah,D.R. and Wang,K. (2003). Light guide with internal mirror array for LCD backlight. Institute of Physics Optical Group & DMAC, ‘ Micro-optics and Metrology ’ meeting, Cambridge: IOP

    Contribution 80%: the author modelled a novel colour separation backlight for LCDs using ray tracing method. the author invented embedded metallic mirrors in the light guide and the modelled result proved that the efficiency of the backlight improved by 38.2%.

Publication in Progress:

1. Wang, K; Selviah, DR; Yu, G; Papakonstantinou, I; Ray Trace Modelling and Measurement of Optical Loss at a Multimode Polymer Waveguide Crossing. Journal of Lightwave Technology

2. Wang, K; Selviah, DR; Papakonstantinou, I; Baghsiahi, H; Pitwon, RCA Development of Design Rules for Polymer Optical Waveguides, Journal of Lightwave Technology